POLITECHNIKA GDAŃSKA

Imię i nazwisko autora rozprawy: **Agata Ducka**
Dyscyplina naukowa: **Inżynieria Materiałowa**

ROZPRAWA DOKTORSKA

Tytuł rozprawy w języku polskim: **Kontrolowanie właściwości funkcjonalnych perowskitów poprzez domieszkowanie metalami przejściowymi**

Tytuł rozprawy w języku angielskim: **Controlling functional properties of perovskites via transition metal doping**

Promotor
dr hab. inż. Beata Bochentyn

Gdańsk, rok 2026

GDAŃSK UNIVERSITY OF TECHNOLOGY

The author of the doctoral dissertation: **Agata Ducka**
Scientific discipline: **Materials Engineering**

DOCTORAL DISSERTATION

Title of doctoral dissertation: **Controlling functional properties of perovskites via transition metal doping**

Title of doctoral dissertation (in Polish): **Kontrolowanie właściwości funkcjonalnych perowskitów poprzez domieszkowanie metalami przejściowymi**

Supervisor
dr hab. inż. Beata Bochentyn

Gdańsk, year 2026

Babci Jasi oraz Rodzicom

"Staring at the blank page before you
Open up the dirty window
Let the sun illuminate the words that you could not find

[…]

No one else, no one else
Can speak the words on your lips
Drench yourself in words unspoken
Live your life with arms wide open
Today is where your book begins

The rest is still unwritten"

Natasha Bedingfield

Table of contents

Abstract 5

Streszczenie 7

List of symbols and abbreviations 9

1. Introduction 14

1.1. Scientific motivation 14

1.2. Research gap 17

1.3. Aim of the work and scientific hypotheses 18

2. Theoretical background 20

2.1. Solid Oxide Cells 20

2.1.1. Solid Oxide Fuel Cell 20

2.1.2. Solid Oxide Electrolysis Cell 25

2.2. Materials for SOCs 27

2.2.1. Requirements 27

2.2.2. State of the art materials 29

2.3. Perovskites 33

2.3.1. Single perovskite - $SrTiO_{3-\delta}$ 33

2.3.2. Double perovskite - $Sr_2Fe_{1.5}Mo_{0.5}O_{6-\delta}$ 35

2.3.3. Ruddlesden-Popper layered perovskite – $Sr_3Fe_{1.5}Mo_{0.5}O_{7-\delta}$ 42

2.4. Exsolution 43

2.4.1. Fundamentals and thermodynamics of the exsolution 43

2.4.2. Alternative exsolution pathways 49

2.4.3. Benefits of the exsolution 51

2.4.4. Exsolution from the fluorite structures 52

3. Materials and methods 55

3.1. Synthesis procedure and reduction 55

3.1.1. $SrTiO_{3-\delta}$ 55

3.1.2. $Sr_2Fe_{1.5}Mo_{0.5}O_{6-\delta}$ 56

3.2. Phase and structural characterization 57

3.2.1. X-ray diffraction 57

3.2.2. Electron microscopy 58

3.2.3. Specific surface area 59
3.2.4. Porosity 59
3.3. Thermal characterization 60
3.3.1. Temperature-programmed techniques 60
3.3.2. Differential Scanning Calorimetry and Thermogravimetry 60
3.3.3. Dilatometry 61
3.4. Electrical characterization 61
3.5. Catalytic characterization 62
3.6. Synchrotron studies 63
3.6.1. Soft X-rays – PIRX 63
3.6.2. Tender X-rays – ASTRA 64
3.6.3. Hard X-rays – LISA 64
4. Results and discussion 66
4.1. Strontium titanate – $SrTiO_{3-\delta}$ 66
4.1.1. Impact of the secondary transition metal on the properties of Ni-doped LSCT 66
4.2. Strontium ferrite molybdate - $Sr_2Fe_{1.5}Mo_{0.5}O_{6-\delta}$ 86
4.2.1. Influence of the lanthanum and niobium doping on the redox stability of SFM 86
4.2.2. Exsolution of the Ni and Co nanoparticles from LSFM lattice for enhanced catalytic efficiency 101
4.2.3. Stabilization of Cu-doped LSFM decorated with bimetallic nanoparticles for efficient RWGS catalyst 111
4.2.4. Dual-doping with Cu-Co or Cu-Ni of the B-site of LSFM for improved stability and intense exsolution 129
5. Summary and final conclusions 134
List of the candidate's publications and achievements 137
List of figures 140
List of tables 144
Literature 145

This research has been supported by the National Science Center under grants: PRELUDIUM No. NCN 2022/45/N/ST5/02933, in which the PhD candidate Agata Ducka is a Principal Investigator, SONATA BIS No. NCN 2021/42/E/ST5/00450, and OPUS No NCN 2021/43/B/ST8/01831.

This thesis was partially developed under the provision of the Polish Ministry and Higher Education project "Support for research and development with the use of research infrastructure of the National Synchrotron Radiation Centre SOLARIS" under contract no 1/SOL/2021/2. We acknowledge SOLARIS Centre for the access to the PIRX and ASTRA beamlines, where the measurements were performed. The access to the European Synchrotron Radiation Facility (France) and National Institute of Material Physics (Romania) was provided by the CERIC-ERIC consortium.

Abstract

The aim of this thesis is the doping of the different perovskite host lattices (single and double perovskites) with affordable transition metals (Fe, Co, Ni, and/or Cu) in order to perform the exsolution process from these oxides. Alongside with the exsolution phenomenon, materials properties like redox stability, reducibility, atomic and electronic states, electrical conductivity, or catalytic performance would be determined with respect to specific host and dopant type. Such an approach will be undertaken with respect to the requirements for SOC electrode materials, thereby this research will allow to select the most promising candidates to use in these electrochemical devices.

In LSCT (La, Ce-doped STO), B-site doping with Ni and a secondary transition metal (Fe, Co, or Cu) allows to obtain single-phase perovskites characterized by thermal expansion compatible with YSZ-based SOC components. After the reduction, these materials retain the perovskite structure and exsolve bimetallic nanoparticles. STEM-EDS analyses allowed to determine the exact composition of these structures, which are Ni_3Fe and $Co_{2.5}Ni$, in agreement with predictions from the respective phase diagrams. Secondary transition metals enhance Ni reducibility, but the highest nanoparticle fraction is still obtained in LSCT-Ni, where the Ni content is the highest. The advanced XAS analyses were performed for these materials, not only on the transition metals edges but also titanium $L_{3,2}$-edge, which proved that Ti^{4+} remains unaffected by the doping type and is not reduced at the reduction temperature of 900 °C. The measurements were also conducted at cerium $M_{5,4}$-edges, providing deep spectroscopic analyses. It was also found that reduction converts low, thermally-activated conductivity in air into partially metallic behavior (up to ~10 S cm^{-1}) for selected compositions.

For SFM double-perovskites, La and Nb doping at A- and B-sites, respectively, yields the formation of cubic phase which transforms to the Ruddlesden-Popper layered perovskite upon reductive conditions. The La-doping (LSFM) leads to the highest redox stability compared to pristine and Nb-doped SFM. The phase transition was found to be reversible and in-situ studies show that re-oxidation above 700 °C restores the double-perovskite structure, with Fe reincorporation beginning near 300 °C. Apart of better redox stability, the La-doping also improves the conductivity in air and hydrogen, identifying LSFM as the most robust host.

Subsequent B-site doping of LSFM with Ni or Co, at various concentrations significantly enhances the exsolution phenomenon under reducing conditions. With increasing dopant content, very intense formation of metallic nanoparticles is observed on the perovskite surface, and these exsolved species evolve to highly dense, almost semi-continuous layers at the highest doping levels. This extensive exsolution is accompanied by progressive formation of a Ruddlesden-Popper layered

perovskite phase, indicating a close link between strong exsolution and the phase decomposition. The conductivity in air and hydrogen was also studied. In air the conductivity gradually increases with the dopant concentration but no specific trend is observed in hydrogen, as the contribution of RP phase share and higher porosity is complex and cannot be neglected. Moreover, it was found in catalytical tests that Ni-doped LSFM shows superior behavior in RWGS reaction with outstanding CO_2 reduction, as a result achieving more than 90% of thermodynamical CO concentration in outlet stream.

Cu-doping of LSFM shows even further enhanced redox stability with RP phase formed only for the highest dopant concentration and the highest reduction temperature. Despite the stability, the nanoparticles were still exsolved on the surface; however, their number was significantly lower than Ni- or Co-doped ones. Additionally, the reduction temperature was a crucial factor in LSFCMs, as the nanometric copper has lower melting temperature and can migrate at higher temperatures or even evaporate from the surface. The STEM-EDS mapping revealed novel quasi core-shell like structures with iron core partially surrounded by Cu-rich spots. Combining XAS and TPR analyses, the enhanced reducibility of the iron was established after copper doping. After the electrical tests, undiscovered before, dendritic 2D structures were revealed, formed only after high-temperature, hydrogen and electrical field combined. Lastly, the excellent catalytic performance was shown with pivotal role of Cu nanoparticles promoting the RWGS reaction.

Finally, preliminary dual B-site doping with Ni+Cu or Co+Cu (total concentration 0.2) allows to obtain mainly double-perovskite phases that remain cubic after reduction at 750 °C but transform partially to Ruddlesden-Popper layered phases at 800 °C. Higher Cu contents enhance structural stability but do not fully suppress the phase transition. Exsolution remains substantial, and ternary nanoparticles combining Fe-Ni regions with Cu-rich shells link behaviors observed in the single-doped systems.

Overall, the work in this thesis shows that rational A- and B-site doping of STO- and SFM-based perovskites enables control of exsolution, phase stability, electrical transport and catalytic performance. Strong exsolution in double perovskites can drive phase decomposition, while Cu doping offers a promising route to combine high redox activity with structural robustness. Ongoing research will further explore dual doping of LSFM and address full-cell fabrication, which remains limited by thermal-expansion mismatch.

Keywords: exsolution, perovskites, doping, strontium titanate, strontium ferrite molybdate

Streszczenie

Celem niniejszej pracy jest weryfikacja wpływu domieszkowania materiałów o strukturze perowskitu (pojedynczego $SrTiO_{3-\delta}$ – STO oraz podwójnego $Sr_2Fe_{1.5}Mo_{0.5}O_{6-\delta}$ – SFM) metalami przejściowymi (Fe, Co, Ni lub Co) oraz zbadanie zdolności do kontrolowanej eksolucji metalicznych nanocząstek. Dodatkowo zbadano także wpływ wprowadzonych domieszek na stabilność w warunkach pracy ogniw SOC oraz określono właściwości istotne z punktu widzenia tych urządzeń elektrochemicznych takie jak przewodnictwo elektryczne czy właściwości katalityczne.

Jako pierwszy materiał wybrano tytanian strontu domieszkowany lantanem oraz cerem w podsieci A. Poprzez wprowadzenie niklu oraz dodatkowego metalu przejściowego (Fe, Co lub Cu) otrzymano jednofazowy perowskit, którego współczynnik rozszerzalności termicznej jest porównywalny z wartościami odpowiadającymi elektrolitowi z YSZ czy cermetowi niklowemu. Po redukcji struktura regularna perowskitu pozostaje stabilna i nie ulega zmianom strukturalnym. Jednocześnie na powierzchni materiału pojawiają się bimetaliczne nanocząstki, co zostało uwidocznione podczas obrazowania TEM. Wykorzystanie mapowania STEM-EDS pozwoliło na określenie dokładnego składu wydzielonych nanocząstek jako Ni_3Fe oraz $Co_{2.5}Ni$. Wprowadzenie dodatkowego metalu przejściowego ułatwia redukcję niklu, jednak najwięcej nanocząstek pojawia się dla LSCT-Ni, co wynika z największej koncentracji niklu w tym składzie. Wykorzystane techniki spektroskopowe (XAS) pozwoliły także potwierdzić wysoką stabilność jonów Ti^{4+}, których stan pozostał niezmienny po redukcji w 900 °C. W wyniku redukcji słaba przewodność o charakterze półprzewodnikowym jest zwiększona (do około 10 S cm^{-1}) oraz charakter zmienia się na metaliczny dla większości prezentowanych domieszek.

W przypadku podwójnych perowskitów SFM, jako pierwszy zbadano wpływ domieszkowania lantanem oraz niobem odpowiednio w podsieci A oraz B. Odkryto, że struktura regularna w trakcie redukcji ulega przekształceniu w perowskit warstwowy Ruddlesdena-Poppera, przy czym najmniejszy udział nowej fazy był obserwowany dla związku domieszkowanego lantanem. Co więcej, zaobserwowano, że pod wpływem grzania w powietrzu, przejście fazowe jest odwracalne i powstaje podwójny perowskit. Przeprowadzone badania in-situ wykazały, że do temperatury 300 °C żelazo wbudowuje się w strukturę, a następnie w temperaturze do 700 °C następuje przejście strukturalne z perowskitu warstwowego do oryginalnej struktury perowskitu podwójnego. Domieszkowanie lantanem nie tylko okazało się być korzystne dla stabilności układu, ale także powoduje zwiększenie przewodnictwa elektrycznego zarówno w powietrzu jak i atmosferze wodoru. Biorąc pod uwagę powyższe benefity, LSFM został wybrany jako podstawa do dalszego domieszkowania i kolejnych badań.

Jako pierwszą domieszkę do podsieci B w LSFM wybrano nikiel lub kobalt. Zaobserwowano, że w wypadku obu tych domieszek, redukcja prowadzi do bardzo intensywnej eksolucji. Dodatkowo wraz ze zwiększającą się koncentracją domieszki, intensywność dalej rośnie, aż prowadzi do powstania pół-ciągłej warstwy na powierzchni nanocząstek. Niestety, tak znacząca eksolucja prowadzi także do powstania znaczącej ilości fazy Ruddlesdena-Poppera, co silnie sugeruje związek między eksolucją, a przejściem fazowym. Zbadano przewodnictwo elektryczne i w powietrzu zaobserwowano związek między koncentracją domieszki, a rosnącą przewodnością. Niestety, w wodorze nie można powiązać ilości domieszki z wynikami, ponieważ powstaje nowa faza RP, która powoduje spadek mechanicznej stabilności próbek. Co więcej, w wykonanych badaniach katalitycznych, wykazano, że LSFM domieszkowany niklem daje się poznać jako świetny katalizator do reakcji RWGS, osiągając ponad 90% teoretycznej koncentracji CO.

Następnie zbadano domieszkowanie LSFM miedzią i odkryto, że dodatek tego metalu przejściowego powoduje dodatkowo zwiększenie stabilności materiału w warunkach redukujących. Jednocześnie, związki te ciągle są zdolne do procesu eksolucji, ale w mniejszym stopniu niż ich odpowiednik z niklem czy kobaltem. Analiza STEM z mapowaniem EDS wykazała powstanie nowych struktur przypominających rdzeń-powłoka, z żelaznym rdzeniem częściowo otoczonym miedzią. Wykorzystane analizy XAS oraz TPR pokazały, że dodatek miedzi ułatwia redukcję żelaza. Odkryto także, że po pełnych testach elektrycznych, powstają rozbudowane, dendrytyczne struktury 2D, które nie były nigdy wcześniej opisane w literaturze dla tego typu związków. Zbadano także właściwości katalityczne podwójnych perowskitów i odkryto kluczową rolę miedzi w reakcji RWGS.

Jako ostatnie wykonano badania wstępne domieszkując podsieć B jednocześnie miedzią oraz niklem lub kobaltem. Odkryto, że w wyniku takiego domieszkowania struktura podwójnego perowskitu pozostaje stabilna po redukcji w 750 °C, ale w 800 ° następuje częściowe przejście fazowe do struktury RP. Im większy dodatek miedzi, tym struktura pozostawała stabilniejsza, ale niemożliwe było całkowite zatrzymanie przemiany. W wyniku obrazowania odkryto powstawanie trójskładnikowych nanocząstek składających się z rdzenia z Fe-Ni otoczonych miedzią, co łączy obserwacje dla wcześniej opisanych układów.

Podsumowując, niniejsza rozprawa pokazuje, że w wyniku domieszkowania STO oraz SFM możliwe jest kontrolowanie zarówno eksolucji, stabilności redoks, transportu elektrycznego jak i właściwości katalitycznych. Pokazano, że silna eksolucja może, niestety, pociągnąć za sobą przejście fazowe, a dodatek innych metali przejściowych może ułatwiać redukcję m.in. żelaza czy niklu. Dalsze badania skupią się na zbadaniu synergistycznych efektów w podwójnie domieszkowanych LSFM.

Słowa kluczowe: eksolucja, perowskity, domieszkowanie, tytanian strontu, żelazian molibdenian strontu

List of symbols and abbreviations

Abbreviations

ADF Angular Dark Field

AFC Alkaline Fuel Cell

AFL Anode Functional Layer

ALD Atomic Layer Deposition

AP As-prepared

APB Antiphase Boundary

AS Antisite (defect)

BET Brunauer-Emmet-Teller (isotherm)

CIF Crystallography Information File

CRM Critical Raw Material

CVD Chemical Vapor Deposition

DFT Density Functional Theory

DI Deionized Water

DP Double Perovskite

DOS Density of States

DRM Dry Reforming of Methane

ESRF European Synchrotron Radiation Facility

FIB Focused Ion Beam

FT Fourier Transform

GHSV Gas Hourly Space Velocity (h^{-1})

GOF Goodness of Fit

H-SOFC Solid Oxide Fuel Cell (with proton conductor as electrolyte)

HER Hydrogen Evolution Reaction

LT-SOC Low-Temperature Solid Oxide Cell

MCFC Molten Carbonates Fuel Cell

MIEC Mixed Ionic-Electronic Conductor

NPs Nanoparticles

O-SOFC Solid Oxide Fuel Cell (with oxygen ion conductor as electrolyte)

OCV Open Circuit Voltage

ORR Oxygen Reduction Reaction

PAFC Phosphoric Acid Fuel Cell

PDOS Projected Density of States

PEMFC Proton Exchange Membrane Fuel Cell

PFY Partial Fluorescence Yield

PMMA Poly(methyl methacrylate)

PVD Physical Vapor Deposition

RP Ruddlesden-Popper Layered Perovskite

RT Room Temperature

RWGS Reverse Water-Gas Shift

SOEC Solid Oxide Electrolysis Cell

SOFC Solid Oxide Fuel Cell

SOC Solid Oxide Cell

SDD Silicon Drift Detector

SSA Specific Surface Area

sSOFC Symmetrical Solid Oxide Fuel Cell

TEC Thermal Expansion Coefficient

TEY Total Electron Yield

TCD Thermal Conductivity Detector

TPB Triple-Phase Boundary

TRL Technology Readiness Level

UHV Ultra-High Vacuum

WHSV Weigh Hourly Space Velocity (mL g^{-1} h^{-1})

Techniques

DC4W Direct-Current 4-Wire (Method)

DRT Distribution of Relaxation Times

DSC Differential Scanning Calorimetry

EDS Energy Dispersive X-Ray Spectroscopy

EIS Electrical Impedance Spectroscopy

EXAFS Extended X-Ray Absorption Fine Structure

H_2-TPR Temperature Programmed Reduction

O_2-TPO Temperature Programmed Oxidation

PEEM Photoelectron Emission Microscopy

SAED Selected Area Electron Diffraction

SEM Scanning Electron Microscopy

STA Simultaneous Thermal Analysis (TG&DSC)

TEM Transmission Electron Microscopy

TG Thermogravimetry

TPx Temperature Programmed Techniques

XANES X-Ray Absorption Near Edge Structure

XAS X-Ray Absorption

XRD X-Ray Diffraction

Materials and compounds:

CA Citric Acid

CGO/GDC Cerium-Gadolinium Oxide/Gadolinium-Doped Ceria

EG Ethylene Glycol

LSC $La_{1-x}Sr_xCoO_{3-\delta}$

LSCF $La_{1-x}Sr_xCo_{1-y}Fe_yO_{3-\delta}$

LSCT-Ni $(La_{0.3}Ce_{0.1}Sr_{0.6})_{0.9}Ti_{0.9}Ni_{0.1}O_{3-\delta}$

LSCT-NiFe $(La_{0.3}Ce_{0.1}Sr_{0.6})_{0.9}Ti_{0.9}Ni_{0.05}Fe_{0.05}O_{3-\delta}$

LSCT-NiCo $(La_{0.3}Ce_{0.1}Sr_{0.6})_{0.9}Ti_{0.9}Ni_{0.05}Co_{0.05}O_{3-\delta}$

LSCT-NiCu $(La_{0.3}Ce_{0.1}Sr_{0.6})_{0.9}Ti_{0.9}Ni_{0.05}Cu_{0.05}O_{3-\delta}$

LSFM $La_{0.3}Sr_{1.7}Fe_{1.5}Mo_{0.5}O_{6-\delta}$

LSGM $La_{0.8}Sr_{0.2}Ga_{0.8}Mg_{0.2}O_{3-\delta}$

LSM $La_{1-x}Sr_xMnO_{3-\delta}$

Ni-CGO/GDC Composite of Ni and Cerium-Gadolinium Oxide

Ni-YSZ Composite of Ni and Yttria Stabilized Zirconia (nickel cermet)

SFM $Sr_2Fe_{1.5}Mo_{0.5}O_{6-\delta}$

SFMNb $Sr_2Fe_{1.425}Mo_{0.475}Nb_{0.1}O_{6-\delta}$

STO $SrTiO_{3-\delta}$

YSZ Yttria Stabilized Zirconia

8YSZ Yttria (8 mol. %) Stabilized Zirconia $Y_{0.16}Zr_{0.84}O_{2-\delta}$

x-LSFMNi $La_{0.3}Sr_{1.7}Fe_{1.5-0.75x}Mo_{0.5-0.25x}Ni_xO_{6-\delta}$

x-LSFMCo $La_{0.3}Sr_{1.7}Fe_{1.5-0.75x}Mo_{0.5-0.25x}Co_xO_{6-\delta}$

x-LSFCM $La_{0.3}Sr_{1.7}Fe_{1.5-0.75x}Mo_{0.5-0.25x}Cu_xO_{6-\delta}$

x-y-LSFNCM $La_{0.3}Sr_{1.7}Fe_{1.35}Mo_{0.45}(Ni_{1-x}Cu_x)_{0.2}O_{6-\delta}$

x-y-LSFCCM $La_{0.3}Sr_{1.7}Fe_{1.35}Mo_{0.45}(Co_{1-x}Cu_x)_{0.2}O_{6-\delta}$

Ions or defects:

$\mathbf{H^+}$ hydrogen ion (proton)

$\mathbf{H^*}$ hydrogen radical

$\mathbf{O^{2-}}$ oxygen ion

$\mathbf{v_O^{\cdot\cdot}}$ oxygen vacancy with 2+ relative charge

$\mathbf{e}'$	Electron
$\mathbf{h}^{\cdot}$	electron hole
$\mathbf{M}_{\mathbf{N}}^{\mathbf{n}\cdot}$	M ion at N-position with n+ relative charge
$\mathbf{M}_{\mathbf{N}}^{\mathbf{n}'}$	M ion at N-position with n- relative charge

Symbols (as they appear in text):

ΔG	change of Gibbs free energy (J)
ΔH	change of enthalpy (J mol^{-1})
ΔS	change of entropy (J K^{-1})
ΔT	change of temperature (K)
W_{el}	electrical work (J)
Q	elemental charge ($1.602 \cdot 10^{-19}$ C)
F	Faraday constant ($9.648 \cdot 10^{4}$ C mol^{-1})
E	cell voltage (V)
E^{0}	standard potential of the reaction/reversible potential (V)
R	gas constant (8.314 J mol^{-1} K^{-1})
T	absolute temperature (K)
a_X	activity of species X (e.g. aH_2O is the activity of water)
pX	partial pressure of species X (e.g. pO_2 is the oxygen partial pressure)
U_{SOFC}	voltage of the SOFC (V)
η_{act}	activation losses
η_{Ohm}	ohmic losses
η_{conc}	concentration losses
R_{Ohm}	ohmic resistance of the cell
R_{pol}	polarization resistance of the cell
σ_{el}	electrical conductivity (S cm^{-1})
σ_{ox}	oxygen ionic conductivity (S cm^{-1})
t	Goldschmidt tolerance factor
r_x	ionic radius of element x (Å)
δ	oxygen deficiency
$g_{A/B}$	occupancy of A- or B-site cation at its correct site
Z_x	oxidation state of x element in the lattice
E_{seg}	co-segregation energy (eV)
A_{sur}, A_{int}	area of surface and interface, respectively
γ_{sur}, γ_{int}	surface and interface tension, respectively

k_B	Boltzmann constant ($1.38 \cdot 10^{-23}$ J K^{-1})
E_{strain}	strain activation energy
$E_{diffusion}$	diffusion activation energy
θ	contact angle of nanoparticle
φ	dihedral angle of nanoparticle
r	nanoparticle radius
r^*	critical radius of nanoparticle
ρ	density (g cm^{-3})
P_{total}	total porosity (%)
P_o	open porosity (%)
σ_{corr}	conductivity corrected for porosity (from Bruggeman correction)

1. Introduction

1.1. Scientific motivation

Transformation of energy systems is one of the main challenges of the 21st century. Continuous global population growth, coupled with the expansion of numerous industrial sectors, has led to a substantial increase in electricity demand. Currently, the majority of electricity generation remains dependent on fossil fuels, which are inherently finite resources. Furthermore, the combustion of fossil fuels, such as coal and natural gas, results in significant emissions of greenhouse gasses, thereby exerting a profound impact on the environment. Consequently, the transition to renewable energy sources (wind, solar, and geothermal energy) is unavoidable. Initiatives such as the European Green Deal exemplify coordinated efforts to reorient the European Union's energy sector toward more sustainable pathways. The primary objective of this framework is to achieve net-zero greenhouse gas emissions by 2050. Its implementation is also expected to enhance the emphasis on a circular economy and further promote the development and integration of clean energy technologies.

As mentioned above, renewables fit into the idea of a Green Deal as no greenhouses are emitted during their use. Unfortunately, they also suffer from their intermittent nature. Whether solar or wind, they are strongly dependent on the season, part of the day, or overall climate conditions. Thus, their efficiency could be limited locally. Moreover, for example, solar energy reaches a production peak during the day, when the overall energy consumption is lower, resulting in misalignment between energy producers and consumers. In this case, energy must be stored or would go to waste. One of the well-known methods to store energy are the batteries; however, they very often rely on the use of Critical Raw Materials (CRMs) such as lithium. These materials are classified as crucial for global development, but their availability can be limited due to geopolitical issues. Among CRMs, cobalt can also be found; thus, in this work these materials are used in a lower amount for doping purposes only. This approach allows to minimize the use of such materials.

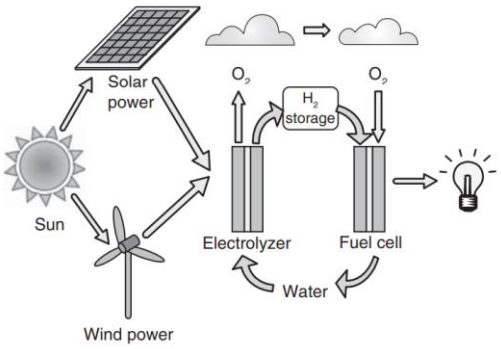


Fig. 1.1. Scheme of H_2-technology for energy conversion [1].

One of the ideas to store energy and later use it back to power devices is the use of hydrogen technologies. Hydrogen technology has emerged several years ago as a solution to aforementioned problems. Furthermore, H_2-technology suits the Green Deal assumptions. Fuel cells technology is the one of the main branches of hydrogen utilization.

The schematic view of the circular hydrogen economy is presented in **Fig. 1.1.** The general idea is to transform excessive energy into valuable chemicals (e.g. hydrogen, syngas). Such mode of operation is known as electrolysis, where electrical energy is used to produce e.g. hydrogen from water. The produced hydrogen can be latter used as a fuel in fuel cell in the times of increased energy need. In this mode the chemical energy of the fuel is transformed to the electricity [2]. Of course, this is only a simplified view of fuel cell technology. The real case is way more complicated, as many different types of fuel cells are known and developed constantly. The fuel cell technology can be briefly divided into two subgroups, regarding the working operation: low-temperature and high-temperature fuel cells. The first group consists of alkaline (AFC), proton exchange membrane (PEMFC), or phosphoric acid (PAFC) fuel cells. These are characterized by fast start-up favoring the portable use or use in transportation. However, they need expensive noble metals, like platinum or iridium, as catalysts, and do not provide the flexibility to fuels different than hydrogen. In fact, many H_2-driven devices are already in use. One of the most known examples are the H_2-fed cars or buses, which are even present on roads in Gdańsk. When it comes to cars, one example is Toyota Mirai.

The second group, high-temperature fuel cells, covers mainly molten carbonates (MCFC) and solid oxide (SOFC) fuel cells. As their working temperature is usually above 500 °C, they need more time to start up, however, their efficiency is undoubtedly higher. Although they are considered high-temperature fuel cells, in SOFC technology a shift to a lower temperature range (<600 °C) is desired and so-called IT-SOFC (intermediate-temperature SOFC) are developed for this purpose. Moreover, SOCs (Solid Oxide Cells = Solid Oxide Fuel Cell or Solid Oxide Electrolysis Cell) allow the various chemicals to be fed as a fuel. A more detailed description of SOC technology is presented in Chapter 2.1.

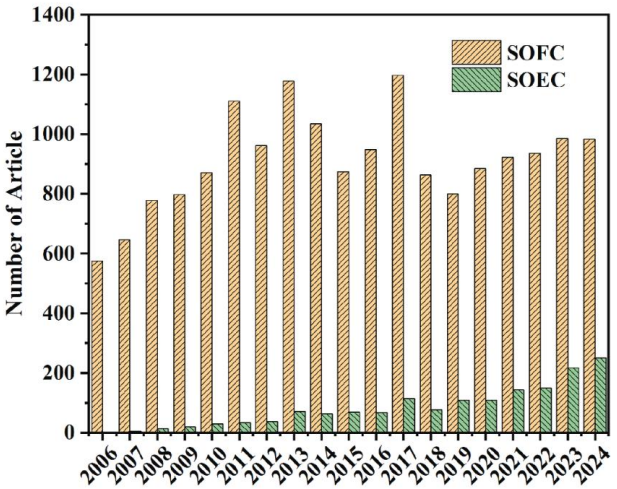


Fig. 1.2. The annual number of publications concerning SOFC or SOEC technologies searched by title in the "Web of Science" [3]

Both SOFCs and SOECs are emerging technologies that are gaining more interest in both the scientific world and the industrial field. **Fig. 1.2** presents the number of publications in the field of SOC technology from 2006, searched by title [3]. As can be clearly seen, the interest in SOFC is gradually increasing, spiking in 2011, 2013, and 2017, but amount of the publications

is impressive. At the same time, SOEC technology was significantly less studied throughout the years, but steady growth is observed.

Not only scientists are interested in the development of SOCs or understanding the mechanisms at lower TRL (Technology Readiness Level), but also several companies are developing and selling this technology. Among them, one may find the most known in the field ones:

- Elcogen AS (Estonia)
- Ceres Power Holdings (United Kingdom)
- Bloom Energy (United States of America)
- Kyocera Corporation (Japan)
- Convion (Finland)
- Sunfire (Germany) focusing on both alkaline and solid oxide electrolysis

Although SOC technology has already been well described and used on an industrial scale, some areas of development are still present. Most of these companies focus on use of the conventional materials, e.g. Ni-YSZ cermet as an anode. This material is well-known and works most efficiently with hydrogen as a fuel. As SOFC technology offers a variety of fuels to be fed, anode materials must withstand conditions other than "ideal". Unfortunately, if, e.g. hydrocarbons are fed to the anode, Ni-YSZ suffers greatly due to its high catalytic efficiency, also for carbon deposition. The formation of coke on the surface deactivates the electrode, leading to a drop in cell efficiency. The more detailed description of state-of-the-art materials and challenges will be more intensively discussed in Chapter 2.2.

One of the ways to stop the formation of surficial carbon is the use of protective layers or the development of new materials. Among the materials suggested as candidates to substitute Ni-YSZ cermet are perovskites. In general, these are oxides with formula ABO_3 and its derivatives such as double perovskites $AA'BB'O_6$. Both these groups would be described and discussed in more detail in Chapter 2.3. Perovskite oxides are found as insulators, superconductors, dielectrics, ferromagnets, antiferromagnets, spin-glasses depending on the elemental composition, electronic structure or defect engineering [4]. Due to their unique range of properties, they cover many different areas, e.g. solar cells, spintronics, magnetic sensors, and electrodes in SOCs. Moreover, they are known for their stability, which makes them particularly interesting in redox cycling in SOCs. Unfortunately, perovskites are very often poor from a catalytic point of view.

The catalytic efficiency of a perovskite host can be boosted by several methods, like infiltration or deposition of catalytically active species on the surface. Despite being relatively simple (depending

on the specific method), the surficial particles are very prone to agglomeration or deactivation upon carbon-rich atmospheres, leading to particles detachment. The other method to form the active nanoparticles is in-situ exsolution from the host lattice. In this case, the exsolved metal is introduced during the synthesis, and NPs form during the reductive treatment. This phenomenon is described in more detail in Chapter 2.4. The exsolution provides well-socketed particles with a high catalytic efficiency and less eager to agglomerate.

1.2. Research gap

Although the exsolution process has been extensively investigated over many years, the existing body of work is heavily concentrated on the formation and behavior of single-metal nanoparticles. This leaves a clear research gap in the understanding of bimetallic exsolution, despite its potential to provide unique and tunable properties arising from synergistic interactions between two metals [5,6]. While it is recognized that bimetallic systems can offer significant advantages, such as reduced temperatures required for nanoparticle exsolution, enhanced functional performance, and access to a broader range of structural configurations [5,7], these systems remain comparatively underexplored. Furthermore, the limited studies available tend to focus predominantly on compositions involving iron or nickel, as illustrated in **Fig. 1.3**, which further highlights the narrow scope of current research in this area.

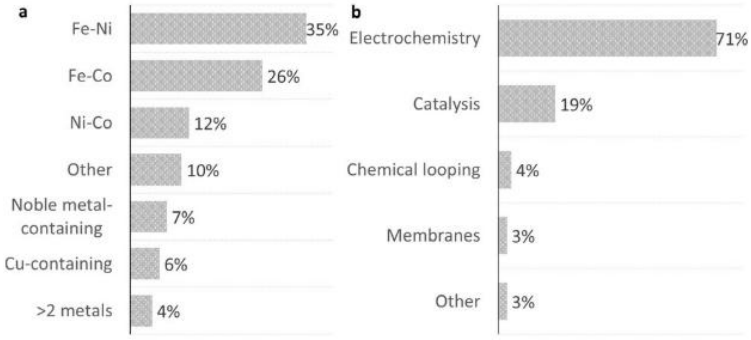


Fig. 1.3. Statistics on publications on bimetallic exsolution: compositions (a) and applications (b) [5].

The present work addresses these gaps by investigating bimetallic exsolution in two distinct material systems: single perovskite based on $SrTiO_{3-\delta}$ (STO) and double perovskite based on $Sr_2Fe_{1.5}Mo_{0.5}O_{6-\delta}$ (SFM). Although the general concept of exsolution in such systems is not entirely novel, there is a notable lack of in-depth studies that comprehensively characterize the underlying mechanisms of this process. In particular, most existing publications emphasize electrochemical performance, often overlooking fundamental aspects related to the evolution of the electronic structure during exsolution. Only a limited number of studies have examined changes in electronic states in detail [8,9], leaving this aspect insufficiently understood and representing a significant knowledge gap. An additional gap is evident in the case of SFM-based compounds, where prior research has focused

mainly on selective doping at either the Fe-site or the Mo-site within the B-lattice [10–15]. In contrast, the approach adopted in this work involves simultaneous and commensurate doping of both B-sites, while preserving the Fe:Mo ratio of 3. To the best of the author's knowledge, this strategy has not been comprehensively explored in the literature, with only a few isolated reports, mainly from the group of Lv *et al.* [16,17], that address similar concepts. This further underscores the existing research gap and motivates the detailed investigation presented here.

1.3. Aim of the work and scientific hypotheses

The aim of this thesis is the doping of the different perovskite host lattices (single and double perovskites) with affordable transition metals (Fe, Co, Ni, and/or Cu) in order to perform the exosultion process from these oxides. Alongside with the exsolution phenomenon, materials properties like redox stability, reducibility, atomic and electronic states, electrical conductivity, or catalytic performance would be determined with respect to specific host and dopant type. Such an approach will be undertaken with respect to the requirements for SOC electrode materials, thereby this research will allow to select the most promising candidates to use in electrochemical devices. The primary objective focuses on materials engineering of stable host matrices and elucidation of the exsolution phenomenon, particularly in relation to dopant incorporation.

The principal hypotheses advanced in this thesis are as follows

1. Incorporation of a secondary transition metal, together with nickel, into STO-based compounds will enhance the exsolution process and facilitate nickel reduction.
2. The double perovskite structure can be stabilized during redox cycling via aliovalent doping, such as La or Nb doping.
3. Doping of double perovskite hosts with transition metals (Ni, Co, or Cu) will promote iron exsolution from Fe-rich B-sites. Moreover, the strain introduced through phase transition would further enhance the NPs formation.
4. Owing to disparities in melting and reduction temperatures between copper and iron, exsolved nanoparticles will not form a solid Fe-Cu solution, rather cation separation will be observed.

In order to verify the stated hypotheses several auxiliary questions were formulated:

1. How does the introduction of a second transition metal modulate the electronic environment surrounding nickel in strontium titanates?
2. In double perovskites undergoing phase transitions, is the transformation reversible at both structural and electronic levels?

3. What constitutes the optimal dopant concentration in double perovskites?

Positive resolution of these hypotheses and auxiliary questions will provide novel insights into the exsolution process in single- and double-perovskite systems. Employment of advanced techniques, such as X-ray spectroscopy, will enable detailed materials characterization, particularly regarding the influence of doping and subsequent reduction on elemental electronic structures. Moreover, successful achievement of these objectives will define subsequent research directions. For instance, if La or Nb doping proves advantageous for redox stability, optimization will proceed with the most efficacious composition. The principal anticipated outcomes of this dissertation are:

- Establishment of correlations between secondary transition metal doping and nickel reducibility in STO-based compounds.
- Comprehensive analysis of double perovskites doped with diverse transition metals at varying concentrations.
- Elucidation of a mechanism governing Fe-Cu nanoparticle exsolution.

This work is divided into three main parts: theoretical background (Chapter 2), experimental methods (Chapter 3), and research results (Chapter 4). The theoretical part presents current knowledge in three subsections: solid oxide cells (SOCs), perovskites, and the exsolution process. Since the study focuses on single and double perovskites, Chapter 4 is split into corresponding sections. Each results subsection ends with a short summary of the main findings. Chapter 5 wraps up the PhD work, outlines future directions, and highlights the novelty of the research. The thesis is further augmented by lists of abbreviations, figures, tables, and references, as well as an appendix detailing the candidate's scientific activities, conference presentations, and publications.

2. Theoretical background

2.1. Solid Oxide Cells

2.1.1. Solid Oxide Fuel Cell

The Solid Oxide Fuel Cell (SOFC) is an electrochemical device, that can convert the chemical energy of the fuel (e.g. hydrogen or hydrocarbons) into electrical energy. It consists of three main constituents: porous electrodes (anode and cathode), at which the electrochemical reactions take place, and dense, impermeable electrolyte. The requirements for the materials used in the SOFC are discussed in more detail in Chapter 2.2.1. The scheme of the working SOFC principle is presented in **Fig. 2.1**. The oxidant (most commonly air) is continuously fed to the cathode side, while simultaneously fuel is delivered to the anode. If the simplest working mode is considered, where H_2 is fed to the fuel electrode, the adsorbed hydrogen is oxidized to form water (steam) and releases electrons. Because the electrolyte must be an electron insulator, the generated electrons are transferred to the cathode side by the external circuit. At the cathode, oxygen adsorption takes place, then electrons are accepted, and oxygen ions are generated. Subsequently, the O^{2-} are transferred through the oxygen ion conducting electrolyte. The driving force for the movement of oxygen ions through the electrolyte membrane is the diffusion of the ions due to the concentration gradient. The final step in this process is the recombination of O^{2-} and H_2 on the anode side, forming water. The reactions at the anode, cathode, and overall SOFC reaction are written as (2.1)-(2.3)

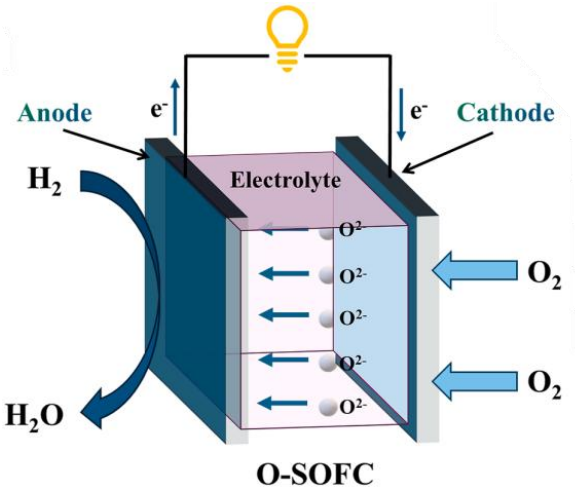


Fig. 2.1. The SOFC working principle [3].

Anode reaction: $$H_2 + O^{2-} \rightarrow H_2O + 2\,e^- \quad (2.1)$$

Cathode reaction: $$\frac{1}{2}\,O_2 + 2\,e^- \rightarrow O^{2-} \quad (2.2)$$

Overall process: $$H_2 + \frac{1}{2}O_2 \rightarrow H_2O \quad (2.3)$$

The description above considered the "so-called" O-SOFC, where the electrolyte is an oxygen-ion conducting material. There is also H-SOFC technology being developed, in which the

electrolyte is a H^+ (proton) conductor; however, this thesis will focus only on the SOC with oxygen conductor as the electrolyte.

As the overall process in SOFC is presented in (2.3), the thermodynamics of working fuel cell can be expressed by linking the Gibbs free energy, enthalpy, and entropy yielding the Eq. (2.4), but if isothermal process is to be considered, it simplifies to Eq (2.5) [1]. Moreover, from the sign of ΔG, we can determine if the reaction is spontaneous. For negative ΔG values, the spontaneous reaction is expected, while 0 is obtained for the products and reactants at equilibrium.

$$\Delta G = \Delta H - T\Delta S - S\Delta T \tag{2.4}$$

$$\Delta G = \Delta H - T\Delta S \tag{2.5}$$

The values of the reaction enthalpy and entropy can be predicted and found in the bases. The Gibbs free energy represents the energy put into the system to create it. Thus, as a result the maximum amount of energy exploited from the system cannot be larger than Gibbs free energy [1]. The correlation between Gibbs free energy and electrical work is expressed in Eq. (2.6)

$$\Delta G = -W_{el} \tag{2.6}$$

As the voltage *(E)* can be correlated with electrical work by Eq. (2.7), and the charge Q described as Eq. (2.8), the potential can be written as Eq. (2.9).

$$W_{el} = EQ \tag{2.7}$$

$$Q = nF \tag{2.8}$$

$$E^0 = -\frac{\Delta G}{nF} \tag{2.9}$$

where n – number of electrons involved in reaction

F – Faraday's constant ($9.648 \cdot 10^4$ C mol^{-1})

E^0 is a standard potential of the reaction also known as reversible potential. In fuel cell mode that is the maximum voltage output of the single cell, higher values are thermodynamically unreachable [1]. Undoubtedly this value is crucial for the assessment of SOFC but it does not consider the concentration of the gases: reactants and products. To include the impact of reagent concentration, Nernst equation was proposed (based on van't Hoff isotherm) and it is presented in Eq. (2.10) for H_2-fed SOFC and more generic in Eq. (2.11) [1].

$$E_{Nernst} = E^0 - \frac{RT}{2F}\ln\left(\frac{aH_2O}{aH_2\ aO_2^{1/2}}\right) \tag{2.10}$$

$$E_{Nernst} = E^0 - \frac{RT}{2F} \ln\left(\frac{\prod a^i_{products}}{\prod a^j_{reactants}}\right) \tag{2.11}$$

where R – gas constant (8.31 J mol^{-1} K^{-1});

T – absolute temperature (K);

F – Faraday's constant (9.648·10^4 C mol^{-1});

a_x – activity of specific species.

In general, the activity of the reagents is raised to the power of the reaction coefficient. For example, in the general SOFC reaction (2.3), the coefficients are 1, 1/2, and 1, for H_2, O_2, and H_2O respectively. That is the reason why in Eq. (2.10) aO_2 is raised to the power of 1/2, the power of unity is omitted for clarity. In case of gaseous reagents like in SOCs, the activities are identic with their partial pressures, thus Eq. (2.12) is true. The Nernst equation omits any unreactive or inert gasses [1].

$$E_{Nernst} = E^0 - \frac{RT}{2F} \ln\left(\frac{pH_2O}{pH_2\, pO_2^{1/2}}\right) \tag{2.12}$$

The values obtained for Nernst equation with respect to the partial pressure of reagents give rise to open circuit voltage (OCV) of the cell. Another very important characteristic of the working fuel cell is the i-V characteristic (**Fig. 2.2)**, from which power density of the cell can be calculated (**Fig. 2.3**). Every i-V curve would start at OCV for 0 A, following the Eq. (2.10). In general, the voltage of the fuel cell is lowered by three types of losses and can be written as Eq. (2.13), where η stands for different losses: activation (η_{act}), Ohmic (η_{Ohm}), and concentration (η_{conc}) [1].

$$U_{SOFC} = E_{Nernst} - \eta_{act} - \eta_{Ohm} - \eta_{conc} \tag{2.13}$$

In brief, the activation losses arise from the electrochemical reactions at the electrodes and its kinetics. Presence of Ohmic losses is associated with the electrical and ionic conductivity of the fuel cell elements like electrodes, electrolyte, and others like interconnects. In this area, the i-V dependence is linear as it follows the Ohm's law. The Ohmic losses are generally dominated by the resistance of the electrolyte; thus, this element should be as thin as possible [1]. Lastly, the concentration loss is related with the limitations of mass transport. In this area, the reagents are not that effectively supplied and removed from the active sites. As a result, less fuel is available leading to decrease in cell performance.

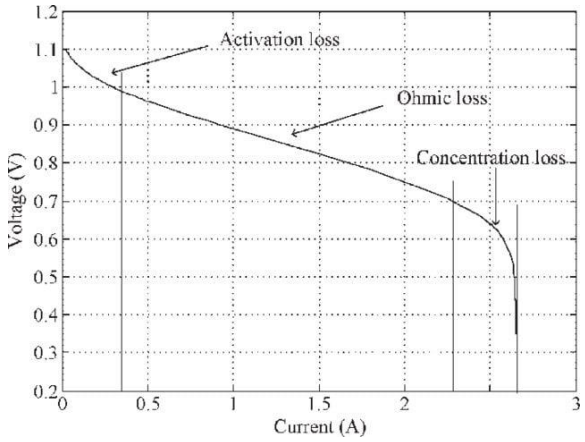


Fig. 2.2. I-V curve of the SOFC with specific losses [18].

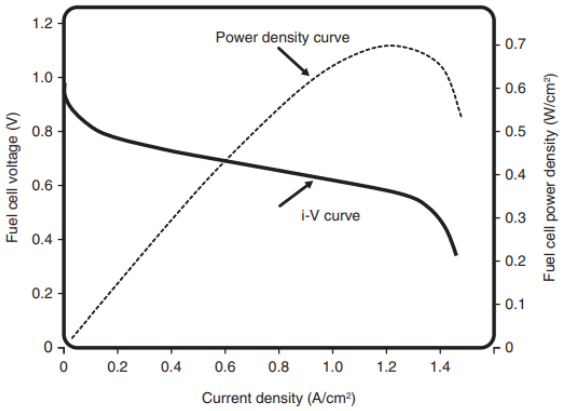


Fig. 2.3. I-V curve with power density of the SOFC [1].

One of the analytical techniques commonly used in SOFC is the Electrical Impedance Spectroscopy (EIS), which is one of the most powerful tools to analyze electrochemical performance [1]. From the basis of the EIS, one can determine not only the Ohmic resistance of the cell but also the polarization resistance. The EIS spectra are commonly plotted as a Nyquist plot where the imaginary part of resistance is plotted vs. the real part. This approach leads to the formation of characteristic semicircles as presented in **Fig. 2.4**. Each semicircle represents different processes occurring in the cell and the equivalent circuit can be modeled. From the Nyquist plots, the Ohmic (R_{Ohm}) and polarization (R_{pol}) resistances can be evaluated. R_{Ohm} can be read as an intercept of the plot with the Z' axis, while the R_{pol} is the resistance of each process (semicircle).

Due to the complicity of the cell work, several processes can overlap resulting in formation of a wider shape, further from ideal semicircles. In this case, several equivalent circuits with different time scales must be applied, which complicates the proper analysis. The EIS can be coupled with the technique called Distribution of Relaxation Times (DRT) to deconvolute the sum of parallel processes [19]. The exemplary DRT spectra are plotted in **Fig. 2.5**, and is the deconvolution of the same system as Nyquist plot from **Fig. 2.4**. Thus, the processes in **Fig. 2.4** correspond directly to the DRT peaks in **Fig. 2.5**. By altering the different parameters of the working cell such as temperature, current, pH_2, pO_2, or pH_2O, each peak can be attributed to each process. According to our previous work: Błaszczak P., Mäkinen P., Mroziński A., **Ducka A.**, Jasiński G., Himanen O., & Jasiński P. (2025). *"Uncovering the electrochemical processes and understanding the causes of the degradation via EIS-DRT in large-scale solid oxide fuel cell."* APPLIED ENERGY, 393, 125983. https://doi.org/10.1016/j.apenergy.2025.125983 [19] these processes are recognized as gas conversion (1-10 Hz), gas diffusion in the anode (10-100 Hz), mass transport, charge transfer reaction at the anode (100-1000 Hz) and ionic conduction of YSZ or LSC (>3000 Hz). Moreover, DRT studies allow

modelling and understanding the electrochemical processes that occur not only in a single cell, but can also be utilized in the analyzes of the fuel cell stacks with respect to the individual component [19].

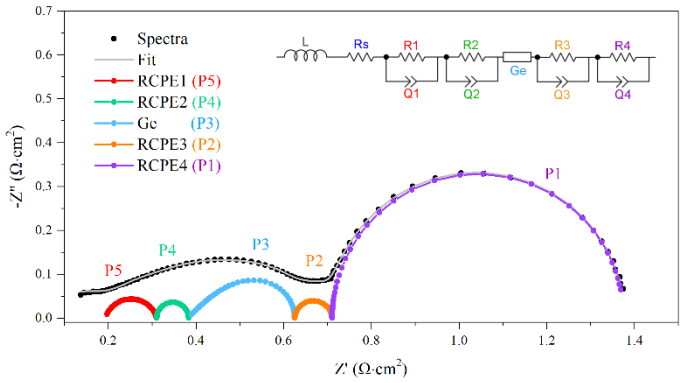


Fig. 2.4. Nyquist plot of the exemplary EIS measurement with equivalent circuit fitted [19].

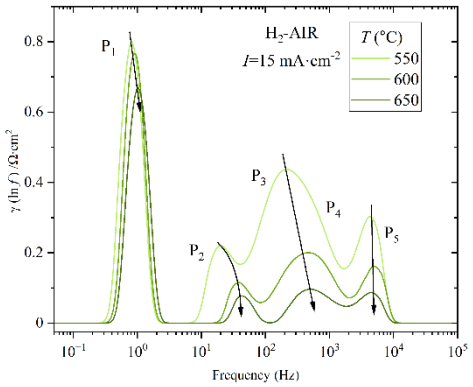


Fig. 2.5. DRT spectra of the cell at different operation temperatures [19].

The main advantage of SOFC technology compared to low-temperature fuel cells is flexibility in the fuel utilization. As mentioned above, not only hydrogen can be fed as a fuel. Among other chemicals, one may find methanol, ethanol, biogas, or ammonia, only to mention a few. As a result, the anode reaction would be more complicated with respect to the fuel used. For example, when considering biogas as a fuel, the number of possible reactions grows rapidly [20]. The exemplary reactions (for methane as fuel) with their enthalpy are listed in reactions (2.14)-(2.20) [20].

Dry reforming	$CH_4 + CO_2 \leftrightarrow 2\,CO + 2\,H_2$	ΔH^0 = 247 kJ mol^{-1}	(2.14)
Steam reforming	$CH_4 + H_2O \leftrightarrow CO + 3\,H_2$	ΔH^0 = 206 kJ mol^{-1}	(2.15)
Reverse Water-Gas Shift (RWGS)	$CO_2 + H_2 \leftrightarrow CO + H_2O$	ΔH^0 = 41 kJ mol^{-1}	(2.16)
Methanation	$CO_2 + 4\,H_2 \leftrightarrow CH_4 + 2\,H_2O$	ΔH^0 = -165 kJ mol^{-1}	(2.17)
Methane pyrolysis	$CH_4 \leftrightarrow C + 2\,H_2$	ΔH^0 = 75 kJ mol^{-1}	(2.18)
Boudouard reaction	$2\,CO \leftrightarrow C + CO_2$	ΔH^0 = -173 kJ mol^{-1}	(2.19)
CO reduction	$CO + H_2 \leftrightarrow C + H_2O$	ΔH^0 = -131 kJ mol^{-1}	(2.20)

Unfortunately, with a growing number of reactions at the anode, the analysis of the cell becomes more complex. At different temperatures different reactions could dominate, leading e.g. to coke deposition, which would decrease the cell performance. Moreover, due to the Le Chatelier's principle, reactions can be easily moved from equilibrium. Lastly, catalysts can be selective towards different reactions and could facilitate one while slowing down another. Thus, before choosing the catalyst

material, it can be noteworthy to examine the purely catalytic performance towards the selected reaction.

The use of different fuels, e.g. such as the aforementioned methane or biogas, possesses several risks. The most prominent ones are carbon deposition at the anode and sulfur poisoning. When hydrocarbons are fed as fuel on the Ni-YSZ anode, carbonization would occur, as nickel is a good catalyst for methane cracking [21]. The formation of elemental carbon may occur both on the surface of the anode and in the bulk. The formation of the carbon species influences the TPB, lowering the catalytic performance and, as result, decreasing the cell performance. Moreover, coking could influence mechanical stability through changes in TEC, leading to cracking or delamination [3]. However, when additional oxygen will be added to the feed gas, CO oxidation or carbon burnout may occur. Unfortunately, the addition of O_2 will also result in the oxidation of Ni to NiO and the deactivation of the catalyst. Saadabadi *et al.* [22] suggested that at a high steam concentration in an inlet stream, carbon deposition may also be suppressed. Another method to prevent the formation of the carbonaceous species is the use of protective layers [23–26].

Sulfur is a common impurity in real-life hydrocarbon fuels, e.g. biogas. It can be present as various species like H_2S or SO_4^{2-}. The interaction of sulfur with electrode materials leads to the formation of sulfides, which reduce catalytic activity and electrical conductivity. For instance, in sulfur-containing conditions, the Ni-YSZ cell anode undergoes degradation as hydrogen sulphide reacts with Ni to produce Ni–S, thus decreasing the effective TPB for ionic transfer, lowering the electrochemically active surface area, and increasing the polarization resistance. Chemical adsorption of sulfur and the eventual saturation of the electrode surface cause a decrease in active sites, while nickel oxidation heightens polarization, leading to reduced cell voltage and catalyst efficacy [3,24]. The addition of O_2 may lead to SO_2 desorption, but once again possesses risk to oxidation of Ni to NiO at anode.

2.1.2. Solid Oxide Electrolysis Cell

The operation of the Solic Oxide Electrolysis Cell (SOEC) can be understood as a reverse operation of SOFC. In SOFC, the electricity is produced from the chemical energy of the fuel. In the electrolysis mode, the electricity is used to power the cell, then

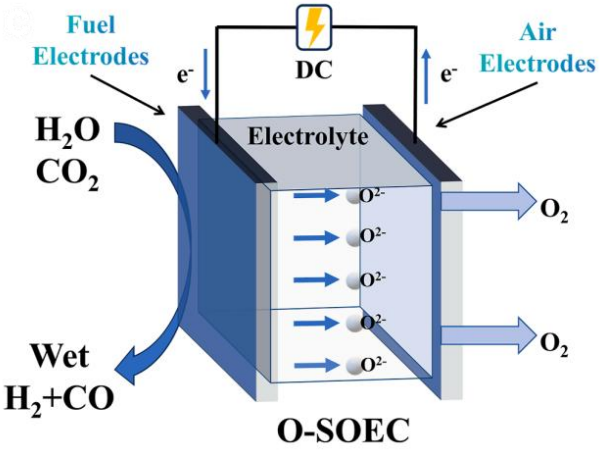


Fig. 2.6. The SOEC working principle [3].

the elecrons are used to split the molecule of the fuel (e.g. H_2O in the simplest setup) into simpler one (e.g. H_2). The remaining oxygen ions are then transferred through the electrolyte and released at air electrode. By this means, reaction occurring at SOEC is the reverse of (2.3) and can be written as reaction (2.21). The splitting of the water (steam) is the endothermic reaction and the thermal or electrical energy must be supplied [27].

$$H_2O \xrightarrow{electricity+T} H_2 + \frac{1}{2}O_2 \tag{2.21}$$

The general working principle is presented in **Fig. 2.6** [3]. The general construction of the SOEC is likewise for SOFC, as both types of operation can be used or easily switched between in one device. One benefit of Solid Oxide Electrolysis Cells is their versatility: they may also operate performing the co-electrolysis of CO_2 and H_2O. This is a particular interesting field, because it could consume excess energy to efficiently produce syngas (CO + H_2), which can be further utilized by the Fischer-Tropsch process to produce synthetic fuel [28–32]. The CO_2 splitting reactions can be written as (2.22)

$$CO_2 \xrightarrow{electricity+T} CO + \frac{1}{2}O_2 \tag{2.22}$$

The splitting of CO_2 and H_2O molecules requires energy due to the endothermic properties of the aforementioned reactions [27]. The total energy demand of both processes at standard pressure is depicted in **Fig. 2.7**. As one can see, the total energy input can be separated into electricity demand and heat demand. With increasing temperature, the need for electrical energy decreases, which is the driving force behind the use of SOEC technology in CO_2 electrolysis. Furthermore, wet CO_2 electrolysis has a lower activation energy than dry, resulting in lower polarization resistance and overpotential compared to dry carbon dioxide electrolysis [33,34]. Another significant disadvantage of dry electrolysis of CO_2 is the high risk of carbon deposition on the cell, leading to material degradation. Despite reactions (2.21) and (2.22), a reverse water-gas shift (RWGS) reaction occurs, in which carbon dioxide is converted into carbon monoxide, according to the reaction (2.23), complicating the process analysis.

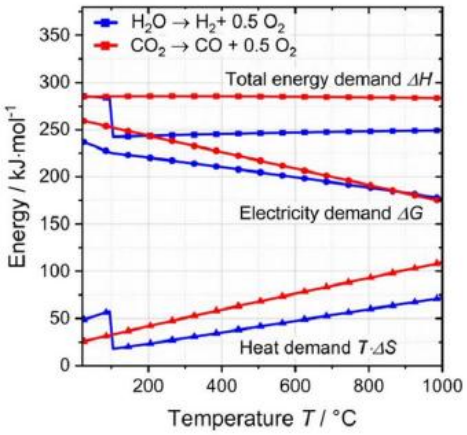


Fig. 2.7. Energy demand of the H_2O and CO_2 electrolysis reactions depicting the total energy needed (squares) with an indication of the electricity demand (points) and the heat demand (triangles) [27]

$$CO_2 + H_2 \leftrightarrow CO + H_2O \tag{2.23}$$

2.2. Materials for SOCs

2.2.1. Requirements

Regardless of the operation mode, the Solid Oxide Cell (SOC) consists mainly of three components, namely, a fuel electrode, an electrolyte, and an air electrode. Depending on the operation mode, the fuel electrode can be either called anode (SOFC) or cathode (SOEC) and vice versa for the air electrode. In general, through this thesis terms for SOFCs technology would be used, unless clearly stated otherwise.

There are several requirements that are common for both electrodes in SOCs [1,35–37]:

- Sufficient porosity for the effective gas flow;
- High electrical conductivity to transfer electrons or electron holes (σ_{el}>10 S cm^{-1} is considered a minimal threshold);
- Ionic conductivity enough to transfer oxygen ions (σ_{ox}>0.01 S cm^{-1} is considered a minimal threshold);
- Long triple-phase boundary (TPB) at which the reaction would take place;
- Good stability in working atmospheres: no phase decomposition, evaporation;
- Thermal expansion coefficient matching with the electrolyte;
- Good catalytic activity towards particular electrochemical reactions at the electrodes.

When it comes to the catalytic activity, as electrodes are working in different atmospheres and different reactions are taking place on them, one should consider the catalytic efficiency toward different processes. The anode materials should be excellent catalysts for the HER (hydrogen evolution reaction), while the cathode should be good for the ORR (oxygen reduction reaction). There are several possible types of materials that can be used as an anode in SOFC. These are metals (pure electronic conductors), metal-ceramic composite (electronic and ionic conductors separately), and extensively studied recently mixed ionic-electronic conductors (MIECs). These approaches are schematically presented in Fig. **2.8.a**. Before one dives slightly deeper into the differences, the importance of Triple Phase Boundary (TPB) must be understood. TPB is the area where gas (reactant), ionic, and electronic conductors meet [3,38] and the reaction takes place. The length of TPB is crucial aspect in SOCs technology, as more active sites are available for reaction to occur, when this boundary is longer. If different types of materials are considered, the pure electronic conductor has a TPB only in areas of contact with the electrolyte (marked with red dots in **Fig. 2.8.a**) offering limited spots for reaction. Pure electronic conductors were used at very early stages of SOFC development and they were mainly platinum or transition metals [36]. However, they possessed serious drawbacks in addition to poor TPB:

platinum tends to spall off, cobalt is expensive and morally questionable (due to the exploitation in Africa), and nickel has thermal expansion coefficient mismatched to commonly-used yttria stabilized zirconia (YSZ). Thus, a need for a better replacement emerged. One possibility is to use the composite of ionic (oxygen ion) and electronic conductors. Such an approach offers benefits of good ionic and electronic conductivity coupled with a long TPB. In addition, the ionic conductor is often the same as the electrolyte, providinh good mechanical match with other fuel cell elements [3,37–39]. Indeed, this approach is currently in dominant use as Ni-YSZ cermet is considered a state-of-the-art anode material. However, there is a third option in O-SOFC and it uses only one compound as electrode: mixed ionic-electronic conductor. In MIEC, the material is able to simultaneously transfer both electrons (or electron holes) as well as ions. The main benefit of MIECs is the maximum TPB that stretches across the entire surface of the material. Unfortunately, these materials are oxides, which offer lower electronic conductivity compared to, e.g. Ni-YSZ cermet [36]. Nevertheless, the use of MIECs is a growing branch in SOC technology, and perovskites are extensively studied as anodes.

The materials for the cathode remain similar; however, pure electronic and electronic-ionic mixtures are rather out of use. Because these materials are fully metals or metal-ceramic composites, in oxidizing atmospheres, the metal can easily oxidize and will stop being good electronic conductors [3,40]. In case of cathode, mostly MIECs are used, with the most popular ones presented in Chapter 2.2.2.

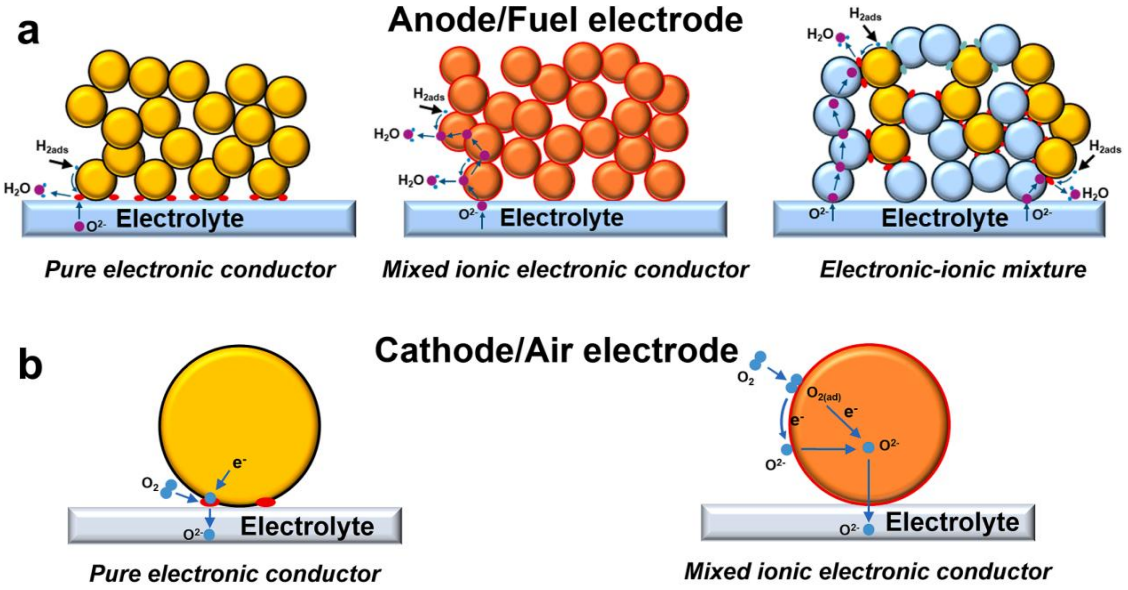


Fig. 2.8. The types of materials considered for anode/fuel electrode (a) and cathode/air electrode (b) [3].

The electrolyte is another crucial constituent of the Solid Oxide Cell. Its main role is to separate two gas chambers and to provide oxygen ion conduction between the anode and cathode. In electrolyte-

supported cells it greatly contributes to the cell's mechanical stability. However, as mentioned in Chapter 2.1.1, the resistivity of the electrolyte is crucial to Ohmic losses. Thus, currently cells are built as anode-supported, where the electrolyte is deposited as a thin layer [1,3,37]. The main requirements can be expressed as:

- High density providing gas tightness to separate the two gas chambers;
- Low electrical conductivity to prevent shortcuts between the cathode and anode;
- High ionic conductivity (σ_{ox}>0.01-0.1 S cm^{-1});
- High stability at high temperatures and different atmospheres: no phase decomposition, no current leakage;
- As thin as possible to minimize the Ohmic losses.

2.2.2. State of the art materials

Anode (fuel electrode)

As mentioned in previous Chapter, the anode materials nowadays are mostly metal-ceramic composites known as cermets. Among them, nickel-yttria stabilized (Ni-YSZ) zirconia has attracted particular interest and is the leading material in this field. It is combining nickel, which has great catalytic activity to hydrogen oxidation and high electronic conductivity with YSZ, owing the ionic conductivity and better fit with the electrolyte [3]. In addition to meeting the requirements for good anode material, the Ni-YSZ cermet has a significant advantage: it is simple in formation. It is very often formed simply by mixing NiO and YSZ powders, and then the resulting composite is reduced to form Ni-YSZ [1]. Since a good anode must be porous to provide gas diffusion, the poreformers (e.g. PMMA, graphite, starch) are added during the synthesis; however, nanostructurization can also induce porosity as described in our previous paper: Błaszczak P., **Ducka A.**, Wolanin B., Matlak K., Machowski G., Prześniak-Welenc M., Wang S.-F., Bochentyn B., & Jasiński P. (2023). *Fabrication of wormhole-like YSZ and Ni-YSZ by the novel soft-hard template CTAB/NaCl-assisted route. Suppressing Ni coalescence in SOFC. JOURNAL OF THE*

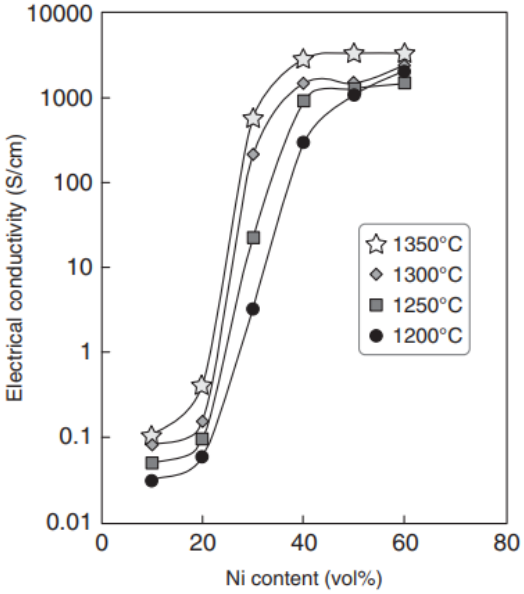


Fig. 2.9. Electrical conductivity of Ni-YSZ cermets with different Ni content [1]

EUROPEAN CERAMIC SOCIETY, *43*, 438-451. https://doi.org/10.1016/j.jeurceramsoc.2022.09.054 [41]. Another benefit in using the Ni-YSZ is that nickel and zirconia do not react with each other. Thus, no impurities are formed during the synthesis [38]. It is also noteworthy to answer the question what is the optimal concentration of metal in the Ni-YSZ cermet to obtain good anode material. The answer lies within the percolation theory [1]. For too low a concentration of nickel in cermet material, the electrical conductivity is low as visible in **Fig. 2.9**. In this region, the grains of Ni are separated by the insulating YSZ grains which blocks the electron transfer. At low Ni concentrations, the Ni-YSZ cermet is a predominantly ionic conductor. With an increase of nickel content, the grains can touch, providing a pathway for charge carriers rapidly increasing the conductivity, which is known as percolation threshold. Further increase in Ni amount does not affect the conductivity significantly but will alter the thermal expansion coefficient and increase the mismatch. Currently, conventionally used Ni-YSZ cermet often consists of 50 vol. % of nickel phase [1,41]. Unfortunately, the Ni-YSZ cermet is prone to coarsening upon long period of work [41] and carbon deposition when fed with hydrocarbons [1,22,38,41].

Due to the already mentioned simplicity of NiO-YSZ preparation, nowadays many commercially available cells are built on anode support. In this approach, the anode is the main scaffold onto which the next components are deposited, e.g. the thin layer of electrolyte, the buffer layer (optional), and then the cathode [1,3]. In anode-supported cells, very often two distinguished areas could be found, differing in nickel concentration and/or porosity [1]. The layer closer to the electrolyte is known as an anode functional layer (AFL) and its aim is to enhance electron transfer in the proximity of the electrolyte. [1]

Although the Ni-YSZ cermet is the most commonly used in SOC technology, different cermets can also be utilized. The choice of ceramic in this composite is directly dependent on the electrolyte used in the cell. For example, Ni-CGO cermet is also used on CGO electrolytes [36,38]. However, the main drawback of the use of ceria-based ceramics in anodes is the reducibility of Ce^{4+} to Ce^{3+} ions during work in reductive atmospheres [3,38]. Although this may be beneficial from the ionic conductivity, it may also lead to the internal strains or cracking as the lattice of CeO_2 would change [1].

Cathode (air electrode)

As briefly mentioned in Chapter 2.2.1, for cathode mostly MIECs are used [1,3] due to their stability in oxidizing atmospheres and simultaneously providing good electronic and ionic conductivity. As these are all oxides, the conductivity of the cathode is always significantly smaller than for anode [1,3]. In general, perovskites are found as cathodes in SOCs, e.g. $La_{1-x}Sr_xMnO_{3-\delta}$ (LSM), $La_{1-x}Sr_xCo_{1-y}Fe_yO_{3-\delta}$ (LSCF), or $La_{1-x}Sr_xCoO_{3-\delta}$ (LSC) [3]. Mn-based perovskite is characterized

by good electrical conductivity, catalytic activity and match with YSZ electrolyte. Unfortunately, LSM has insufficient ionic conductivity which remains crucial requirement for the cathode. In order to overcome this, composites of LSM-YSZ are produced, boosting the oxygen transport [3]. Unfortunately, this approach leads to the shortening of TPB and nanostructurization of LSM is required [42]. Other materials are Co-based composites with better oxygen transport and sufficient catalytic response. On the other hand, the thermal expansion coefficient (TEC) is higher than YSZ electrolyte, which can lead to difficulties in deposition, sintering, and layer delamination under operation [43]. This could be overcome by doping with iron cations; however, this affects the electrical conductivity by lowering it [1,3,43]. In order to benefit from better TEC and good ionic conductivity of LSCF and better electronic conductivity of LSC, dual-layer approach is used [31]. In this case the LSCF is deposited firstly and then, LSC layer is added, more like contact layer between cathode and interconnector [31]. Unfortunately, the cathode materials are also susceptible to processes lowering cell performance. Among them the most prominent is the formation of insulating species at the cathode-electrolyte interface. As the Sr^{2+} cations can migrate to YSZ electrolyte during long period of work. Then, insulating $SrZrO_{3-\delta}$ phase could form which would lower the cell performance by increase in ohmic resistance of cell [19]. To avoid this, the buffer layers are added, which should prevent or slow down the formation of such species.

Electrolyte

The crucial role of the electrolyte is to separate fuel from air and to provide good transport of oxygen ions without transfer of electrons. The state-of-the-art electrolyte material used is yttria-stabilized zirconia (YSZ). The most commonly used Y_2O_3 concentration is 8 mol. % which leads to 8YSZ formation [1,3,44]. To stabilize the structure lower-valence Y^{3+} is introduced at Zr^{4+}, which can be presented in Kröger-Vink notation as (2.24) [45]

$$Y_2O_3 \xrightarrow{ZrO_2} 2Y'_{Zr} + 3O_O^{\times} + v_O^{\cdot\cdot} \tag{2.24}$$

Where: Y'_{Zr} - ittrium ion in zirconium position leading to -1 relative charge

$O_O^{\times}$ - oxygen in its original position without any relative charge

$v_O^{\cdot\cdot}$ - oxygen vacancy with +2 relative charge

From (2.24) it can be clearly seen that the substitution of Zr with Y leads to the formation of an oxygen vacancy. This defect is crucial for ionic conduction, as there must be a vacancy to provide the oxygen movement in the lattice [45]. In fact, the ionic conductivity of 8YSZ reaches 0.1 S cm^{-1} at 1000 °C [44]. In general, (2.24) would be true for any other 3+ cations, such as Sc^{3+}, but the use of

ScSZ (scandia-stabilized zirconia) is limited due to the high cost of this element [3]. The YSZ has also the significant advantage of being stable in a wide range of pO_2, which makes it able to withstand both anodic and cathodic atmospheres. Unfortunately, at lower operating temperatures, the conductivity of YSZ is decreased [46], limiting its use in low-temperature SOCs (LT-SOCs). The conductivity of selected electrolyte materials is presented in **Fig. 2.10** [1,44].

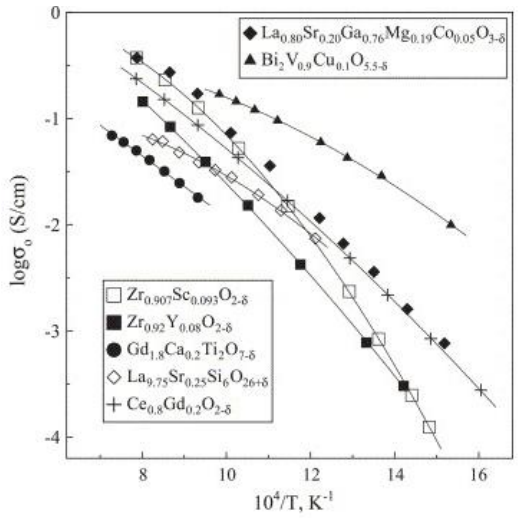


Fig. 2.10. The ionic conductivity in air for most common electrolyte materials [44]

Another candidate for electrolyte material is a doped cerium (IV) oxide $CeO_{2-\delta}$, among which gadolinium-doped ceria (CGO or GDC) is the most used [1,3]. Trivalent doping with gadolinium of tetravalent cerium enhances the ionic conductivity in the same manner as explained for YSZ. Moreover, the ionic conductivity of doped ceria is higher than that for YSZ (see **Fig. 2.10**). Unfortunately, the stability of ceria-based compounds as electrolytes is limited due to the ease of partial reduction from Ce^{4+} to Ce^{3+} in a hydrogen atmosphere. Therefore, the requirement for the electrolyte stability in anodic conditions is not fulfilled. This behavior would not only change lattice parameter, thermal expansion coefficient, but more importantly would increase the electronic conductivity according to reaction (2.25) [44]. This possesses a serious risk of short circuit between the anode and cathode [1,44].

$$Ce^{4+} \overset{H_2}{\rightarrow} Ce^{3+} + e' \tag{2.25}$$

On the basis of cerium reduction, the use of ceria as an electrolyte has limited use, but it can still be found in the SOCs. CGO is used very often as a buffer layer between electrolyte and cathode; thus, it is not exposed to reducing atmospheres. In this application, ceria prevents the interdiffusion of ions between the electrolyte and the cathode perovskite and as a result no insulating species are formed [1,3].

Lastly, a perovskite-based electrolyte can be used in SOCs. In this area, $La_{0.8}Sr_{0.2}Ga_{0.8}Mg_{0.2}O_{3-\delta}$ (LSGM) is a prominent example, characterized by high ionic conductivity (see **Fig. 2.10**). At high temperatures, it is significantly higher than YSZ or CGO [44], reaching even 0.15 S cm^{-1} at 800 °C [3,44,47]. Another benefit is that due to the similarity in structures with cathode materials, the formation of parasitic insulating phases is limited. At the same time, it shows good stability at low pO_2 being able

to stable withstand an anodic atmosphere [37]. The aspect limiting the application of LSGM in commercial electrolytes is its price, since gallium is an expensive metal. However, LSGM is widely used in the research of perovskite-anode SOCs [14,48–52]

2.3. Perovskites

2.3.1. Single perovskite - $SrTiO_{3-\delta}$

Perovskite is the family of compounds with the general formula ABX_3, where X in principle can be any chalcogen or halogen, but the vast majority of perovskites have an oxygen at the X-site [53]. A-site is occupied by alkaline-earth (e.g. Sr^{2+}, Ca^{2+}, or Ba^{2+}) or rare-earth (e.g. La^{3+}) metal cations, while transition (e.g. Ti^{4+}, Cr^{3+}, $Fe^{3/4+}$, Mo^{4+}) metals are present at B-site [39]. Generally, the B-site cations are smaller than the ones occupying the A-site of perovskite. The coordination numbers are 12 and 6 for the A- and B-site cations, respectively. The perovskite structure (presented in **Fig. 2.11**) can be understood as a network of BO_6 octahedrons sharing corners, where A-site cations are occupying the remaining voids [54]. Ideally, the perovskite adapts the close-packed cubic structure, however, due to the various cations' radii, structural mismatch is possible. The perovskite structure can be predicted using the unitless Goldschmidt tolerance factors expressed in Eq. (2.26) [39,53,54]

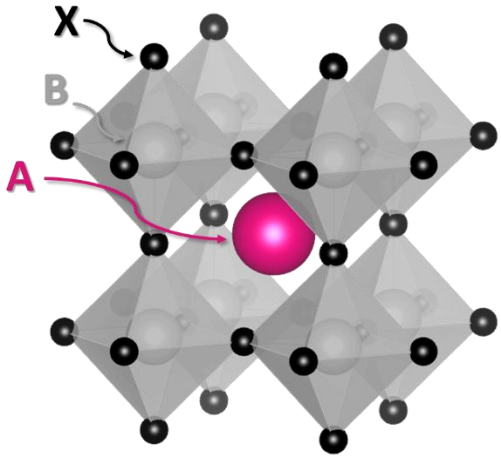


Fig. 2.11. The ideal cubic crystal structure of single perovskite ABX_3. Created in VESTA software.

$$t = \frac{r_A + r_O}{\sqrt{2}(r_B + r_O)} \tag{2.26}$$

Where: t – Goldschmidt tolerance factor

r_A, r_B, r_O – ionic radii of A-, B-site cations, and oxygen anion

The ideal perovskite should give the result of t=1 leading to the *Pm-3m* or *Fm-3m* structures with high symmetry [55], however, values between 0.9 and 1 would preserve the cubic structure. For t less than 1, this means that A-site cation is too small for the ideal structure. In this case, the size mismatch is compensated by the tilting of the BO_6 octahedrons and structural distortions such as bond length change [21,54,56]. When t is lower than 0.9, the structure would transform into orthorhombic [56].

On the other hand, too large A-site cation would result in a tolerance factor above 1. In this case, the structural mismatch cannot be relieved by tilting of the octahedrons, and hexagonal structure is adapted [54,56]

Even if the oxygen would be fixed at X-site of perovskite lattice, the variability of A- and B-site cations give rise to enormous number of possible formula combinations. As mentioned in Chapter 1, this leads to huge variety of perovskite properties from insulating to metallic, halfmetallic or spin-polarized electrical conductivity; ionic conductivity; antiferro-, ferri- or ferromagnetics [54]. If other chalcogens or halides would be considered at X-site, the number of available compositions grows rapidly.

One of many representatives of the single perovskite family is strontium titanate with the formula $SrTiO_{3-\delta}$ (STO), where δ denotes oxygen deficiency. The calculated value of the Goldschmidt tolerance factor for STO is equal to 1.001, indicating the presence of a cubic structure. Indeed, STO crystallizes in a *Pm-3m* structure with high symmetry. Strontium titanate is a widely known dielectric material, utilized e.g. in water photolysis or as an oxygen sensor [57]. One of its benefits is extraordinary structural stability, also in redox cycles, due to the to high stability of Ti^{4+} ions [58], since the change in Gibbs free energy is positive even at higher temperatures. Furthermore, STO has been extensively studied as material for SOC aplications and has shown promising electrocatalytic behavior towards hydrogen [59] and methane [60,61] oxidation. As an additional benefit, it was described as tolerant towards sulfur containing atmospheres [24,62], which is a common impurity in hydrocarbon-based fuel.

Because doping of the perovskites offers adjustment of many properties, STO shows no difference from this trend. In Google Scholar, there can be almost 10 000 papers found on doping of $SrTiO_{3-\delta}$. In this dissertation, most attention would be paid on the doping of transition metals for exsolution at higher temperatures. The exsolution is described in more details in Chapter 2.4. Briefly, it is the process in which catalytically active nanoparticles form on the oxide host during reductive treatment. Considering excellent host stability in STO, the use of strontium titanate as a scaffold for exsolution is extensively studied. For example, Ni-doped $SrTiO_{3-\delta}$ was reported to exhibit vigorous exsolution and performs well for steam electrolysis or steam methane reforming by O'Leary *et al.* [63]. Mizera *et al.* [64] studied the impact of Ni, Co, or Cu doping on catalytic efficiency toward dry reforming of methane (DRM). In their work, Ni-doping led to the be most efficient in DRM reaction, while cobalt or copper were less active. Ni-doping was also studied by Chien *et al.* [65], who aimed for good catalysts for CH_4/O_2 redox cycling. They found that exsolved Ni nanoparticle favors the formation of hydrogen and carbon dioxide in each cycle, respectively. The enhancement in performance was explained by good catalytic activity of NPs and resistible to deactivation.

The $SrTiO_{3-\delta}$-based compounds were also studied for ammonia-SOFC by Cavazzani *et al.* [66]. They have studied the La- and Ni-doped STO, which was used as electrodes in symmetric cells. The exsolution of Ni nanoparticles has led to lower polarization resistances. Although, the power densities were rather low (below 5 mW cm^{-2}), the cell withstand harsh ammonia conditions. The use of STO in ammonia cracking was further studied by group of Ren *et al.* [67], who focused on exsolution of Ni-Co nanoparticles. The in-situ exsolved NPs shown the activity to NH_3 decomposition even 3 times higher than their impregnation counterparts. Interestingly, one of synthesized compounds shown equilibrium-near conversion of ammonia during catalytic tests. Moreover, they obtained power density of almost 100 mW cm^{-2}, which is significantly higher than Cavazzani *et al.* [66].

Many studies present simultaneous doping of both A- and B-sites of the perovskite [63,66,69–71]. In the case of STO, aliovalent doping with La^{3+} is quite common and aim to increase the conductivity of strontium titanates. Moreover, as lanthanum has a higher oxidation state, it could ease the incorporation of lower-valence cations at the B-site, like nickel, cobalt or copper, to maintain the electroneutrality of the compounds. Unfortunately, there is no agreement on how La-doping influences the exsolution. Some studies [72,73] show that with La-doping the exsolution of nickel nanoparticles would be enhanced, while other [74] suggest that this would limit the diffusion of cations to the surface.

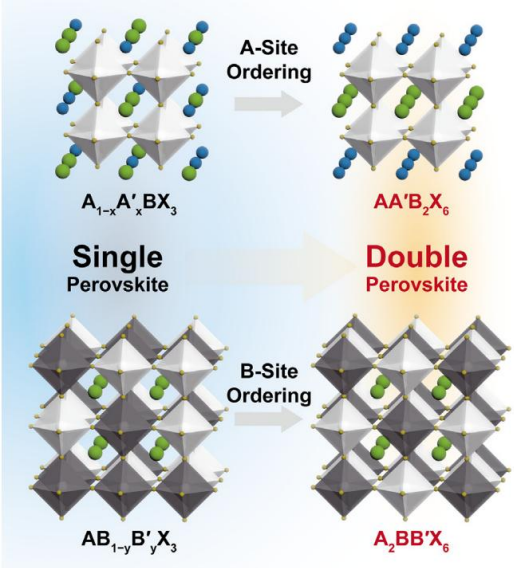


Fig. 2.12. The difference between doped single perovskites and ordered double perovskites [68]

Generally, if the concentration of either an A- or B-site dopant remains sufficiently low, one can consider the formation of the doped single perovskite. However, when the dopant concentration is higher and the order of the dopant is present, double perovskite structure should be considered [54,68]. The schematic presentation of this situation is shown in **Fig. 2.12**. More attention is devoted to double perovskite and ordering types in Chapter 2.3.2.

2.3.2. Double perovskite - $Sr_2Fe_{1.5}Mo_{0.5}O_{6-\delta}$

Double perovskites (DP) are another part of the perovskites family. As their name suggests, their formula can be considered to be doubling of the amount of single perovskite. For simplicity, the X anion would be oxygen; then the formulas can be expressed as $AA'B_2O_6$ or $A_2BB'O_6$ [54]. In this

case, either the A-site or the B-site has two different cations, respectively. Firstly, the double perovskites with equal occupation at either A- or B-site will be considered. The main difference between highly doped single perovskite e.g. $SrTi_{0.5}Fe_{0.5}O_{3-\delta}$ and double perovskite is the ordering. In double perovskites, the AA'- or BB'- cations are not randomly oriented in the lattice, they rather are located in some order. **Fig. 2.13** shows three B-sites ordering in $A_2BB'O_6$ perovskites. The first and most commonly encountered in B-site ordered is the rock-salt arrangement, also known as the elpasolite structure [54]. In this case, the cations are located alternately. Another possible ordering types are layered and columnar. If the double perovskite is A-site ordered with formula $AA'B_2O_6$, the layered arrangement is more common [68,75].

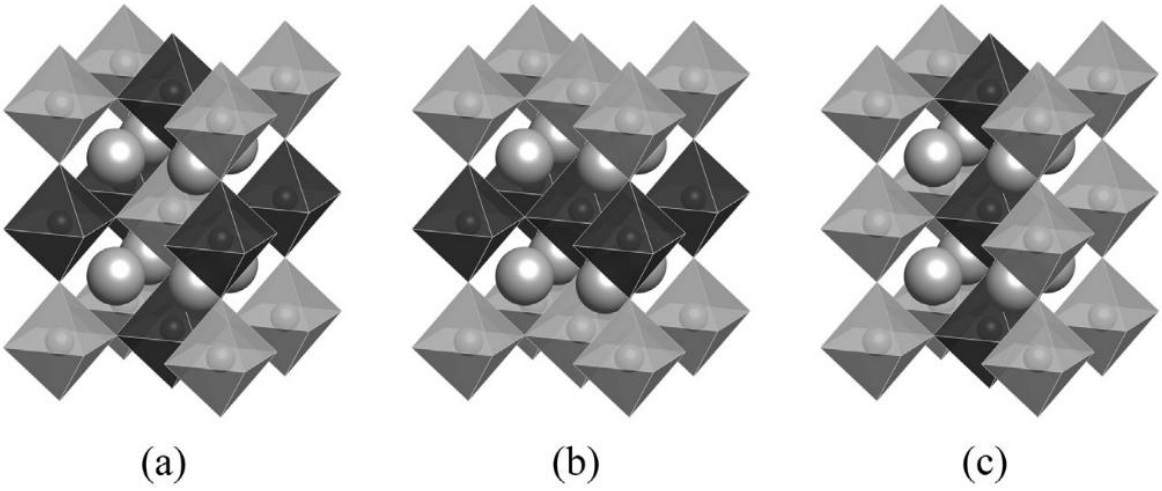


Fig. 2.13. Representation of different B-site ordering types in double perovskites: (a) rock-salt, (b) layered, and (c) columnar [54].

The crystallographic structure and description are likewise for single perovskites explained in more detail in Chapter 2.3.1. Ideal double perovskite crystallizes in cubic structures and the Goldschmidt tolerance factor can also be calculated as expressed in (2.26). However, for ionic radii, the mean radius of A- or B-site cations must be taken. Undoubtedly, the single perovskites already offered a huge range of elements forming the structure, leading to various properties. In the case of double perovskites, the number is even higher. As the, B-site ordering is more common and more adequate for this dissertation, a great deal of attention will be put on $A_2BB'O_6$ perovskites. First, let us consider the divalent cations at the A-site, such as Ca, Ba or the most common Sr. In this case, if one analyzes only the unity ratio of B:B', the sum of the B-site elements' valence states must be equal to +8 to keep the electroneutrality of the compound as a whole. To fulfill this requirement, 4 different combinations may be used: B^{4+}/B'^{4+}, B^{3+}/B'^{+5}, B^{2+}/B'^{6+}, and B^{+}/B'^{7+} [54]. Such a wide combination of different valence states allows us to cover all available oxidation states in metals. Of course, the cation size remains crucial, and not all elements would be successfully incorporated into the B-site lattice.

If a trivalent cation occupies the A-site (e.g. La^{3+}) the number of available B-site combinations shrinks to B^{3+}/B'^{3+}, B^{2+}/B'^{4+}, and B^{+}/B'^{5+}. Vasala *et al.* [54] stated that the number of possible combinations for $A_2B'BO_6$ perovskites reaches 2000 meeting requirements such as tolerance factor *t* in the range of 0.85-1.05; presence A^{+}, A^{2+}, or A^{3+} cations and excluding radioactive cations.

As mentioned in the previous paragraph, the ordering of the sublattice is the crucial part to identify the double perovskite from the single one. The degree of this order S can be expressed mathematically as Eq. (2.27)

$$S = 2g_{A/B} - 1 \tag{2.27}$$

Where $g_{A/B}$ – occupancy of A- or B-site cation at its correct (ordered) site

When the structure is completely ordered the parameter *S*=1, while *S*=0 corresponds to the disordered arrangement [54]. Anything in between means that cations are partially ordered, for example, by the defect formation, which is presented in **Fig. 2.14**. Because the configural entropy is always present at $T > 0$K, some number of defects would always be present in the crystal. One of the defects that affect the ordering in double perovskites is the antisite (AS) disorder, which is the change of B and B' cations position. Another possibility is the formation of a more complex antiphase boundary, where two ordered parts are separated by the boundary of reversed periodicity [54].

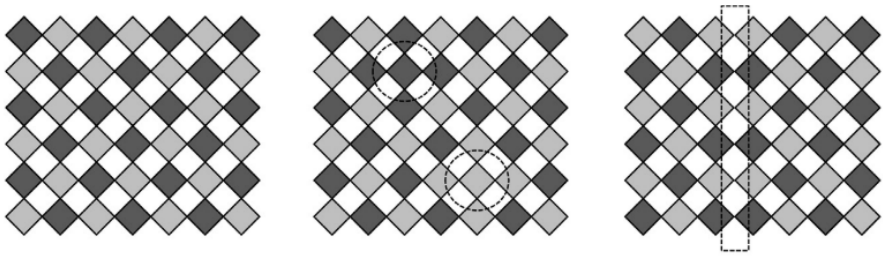


Fig. 2.14. Scheme of disorder in double perovskites: (a) completely ordered, (b) antisite (AS) disorder, and (c) antiphase boundary (APB) [54].

Other factors affecting the order in the $A_2BB'O_6$ perovskites are the sizes of the B-site cations size and their valence states. These aspects can be written as Eq. (2.28) and (2.29), respectively.

$$\Delta r_B = |r_{B'} - r_B| \tag{2.28}$$

$$\Delta Z_B = |Z'_B - Z_B| \tag{2.29}$$

Where Δr_B – relative difference in ionic radii between B-site cations;

r_B, $r_{B'}$ – ionic radii of respective B-site cations;

ΔZ_B – relative difference in oxidation states between B-site cations;

Z_B, $Z_{B'}$ – oxidation states of respective B-site cations.

In general, if any of these parameters (Δr_B, ΔZ_B) is larger than the other, the more probable the ordering is. If the ionic radii are taken into consideration, the more significant difference in the ionic radii is, the bigger the lattice strain. As a result, this strain dominates over the entropy, and structure should be ordered [76]. If the oxidation states are to be considered, the boundary is set at 2. If ΔZ_B is higher, then the structure is ordered. The explanation behind this behavior lies simply in electrostatics. Placing two B-site cations with high charge near each other (in disordered structure) will result in formation of repulsive forces and would be energetically unfavorable [54]. An additional factor to consider to analyze the order in double perovskites is the electron transfer between B-site cations and the presence of oxygen vacancies, which would lower the ordering [54]. **Tab. 2.1** shows the ordering in the available combinations showing whether the structure is ordered or not with respect to ΔZ_B.

Tab. 2.1. Summary of order in $A_2BB'O_6$ double perovskites [54]

ΔZ_B	Compound	Order
0	$A_2^{2+}B^{4+}B'^{4+}O_6$	Ordered if Δr_B>0.17 Å
	$A_2^{3+}B^{3+}B'^{3+}O_6$	Disordered
2	$A_2^{2+}B^{3+}B'^{5+}O_6$	Order increasing with increasing Δr_B
	$A_2^{3+}B^{2+}B'^{4+}O_6$	Mostly ordered (at least partially)
4	$A_2^{2+}B^{2+}B'^{6+}O_6$	Highly ordered
	$A_2^{3+}B^{+}B'^{5+}O_6$	Ordered
6	$A_2^{2+}B^{+}B'^{7+}O_6$	Ordered

Similarly to single perovskites, the wide range of possible elements leads to a variety of properties. From the point of view of this thesis, the use of double perovskites in SOCs remains most important. **Tab. 2.2** summarizes several different uses of double perovskites in high-temperature fuel cells. As can be seen, mostly two families are used: the A-site ordered $PrBaM_2O_{6-\delta}$ or the B-site ordered $Sr_2MMoO_{6-\delta}$ (where M-other metal, e.g. Co, Mn, Fe, Mg, Ni).

Tab. 2.2. The exemplary double perovskites, their ordering, structure, and potential application in SOCs [68].

Formula	Ordering type	Structure	Application
$PrBaCo_2O_{6-\delta}$	A-site	Orthorhombic (*Pmmm*)	ORR in SOFC cathode
$PrBa_{0.5}Sr_{0.5}Co_{1.5}Fe_{0.5}O_{6-\delta}$	A-site	Tetragonal (*P4/mmm*)	ORR in SOFC cathode
$PrBaMn_2O_{6-\delta}$	A-site	Tetragonal (*P4/mmm*)	Fuel oxidation in SOFC anode/CO_2 reduction in SOEC cathode
$Sr_2MgMoO_{6-\delta}$	B-site	Cubic (*Fm-3m*)	Fuel oxidation in SOFC anode
$Sr_2Fe_{1.5}Mo_{0.5}O_{6-\delta}$	B-site	Cubic (*Fm-3m*)	Fuel oxidation and ORR in sSOFCs/co-electrolysis in SOECs
$Ba_2Bi_{0.1}Sc_{0.2}Co_{1.7}O_{6-\delta}$	B-site	Cubic (*Fm-3m*)	ORR in SOFC cathode

As visible above, one of the interesting compounds in the double perovskite family are the $Sr_2MMoO_{6-\delta}$ molybdates, where M=Mg, Ni, or Fe. Particularly interesting are the compounds with magnesium and iron. For Mg at the B-site, the structure varies from the ideal perovskite as it can be present in cubic, tetragonal, monoclinic or triclinic form with respect to the synthesis method [21]. Unfortunately, the $Sr_2MgMoO_{6-\delta}$ tends to partially decompose under oxidizing atmospheres [21,77]. However, this material exhibited good performance in oxidation of hydrocarbons and tolerance to sulfur or coke [78]. Another interesting compound is $Sr_2FeMoO_{6-\delta}$, which offer mixed Fe^{2+}/Fe^{3+} and Mo^{5+}/Mo^{6+} valences for effective electron transport [21]. The main drawback of equally occupied $Sr_2FeMoO_{6-\delta}$ is similar to the that with magnesium: it is found to be stable in hydrogen but tends to decompose in air [21,79]. Moreover, during the synthesis, the reductive treatment is required, making it more complicated [10]. In order to stabilize the structure, the Fe:Mo ratio is altered to 3 forming $Sr_2Fe_{1.5}Mo_{0.5}O_{6-\delta}$ (SFM) compound. The higher concentration of Fe increases its oxidation state, enhancing the metal-oxygen hybridization. As a result, the O p band is shifted closer to the Fermi level, as illustrated in **Fig. 2.15**. By this means, the catalytic activity of the material is also enhanced [80].

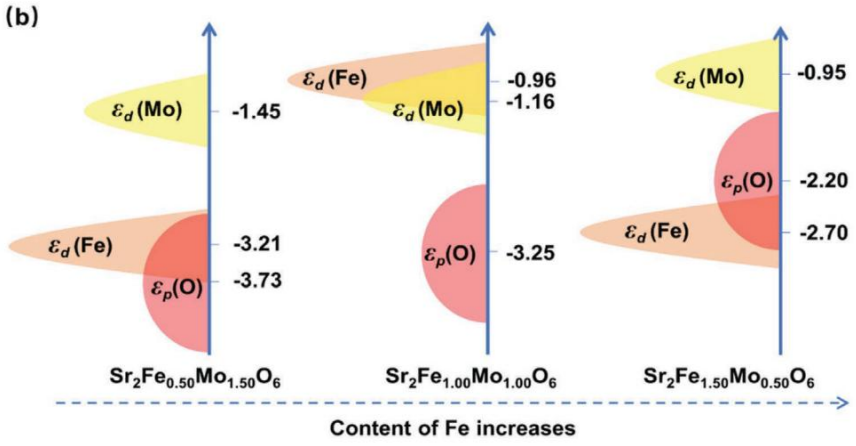


Fig. 2.15. Presentation of Mo and Fe d band and O p band center for different Fe:Mo ratio [80].

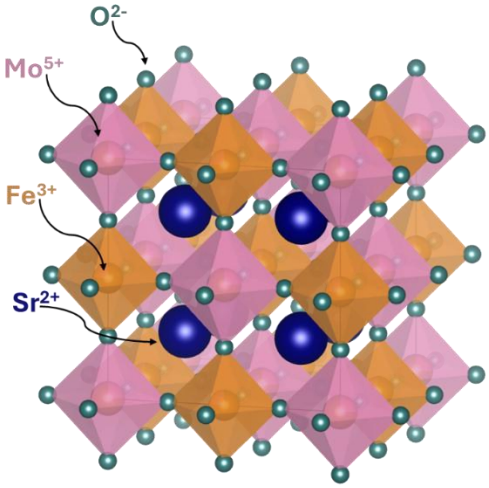


Fig. 2.16. The ideal cubic crystal structure of $Sr_2Fe_{1.5}Mo_{0.5}O_{6-\delta}$. Created in VESTA software.

Compared to $Sr_2FeMoO_{6-\delta}$, $Sr_2Fe_{1.5}Mo_{0.5}O_{6-\delta}$ (SFM) has attracted significant interest due to its remarkable properties. The structure of SFM is presented in **Fig. 2.16**. A high concentration of oxygen vacancies, which are transported through relatively weak Fe-O-Fe bonds, has resulted in a high ionic conductivity of SFM [21,81–83]. Furthermore, in both reducing and oxidizing atmospheres, it is characterized by high electrical conductivity [84] and high stability [85], making the SFM compound a promising candidate for electrodes for symmetrical Solid Oxide Fuel Cells (sSOFC). However, the stability concern remains questionable, as there is no complete agreement on this. In fact, in this thesis the redox stability of SFM is a crucial aspect. Unfortunately, the use of $Sr_2Fe_{1.5}Mo_{0.5}O_{6-\delta}$ forces the use of an electrolyte other than state-of-the-art YSZ. When deposited on YSZ and sintered at temperatures above 1000 °C, interdiffusion between SFM and the YSZ electrolyte can occur, resulting in the formation of foreign phases such as $SrZrO_{3-\delta}$ or $SrMoO_4$. Regrettably, $SrZrO_{3-\delta}$ is insulating for O^{2-} ions and can significantly decrease the overall performance of the SOFC [85]. The same studies have also proven that SFM remains stable on CGO ($Ce_{0.8}Gd_{0.2}O_{2-\delta}$) up to 1200 °C, suggesting that other ceria compounds may be suitable for use as a SOFC component. Unfortunately, as mentioned in Chapter 2.2.2, ceria is prone to reduction in atmospheres with low pO_2. If the cerium reduction takes place, the release of the electrons would take place according to Eq. (2.25) and undesired short-circuiting is likely to occur. To overcome the problem mentioned with the YSZ and CGO

electrolytes, cells are mostly built on the LSGM ($La_{0.8}Sr_{0.2}Ga_{0.8}Mg_{0.2}O_{3-\delta}$) electrolyte [86,87]. Another aspect of non-stability of SFM material is the possible decomposition at low temperatures in a humid atmosphere. As a result of the reaction with water, $Sr(OH)_2$, Fe_3O_4, $SrMoO_4$, and SrO_2 are formed, leading to mechanical stress of SOFC during heating/cooling [88]. Wright *et al.* [88] have also shown that after heating at 800 °C, the newly-formed $Sr(OH)_2$ phase does not react back to form an SFM perovskite. Last but not least, however, one may find many publications in which SFM is said to be redox stable; some others point out that in highly reductive atmospheres it may lose its stability [17].

Because of their wide formula flexibility, the double perovskite structures are capable of performing the exsolution process, the fundamentals and driving forces of which are described in more detail in Chapter 2.4. The exsolution has already been studied in SFM based systems, leading to the enhancement of its catalytic performance. Yang *et al*. [89] have studied the exsolution in Co-doped SFM double-perovskites. They have substituted Fe with Co and reduced this compound at 850 °C. The strong enhancement of catalytic performance was observed, and this was attributed to Co exsolution. Electrical conductivity of 13.9 S cm^{-1} was achieved at 600 °C in H_2 and the lowest polarization resistance of 0.15 Ω cm^2 at 800 °C, which is comparable to other anodes. When methane was used, no carbon deposition was observed, indicating that SFM decorated with Co nanoparticles is a promising candidate for anodes fed with alternative fuels. Xu *et al.* [90] also studied Co-doping at the Fe-site of SFM. Their research proved that Co NPs enhance H_2 and C_3H_8 adsorption and this compound is characterized by high oxygen-ion conductivity, which resulted in a maximum power output of 0.771 W cm^{-2} at 750 °C when fueled with H_2. Furthermore, long-term tests have proved the stability of the compound under working conditions. In the work by Lv *et al.* [16] Co was introduced not only at the Fe site, but also at the Mo site with a constant Fe:Mo molar ratio of 3. Interestingly, upon reduction, the orthorhombic SFM phase partially transforms into the Ruddlesden-Popper phase, which was not observed for the studies mentioned above. They have proven that it is feasible to dissolve NPs back into the perovskite backbone, which occurs during re-oxidation at 800 °C with possible formation of spinel structure at 600 °C. Unlike other studies mentioned previously, Lv *et al.* [16] studied the Co@SFM for SOEC and reported the regenerative properties of Co-Fe nanoalloys during 12 redox cycles. The exsolved nanoparticles improved the electrolysis of CO_2 and the stability of the cathode. Ni doping at the Fe site was studied by Osinkin *et al.* [12]. They have investigated the impact of temperature and partial oxygen pressure on SFM electrical conductivity. In reductive atmospheres, exsolved Ni NPs accelerate reactions related to hydrogen adsorption and dissociation on the anode. For symmetrical fuel cells based on the LSGM electrolyte, a maximum power density of approximately 0.5 W cm^{-2} was achieved at 800 °C. Wang *et al.* [91] focused on Ni exsolution for electrolysis cells and showed that Fe-Ni nanoalloys increase the catalytic activity toward water splitting, resulting in

an electrolysis current density of 1257 mA cm^{-2} at 1.3 V at 850 °C. Because of the strong interaction between the metal and oxide interfaces, good short-term stability was observed. Cu-exsolution was studied for CO_2 electrolysis in SOEC by Xi *et al.* [86]. The increased electrocatalytic performance was observed, which resulted in an electrolysis current density of 1.7 and 2.5 A cm^{-2} at an applied voltage of 1.4 V and 1.5 V, respectively. As one can see from aforementioned examples, most studies are focused on the doping on only one site of double perovskite, mostly Fe-site. Studies such as those of Lv *et al*. [16,17] are in a great minority, therefore, the impact of simultaneous doping of Fe and Mo-sites needs to be further studied.

2.3.3. Ruddlesden-Popper layered perovskite – $Sr_3Fe_{1.5}Mo_{0.5}O_{7-\delta}$

Among the perovskite oxide family, one may also find Ruddlesden-Popper layered perovskites (RP), named after two scientists who first synthesized and described its structure back in 1958 [92]. Its general formula can be written as $A_{n+1}B_nO_{3n+1}$ [93] and the structure can be understood as a layer of perovskite ABO_3 divided by the slabs consisting of AO. Depending on the number *n*, more perovskite layers are present in its structure [93,94]. RP perovskites crystallize in the tetragonal *I4/mmm* space group and the exemplary structure for representative $Sr_3Fe_{1.5}Mo_{0.5}O_{7-\delta}$ (*n*=2) is presented in **Fig. 2.17**. Because the Ruddlesden-Popper phase still belongs to the perovskite family, similar rules apply to the selection of A- and B-site cations. RP perovskites are known for their rapid oxygen exchange on the surface followed by good oxygen migration [3,93]. These properties are mainly based on the different crystal structure than single perovskites. The addition of the AO plane promotes not only the diffusion of oxygen through the vacancies, but also allows the interstitial movement [93,95]. However, due to the presence of insulating AO layers, the charge transfer can be limited within the c-axis. For higher-order RP perovskites (*n*>2) the electrochemical performance is improved [96].

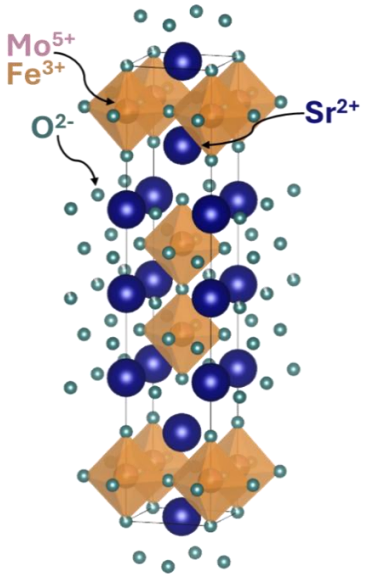


Fig. 2.17. The ideal cubic crystal structure of $Sr_3Fe_{1.5}Mo_{0.5}O_{7-\delta}$. Created in VESTA software.

The Ruddlesden-Popper layered perovskite can be formed directly from reagents [96,97] or as a by-product of double perovskite reduction that is observed for $Sr_3Fe_2O_{7-\delta}$ and its derivatives [49,98,99]. The main challenge with the second approach is the expansion of the unit cell and the change in the c-axis. This could induce mechanical stresses during the transition, leading to cell failure if used as an electrode [98].

2.4. Exsolution

2.4.1. Fundamentals and thermodynamics of the exsolution

One of the ideas to boost the catalytic efficiency of oxides such as perovskites is the introduction of additional catalytically active metals on the surface. These metals can be deposited by various methods like infiltration, atomic layer deposition (ALD), chemical or physical vapor deposition (CVD and PVD, respectively). These methods, however, very often require specialistic equipment, limiting their use. Furthermore, nanoparticles deposited by the aforementioned techniques are very prone to agglomeration due to weak NPs-interface interactions and do not offer good control over the size [73,100]. The exsolution process is considered a good alternative for conventional deposition methods, without the aforementioned disadvantages. In the exsolution phenomenon, the catalytically active metals (e.g. noble or transition metals) are introduced, most often into the B-site lattice of perovskite, during the synthesis of the desired material forming a solid solution [100,101]. Then the B-site dopant could be exsolved during reductive treatment allowing for in-situ formation of nanoparticles [72,73]. The exsolution offers the benefits of well anchoring NPs, better control of size by temperature, and simplicity of the process [73]. The term "exsolution", however, is not only reserved for solid state chemistry. It was first used in earth sciences to describe the separation of a homogeneous solid solution into a minimum two different crystal structures [100]. This term in solid state chemistry was popularized after it was used in several well-known publications by John T. Irvine's group [72,73,102,103]. However, the idea of exsolution similar to that was introduced back in 1993 by Schmalzried *et al.* [104] and it was explained as an internal solid-state reaction.

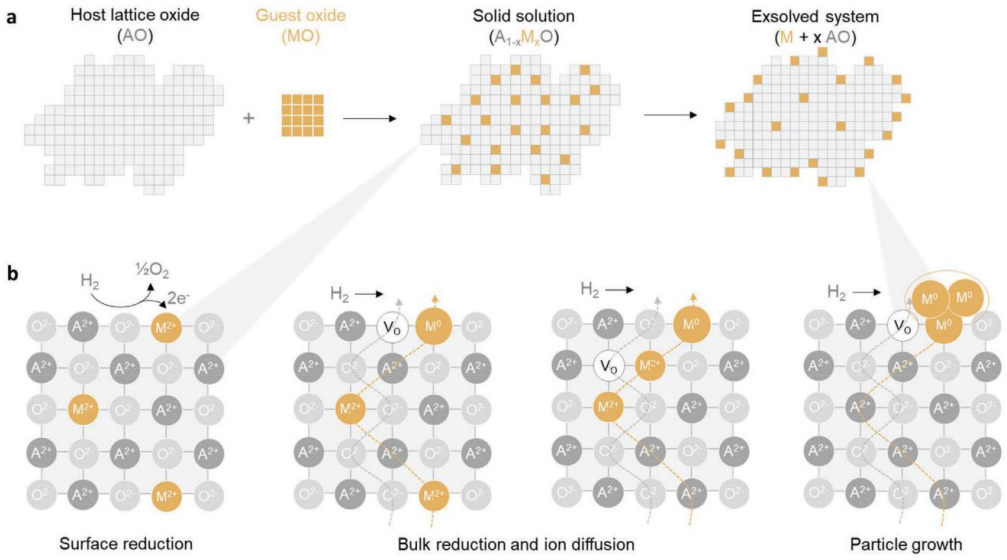


Fig. 2.18. a. The scheme of exsolution process in oxides; b. processes in the exsolution phenomenon: steps include surface, then bulk reduction, ion diffusion, and particle nucleation and growth [101].

The exsolution process can be divided into four fundamental steps, namely diffusion, reduction, nucleation, and growth [7,100,101]. Schematic illustration is presented in **Fig. 2.18**. First, in the presence of reducing conditions, the surface is partially reduced, forming oxygen vacancies $v_O^{\cdot\cdot}$ and electrons. The subsequent diffusion of oxygen ions would trigger a bulk reduction of oxides. Then, the exsolvable cations would be reduced to the metallic state, which is the core of the exsolution process. This process can be described in the Kröger-Vink notation like (2.30) [100] or simplified as (2.31) if the hydrogen is used as a reducing agent [7,100].

$$M_M^{\times} + \frac{x}{2} O_O^{\times} \xrightarrow{T,H_2} M_{surface} + v_M^{x'} + \frac{x}{2} v_O^{\cdot\cdot} + \frac{x}{4} O_2 \uparrow \tag{2.30}$$

$$\frac{1}{x} M_x O_y + \frac{y}{x} H_2 \xrightarrow{T} M + \frac{y}{x} H_2 O \tag{2.31}$$

For the reaction to be thermodynamically favorable, the Gibbs free energy of the products must be lower than for reactants, which can be described as in Eq. (2.32).

$$\Delta G = \sum G_{products} - \sum G_{reactans} \tag{2.32}$$

As a result, the change in Gibbs free energy must be negative. **Fig. 2.19** summarizes the values of ΔG for the reduction of several metal oxides at different temperatures [100]. It can be noticed that the A-site cations are generally hard to reduce; thus, their exsolution is also unlikely. The only exception is the silver, sometimes used as a dopant at the A-site. D-block metals occupying the B-site of the perovskite act differently: some of them are very unlikely to be reduced e.g. Y^{3+}, Yb^{3+}, or Zr^{4+}, while others are easily reducible. The first group is very often used as a dominant B-site cation to provide stability during the reduction [7]. The second group consists mainly of noble metals such as Pt^{4+}, Pd^{2+}, Ir^{4+}, or Ru^{4+}. The main drawback from using noble metals is their price and their classification as critical raw materials (CRMs). Slightly less reducible (based on the change of Gibbs free energy) are transition metals e.g. Fe^{3+}, $Co^{2,3+}$, Ni^{2+}, or Cu^{2+}, and their use is preferable in this thesis. Although cobalt is also in the CRM group, its price is significantly lower compared to noble metals. For the purpose of exsolution, only small concentrations of cobalt are yielding the sufficient number of the exsolved nanoparticles, minimizing the use of CRMs.

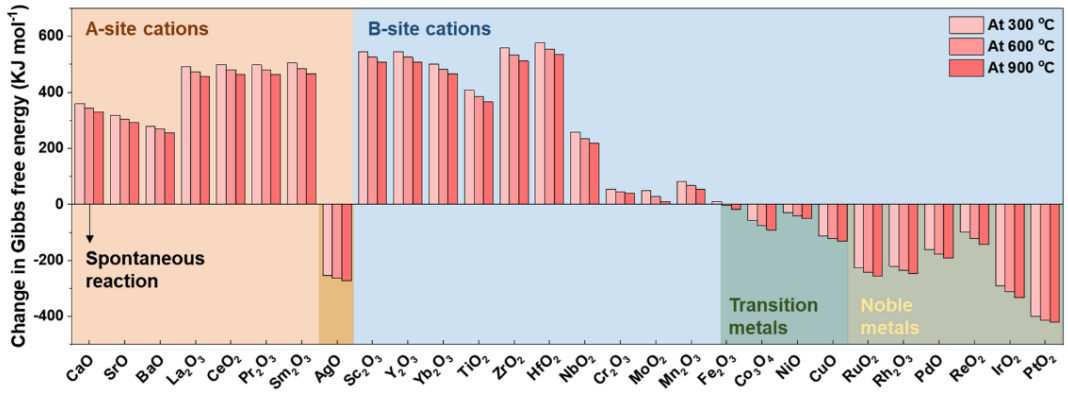


Fig. 2.19. Change in the Gibbs free energy of reduction reaction of different oxides at various temperatures [7].

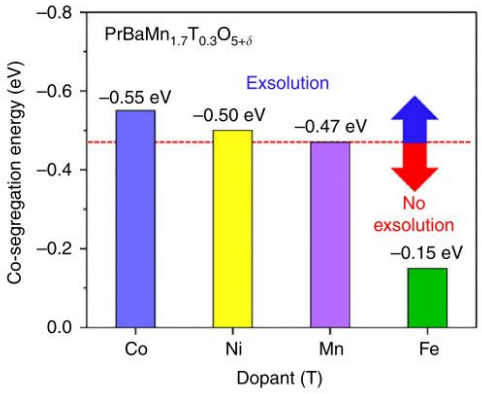


Fig. 2.20. Co-segregation energies for different dopants in $PrBaMn_{1.7}T_{0.3}O_{6-\delta}$ calculated by DFT [105,106].

Although the analysis of Gibbs free energy is a reasonable starting point, the energetics between ideal oxides and the behavior of cations in perovskite may differ greatly. Therefore, the term "segregation energy" or "co-segregation energy" (E_{seg}) can sometimes be found in publications concerning exsolution. This parameter is used to describe the energetics of the exsolution of two species, e.g. transition metal cation and oxygen vacancy. It determines how much energy is required or gained by the diffusion of these species to the host surface. By comparison of the co-segregation energy, it can be predicted if the exsolution of a specific element is favorable. The segregation energy can be calculated by means of Density Functional Theory (DFT), considering both the host lattice and exsolved cations [74,106,107]. For example, in $PrBaMn_{1.7}T_{0.3}O_{6-\delta}$ system (**Fig. 2.20**), Mn cations were dominant B-site cation, while dopants were Co, Ni, or Fe. By means of DFT calculations it was found out that Fe-exsolution would be unfavorable in this compound, which was further proved experimentally [106]. Moreover, E_{seg} is an important factor in bimetallic exsolution, where cations of high co-segregation energy (e.g. iron) can exsolve simultaneously with lower energy cations (e.g. Ni or Co) [5].

One of the important steps in the exsolution process is the nucleation, which could be explained by the change in Gibbs free energy of nuclei ($\Delta G_{nucleation}$). If the exsolution is considered, the change in $\Delta G_{nucleation}$ can be expressed as Eq. (2.33), where $\Delta G_{interface}$ and $\Delta G_{surface}$ can be written as Eq. (2.34-35). [7,108].

$$\Delta G_{nucleation} + E_a = \Delta G_{bulk} + \Delta G_{interface} + \Delta G_{surface} + E_{strain} + E_{diffusion} \quad (2.33)$$

$$\Delta G_{interface} = \gamma_{int} A_{int} \quad (2.34)$$

$$\Delta G_{surface} = \gamma_{sur} A_{sur} \quad (2.35)$$

Where: A_{sur}, A_{int} – area of surface and interface, respectively;

γ_{sur}, γ_{int} – surface and interface tension, respectively;

E_a – activation energy of the nucleation;

E_{strain}, $E_{diffusion}$ – activation energies for strain and diffusion, respectively.

The areas of interface and surface areas can be linked with the wetting angle (θ) of the nanoparticle and its dihedral angle (φ) by Eqs. (2.36-37), respectively. The visual representation of these parameters is presented in **Fig. 2.21**.

$$S_{int} = 4r^2(\pi - \theta) \quad (2.36)$$

$$S_{sur} = 2r^2\varphi \quad (2.37)$$

In general, all parameters in Eq. (2.33) are temperature-dependent and system-dependent [108]. The studies show that the surface has an enormous impact on the nucleaction, e.g. the highest share of particle is visible in the boundaries and concave states. The nucleation, and as a result, the exsolution, is more preferable there, since the dihedral angle φ is lower than π, leading to lower surface area. The lower surface area with the same surface tension directly translates into the lower free Gibbs energy of the surface [108].

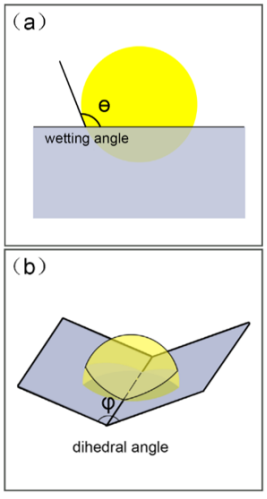


Fig. 2.21. Visual representations of a. wetting angle and b. dihedral angle [108].

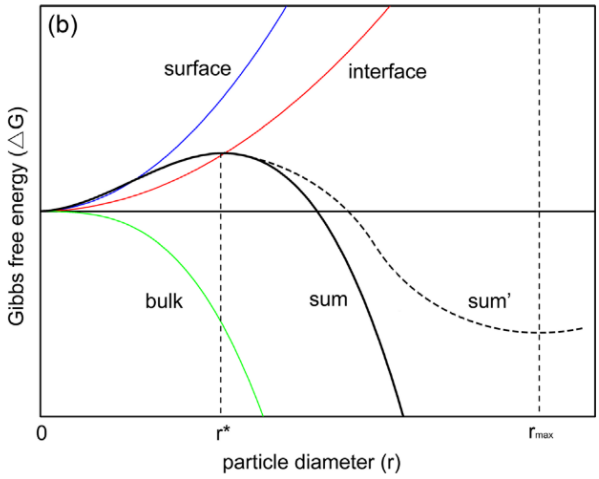


Fig. 2.22. Change of ΔG during nucleation and growth of nanoparticles [108]

According to nucleation theory, nuclei growth would be favorable only if the nuclei reach a critical radius (r*), which can be calculated from $\frac{d\Delta G_{nucleation}}{dr} = 0$, where the Gibbs free energy would reach maximum [7]. The equation describing the critical radius can be expressed as Eq. (2.38), and the change in Gibbs free energy with respect to the bulk, interface, and surface is presented in **Fig. 2.22**.

$$r^* = \frac{(1 - \cos\theta)\gamma_{sur} + (1 + \cos\theta)\gamma_{int}^*}{\Delta G_{bulk}} \tag{2.38}$$

The subsequent process after nucleation is the socketing and growth of the nanoparticles. Growth of NPs arises from the minimization of the surface energy; however, growth is limited by strain, reactant, and diffusion as suggested by Gao *et al.* [108]. The first one is related to the strain formed at the particle-perovskite interface, the second is corelated with the availability of exsolvable cations (e.g. substitution level), while the last originates from the diffusion of exsolvable ions [109]. The particle growth in these models can be expressed as Eq. (2.39), (2.40), and (2.41), respectively.

$$r_s(t) = r_{s-limit}\left[\ln\left(1 + \frac{t}{\tau_s}\right)\right]^{1/3} \tag{2.39}$$

$$r_r(t) = r_{t-limit}\left[1 - \exp\left(-\frac{t}{\tau_r}\right)\right]^{1/3} \tag{2.40}$$

$$r_d = r_{d-limit}\left(\frac{t}{\tau_d}\right)^{1/6} \tag{2.41}$$

where: $r_{s\text{-}limit}$, $r_{r\text{-}limit}$, $r_{d\text{-}limit}$ – characteristic radii for strain-, reactant, and diffusion-limited models, respectively;

τ_s, τ_r, τ_d – characteristic time scales for strain-, reactant, and diffusion-limited models, respectively.

In the original work of Gao *et al.* [108], it was found that the exsolution of nickel nanoparticles from $La_{0.4}Sr_{0.4}Ti_{0.9}Ni_{0.1}O_{3-\delta}$ follows both strain- and reactant-limited models. More perovskite systems are in good agreement with reactant-limited models such as Ni-exsolution in $La_{0.43}Ca_{0.37}Ti_{0.94}Ni_{0.06}O_{3-\delta}$ [109] or Co-exsolution from $SrTi_{0.75}Co_{0.25}O_{3-\delta}$ [110]. On the other hand, there are also works in which the diffusion plays a crucial role such as Ni-exsolution in (La,Ca)(Ni,Ti)$O_{3-\delta}$ thin films [111]. Unavoidably, the experimental methodologies and conditions (composition and reduction parameters) varied between studies. Consequently, the rate-determining step that governs particle growth is system-dependent and may differ with respect to the sample, the characteristics of the targeted particle, and the specific reduction conditions.

One of the aspects that affect exsolution is the non-stoichiometry at the A-site, which was first reported by Neagu *et al.* in one of the pioneering works in exsolution [73]. Introduction of the non-stoichiometry stabilizes the perovskite host after reduction and exsolution according to reaction (2.41). Neagu *et al.* [73] suggested that A deficiency leads to equilibrium changes and local destabilization of the lattice, which leads to more dynamic exsolution. The scheme for this process is presented in **Fig. 2.23**. The A-site deficiency (marked with dashed red) leads to the local B-site excess, which is then expelled to the surface. Although it still remains part of the perovskite host, locally it can be considered more like a BO_n oxide cluster. During the high-temperature treatment in H_2, this cluster is more likely to be reduced than B-site cations in the bulk, promoting the exsolution of B metal.

$$A_{1-\alpha}BO_{3-\delta} \xrightarrow{H_2,T} (1-\alpha)ABO_{3-\delta'} + \alpha B \tag{2.41}$$

$$ABO_{3-\delta} \xrightarrow{H_2,T} (1-\alpha)ABO_{3-\delta'} + \alpha AO + \alpha B \tag{2.42}$$

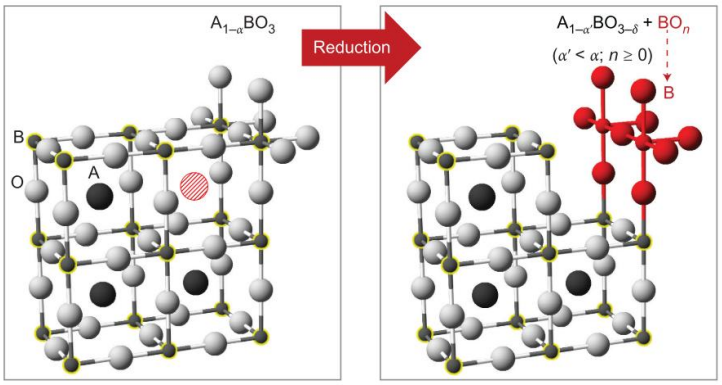


Fig. 2.23. Scheme for beneficial exsolution from A-site deficient perovskites [73].

However, when the stoichiometric amount of A-site cations would remain, the formation of AO oxides during the reduction is likely as presented in reaction (2.42). Although in the stoichiometric ones, the new phase is formed and the rate of exsolution is limited, this may promote the reversibility of exsolution. In non-stoichiometric oxides, reversibility is unlikely [73,101].

Based on the reports by Neagu *et al.* [73], in this thesis, non-stoichiometry is introduced for the purpose in STO-based perovskites. This was aimed at promoting the exsolution of the B-site dopants. Because of possible redox non-stability, the SFM-based materials are kept in stoichiometry, in order not to introduce another variable into this system.

2.4.2. Alternative exsolution pathways

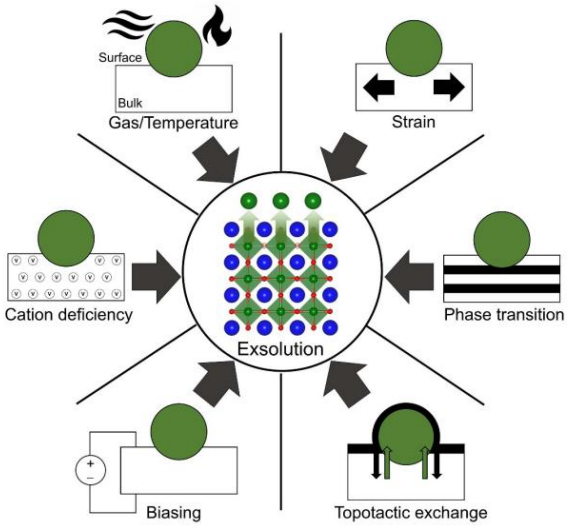


Fig. 2.24. A scheme for different exsolution mechanisms and pathways [112].

Although typical exsolution is mainly based on the reductive treatment of the perovskite host, several other approaches to this phenomenon were also recognized and are schematically presented in **Fig. 2.24** [100,112]. First, electroswitching was found to be able to exsolve nanoparticles quickly and without reducing agent [113]. It was performed on $La_{0.43}Ca_{0.37}Ti_{0.94}Ni_{0.06}O_{3-\delta}$ under 2 V potential in a 50% H_2O/N_2 atmosphere. Myung *et al.* [113] have found that exsolution requires two orders of magnitude less time to occur compared to conventional reduction in hydrogen. Regardless of the methodology, the driving force remains the same: pO_2 gradient between the oxide and the environment around it. The application of 2 V could be calculated to result in $pO_2 \approx 10^{-35}$ atm based on the Nernst equation (2.12) [113]. Such an approach suggests that biasing could be an interesting method for exsolving NPs during the SOCs operations. Moreover, the additive effect of biasing and the presence of a reducing atmosphere could result in an enhanced formation of nanoparticles.

Despite the exsolution of the dopant cation from the host lattice, Kwak *et al.* [114] reported a synthesis via heterogeneous doping of catalytically active metal cations along the grain boundaries of the host oxide. First, the metal source is deposited on the oxide surface, then the material is annealed to obtain the diffusion of the metal on the grain boundaries. The annealing temperature is about one third of the melting point of host oxide. This particular temperature is known as Hüttig temperature, at which the atoms on the surface start to be mobile allowing for surficial diffusion [115,116]. At the same time, the bulk diffusion is still not favorable until point known as Tammann temperature (half of the melting temperature of the compound) is reached [115,116]. Finally, the metal source is etched from the oxide surface. The metallic nanoparticles nucleate in the corners of the grain boundaries after the reductive heat treatment is carried out. Such nanoparticles are embedded between two grains, which provides a good attachment comparable to that of conventionally exsolved particles. What is more, this method allows doping above the metal solubility limit in the host oxide [114].

Another approach to use of the exsolution process is the formation of bimetallic or even ternary alloys. The catalytic activity of perovskite materials decorated with exsolved nanoparticles can be even further improved when two or more types of metallic particles are exsolved from the structure and form metallic alloys on the surface. Compared to the monometallic Ni nanoparticles, the Fe-Ni alloy nanoparticles exhibit higher site activities, greatly improved durability over long-term testing, and increased tolerance to sulfur-based atmospheres [102]. At the same time, these bimetallic alloys demonstrate outstanding microstructural stability and high tolerance to coking, similar to those presented by monometallic Ni nanoparticles [102]. Furthermore, the activation energy measured for electrochemical oxidation of hydrogen at $La_{0.4}Sr_{0.6}Fe_{0.75}Ni_{0.1}Nb_{0.15}O_{3-\delta}$ anode with exsolved Fe-Ni alloy was few times smaller (25-69 kJ mol^{-1}) than the value (>160 kJ mol^{-1}) observed at the Ni-YSZ anode [117]. One of the methods to exsolve alloy is co-doping of two transition metals, which allowed to obtain the Ni-Cu alloy exsolved from $(La_{0.75}Sr_{0.25})_{0.9}(Cr_{0.5}Mn_{0.5})_{0.9}(Ni_xCu_{1-x})_{0.1}O_{3-\delta}$ by Lu *et al.* [118]. Moreover, bimetallic Ni-alloys have enhanced sulfur tolerance compared to Ni nanoparticles [119,120]. Taking into consideration that the exsolution is possible for transition and precious metals, there is a great number of alloys that can be formed. However, so far, the exsolved Cu-Fe, Co-Fe, Co-Ni, and Ni-Fe transition metal alloys have been experimentally confirmed. Moreover, the solubility of metals is another crucial factor that needs to be considered when preparing alloy nanoparticles. When metals do not form a homogeneous alloy, metal nanoparticles can be exsolved separately as reported for Pd-Fe by Li *et al.* [70] or may form a core-shell structure like Pd-Ni [121] or Fe-Ni [122]. The scheme for possible bimetallic exsolution structures is presented in **Fig. 2.25** [5].

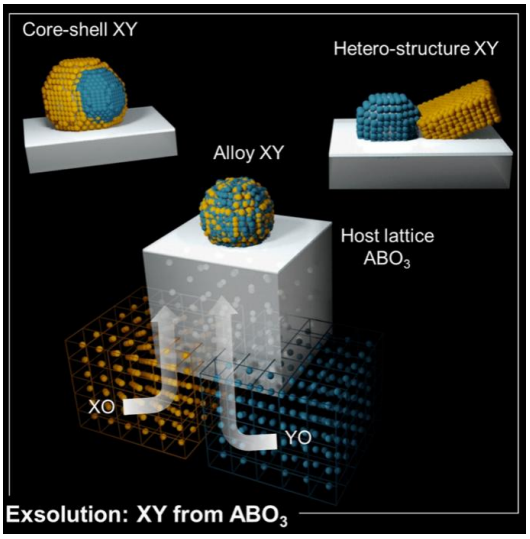


Fig. 2.25. Possible nanoparticle structures for bimetallic exsolution [5].

In addition to alloys co-exsolved from the host lattice, there are few reports on the formation of bimetallic alloys from layers deposited on the perovskite's surface. Among them, one may find the topotactic ion exchange. One benefit of this method is that it produces perovskite without B-site vacancies [105,123]. For doped perovskites, the reaction can be presented as (2.41), where G denotes the guest cation from the deposited layer.

$$AB_{1-x}C_xO_3 + xG_{deposited} \rightarrow AB_{1-x}G_xO_3 + xC_{exsolved} \quad (2.41)$$

This approach was first introduced in pioneering work by Joo *et al.* [105], in which they studied $PrBaMn_{1.7}Co_{0.3}O_{5+\delta}$ as a host perovskite with deposited Fe as a guest material. The scheme of proposed mechanism is shown in **Fig. 2.26** and consists of several steps. During step 1 the guest ions are swapped with surficial B-site atoms (Co in the primary Joo's work [105]). Then, the exchange between the guest ion and exsolved cation with high segregation energy lever occurs as shown in step 2. This prevents the B-site vacancy and structural changes in the host oxide. Lastly, the host cation forms an alloy with guest ions remaining on the surface. So far, topotactic ion exchange has been employed in Ni-Fe [105] and Co-Fe [123]. The methods for applying the guest ion layer differ and atomic layer deposition (ALD) and infiltration have been reported so far [105,123]. The infiltration method has been applied to deposit iron ions on the surface of $PrBaMn_{1.7}Co_{0.3}O_{5+\delta}$. Then, the exsolution process followed by topotactic ion exchange occurred to form a Co-Fe nanoalloy. Later, Joo *et al.* [123] reported that the diffusion rate of the guest cation into the host lattice is a crucial factor and may be provided by atomic layer deposition. However, their DFT calculations have shown that the co-segregation energy of the deposed ion needs to be lower than that of the exsolved host ion to allow topotactic exsolution. For lanthanum strontium titanates (LST) the co-segregation energy follows the order: Cu→Ni→Co→Fe→Cr→Ti [123].

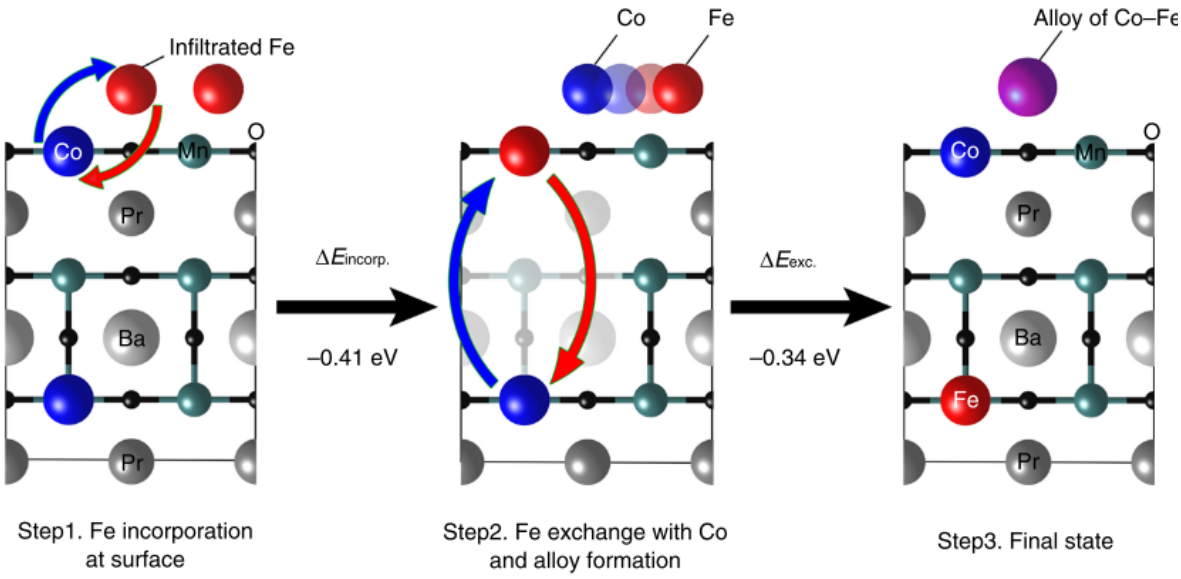


Fig. 2.26. The mechanism of topotactic ion exchange exsolution [105].

2.4.3. Benefits of the exsolution

The exsolution process offers many benefits, several of which have already been mentioned in previous chapters. One of the most prominent is the anchoring of nanoparticles, making them less prone to detachment and deactivation [101]. This is particularly interesting in the field of hydrocarbon-fed SOFCs, where carbon deposition may take place. In conventionally deposited nanoparticles, the

carbon growth could lift up the particle from the host, decreasing its performance. However, exsolved nanoparticles, due to the strong NPs-substrate interaction are less prone to such a process [72,101]. Additionally, this strong interfacial force also makes nanoparticles more stable for different functionalization processes (e.g. partial oxidation, phosphatization, nitrification) [72,100,101].

Another attractive property of exsolution is the possible reversibility of this process. During oxidative treatment, the nanoparticles are expected to be diffused back to the lattice, from which they can be exsolved during the next redox cycle. In this approach, exsolution can be associated with the concept of "intelligent" catalysts [16,100,124–126]. Although it is an interesting and promising approach, there is no agreement on the reversibility of this process, and it seems to be extremely dependent on the host. For example, double perovskites such as SFM seem to favor the reversibility [16,98], which is correlated with phase changes between double and layered perovskite structures during redox cycling. At the same time, the exsolution in strontium titanates is unlikely to be reversed, which was studied by Weber *et al.* [127].

2.4.4. Exsolution from the fluorite structures

The exsolution studies focus vastly on the perovskites as hosts due to their stability and high variety of dopants in B-sites. Another family of compounds that may be interesting for exsolution are oxides in the fluorite structure, e.g. YSZ or ceria. In this field, the solubility of additional exsolvable cations remains a serious challenge. Joo *et al.* [128] have reported successful doping with just 3 mol. % of Ni into yttria stabilized zirconia. Then during the reduction, Ni nanoparticles exsolve from the lattice, leading to better performance in dry reforming of methane. Jiang *et al.* [129] reported the successful exsolution of Fe from ceria doped with samarium. They managed to incorporate 10 mol. % of Fe into the lattice, which was then exsolved under a CO/CO_2 mixture instead of hydrogen. Similar solubility concerns arise for doped-ceria. So far, no agreement is reached on what are the solubility limits of e.g. Mn, Fe, Ni, Co, and Cu in ceria lattice. If the cations are not present in the $CeO_{2-\delta}$ lattice before the reduction but rather form a well-dispersed foreign phase (e.g. in the form of oxide) on the surface, then the formation of transition metal nanoparticles is not an exsolution but a simple reduction of the oxides. Furthermore, ceria doped with transition metals are very often prepared by wet chemistry methods that allow the formation of various nanopowders [130–133]. In these cases, unfortunately the XRD alone cannot give a direct answer to whether a single phase is formed.

Prior to switching the main interest to exsolution from perovskites, the cerium (IV) oxides doped with transition metals were synthesized and thoroughly analyzed by a PhD candidate. The results are described in the publication [134]: **Ducka A.,** Błaszczak P., Zajac M., Mizera A., d'Acapito F., Bochentyn B.: *Limited dissolution of transition metals in the nanocrystalline cerium (IV) oxide*//

CERAMICS INTERNATIONAL -Vol. 50, iss. 23 Part B (2024), s.50921-50933. The main aim of this work was to analyze whether the 10 mol. % of transition metal can be successfully synthesized. As a result, the solubility concern was systematically addressed, and it was found that the limit is lower than 10 mol. %.

In the publication [134], the doped with transition metals (10 mol.%) ceria powders were synthesized by the reverse microemulsion method to form nanoparticulate powders. The results of the XRD analysis are presented in **Fig. 2.27**. Directly after the synthesis, diffraction peaks were wide due to the nanometric size of the crystallites and no additional phases were formed. However, they could be below the detection limit of the apparatus and/or be lost within the noise. Therefore, all powders were annealed at 800 °C to crystallize cerium (IV) oxide and possibly any impurities. After this, small peaks from the respective oxides formed. Another possibility is that dopants are present in a metastable state and, upon heat treatment, form their respective oxides on the grain boundaries, as suggested by Avila-Paredes *et al.* [135].

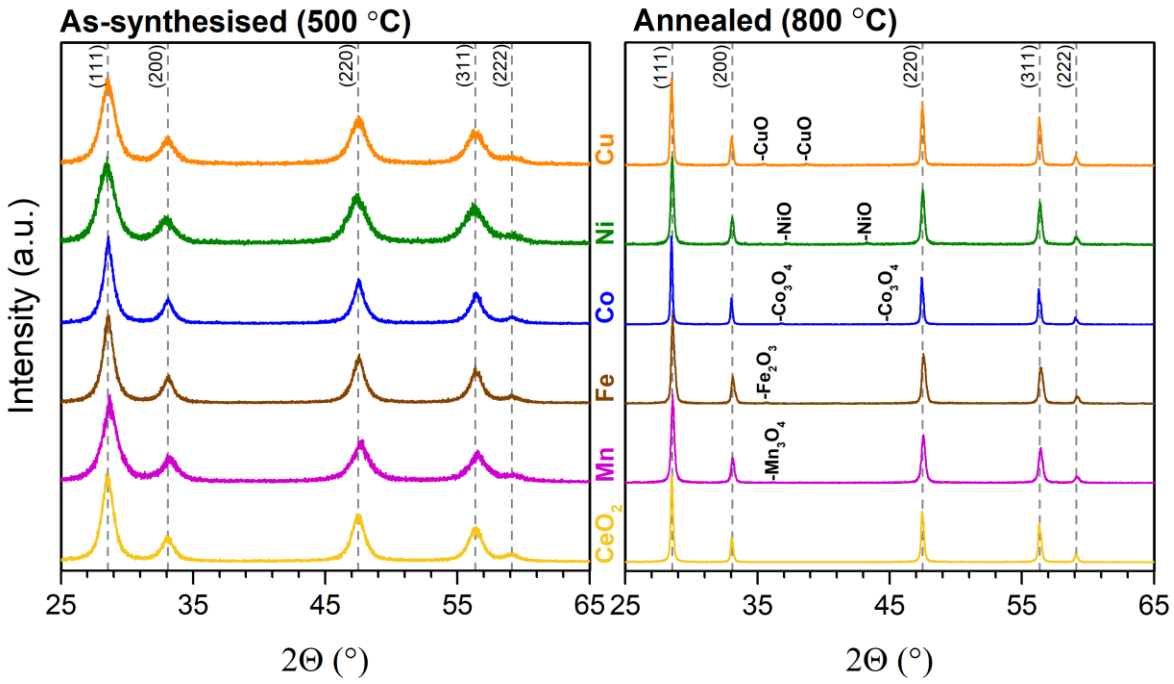


Fig. 2.27. XRD patterns for transition metal-doped ceria [134].

To determine whether transition metals form within the lattice or as external oxides, additional techniques such as TPR or XAS were employed. By means of the TPR technique, it was found that the reduction profiles resemble those characteristic for the well-dispersed nanometric oxides of the respective transition metals. These results were further proved by the advanced XAS analyses. The XAS results for as-prepared and annealed oxides appear in **Fig. 2.28**. In summary, the spectra indicate

that the transition metal oxides crystallized during annealing, rather than existing post-synthesis. This provides further evidence for oxide clusters within the ceria matrix. Nevertheless, most of the dopants were not fully incorporated into the lattice and remained only partially dissolved. When the reference spectra are compared, the vast majority of the transition metals can be found in the states corresponding to its different oxides. Another proof for the formation of metastable oxides is the significant change of the XAS spectra after the annealing, indicating the crystallization to more stable counterparts. According to [134], Mn exhibited the highest degree of dissolution into $CeO_{2-\delta}$ among all transition metals. Cu ions proved the most challenging to integrate into $CeO_{2-\delta}$, with most Cu_xO_y remaining as surface scales. Nanocrystallinity, while beneficial for catalysts, obscures additional phases. Most metals exist primarily as dispersed surface oxides, with only a minor solid solution forming between $CeO_{2-\delta}$ and the metals.

Unfortunately, after these findings and the misdoubt about the formation of doped ceria, further examination of exsolution from ceria was abandoned.

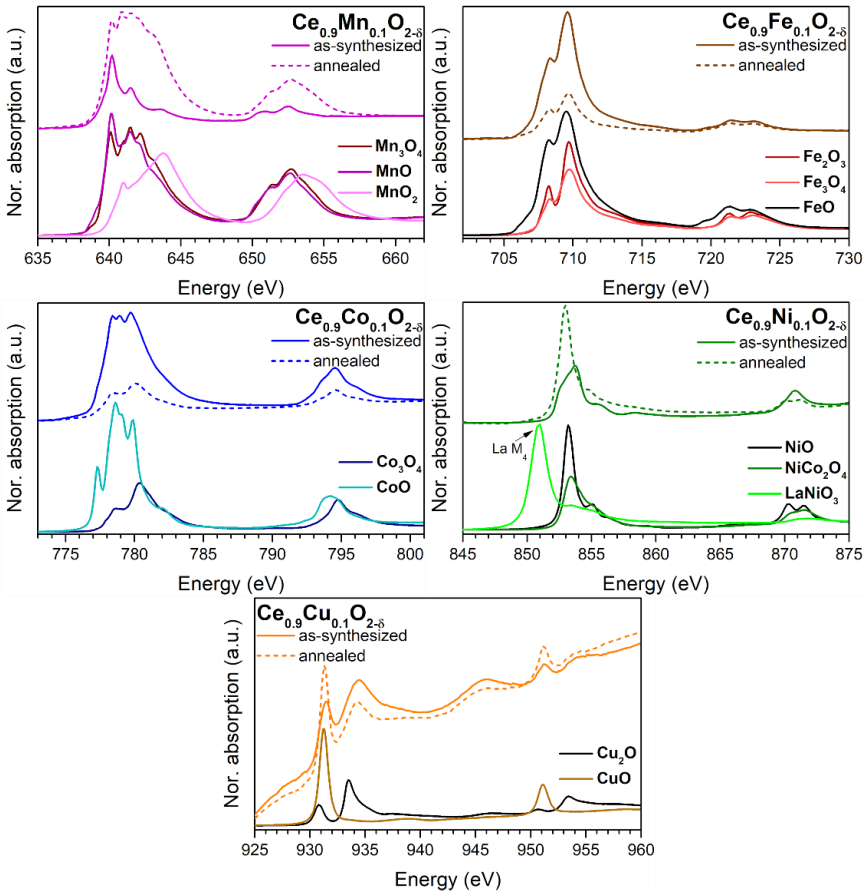


Fig. 2.28. $L_{3,2}$-edges of transition metals in doped ceria [134].

3. Materials and methods

3.1. Synthesis procedure and reduction

3.1.1. $SrTiO_{3-\delta}$

Single perovskites based on strontium titanate were chosen to have a specific formula $(La_{0.3}Ce_{0.1}Sr_{0.6})_{0.9}Ti_{0.9}Ni_{0.05}M_{0.05}O_{3-\delta}$, where M= Fe, Co, Ni, or Cu. The abbreviation used in this thesis is LSCT-NiM. For M=Ni the resulting formula is $(La_{0.3}Ce_{0.1}Sr_{0.6})_{0.9}Ti_{0.9}Ni_{0.1}O_{3-\delta}$, abbreviated simply as LSCT-Ni. Each dopant served a specific role in the perovskite: lanthanum was added to improve the electrical conductivity [63,74,85,136–138], cerium to increase carbon gasification due to the ease of switching between Ce^{4+} and Ce^{3+} states, [24,71], and transition metals to work as catalytic centers after exsolution [7,107]. In case of doping with two transition metals at the B-site, exsolution of bimetallic nanoparticles is expected [5,6,139,140]. Moreover, in order to enhance the exsolution, the A-site non-stoichiometry was introduced [73,101].

The Pechini method was used to synthesize the final products. Titanium (IV) butoxide ($Ti(OBu)_4$) was used as a precursor for Ti^{4+} ions, while the rest of the metals were used in the form of nitrates. Citric acid (CA) and ethylene glycol (EG) were used as chelating agent and fuel, respectively. All reagents used were analytical grade, with at least 3N purity. The chemicals were purchased from reputed brands such as Thermo-Fischer, Sigma Aldrich, Chempur, or Eurochem. The appropriate amount of titanium (IV) butoxide was put into the beaker, then CA and EG were added to form a slurry at room temperature (RT). No water was added at this point to avoid Ti^{4+} hydrolysis. The rest of the metal nitrates were mixed with deionized water (DI) separately until a clear solution was formed. When a homogenous slurry of $Ti(OBu)_4$, CA, and EG was obtained, only then the nitrates solution was added. The mixture was then gradually heated to 150 °C with vigorous stirring. After the gel was formed in the beaker, it was transferred to alumina crucibles for calcination. Calcination consisted of several steps: heating to 400 °C, dwelling for 1 hour at 400 °C, heating to 600 °C and dwelling for 1 hour, lastly heating to 1200 °C with 12 hours of dwelling time. The heating-cooling ratio was 3 °C min^{-1}. If perovskites underwent any characterization after this point but before reduction, should be referred to as “as-prepared” or abbreviated AP

In order to perform the exsolution process, the compounds had to be reduced. To do so, the well-ground powders were placed in the tube furnace. Prior to the heating process, the tube was rinsed for at least 2 h with H_2 at RT. The powders were then heated to 900 °C in pure hydrogen and were kept for 12 hours at this temperature. The heating and cooling rate was kept at 3 °C min^{-1}. After this process, the powders will be referred to as “reduced” or RED.

3.1.2. $Sr_2Fe_{1.5}Mo_{0.5}O_{6-\delta}$

First, pristine, La-, or Nb-doped $Sr_2Fe_{1.5}Mo_{0.5}O_{6-\delta}$ were synthesized to study the stabilization of double perovskite during redox treatment. The formulas are presented in the **Tab. 3.1**. Niobium was doped at the B-site of double perovskite, but it was aimed at proportionately occupying Fe- and Mo-sites. As a result, the ratio between Fe:Mo was kept constant at 3, to avoid or minimize the formation of Fe- or Mo-rich phases. Both dopants were chosen based on the literature, regarding the positive impact on the electrical properties and redox stability [15,136].

After La-doping was found to be most effective for both stabilization of the structure and electrical conductivity (see Chapter 4.2.1), transition metals (Ni, Co, or Cu) were introduced into the B-site in order to improve the catalytic efficiency of the material. Similarly, like in Nb-doping, the transition metal was proportionately incorporated into both sub-lattices and Fe:Mo was kept at 3. After further stability improvement due to Cu-doping, it was decided to try bimetallic doping at the B-site, where two transition metals (Ni+Cu or Co+Cu) were simultaneously added to the lattice. In this case, the total amount of dopant was kept constant and the only variable was the ratio between Ni/Co:Cu. All of the formulas of the aforementioned compounds are presented in **Tab. 3.1**.

Tab. 3.1. The summary of synthesized double-perovskite compounds based on $Sr_2Fe_{1.5}Mo_{0.5}O_{6-\delta}$.

Dopant(s)		**Formula**	**Abbreviation**
None (pristine)		$Sr_2Fe_{1.5}Mo_{0.5}O_{6-\delta}$	SFM
Nb (B,B'-sites)		$Sr_2Fe_{1.425}Mo_{0.475}Nb_{0.1}O_{6-\delta}$	SFMNb
La (A-site)		$La_{0.3}Sr_{1.7}Fe_{1.5}Mo_{0.5}O_{6-\delta}$	LSFM
La (A-site)	Ni or Co (B, B'-sites)	$La_{0.3}Sr_{1.7}Fe_{1.5-0.75x}Mo_{0.5-0.25x}TM_xO_{6-\delta}$ TM=Ni, Co x=0.05; 0.1; 0.15; 0.2	x-LSFMNi x-LSFMCo x=5; 10; 15; 20
	Cu (B, B'-sites)	$La_{0.3}Sr_{1.7}Fe_{1.5-0.75x}Mo_{0.5-0.25x}Cu_xO_{6-\delta}$ x=0.1; 0.15; 0.2	x-LSFCM x=10; 15; 20
	Ni and Cu (B, B'-sites)	$La_{0.3}Sr_{1.7}Fe_{1.35}Mo_{0.45}(Ni_{1-x}Cu_x)_{0.2}O_{6-\delta}$ x=0.25; 0.5; 0.75	x-y-LSFNCM x (Ni conc.) = 5; 10; 15 y (Cu conc.) = 5; 10; 15
	Co and Cu (B, B'-sites)	$La_{0.3}Sr_{1.7}Fe_{1.35}Mo_{0.45}(Co_{1-x}Cu_x)_{0.2}O_{6-\delta}$ x=0.25; 0.5; 0.75	x-y-LSFCCM x (Co conc.) = 5; 10; 15 y (Cu conc.) = 5; 10; 15

Regardless of the composition, the perovskites were synthesized by the Pechini method. Similarly, like for single perovskites, salts, mostly nitrates, were used as cation precursors. Only for Nb and Mo other salts were used, namely niobium (V) chloride ($NbCl_5$) and ammonium molybdate ($(NH_4)_6Mo_7O_{24}$), respectively. Once again, CA was used as a chelating agent and EG as a fuel. All reagents were of analytical grade with purity at least 3N. Compared to the synthesis of $SrTiO_{3-\delta}$ derivatives, the process was simplified for double perovskites. Appropriate amounts of the respective reagents were placed into the beaker and mixed with DI until a clear solution was obtained. Then, the mixture was gradually heated to 130 °C until gel was formed. Finally, the temperature was increased to 180 °C until the gel was burned to form a more ashy structure. The ashes were transferred to an alumina crucible, in which a further thermal treatment was performed. The calcination was also simplified and consisted of two main steps: heating to 600 °C with 1 h dwell, then heating to 1200 °C for 10 hours. The heating rate was kept at 3 °C min^{-1}. Similarly, as for single perovskites, the term "as-prepared" (abbreviated AP) would be used for any characterization beyond this point but prior to any reduction.

For the reduction, finely ground powders were used. The reduction procedure was analogous to the reduction of single perovskites: powders were placed in the tube furnace, rinsed with H_2 for at least 2 h at RT, and lastly heated. Double perovskites were reduced at lower temperatures between 700 – 800 °C for 4 h. The heating-cooling rate was 4 °C min^{-1}. Any characterization result of these powders will be referred as "reduced", with the temperature given, if necessary. SFM, LSFM, and SFMNb also underwent re-oxidation to examine the reversibility of the phase transition. The re-oxidation process was carried out on pre-reduced powders for 4 h at 800 °C in ambient air.

3.2. Phase and structural characterization

3.2.1. X-ray diffraction

To investigate the phase composition of the materials, X-ray diffraction (XRD) measurements were performed, using Bruker D2 PHASER XE-T. XRD patterns were collected predominantly at room temperature, unless otherwise indicated. High-temperature XRD measurements under air atmosphere were performed on a Philipps X'Pert Pro diffractometer with the high-temperature Anthon Paar HT-1200 oven adapter. Both diffractometers operate with Cu-Kα (1.54 Å) radiation sources. The HighScore Plus 3.0.2 software from PANalytican was used to analyze the obtained diffraction patterns and to perform Rietveld refinement on them. As a reference, CIFs (Crystallography Information Files) were used: 1512124, 1531825, and 1528687; for STO, SFM-DP, and SFM-RP, respectively. From the

Rietveld refinement, the lattice parameters were obtained as well as the phase composition of the compounds.

3.2.2. Electron microscopy

The microstructure and morphology of the materials were revealed using the Scanning Electron Microscope (FEI Quanta FEG 250) with a secondary electron detector operating in high vacuum mode with an accelerating voltage of 10 kV. A quantitative elemental composition analysis was performed using an EDS technique (Energy Dispersive X-ray Spectroscopy, EDAX Genesis APEX 2i) with an ApolloX SDD and at an accelerating voltage of 30 kV.

The more advanced imaging was performed by Transmission Electron Microscopy (TEM). In this technique, not only the structure and the elemental composition can be revealed, but also more sophisticated techniques can be utilized. For example, in High Resolution TEM (HRTEM) it is possible to visualize the lattice fringes in the crystallites. By this, the d-spacing can be determined or even defects can be visualized. Another powerful tool in the TEM-arsenal is Selected Area Electron Diffraction (SAED). In this approach, the electron beam passes through the thin area, hitting the atoms in the lattice. As a result, electrons scatter in the directions that can be predicted based on the basis of the crystal lattices. If the material is polycrystalline, instead of the dots, the rings are formed. Similarly to powder diffraction it allows one to determine the phases and calculate the lattice constants.

High resolution Transmission Electron Microscopy (TEM) imaging was performed at two different facilities using different approaches. The STO-based compounds were measured after the reduction in the form of lamellas, which were prepared by LYRA I FE XMH FIB-SEM (Focused Ion Beam-Scanning Electron Microscopy) by Jaroslava Nováková at Charles University in Prague. Then the lamellas were analyzed by STEM coupled with EDS elemental mapping and SAED (Selected Area Electron Diffraction) on the LSCT-NiCo sample. The measurements were performed by Corneliu Ghica (National Institute of Material Physics, Bucharest) on a JEOL JEM ARM 200F microscope operating at 200 kV of accelerating voltage. This collaboration was the result of a CERIC-ERIC proposal. The analysis of SFM-based compounds was undertaken in cooperation with Prof. Muhammad Imran Ashgar from the Tampere University (Finland) using a JEOL (F200 S/TEM) microscope equipped with EDS. For these measurements, the reduced powders were suspended in isopropanol and then deposited onto the carbon grid followed by an evaporation of the alcohol from the slurry.

3.2.3. Specific surface area

The specific surface area (SSA) was measured based on the BET (Brunauer–Emmett–Teller) isotherm model on an N_2 sorption unit (NOVAtouch LX1, Quantachrome). Prior to the sorption measurements, the samples were subjected to adsorbate removal under a high vacuum at 300 ℃ for 3 h.

3.2.4. Porosity

The values of the total and open porosity of the pellets were calculated by the means of the Archimedes principle of density measurement. The dry samples were first weighed then immersed in kerosene and subjected to vacuum treatment at RT until no more bubbling occurred. The soaked samples were reweighed when submersed in the kerosene (called submerged) and in ambient air after the removal of excess surficial fluid (saturated). The calculations were performed according to the standard procedure of the Archimedes density and porosity measurements. The density, total porosity and open porosity values were calculated based on Eq. (3.1-3.3), respectively

$$\rho = \frac{m_{dry}}{m_{sat} - m_{sub}} \cdot \rho_{kerosene} \tag{3.1}$$

$$P_{total} = \left(1 - \frac{\rho}{\rho_{theory}}\right) \cdot 100\% \tag{3.2}$$

$$P_o = \frac{m_{sat} - m_{dry}}{m_{sat} - m_{sub}} \cdot 100\% \tag{3.3}$$

Where: ρ – density of measured material (g cm^{-3})

ρ_{theory} – theoretical density of the material (g cm^{-3})

$\rho_{kerosene}$ – density of kerosene (0.7958 g cm^{-3})

m_{dry} – mass of dry pellet (before immersion in kerosene) (g)

m_{sat} – mass of pellet saturated with kerosene (g)

m_{sub} – mass of pellet submerged in kerosene (g)

P_{total} – total porosity (%)

P_o – open porosity (%)

3.3. Thermal characterization

3.3.1. Temperature-programmed techniques

Temperature-programmed techniques (TPx) offer a wide variety of materials properties that can be analyzed. Regardless of the type, all of them depend on the change in the composition of the gas stream leaving the reactor. When the TCD (thermal conductivity detector) is used, the difference in the composition of the outlet stream and the make-up gases (leading to a change in thermal conductivity of each of them) can be determined and visible as an electrical signal. Among the variety of TPx techniques, two most commonly known and used are TPR and TPO. In the first one, the harmix is fed to the reactor bed. At specific temperatures, where the reduction occur, hydrogen is consumed from the stream, lowering the H_2 amount. Meanwhile, the composition of the make-up stream remains unaffected. As a result, a voltage signal from TCD is formed indicating the reduction of the species. The TPO works analogously, with the fed and make-up streams consisting of O_2-He mixture. When the material is oxidized, it consumes O_2, impoverishing this gas in the stream.

H_2-TPR (temperature-programmed reduction) and O_2-TPO (temperature-programmed oxidation) measurements were performed using an in-house-built apparatus equipped with a TCD detector (Buck Scientific, USA), a coldtrap, and a heated gas transfer line. Each time, the appropriate mass (ranging between 100 and 200 mg) of the sample was placed in a quartz reactor with an internal measurement of the bed temperature. The powders were degassed at 200 °C for 20 min in a stream of 5N He prior to the measurements. The samples were reduced under the flow of 40 ml min^{-1} 6 vol.% H_2-Ar gas mixture. The tests were performed up to 900 °C with a heating rate of 10 °C min^{-1}. Afterwards, the samples were cooled down to RT and the gas stream was switched to a mixture of 5 vol.% O_2 in He. The powders were left for equilibration for 1 h under O_2-He stream and oxygen uptake tests were carried out using the same regime as during the TPR measurements. Profiles were collected using the PeakSimple software with a frequency of 1 Hz.

3.3.2. Differential Scanning Calorimetry and Thermogravimetry

To study the oxidation process in the pre-reduced SFM-based powders simultaneous thermogravimetry (TG) and differential scanning calorimetry (DSC) measurements were performed under synthetic air on the Netzsch STA 449 F1 Jupiter apparatus. Data were collected from room temperature up to 900 °C at a heating rate of 5 °C min^{-1}. For each analysis, around 10 mg of a powder with ±10% tolerance factor was used.

3.3.3.Dilatometry

In order to determine the mechanical compatibility between novel materials and conventional SOC components, the thermal expansion coefficient was measured by dilatometry. It was performed using the Netzsch DIL 402 PC dilatometer working in the 100–1000 °C temperature range under a synthetic air stream at 3 °C min^{-1} heating-cooling rate. The data were collected on sintered samples and the TEC value was calculated from the cooling curve.

3.4. Electrical characterization

The conductivity of the compounds was measured using the direct current 4-wire method (DC4W). For this purpose, the samples were pressed into square pellets and sintered at 1400 °C for 10 h for densification (both STO- and SFM-based). Subsequently, dense (>95% relative density) pellets were cut into narrow, rectangular bars, onto which platinum paste (Heraeus) was brush-painted and fine Pt wires were attached. The schematic presentation of sample ready for measurement is shown in **Fig. 3.1**. For the measurements, the Keysight DAQ970A apparatus was used. Each sample was first heated to 800 °C in air, then conductivity measurements were taken every 50 °C during cooling to 300 °C. After each temperature change, the samples were stabilized for at least one hour. Before the atmosphere was changed to hydrogen, the cell was rinsed with Ar until no air remained inside, and then the procedure was repeated in hydrogen for SFM-based compounds. The only difference was that the samples were kept at 700-800 °C (depending on the sample) for 4 hours to mimic the reduction process. To reduce the STO-based perovskites, the samples were removed from the measuring cell, reduced at 900 °C for 10 h in an external tube furnace under H_2 flow. Such a process allowed to reduce the perovskites and perform an exsolution process. After the reduction, the samples were mounted into the measuring cell, heated up to 800 °C with a 4 °C min^{-1} heating range in hydrogen. The remaining procedure was kept similar as described above.

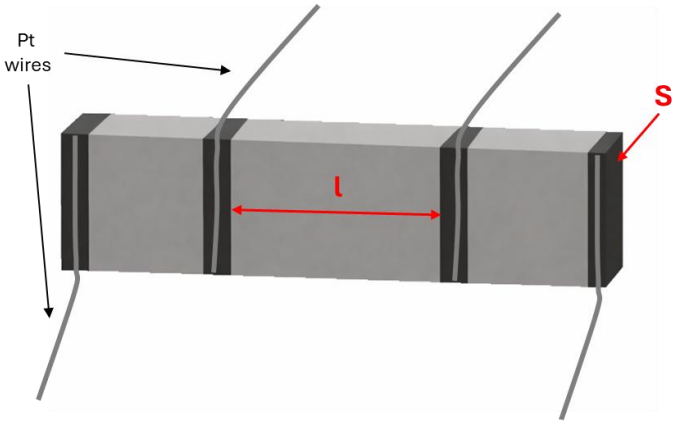


Fig. 3.1. Sample prepared for DC4W measurements.

The conductivity of the samples was calculated using the following formula

$$\sigma = \frac{l}{R \cdot S} \tag{3.4}$$

Where: l – the distance between inner, voltage electrodes (cm)

R – measured resistivity (Ω)

S – cross-section area of the pellet (cm^2)

To calculate the activation energy E_A in thermally driven conduction mechanism, the Arrhenius formula was used as presented in Eq. (3.5):

$$\sigma_{el}T = \sigma_0 \exp\left(-\frac{E_A}{k_B T}\right) \tag{3.5}$$

For the calculation of electrical conductivity in STO-based materials, the Bruggeman correction was applied, which can be written as Eq. (3.6), linking measured conductivity σ and porosity P of the samples.

$$\sigma_{corr} = \sigma(1 - P)^{-1.5} \tag{3.6}$$

3.5. Catalytic characterization

Although the electrocatalytic efficiency of the material is crucial, it can be convenient to test the compounds before and to select only the best ones to be applied on the working SOC. In order to do so, the purely catalytic tests can be conducted, where the powders are exposed to the reactive gases in fixed-bed reactor. This allows to determine purely chemical catalytic performance without external electric field.

Prior to the catalytic tests, the powders were ball-milled in isopropyl alcohol at 450 RPM for 12 h using Ø 0.5 mm zirconia balls. After milling and drying, the powders were subjected to calcination at 800 °C for 2 hours to release any residual stresses induced during milling. The in-house built experimental set-up was very similar to the one described in TPx section (3.3.1). Firstly, quartz wool was placed at the bottom of the U-shape reactor. The appropriate amount of milled powder (usually 75 mg) mixed with Ø 1 mm alumina balls (0.8 g) was then placed on top and covered with another thin layer of quartz wool. The thermocouple was placed for internal measurement of the bed temperature. The gases were fed using Alicat flow controllers. First, the reactor was heated in H_2 to desired temperature (700-800 °C, depending on the compound and dopant) in order to activate the catalyst. Subsequently, the temperature was decreased to 600 °C, at which the gases were switched to the desired mixture. Gases were analyzed using a gas chromatograph (GC-2010 Pro, Shimadzu). The temperature was changing in 50 °C increments up to 800 °C and 2 hours were allowed for the complete gas exchange at each temperature. The powders were cooled down in hydrogen to avoid coking of the catalysts at lower temperatures or formation of toxic species.

3.6. Synchrotron studies

X-ray absorption spectroscopy (XAS) allows determining many properties of the materials on the atomic level. The presence of the edge in the spectra arises when the photon energy matches the energy required to specific transition, e.g. from the 1s orbital (K-edge) or 2s or 2p (L-edges). The K-edge XAS spectra can be divided into two parts: XANES (X-Ray Absorption Near Edge Structure) and EXAFS (Extended X-ray Absorption Fine Structure). The first one, as the name suggests, focuses on the white line and its nearest surroundings. On the basis of this, the oxidation state of the element, the chemical environment, or molecular geometry can be determined. Moreover, information can also be hid in the pre-edge features, like centrosymmetry. The EXAFS focuses mostly on the far range post-edge. By applying Fourier Transform it is possible to determine the local atomic structure like interatomic distance or coordination numbers. Unfortunately, the EXAFS simulations become complicated with more elements present in the structure. Thus, for the materials in this thesis, which consists of at least 4 elements (often even more), the simulations were not performed and the EXAFS analysis was kept more qualitatively, rather than quantitatively.

X-ray absorption spectroscopy (XAS) measurements were conducted at two different facilities: the SOLARIS National Synchrotron Radiation Center in Kraków (Poland) and the European Synchrotron Radiation Facility (ESRF) in Grenoble (France). In SOLARIS, two different beamlines were used: PIRX and ASTRA. They cover different energy ranges for XAS measurements (PIRX 300-1600 eV; ASTRA 1-15 keV); thus, they give information about different edges and require different sample preparation. At ESRF access to LISA beamline was granted, covering the highest energy possible in the world (4-90 keV). The use of those three beamlines allows to probe different elements in both single and double perovskites.

3.6.1. Soft X-rays – PIRX

For measurements at PIRX beamline, powders of interest were finely ground and dispersed onto carbon tape, which was glued onto standard flag-type holder. The powders were measured in ultra-high vacuum (UHV) using total electron yield (TEY) and/or partial fluorescence yield (PFY) modes. For collection of PFY spectra, SDD window C2 detector from Amptek was used. For the normalization of the data, PyMca 5.8.7 freeware software was utilized.

At PIRX the following edges were collected, regardless the samples formula and composition:

- K-edge of oxygen;
- $L_{3,2}$-edges of transition metals: Fe, Ni, Co, or Cu;
- $M_{5,4}$-edges of cerium.

3.6.2. Tender X-rays – ASTRA

The spectra of Fe and Cu K-edges (in SFM-based double perovskites) were measured in as-prepared and reduced powders at ASTRA beamline at SOLARIS. In order to measure the XAS spectra, the appropriate amount (calculated using XAFSmass software) of finely ground powder was mixed with the ethyl cellulose (50 μm, Pol-Aura) and pressed into thin pellets. The incident photon beam was provided by a double bend achromatic 1.3 Tesla bending magnet with critical energy of ~2keV. The monochromatized beam was formed by the slits and its size was 7 x 1 mm on the sample position. K-edges of transition metals were collected at room temperature under ambient pressure of N_2 and Ge (220) modified Lemonnier type double crystal monochromator was used. The iron edges were collected in the transmission mode, while, due to the lower concentration of the Cu in the samples, the copper edges were collected in fluorescence mode. Simultaneously with the collection of the spectra of interest, Fe or Cu foil (Exafs Company) was measured as reference. For data processing and analysis, mostly the Demeter software package was used. For Wavelet analysis of Fe K-edge, Fastosh software was utilized. For Fourier and Wavelet transforms of EXAFS, wave vector k was considered in the range 2.9-8.5 $Å^{-1}$. For the Wavelet transform, Morlet function was used to differentiate between Fe-Fe and Fe-Mo bonds, due to overlap in FT-EXAFS. η=7.5 and σ=0.5 were used as parameters for Wavelet transform.

At the same beamline, L_3-edge of molybdenum was measured. The fine ground powder was evenly distributed on sulfur free Kapton tape. To obtain better spectra two layers were stacked together. The measurements were performed at around 30 Torr using Si (111) monochromator.

At ASTRA the following edges in double perovskites were collected:

- K-edges of several transition metals: mostly Fe due to high concentration and good quality of spectra; also, copper in LSFCM;
- L_3-edges of molybdenum.

3.6.3. Hard X-rays – LISA

The preparation for measurements at LISA beamline at ESRF was similar to ones at ASTRA. The appropriate amount of powders (calculated with XAFSmass software) was mixed with ethyl cellulose and pelletized. The prepared pellets were mounted in the aluminum holder. As both the transmission and fluorescence signals were collected simultaneously, the holder was mounted at 45° angle. The spectra were collected after cooling the samples with the cryostat using liquid nitrogen. Such procedure allowed to collect high-quality spectra by minimizing the thermal vibrations in the lattice. For measurements, Si (111) monochromator was used. The data was once again analyzed by the

Demeter software. Fourier transform for EXAFS analysis was executed in the respective k-ranges for normalized spectra: 3-12 $Å^{-1}$ for Fe and Ni, 3-9.7 $Å^{-1}$ for Co, and 3-11 $Å^{-1}$ for Cu. Phase correction of 0.5 Å was also applied during calculations.

At LISA the following edges in single perovskites were collected:

- K-edges of transition metals: Fe, Ni, Co, and Cu in STO

4. Results and discussion

4.1. Strontium titanate – $SrTiO_{3-\delta}$

4.1.1. Impact of the secondary transition metal on the properties of Ni-doped LSCT

The compounds with a perovskite formula and capable of performing the exsolution process were synthesized by the Pechini method. First, to prove the formation of desired phases, XRD analysis of $(La_{0.3}Ce_{0.1}Sr_{0.6})_{0.9}Ti_{0.9}Ni_{0.05}M_{0.05}O_{3-\delta}$ (M=Fe, Ni, Co, or Cu) was performed and the diffraction patterns for both the as-prepared and reduced compounds are shown in **Fig. 4.1**. In all samples, main phase was found to be $SrTiO_3$ in its *Pm-3m* structure, typical for single cubic perovskites. The Miller indices of the main peaks are presented for compounds in as-prepared states. The amount of additional phases can be found in the **Tab. 4.1**, along with the lattice constants. In the Ni-doped sample an additional phase was found, which can be associated with $NiTiO_3$, and its amount was stated by the Rietveld refinement to be equal to 3.5 wt.%. Also, when Cu was incorporated as a dopant in addition to Ni, cerium (IV) oxide can be found in a diffraction pattern and it was calculated to be 3.3 wt.%. Expectedly, the lattice constants change with different doping approaches, and the calculated values are presented in **Tab. 4.1**. Due to the identical (or almost identical) A-site composition and similarity in the B-site dopants, the changes in unit cell sizes are mainly explained by the changes in the ionic radii of the different transition metals' cations. Here, Ce-ions are assumed to be in Ce^{3+} since the incorporation of Ce^{4+} into the A-site lattice is unlikely due to the too high oxidation state and significantly smaller radii. After calculating the Goldschmidt tolerance factor from Eq. (2.26) assuming the Ce^{3+} or Ce^{4+} states the values obtained were 0.985 and 0.978, respectively, suggesting a more favorable presence of Ce^{3+} at the A-site. Of course, the Ce^{4+} can also be present but it should not overwhelm the mean cerium oxidation state.

The Ni-doped LSCT would be considered as the reference. In the remaining cases, 50% of nickel cations were exchanged for different transition metals. When LSCT-NiFe is taken into consideration, the lattice constant of the as-prepared compound is slightly smaller than that of LSCT-Ni. This behavior arises from slightly smaller ionic radii of Fe^{3+} (0.645 Å - high-spin) compared to Ni^{2+} (0.69 Å) [141]. When nickel is partially replaced with cobalt or copper, enlargement of the cell is observed compared to that of the purely Ni-doped compound. By this behavior, it can be deduced that the Co ions are predominantly Co^{2+}, which would not only maintain the electroneutrality when introduced instead of Ni^{2+}, but would also lead to the cell expansion, as Co^{2+} in high-spin has a radius of 0.745 Å [141]. Of course, the presence of Co^{3+} can also be expected, however, in a lower amount and cannot be determined solely on the XRD technique. The smaller change in unit cell size is visible for LSCT-NiCu.

As larger Cu^{2+} (0.73 Å) is introduced instead of Ni^{2+}, it leads to the expansion of the cell. However, the cerium vacancies in the A-site sublattice can also cause distortion and slight decrease in the size of the cell. As a result, two competing effects can be present. Unfortunately, the explanations presented here are complex because both A- and B-site elements can independently change their oxidation states, shrinking or expanding the cell in the result.

After the reduction step, the original perovskite structure was retained and no phase transformations were detected. In the LSCT-Ni, Ni-rich impurity phases disappeared, most likely because Ni was reincorporated into the perovskite oxide lattice during the thermal treatment. In the case of LSCT-NiCu, reflections attributed to $CeO_{2-\delta}$ are still present, but their amount decreased by nearly half, to 1.7 wt.%. The unit cell parameters of all four compositions are listed in the **Tab. 4.1**. For every sample, the unit cell parameter increased after reduction, which can be attributed to the formation of oxygen vacancies, causing lattice expansion [142]. LSCT-NiCu shows the smallest change in the lattice parameters, which may be due to the incorporation of $Ce^{3+/4+}$ from the impurity phase, providing additional structural stabilization. An alternative explanation is that if the cerium oxidation state significantly affects the unit cell dimensions, then in LSCT-NiCu only a small fraction of Ce^{x+} remains within the lattice, making the change less pronounced. With regard to exsolution, no diffraction peaks could be clearly assigned to metallic nanoparticles. Consequently, it cannot be concluded whether any formed nanoparticles are bimetallic alloys. A further inherent limitation in identifying nanoalloy formation by XRD is that the metallic elements involved and their corresponding alloys exhibit very similar unit cell parameters [143], which makes it extremely difficult to distinguish between metals and their alloys by XRD alone.

Tab. 4.1. Lattice unit constants and concentration of impurities in STO-based compounds. The goodness of fit was below 2.

		LSCT-Ni	**LSCT-NiFe**	**LSCT-NiCo**	**LSCT-NiCu**
a=b=c (Å)	**As-prepared**	3.8980(1)	3.8972(3)	3.9017(1)	3.9001(1)
	Reduced (900 °C)	3.9041(2)	3.9047(1)	3.9049(1)	3.9006(2)
Impurities (wt.%)	**As-prepared**	$NiTiO_3$ – 3.5	n/a	n/a	CeO_2 – 3.3
	Reduced (900 °C)	n/a	n/a	n/a	CeO_2 – 1.7

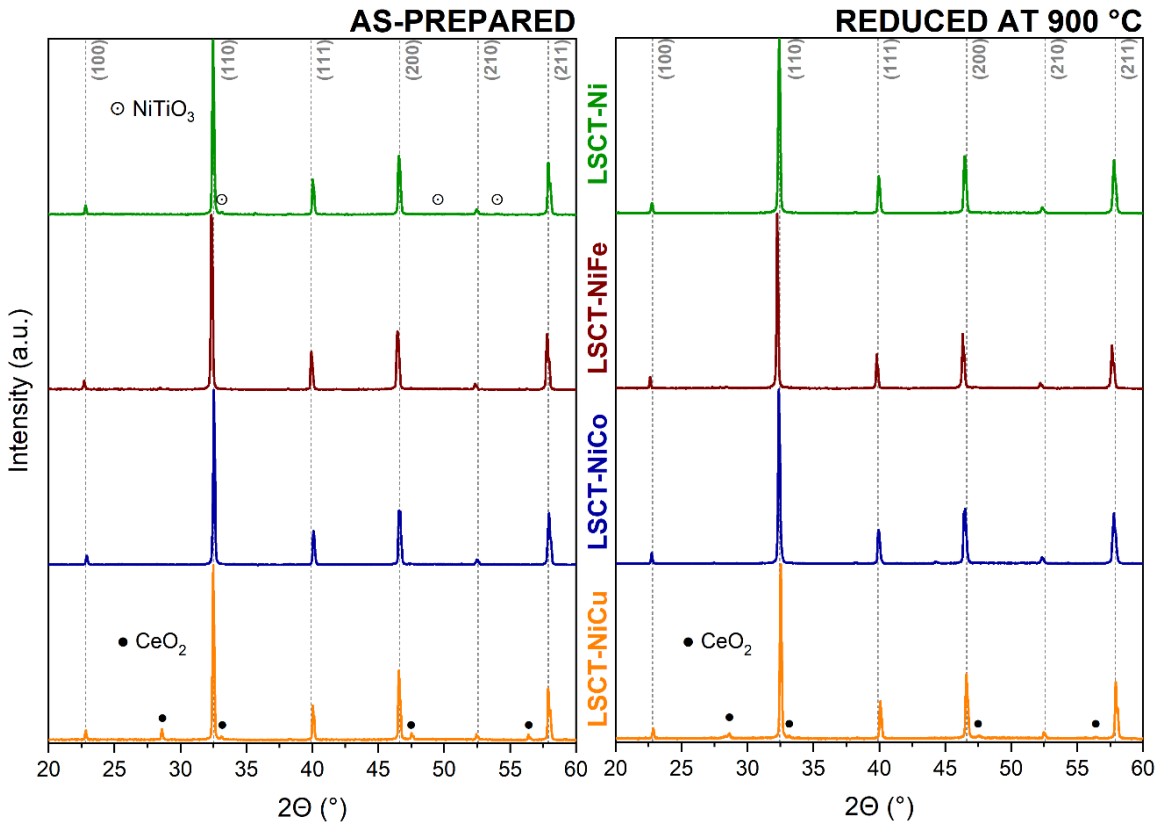


Fig. 4.1. XRD diffraction patterns of LSCT-NiM in as-prepared and reduced at 900 °C states.

The dilatometry tests were performed in air on the LSCT-based pellets to determine the compatibility with the state-of-the-art electrolyte YSZ and the conventional SOFC anode material: NiO-YSZ cermet. As seen in **Fig. 4.2** the relative length change is linear in the whole analyzed temperature range with no slope changes, meaning that no thermal transition occurs in the analyzed materials. The results for the thermal expansion coefficient (TEC) are in the range (11.42-11.71)×10^{-6} K^{-1}. The LSCT-NiCo compound stands out slightly, which originates from a larger unit cell. Nevertheless, the results obtained are comparable to

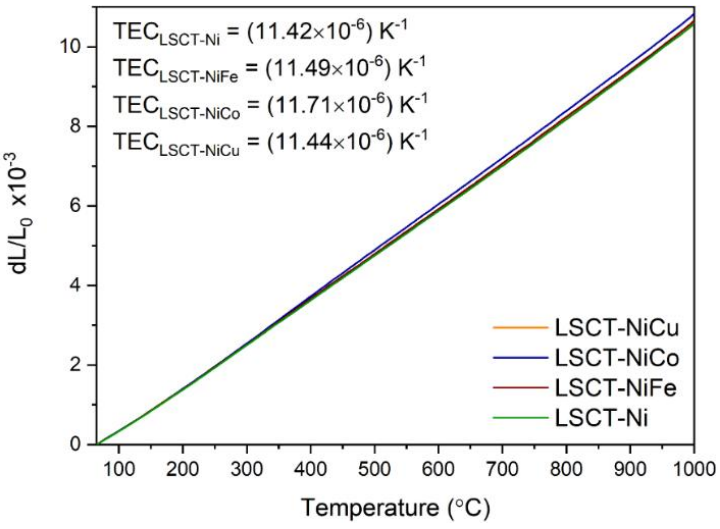


Fig. 4.2. Thermal expansion of the LSCT-NiM bars in the oxidized form.

those obtained for YSZ TEC_{YSZ}=(10.3-10.7)×10^{-6} K^{-1} [144], and they are even closer to TEC_{YSZ} than NiO-YSZ ($TEC_{NiO\text{-}YSZ}$=(11.81-12.48)×10^{-6} K^{-1} [145]), suggesting good compatibility between those materials, since no thermal mismatch is expected.

To study the exsolution process, the compounds were reduced at 900 °C for 12 h. Samples were in the form of rectangular bars, likewise for DC4W tests. Such a procedure allowed for exactly the same thermal processing as for electrical tests, and as a result enabled the establishment of a relationship between the structure and electrical properties. The SEM images of the reduced pellets are presented in **Fig. 4.3**. The microstructures of LSCT-Ni and LSCT-NiCo are quite similar with respect to the presence of growth terraces in which the exsolved nanoparticles are present. Moreover, the Co-doped compound was visibly denser than others, which occurs due to the sintering-aid properties of the cobalt species. The calculated values of density and porosity are presented later in the **Tab. 4.4**. The exsolved nanoparticles in LSCT-Ni are not exceeding 50 nm in diameter, however, several larger NPs can also be spotted. The size distribution is even and the NPs cover the entire visible area, which is favorable from the catalytic point of view, however, it can also influence the electrical properties of the compound. Despite similarities in structure, the LSCT-NiCo yielded less nanoparticles, they are not covering the surface fully like in only Ni-doped LSCT. On the surface of LSCT-NiCu shorter terraces are visible, and they are present more locally. The nanoparticles are also exsolved more locally, and they do not cover the whole surface like in LSCT-Ni. However, the size of the NPs remains comparable between those three compounds, and they do not exceed 50 nm. Lastly, LSCT-NiFe is characterized by a different structure, the grains are rotund with an evener surface with almost no terraces visible. Unfortunately, in the case of Ni-Fe co-doping, the exsolution is definitely weaker. One of the reasons is the higher reduction temperature of iron compared to that of nickel. With a higher reduction temperature of Fe, 900 °C may not be high enough to sufficiently exsolve most of the iron from the STO-lattice. As the amount of remaining nickel is lower than that of LSCT-Ni, the exsolution is suppressed in this case.

To analyze the exsolution beyond the limitations of SEM imaging, Transmission Electron Microscopy was utilized. The main focus was to determine if the bimetallic alloy was formed and what is the exact composition of the exsolved nanoparticles. The analysis was performed on LSCT-NiCo and LSCT-NiFe in the form of TEM lamellas fabricated by FIB (Focused Ion Beam) from bulk samples.

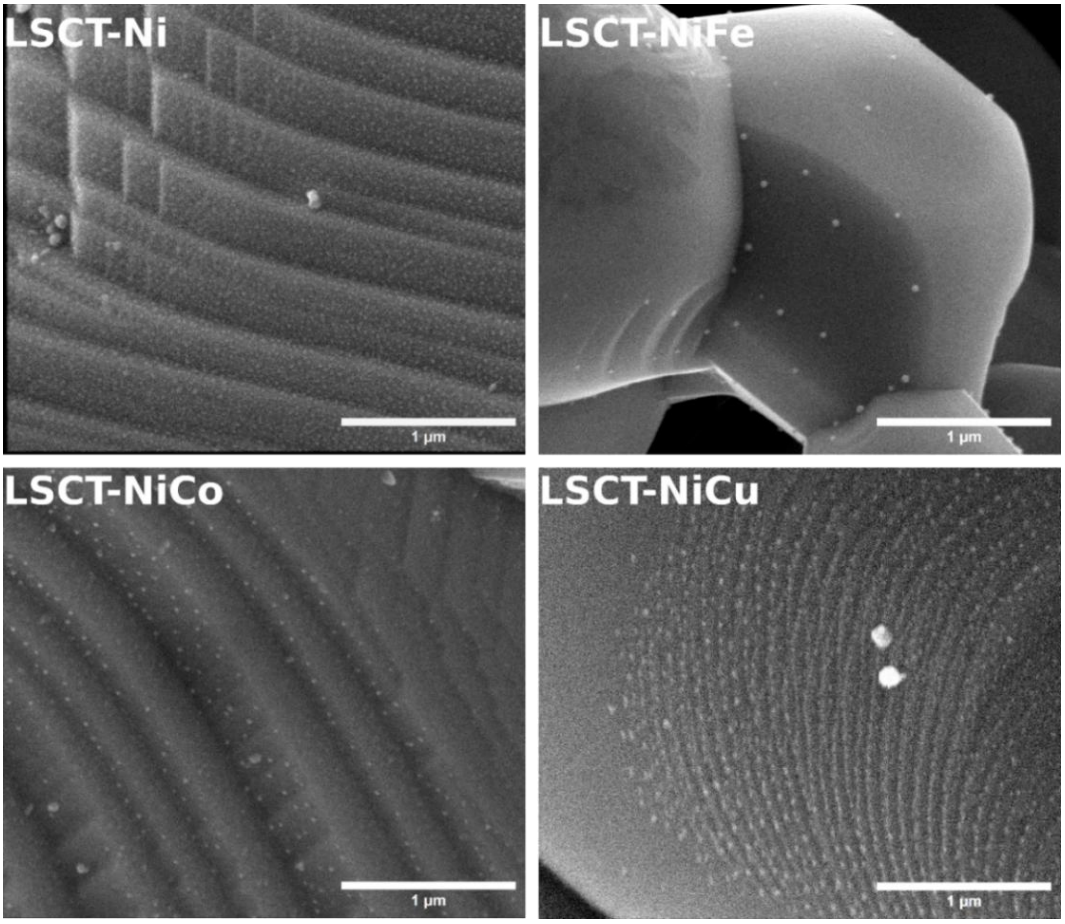


Fig. 4.3. The SEM images of reduced pellets of LSCT-NiM.

The **Fig. 4.4.** presents the STEM-EDS analysis of a round-shaped exsolved nanoparticle on the surface of LSCT-NiCo. The local spatial distribution of Ni and Co obtained by STEM-EDS mapping reveals the formation of a Ni-Co nanoparticle with a size of ca. 45 nm. The atomic concentrations obtained from EDS analysis are presented in **Tab. 4.2.** The ratio of the A-site elements Sr:La:Ce in host material (0.56:0.33:0.11) is almost identical to the nominal values (0.6:0.3:0.1), with only small differences between Sr and La concentrations. Surprisingly, the atomic ratio Co:Ni was found to be equal to 2.3, while during the synthesis it was calculated to

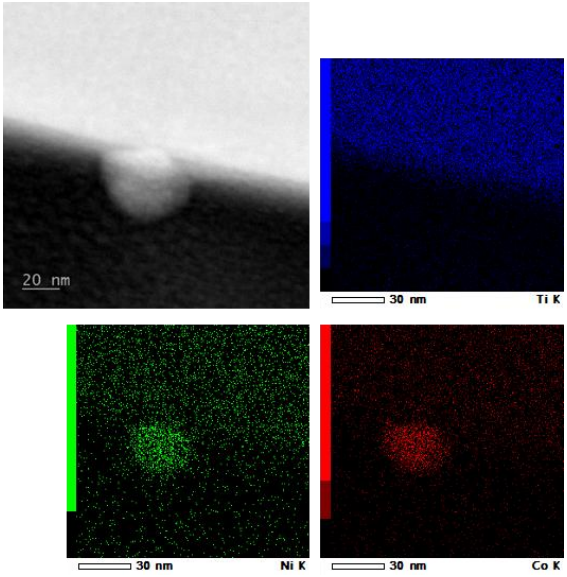


Fig. 4.4. STEM-ADF image of reduced LSCT-NiCo, STEM-EDS elemental maps of Ni (green) and Co (red) with respect to Ti (blue).

be equal to unity. Three explanations can be suggested: (i) diffusion of cobalt ions to the surface during the sintering step, (ii) faster diffusion of cobalt ions than nickel ions during the reduction and exsolution, or (iii) formation of alloys already in the bulk in proximity of the surface. All possibilities could occur simultaneously, altering the surficial composition, however, from the PhD candidate's experience the first suggestion may be more possible, as cobalt diffusion after sintering is visible with the naked eye when the alumina plates are left intensely blue. The local composition of the exsolved nanoparticle was also determined from the EDS spectrum and results are presented in **Tab. 4.2**. The ratio of Co:Ni is calculated to be 2.5, almost identical to that the host. On the basis of these observations, it may be stated that in LSCT-NiCo, the nanoparticles are exsolving in a form of bimetallic alloy with even distribution of elements within each other. This can also suggest the third aforementioned possibility. Since the Ni:Co ratio remains the same in the nanoparticle and in the host in the proximity to the surface, the explanation that the bimetallic alloys are already form within the host and exsolve simultaneously. Their presence in the form of spherical NPs would not be visible due to their nanometric size. Moreover, the STEM-ADF (**Fig. 4.4**) image shows a nanoparticle that is embedded in the perovskite lattice as expected on the basis of the exsolution process offering good attachment to the host. Lastly, the question arises: is this particular composition ($Co_{2.5}Ni$) the only one available from the Co-Ni phase diagram? The answer is no; more different formulas can be found since cobalt and nickel are similar metals and they form a solid solution in a wide range of compositions [146].

Tab. 4.2. Atomic concentration obtained from EDS method on TEM lamella of LSCT-NiCo with respect to host and nanoparticle exsolved.

	Atomic concentration (%)						
	O	**Ti**	**Co**	**Ni**	**Sr**	**La**	**Ce**
Host	44	22.9	4.2	1.8	15.3	8.9	2.9
Nanoparticle	31.1	9.1	33.7	13.7	8.2	3.3	0.9

The oxidation state of the exsolved nanoparticles was further verified through a detailed analysis of the diffraction patterns specifically performed at the precise interface between the exsolved nanoparticle and the adjacent host grain. The particular nanoparticle which interface was carefully analyzed in this study is clearly presented in **Fig. 4.5a**. Meanwhile, two distinct SAED (Selected Area Electron Diffraction) patterns are shown in **Figs. 4.5b-c**.

In the first case, the SAED pattern captured from an area selected strictly inside the host material, as depicted in **Fig. 4.5b**, may be confidently assigned and has been thoroughly indexed according to a cubic perovskite structure that derives directly from $SrTiO_{3-\delta}$, characterized by a lattice parameter of

approximately 3.9 Å. This measured value stands out as almost identical to the one precisely obtained from the Rietveld refinement performed on powder X-Ray Diffraction data of the reduced LSCT-NiCo sample (see **Tab. 4.1**), thus reinforcing the consistency across complementary analytical techniques. Notably, the family of spots pointed out by the white arrow in this pattern appears in positions that are forbidden within the standard structure, which indicates the presence of a chemical ordering occurring inside the host lattice, with the consequence of effectively doubling the lattice parameter.

The second SAED pattern, illustrated in **Fig. 4.5c**, corresponds to a carefully selected area that consists of the exsolved nanoparticle along with the surrounding host grain, allowing for a direct comparison of their structural features. In this pattern, additional diffraction spots emerge clearly next to the ones originating from the host lattice, which not only confirms that the exsolved nanoparticle is fully crystalline but also reveals, moreover, that it maintains a well-defined and highly precise orientation with respect to the host lattice. To systematically distinguish the contributions, the diffraction spots associated with the host matrix have been labeled with STO subscripts, while the second family of spots aligns perfectly with the expected structures of metallic cobalt and/or nickel (a_{Co} = 3.548 Å and a_{Ni} = 3.524 Å) or a Ni-Co metallic alloy, as directly observed by the EDS analysis of the nanoparticle itself (Fig. 4.4). The relative positions of the diffraction spots indicate an epitaxial growth of the exsolved Ni-Co nanoparticle on top of the perovskite lattice of the host material, with (200)Ni-Co||(200)STO and (111)Ni-Co||(111)STO parallelism between similar lattice planes in the exsolved nanoparticle and the host material.

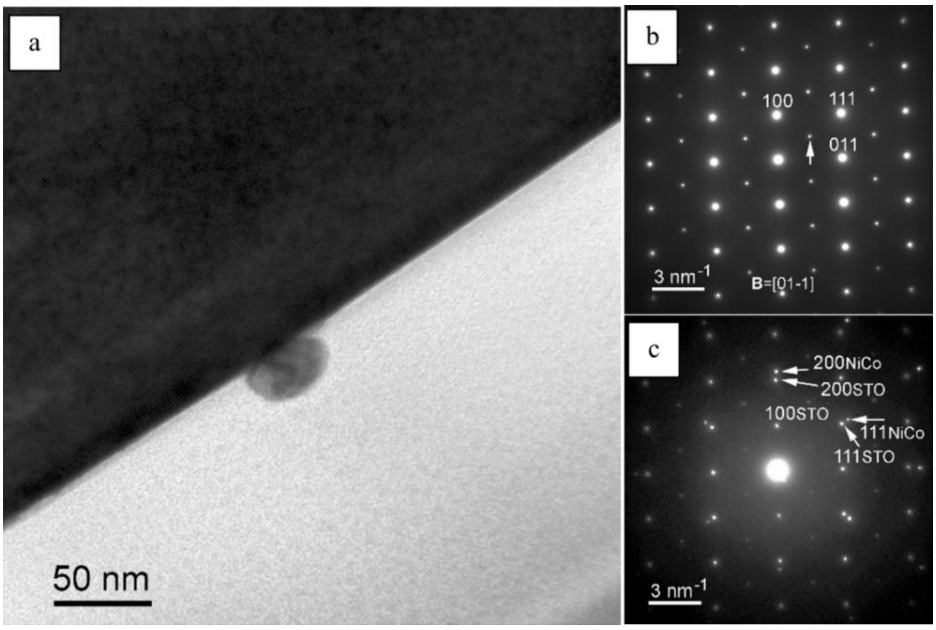


Fig. 4.5. (a) TEM image of an exsolved nanoparticle attached to the host matrix; (b) SAED pattern from an area selected inside the host material; (c) SAED pattern from a selected area including the exsolved nanoparticle along with the host material.

The next sample to be analyzed was LSCT-NiFe which first underwent the STEM-ADF and STEM-EDS analyses presented in **Fig. 4.6**. A low magnification STEM-ADF in **Fig. 4.6** shows two different categories of features: large particles (100-250 nm) pointed by vertical arrows and small nanoparticles (ca. 50 nm) pointed by horizontal arrows. The EDS analysis was performed on the whole area presented in **Fig. 4.6** and the atomic composition is presented in the **Tab. 4.3** as "host". The relative elemental composition of La, Sr, Ce, Ni, Fe, Ti and O shows an almost unitary atomic ratio between Ni and Fe, Ni/Fe=1.08. In the case of LSCT-NiFe, no Ni or Fe enrichment was observed as the ratio is close to the nominal value. Similarly as in LSCT-NiCo, the A-site dopants are in a ratio of 0.55:0.33:0.12 (Sr:La:Ce), however, in LSCT-NiFe, the cation segregation is visible. The chemical mapping by STEM-EDS on this scale reveals that the large particles pointed by vertical arrows correspond to Ce-rich and Sr, Ti, La-poor areas, demonstrating the partial segregation of $CeO_{2-\delta}$ from the host lattice. In powder diffraction patterns, the impurity from ceria was not visible, yet its concentration may be below the detection limit of the apparatus.

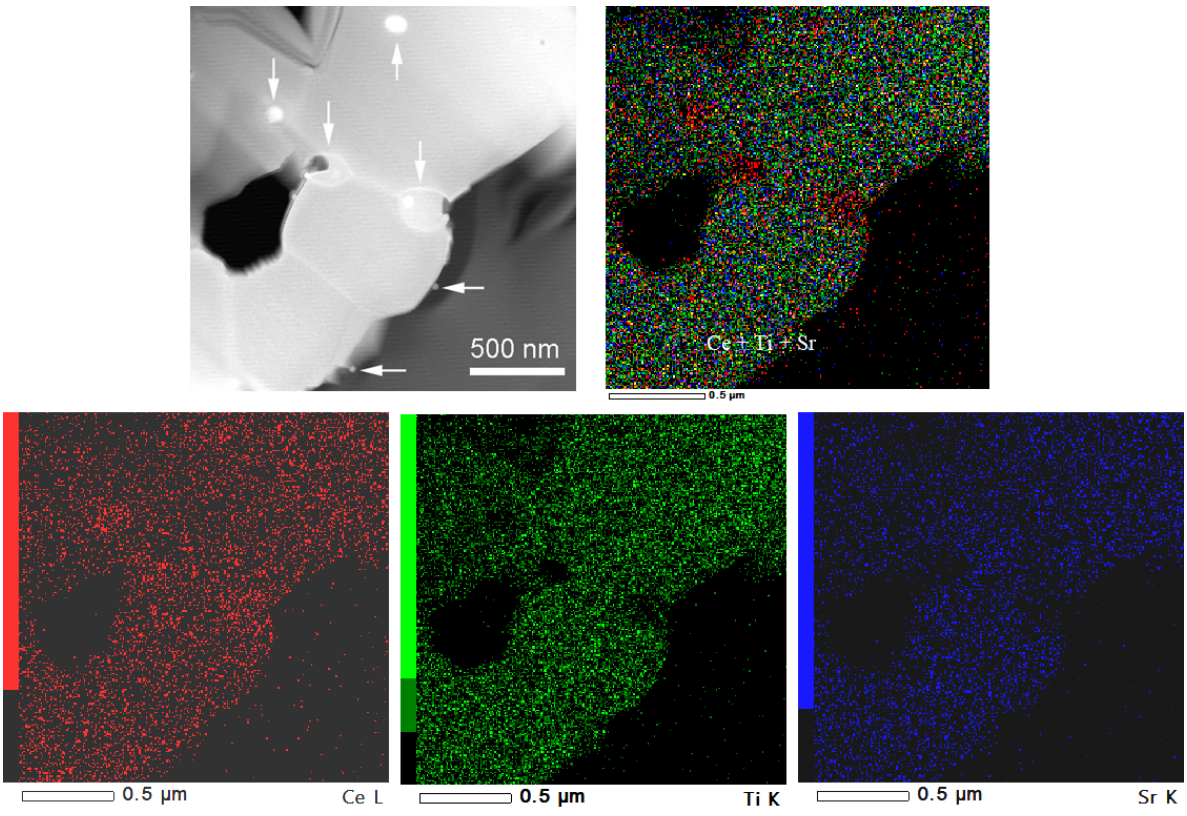


Fig. 4.6. STEM-ADF image of LSFC-NiFe (up), overlapped (up) and individual (down) large-area STEM-EDS elemental maps of Ce (red), Ti (green) and Sr (blue) revealing the partial segregation of CeO_2.

In addition to the larger particles originating from the segregation of $CeO_{2-\delta}$, smaller nanoparticles were visible on the surface and their origin is the exsolution process. The enlarged STEM-ADF image at a higher magnification in **Fig. 4.7** presents one of such spherical nanoparticles with a size of ca. 30 nm. The individual and overlapped EDS maps of Ni and Fe clearly reveal the exsolution of both Ni and Fe as a spherical Ni-Fe nanoparticle, with an atomic ratio of Ni:Fe=3.3. The EDS analyses were performed on two different nanoparticles (one of them is shown in **Fig. 4.7**). The composition of the second nanoparticle was also found to consist of nickel and iron, with a slightly different atomic ratio Ni:Fe=3.57. The predominant concentration of nickel in this compound is due to the higher reduction temperature of iron compared to nickel [134]. However, the synergistic effect should also be taken into account, as iron cannot be that easily reduced, it could promote the exsolution of different metals (Ni in this case) [147]. An additional crucial factor in the formation of this particular composition is the phase diagram of Ni-Fe. Based on the literature[148,149], the initial 1:1 Fe:Ni ratio as a result will yield the mixture of Fe and Ni_3Fe with a dominant presence of bimetallic alloy. Thus, this experimental observation correlates very well with the theory.

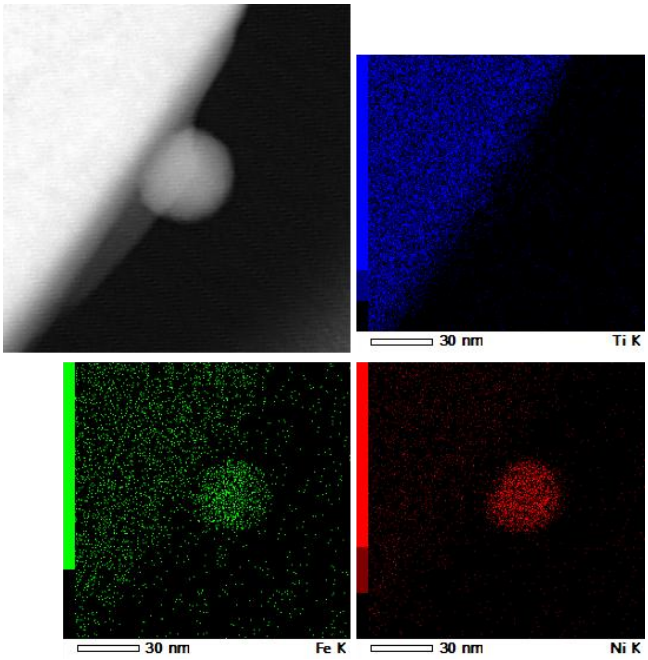


Fig. 4.7. STEM-ADF image of exsolved nanoparticle from LSCT-NiFe with respective STEM-EDS elemental maps of Fe (green), Ni (red), and Ti (blue).

Tab. 4.3. Atomic concentration obtained from EDS method on TEM lamella of LSCT-NiFe with respect to host and two different nanoparticles exsolved.

	Atomic concentration (%)						
	O	**Ti**	**Fe**	**Ni**	**Sr**	**La**	**Ce**
Host	59.1	17.6	1.2	1.3	11.5	6.9	2.5
Nanoparticle 1	44.1	2.3	11.2	37.2	2	1.5	1.8
Nanoparticle 2	42.5	6.2	8.9	31.8	4.9	3.8	1.9

To further analyze the behavior of the compounds before and after exsolution, X-Ray Absorption Spectroscopy (XAS) was utilized. It allowed to determine the changes in local atomic structure and oxidation states of different cations in LSCT-based structures. Regarding the availability of different synchrotron radiation facilities and their allowed energies, different edges of metals were measured. Firstly, the focus was put on the K-edges of transition metals measured at the European Synchrotron Radiation Facility (ESRF). The first metal to be analyzed was the nickel as it was present in all samples. Normalized K-edges of nickel in all compounds in both as-prepared and reduced states are presented in **Fig. 4.8**. Two insets show close-ups on the white line peak (inset 1°) and pre-edge features (inset 2°). In general, before the reduction, all four perovskites were characterized by a similar shape and intensity, only with slight difference of LSCT-NiCo at the white line. This difference means a change in the nickel Density of States (DOS) via Co-doping. Hou *et al*. [147] examined the energetics of bimetallic exsolution of STO by using first-principle studies and shown how the Projected Density of States (PDOS) is influenced by different dopants. The shape of the white line with two peaks (E1-8349 and E2-8354 eV) indicates the successful substitution of nickel at the Ti-site in STO perovskite [150]. The shape of the spectra of as-prepared compounds is also characterized by the pre-peak features at 8333.9 eV (PE1) and 8340.5 eV (PE2). Their presence arises from the 1s→3d quadrupole and 1s→4d dipole transitions, respectively [98,150–152]. These transitions would be forbidden by selection rules in ideal perovskite, but the hybridization between the Ni 3d and O 2p orbitals would result in the formation of new states available for these transitions [150,152]. Furthermore, the formation of new orbital states resulting from Ni 3d-O 2p hybridization would be strengthened with a lowering of the symmetry around the scatterer (here Ni). Thus, by similarities in pre-edge in as-prepared states, it can be concluded that the symmetry around the Ni atoms is likewise regardless of the additional B-site dopant. All of the discussed peaks can also be easily identified as minima in second derivatives of the spectra presented in **Fig. 4.9**.

After reduction, the intensity of the white line decreases for all of the compounds. At the same time, the intensity of pre-peak features increases, which in general is considered as a characteristic for the formation of Ni^0 species [153]. Moreover, as mentioned above, the increase in the pre-edge feature intensity indicates a greater distortion around the nickel cations. Considering both lower white line intensity and higher pre-peak features, it can be deduced that the addition of another transition metal to Ni enhances the reducibility of this metal. This enhancement is most seen for Fe and Cu addition and they are characterized by exactly the same pre-edge line; however, for LSCT-NiCu the white line is slightly less intense. Such behavior experimentally proves the suggestion of Hou *et al.* [147], who has shown that the separation energy of Ni-M (M=Cr, Fe, Co, Cu) doped STO should be lower than Ni atoms alone, promoting exsolution. What is even more, herein the LSCT-NiFe compound has shown

the highest extent of Ni reduction, similarly to what would be seen from the theoretical calculations [147]. This observation also agrees with the nanoparticle composition obtained by STEM-EDS. In Ni-Fe doped compounds, the NPs are predominantly nickel-containing, while in LSCT-NiCo, the cobalt concentration is higher than that of nickel in the exsolved bimetallic alloy. It should be noted that even if iron is less eager to be reduced and exsolved in this case, its presence is resulting in higher reduction of the remaining nickel. As already seen in SEM images (**Fig. 4.3**), the exsolution in purely Ni-doped LSCT is rather intense, as NPs cover the vast majority of the surface. Thus, the question "Why does the white line have the highest intensity among others?". The answer is relatively simple; as in this exact compound, the total concentration of the nickel is higher at the beginning. After the reduction, despite intense exsolution, many nickel cations are still remaining in the structure in its oxidized form, which would lead to this averaged white line intensity. Interestingly, in the contrast to the literature [153], no shift to lower energies after the reduction was found and for all the materials, the white line is located at 8347.6 eV, which can be clearly seen in the first derivative presented in **Fig. 4.9**.

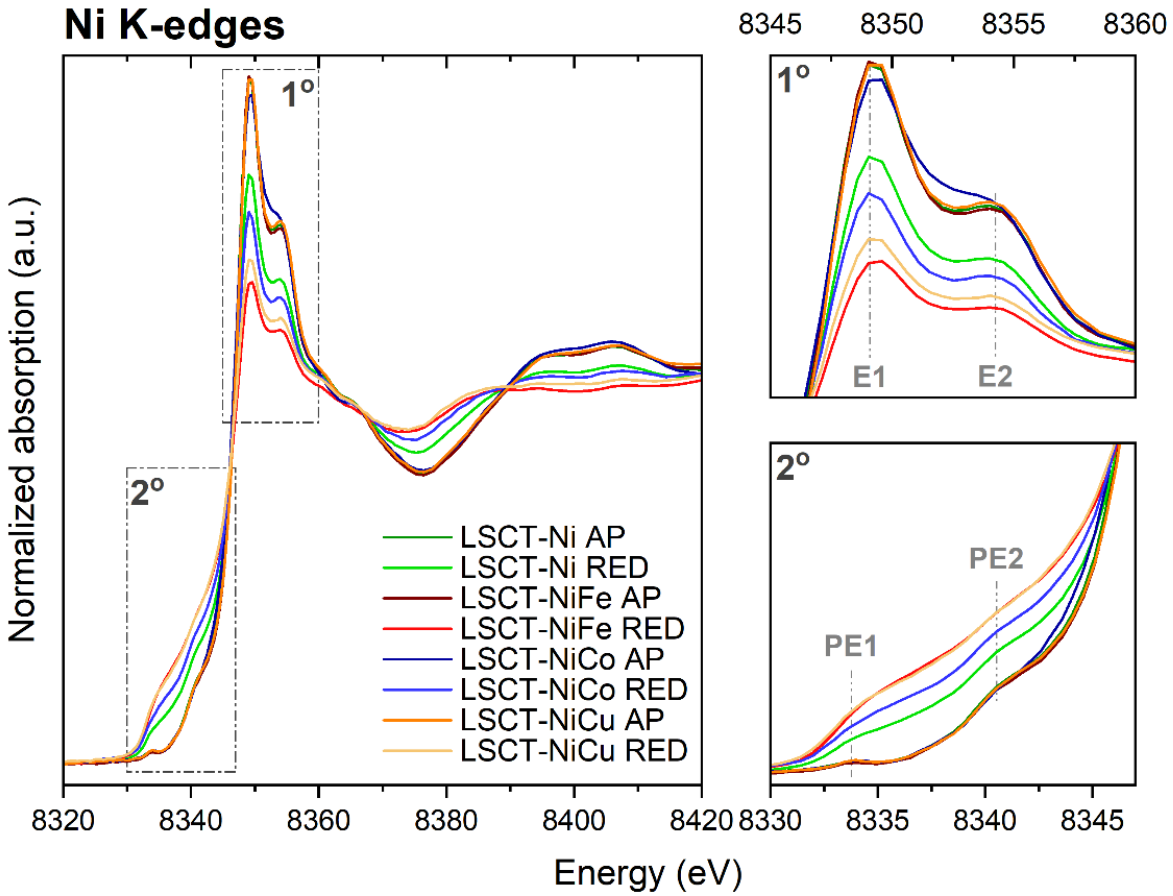


Fig. 4.8. The Ni K-edges of LSCT-NiM compounds: as-prepared (AP) and reduced (RED). The insets enlarge the changes in edge (inset 1°) and pre-peak (inset 2°).

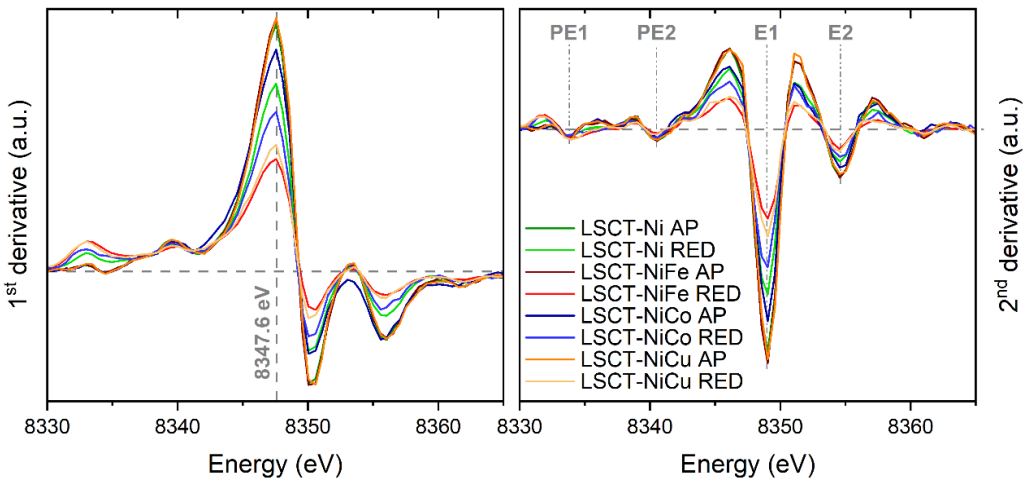


Fig. 4.9. The first (left) and second (right) derivatives of Ni K-edge of LSCT-NiM compounds.

To demonstrate the changes in the local neighborhood structure, Fourier Transform analysis was applied to the EXAFS range, and FT-EXAFS spectra (corrected for phase shift) are presented in **Fig. 4.10**. While a precise quantitative analysis of these results cannot be achieved without a full structural reconstruction, a direct comparison among the spectra provides a clear general insight into the structural differences between the various samples. Before reduction, the FT signals appear quite similar across all compounds, with the main peak located at approximately 1.9 Å attributed to Ni-O bonds in the LSCT phase [143]. This distance is remarkably close to the Ti-O bond length of 1.96 Å [143], as both of these elements occupy similar positions. However, following the reduction process, the spectra no longer exhibit such close resemblance to one another. A consistent observation is the emergence of a new peak that reaches its maximum at approximately 2.34 Å, whereas Ni-Ni bonds in cubic nickel are measured at 2.46 Å [143], strongly indicating that these new peaks arise from the formation of Ni-Ni bonds. At the same time, there is the possibility that Ni-M bonds, where M represents another metal, could contribute, as bimetallic alloys display very comparable lengths (such as Ni-Fe in hexagonal FeNi at 2.5 Å or in cubic Ni_3Fe at 2.48 Å [143]). Such small differences make it almost impossible to unambiguously distinguish whether the presence of a new peak in FT-EXAFS comes from Ni or the respective alloy. By the STEM-EDS, it is already confirmed that the exsolved nanoparticles consist of bimetallic alloys in both LSCT-NiFe and LSCT-NiCo. To conclude a similar observation from the EXAFS alone, the analysis of another edge must be performed. If the peak characteristic for Ni-M bonds occurs, it will also be a direct proof for the formation of the bimetallic NPs from XAS studies.

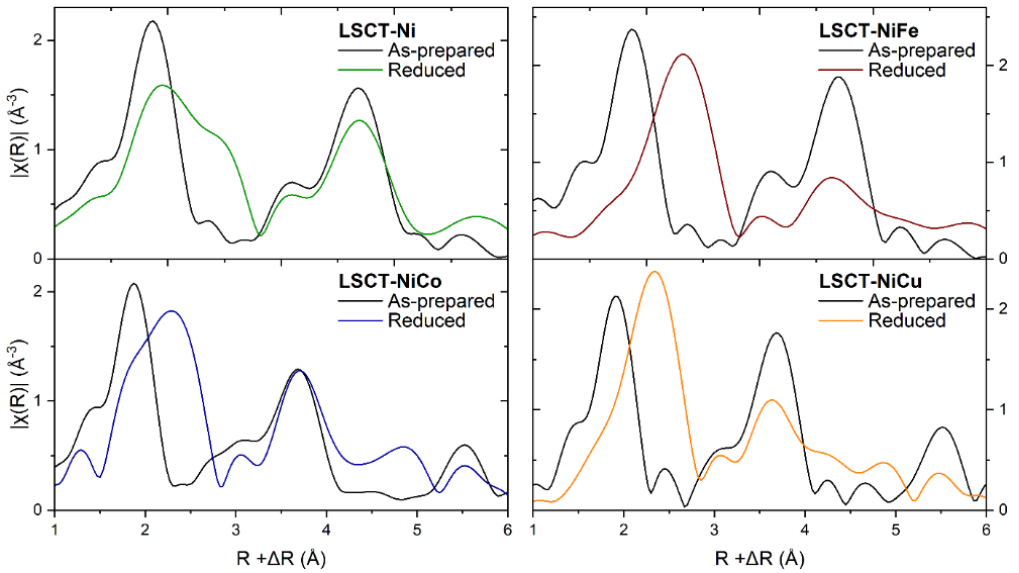


Fig. 4.10. Fourier-Transformed EXAFS of Ni K-edges of LSCT-NiM.

An analogous analysis procedure was applied for other transition metals' K-edged, at which FT-EXAFS was also performed. The spectra for the respective edges are presented in **Fig. 4.11a-c** with reference signal from metallic foils When LSCT-NiFe was reduced, the edge was significantly moved to lower energy, clearly indicating a reduction in Fe oxidation state. Also, similar to the Ni edge, after the reduction, the pre-edge peaks are more intense, meaning that the symmetry of the Fe atom was changed. When taking into consideration near EXAFS range, the oscillations have a comparable frequency with a shift resulting from a change in the white line position. This means that the local neighborhood of Fe atoms remains dominated by oxygen. This observation was further proved by the Fourier analysis, the results of which are plotted in Fig. **4.11d-f**. In case of iron, FT-EXAFS remains almost unaffected, with no formation of the additional peak characteristic for Ni-Fe bonds. This is in contrast to STEM-EDS where the formation of Ni_3Fe nanoparticles was revealed. Although no clear peak is formed in Fe FT-EXAFS, one must keep in mind that the XAS technique is not purely surface-sensitive. Even if the fluorescence (in which these spectra were collected) yields more information about the surface, it is still also collected from the outermost layers of the bulk. As a result, if the concentration of the exsolved nanoparticles is not high, then the oxide can still dominate the signal. The low amount of the NPs exsolved was indeed observed in the SEM imaging (**Fig. 4.3**), which is also correlated with the ΔG of reduction to Fe^0 (e.g. in **Fig. 2.16**) [7], the temperature may not have been sufficiently high to reduce the majority of the iron, and only a small amount was exsolved to form Ni_3Fe alloys. When the Co K-edge is considered, one may see a behavior quite similar to that which was described for Ni. Spectrum for the reduced sample are characterized by a lower intensity of the white line and enhanced formation of pre-peak features; however, the position of the edge remains unaffected

by the thermal treatment. Subtle changes in oscillation frequency and intensity are visible in the EXAFS range. Furthermore, by Fourier analysis one can notice the formation of new peak at the radial distance characteristic for Co-Co(Ni) bonds [143]. Indeed, STEM-EDS imaging revealed not only the formation of the bimetallic $Co_{2.5}Ni$ alloy, but also the increased concentration of cobalt was revealed in the proximity of the surface. Combining these two techniques, it can be deducted that the cobalt-nickel exsolution is started by formation of metallic species in the bulk but in surface proximity. Then they migrate to the surface, where they are found by microscopic methods. Last, but not least, Cu in LSCT-NiCu after the reduction was almost completely reduced to metallic Cu^0; however, it must be noted that during high reduction temperatures the copper is prone to evaporation and may not remain on the surface in its initial composition. The spectrum of reduced compound is almost identical to that of the Cu reference foil with similar oscillations closer to the EXAFS region. Subtle changes, such as slightly higher intensity of the white line and lower intensity for pre-peaks means that not all Cu cations were completely reduced. Such an observation was also further confirmed by the FT analysis, in which an intense peak characteristic for Cu-Cu bonds appears after the reductive treatment. Compared to the intensity of other M-M bonds in FT signal, the one in copper is the most intense, meaning that the highest amount of M^0 species was formed in LSCT-NiCu. Considering that the intensity of the Ni-Ni peak was more intense for this compound, one may state that the reduction of both nickel and copper was the most efficient in this system.

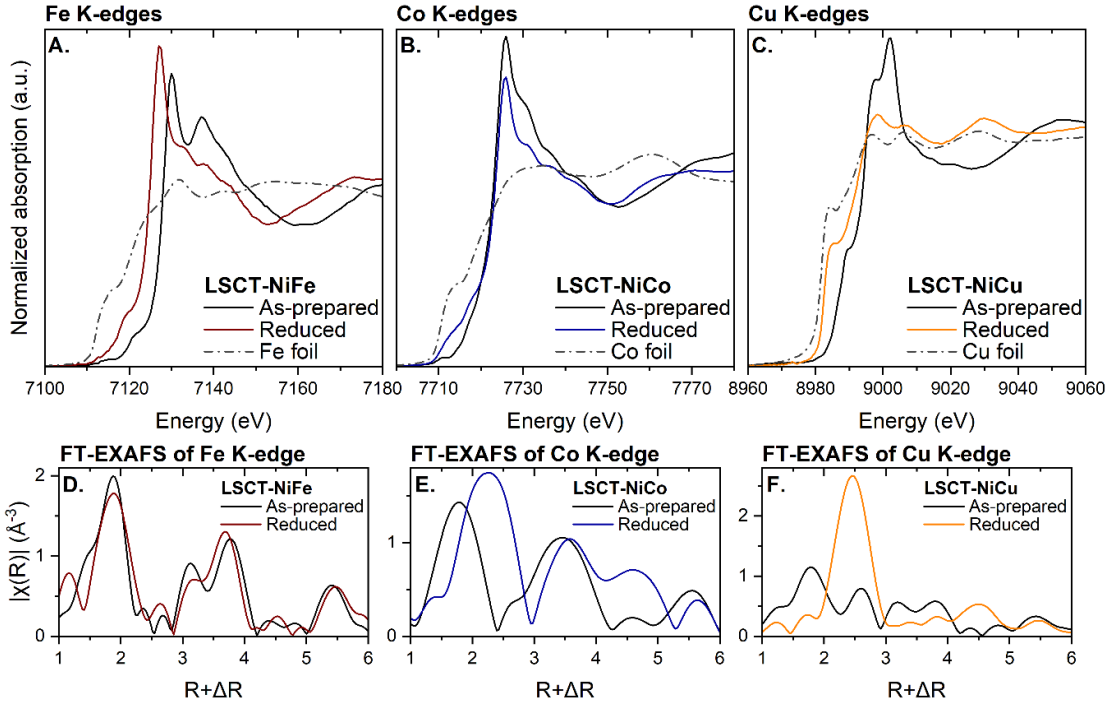


Fig. 4.11. K-edges of Fe, Co, and Cu in doped LSCT-NiM in as-prepared and reduced states (A.-C.) with corresponding FT-EXAFS spectra (D.-F.).

To determine whether the titanium surroundings were affected by the different dopants, the XAS measurements at the Ti $L_{3,2}$-edges were performed at the PIRX (SOLARIS) beamline. Normalized spectra are presented in **Fig. 4.12**. Due to the spin-orbit coupling, the 2p orbital of titanium is split into $2p_{3/2}$ and $2p_{1/2}$ levels which give a rise to L_3- and L_2-edges visible in the spectra and marked with different colors. The spin-orbit coupling can be calculated as a difference between the respective peaks and in presented compounds was found to be around 5.3 eV, a value comparably close to the values in the literature [154–156], both theoretical and experimental for $SrTiO_{3-\delta}$. In the octahedral coordination like present around the titanium in $SrTiO_{3-\delta}$, the 3d orbit splits into triple degenerate t_{2g} and double degenerate e_g states [155] resulting in the splitting of the L_3 and L_2 ranges into two distinguished peaks. The crystal-field splitting parameter can be obtained by subtraction of the e_g and t_{2g} positions and is known as 10Dq parameter and is found to be 2.2 eV, almost exactly equal to the value obtained by Begum-Hudde *et al.* [156]. Herein, in the spectra all aforementioned orbitals are present and marked respectively in **Fig. 4.12**. In addition to these four, clearly distinguished peaks, two smaller ones in the pre-edge region can be found known in the literature as leading peaks characteristic for $3d^0$ compounds like $SrTiO_{3-\delta}$ [157] and their presence, although forbidden by selection rules, arises due to p-d interactions as suggested by Mesquita *et al.* [154]. Notably in doped LSCT-based compounds all spectra look similar, except for the changes in Cu-doped ones, since they are characterized by a slight shift to higher energies. This change is attributed to the Ti displacement from the centrosymmetric site in TiO_6 octahedra and lowering the local symmetry around Ti^{4+} cations [154]. Importantly, no changes in the peaks position are observed after reduction and the spectra remains as the one characteristic of Ti^{4+} in octahedral coordination, typical for $SrTiO_{3-\delta}$. If the reduction of Ti^{4+} to Ti^{3+} were to occur, the shift to lower energies would be expected, as theoretically demonstrated by Zhao *et al.* [155]. The lack of such a shift proves the good redox stability of Ti^{4+} in strontium titanates even after a high-temperature reduction (900 °C), which was not sufficient to decrease the oxidation state of Ti to 3+.

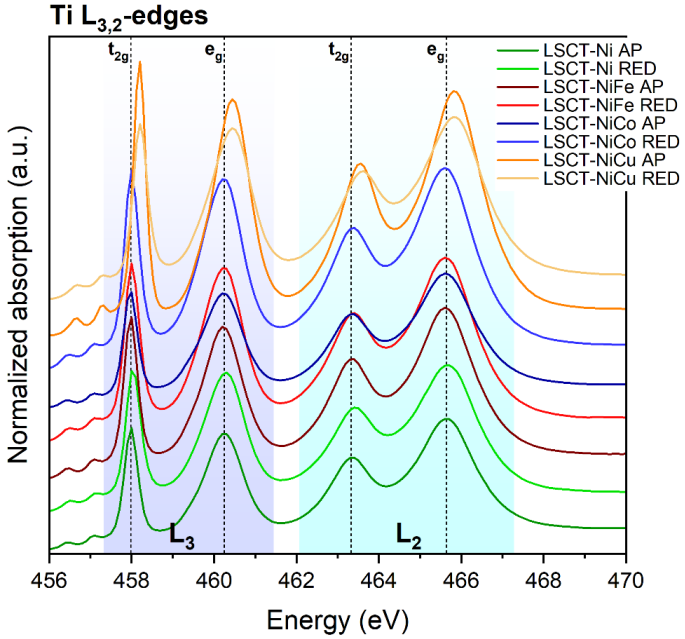


Fig. 4.12. The $L_{3,2}$-edges of Ti in doped titanates.

Lastly, the cerium $M_{5,4}$-edges were measured at the same beamline (PIRX), and the normalized spectra are presented in **Fig. 4.13** with marked peaks as originating either from Ce^{3+} or Ce^{4+} states taken from the work by Melcher *et al.* [158]. Spectra were dominated by Ce^{3+} rather than Ce^{4+} already prior to the reduction. The explanation for the predominant Ce^{3+} oxidation states at the A-site is explained in the XRD section of this chapter. Shortly, due to the similar ionic radius and oxidation state, Ce^{3+} is favorably incorporated at the Sr-site rather than Ce^{4+}. The highest share of the higher oxidation state of cerium was found in Cu-doped LSCT, which could be the result of the residual $CeO_{2-\delta}$ phase visible in the XRD patterns. After the reduction, the Ce^{4+} peaks disappeared, and considering the decrease in $CeO_{2-\delta}$ peaks in the XRD pattern, this implies the incorporation of Ce^{3+} into the perovskite lattice. In a purely nickel-doped one, the Ce^{4+} is also present but the intensity of the peaks is relatively low. This indicates that $CeO_{2-\delta}$ phase can also be present in this material, but it is undetectable by means of the XRD technique. Interestingly, after reduction, the Ce^{4+} peaks are still clearly visible. Finally, the spectra of as-prepared LSCT-NiFe and LSCT-NiCo mostly consists of peaks characteristic for the Ce^{3+}.

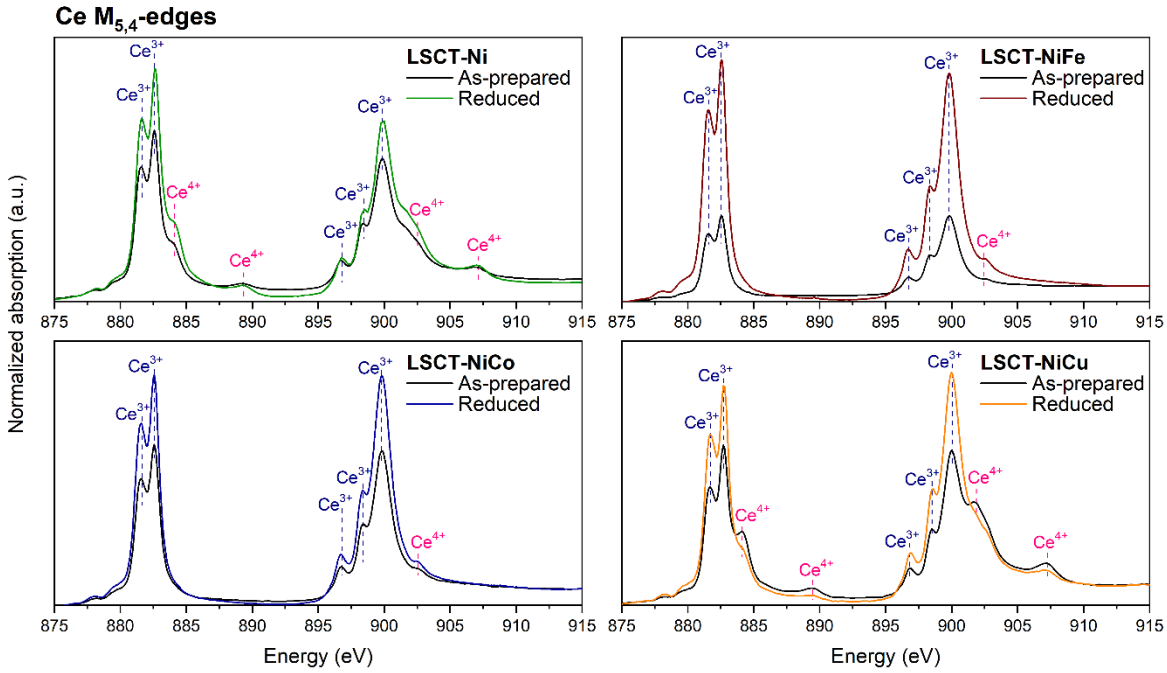


Fig. 4.13. $M_{5,4}$-edges of cerium in LSCT-NiM. The peaks from specific Ce oxidation states are marked.

Lastly, electrical tests were performed to determine if the obtained perovskites have sufficient conductivity to be used as anodes or even catalytic layers in SOC technology. The results from synthetic air and hydrogen are plotted in **Fig. 4.14.** Furthermore, to apply Bruggeman correction (Eq. 3.6), the density of the pellets was measured and calculated using the Archimedes principle (Eq. 3.1-3.3). The density and porosity for both as-prepared and reduced states are presented in **Tab. 4.4**. As expected, the sample containing cobalt was characterized by the lowest porosity, as cobalt is known as a sintering

aid. The second most dense was LSCT-Ni. The LSCT-NiFe and LSCT-NiCu are characterized by similar porosity values with nearly a quarter of the pellet being pores. After reduction and release of oxygen, the porosity in all cases has increased by several %pt.

Tab. 4.4. The density and porosity of as-prepared and reduced LSCT-based pellets measured and calculated using Archimedes principle. The values are given with 5% uncertainty.

		LSCT-Ni	**LSCT-NiFe**	**LSCT-NiCo**	**LSCT-NiCu**
As-prepared	**Theoretical density (g cm^{-3})**	5.45	5.45	5.44	5.45
	Measured density (g cm^{-3})	4.76	4.13	5.09	4.03
	Total porosity (%)	12.73	24.23	6.33	26.14
	Open porosity (%)	11.23	23.15	1.11	25.78
Reduced	**Theoretical density (g cm^{-3})**	5.43	5.42	5.42	5.45
	Measured density (g cm^{-3})	4.71	4.03	4.88	3.84
	Total porosity (%)	13.31	25.68	10.03	29.62
	Open porosity (%)	12.94	19.90	3.88	28.62

In an air atmosphere, all materials are characterized by the low electrical conductivity ranging between 10^{-5} and 10^{-3} S cm^{-1}, similar to those reported elsewhere [159–163]. With a decrease in the temperature, the electrical conductivity decreases, as expected for the thermally activated conduction mechanism. In air, the dominant charge carriers are electron holes and oxygen vacancies [164]. However, due to the limited mobility of oxygen ions compared to electron holes, it can be assumed that electronic conduction dominates here [161]. Moreover, the addition of secondary transition metal to nickel leads to the increase in the conductivity already in the air. In general, the conduction in perovskites occurs through the B-O-B bonds when the B-atoms can easily switch oxidation states. Here, due to the high stability of Ti^{4+}, the conduction would be enhanced by the introduced dopants. Considering that nickel is likely be present in the Ni^{2+} state [24,165], the other transition metals have more than one easily accessible oxidation states. Thus, in order to transform the charge carriers, Co, Fe, or Cu can be temporarily reduced or oxidized, which due to the locality of the process, unfortunately will not be visible in the XAS spectra. The enhancement follows the order Fe → Co → Cu which is the inverse order of the specific cation reducibility. Copper is the most easily reduced, promoting the conduction mechanism. The activation energies have also been calculated and are presented in the graph. In general, the values obtained vary between 0.34 – 0.55 eV, which are characteristic values for the electron hole conductivity in the perovskite structure [161]. For LSCT-NiCo, the activation energy

value is the lowest, originating from the partial reduction of cobalt. As a result, more oxygen vacancies are formed, consuming the electron holes and decreasing the charge carrier concentration, leading to the a slower increase in conductivity with temperature.

After reduction (900 °C, 10 h), the conductivity of titanate-based perovskites increased by several orders of magnitude reaching the maximum value of 10.3 S cm^{-1} for LSCT-NiFe at 500 °C. In contrast to measurements in air, the metallic character of conduction is observed for all the dopants considered, except LSCT-NiCo. This particular compound is still characterized not only by thermally activated behavior, but also by significantly lower values of conductivity. Such a diminished performance is a result of the high relative density of this particular pellet. With a lower volume of available pores, the hydrogen was not able to penetrate the material sufficiently. On the other hand, the enhancement of the conductivity and change in the slope of the curve in all three remaining compounds are associated with the exsolution or, more specifically, with the diffusion of the reduced ions to the surface. Even if the nanoparticles in LSCT-NiFe and LSCT-NiCu do not cover the surface densely enough to provide the percolation path, the local change in the transition metals' concentration in the surface proximity could significantly increase the conductivity of the perovskites. Moreover, metallic behavior in STO-based compounds has already been reported in the literature [166–168]. Another possibility is the migration of the platinum during the reduction, which could form a thin surficial layer favoring electrical transport. However, in this case the reason why it did not happen only in the LSCT-NiCo sample remains unknown.

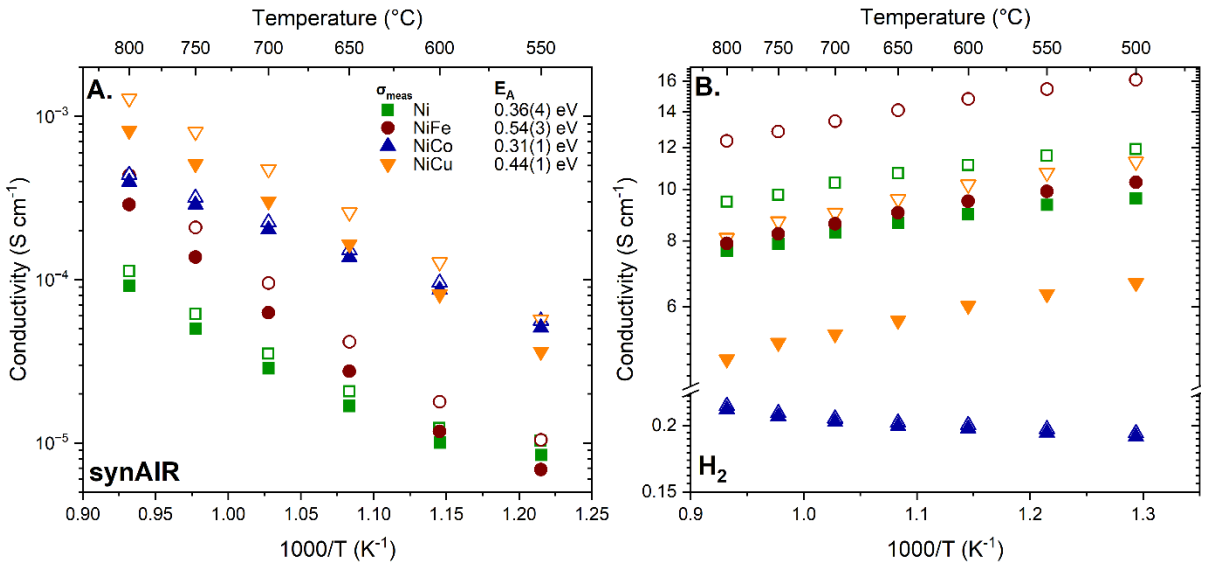


Fig. 4.14. Electrical conductivity of LSCT-based perovskites measured in air (A.) and in hydrogen after external reduction (B.). The empty shapes represent the calculated conductivity with Bruggeman correction.

Conclusions of this section:

- Strontium titanate can be simultaneously doped with lanthanum and cerium at A-site as well as nickel and other transition metal (iron, cobalt, or copper) at B-site without significant formation of foreign phases. Only a small amount of $NiTiO_3$ and $CeO_{2-\delta}$ is formed in LSCT-Ni and LSCT-NiCu, respectively. After the reduction, the perovskite phase is preserved with no peaks arising from the metallic nanoparticles.
- The TECs of all LSCT-based compounds are comparable with those of both YSZ and NiO-YSZ, minimizing the mechanical mismatch between typical cell counterparts.
- Microscopic imaging revealed the exsolved nanoparticles after the high-temperature reduction. Surprisingly, the highest amount of exsolved nanoparticles was found for the LSCT-Ni sample without any secondary transition metal. The reason for this behavior is the highest concentration of Ni in the initial perovskite. TEM-EDS maps revealed that the exsolved nanoparticles are in form of bimetallic alloy forming either $NiCo_{2.5}$ or $Ni_{3.5}Fe$ in LSCT-NiCo and LSCT-NiFe, respectively.
- X-ray absorption studies revealed that in the as-prepared state, the nickel state remains almost unaffected by the introduction of additional transition metal. However, after the reduction, the changes are more visible as the presence of a secondary metal enhances the reducibility of the nickel.
- No impact on titanium in its octahedral coordination is made regardless of the B-site doping. Cerium was found mainly in the Ce^{3+} state, which combined with the presence in the cubic structure proves the incorporation of Ce ions into the A-site lattice as intended during the synthesis. Only in LSCT-NiCu, some peaks from Ce^{4+} were detected, arising from $CeO_{2-\delta}$ impurity.
- In air, LSCT-based compounds exhibited low electrical conductivity, being within range of 10^{-5} – 10^{-3} S cm^{-1}. The behavior was characteristic for the thermally activated conduction mechanism. However, after the reduction, the conduction characteristic differed, as LSCT-Ni, LSCT-NiFe, and LSCT-NiCu showed a decrease in conductivity with temperature. This was explained by the increase in the concentration of transition metals in the proximity of the surface, allowing for metallic conduction. Moreover, the values obtained increased up to 10 S cm^{-1}, which is several orders of magnitude compared to measurements in the air. LSCT-NiCo was still characterized by the semiconducting temperature dependence and significantly lower values, which arose from the limited hydrogen permeation leading to insufficient reduction.
- Considering good TEC match compared to the conventional SOC constituents and satisfactory exsolution, the LSCT-based compounds offer promising properties for SOFC. Unfortunately, due to not extraordinary conduction, they are rather unlikely to replace the Ni-YSZ anodes. However,

the stability of the structure and the exsolution phenomenon yielding bimetallic nanoparticles, makes them particularly interesting as an additional layer. This can be specifically important in the DIR-SOFC, where LSCT may work as the catalytically active, yet protective barrier, limiting the coke deposition on nickel cermet.

By means of aforementioned conclusions, the hypothesis 1 of this doctoral dissertation *"Incorporation of a secondary transition metal, together with nickel, into STO-based compounds will enhance the exsolution process and facilitate nickel reduction."* is partially confirmed as the addition of secondary transition metal does enhance the reduction of nickel. However, due to the higher concentration of Ni in single-doped LSCT (10 mol. % vs. 5 mol. % in co-doped ones), no positive impact on the exsolved nanoparticles quantity is observed.

4.2. Strontium ferrite molybdate - $Sr_2Fe_{1.5}Mo_{0.5}O_{6-\delta}$

4.2.1. Influence of the lanthanum and niobium doping on the redox stability of SFM

Another family of compounds analyzed was double perovskites based on $Sr_2Fe_{1.5}Mo_{0.5}O_{6-\delta}$. Similarly to that in the previous chapter, the main aim was to exsolve the nanoparticles from the lattice. However, SFM can be prone to phase decomposition after reductive treatment. Thus, the redox stability must be addressed. To stabilize the structure, La- or Nb-doping was introduced resulting in the formation of LSFM or SFMNb compounds, respectively. For full formulas, please be referred to **Tab. 3.1** in Chapter 3.1.2. The results of studies presented here have already been published as **Ducka** *et al.* (2025). *"Investigation of the phase transition to the Ruddlesden–Popper phase in La- or Nb-doped $Sr_2Fe_{1.5}Mo_{0.5}O_{6-\delta}$ double perovskites and the impact of lanthanum or niobium doping"*. NANOSCALE, 17, 12371-12384. https://doi.org/10.1039/d5nr00596e [98].

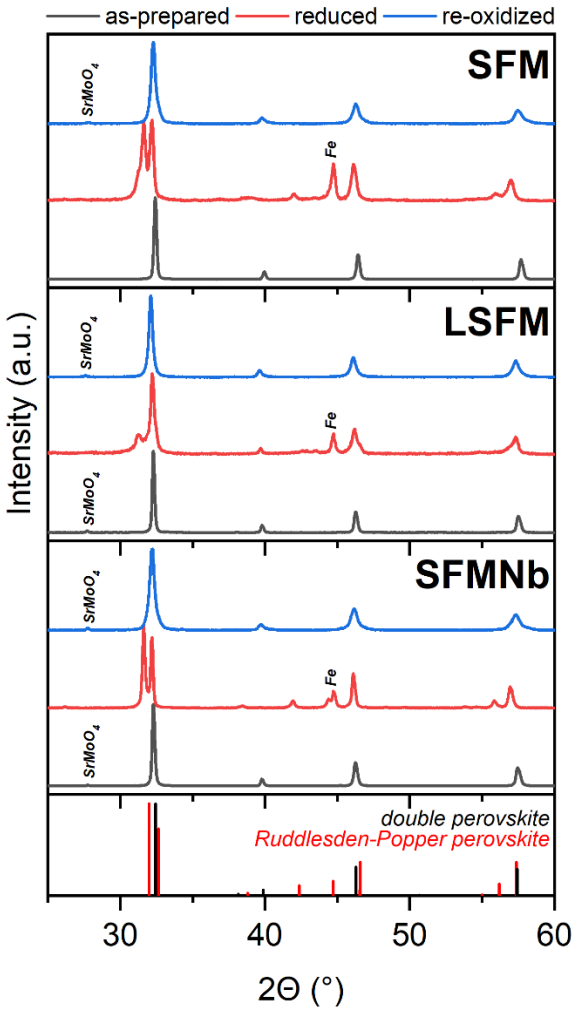


Fig. 4.15. XRD patterns for SFM, LSFM, and SFMNb in as-prepared, reduced and re-oxidized states [98].

X-ray diffraction analyses indicated that all synthesized compounds adopt the double perovskite structure with *Fm-3m* space group, consistent with the patterns shown in **Fig 4.15**. In doped samples, trace amounts of $SrMoO_4$ were detected, calculated by Rietveld refinement to be below 2 wt.%. The literature commonly documents $SrMoO_4$ presence in as-synthesized materials [77,84,169,170], which typically disappears after reduction. Comprehensive Rietveld refinement results are presented in **Tab. 4.5**. Doped perovskites exhibit unit cells expanded compared to those of undoped strontium ferrite molybdate. Despite the smaller ionic radius of La^{3+} compared to Sr^{2+}, the aliovalent substitution induces valence adjustments in Fe or Mo to maintain charge neutrality. The lower oxidation states of both Fe and Mo yield larger ionic radii than their higher-valence forms [141], thus expanding the unit cell [169]. Yang *et al.* [136] attributed La-doping-induced unit cell expansion to the

dominance of La^{3+} electronic effects over ionic size disparities. They suggested that the extra electron from La^{3+} predominantly alters the Mo valence, minimally affecting Fe [136]. Unit cell expansion in SFMNb arises directly from ionic size effects. Niobium is aimed to occupy the B-site of the perovskite lattice, as Nb is the transition metal neighboring molybdenum. Nb^{5+} ionic radius (0.64 Å) exceeds those of Mo^{5+} (0.61 Å) and Mo^{6+} (0.59 Å), while being slightly smaller than Fe^{3+} (0.645 Å) and significantly smaller than Fe^{2+} (0.78 Å) [141]. According to reference [15], niobium doping promotes an increase in Fe^{2+} fraction, fostering further cell expansion.

The emergence of a diffraction peak at approximately 31° indicates that reduction at 800 °C induces a phase transformation to a layered perovskite structure. This particular peak can be identified as originating from the (015) plane of the Ruddlesden-Popper layered perovskite. Unfortunately, the main peaks of double perovskite (022) and RP (110) overlap at ~32.4°. However, analysis of the intensity ratio of the split reflection in the 31-32° range suggests that the transformation is incomplete, with residual double perovskite still present. The relatively low intensity of the reflection associated with the layered perovskite in La-doped samples implies that lanthanum incorporation may stabilize the original structure and hinder the phase transition. Phase composition was determined using Rietveld refinement, considering a double perovskite structure ($Sr_2Fe_{1.5}Mo_{0.5}O_{6-\delta}$, *Fm-3m*), an oxygen-deficient Ruddlesden-Popper layered perovskite ($Sr_3Fe_{1.5}Mo_{0.5}O_{7-\delta}$, *I4/mmm*), and metallic iron (*Im-3m*), which may exsolve from the lattice. The refinement results are summarized in the **Tab. 4.5**. For both pristine and Nb-doped samples, the fraction of the newly formed layered perovskite ranges from 70 to 80 wt.%, whereas in the LSFM sample it is approximately 40 wt.%.

Although the presence of the Ruddlesden-Popper phase can be advantageous in promoting the exsolution of catalytically active species [16,170,171], it also introduces some challenges. As indicated in the **Tab. 4.5**, the double perovskite exhibits a larger unit cell volume than the Ruddlesden-Popper phase. Consequently, reduction-induced phase transformation may generate substantial lattice strain due to this volume mismatch. In the context of solid oxide cell applications, such strain could lead to electrode delamination and a reduction in the triple phase boundary. While previous studies report that pristine SFM is redox-stable at elevated temperatures and resistant to exsolution phenomena [16,84,172], XRD analysis of the reduced samples reveals the formation of metallic iron. A comparable effect was reported by Qiu *et al.* [171] for Co-doped SFM. In particular, the highest fraction of exsolved iron, approximately 13 wt.%, was observed in the SFMNb sample, indicating that Nb substitution at the B-site enhances iron exsolution. Although the relatively high segregation energy of Fe (0.91 eV) disfavors exsolution, the incorporation of additional transition metals can introduce cation defects

and/or oxygen vacancies [16], thus lowering the segregation energy and facilitating nanoparticle formation.

The reversibility of the phase transition was evaluated by re-oxidizing the materials at 800 °C for 4 hours. All samples reverted to the initial double perovskite structure, with no detectable layered perovskite phase. Additionally, $SrMoO_4$ was identified in all XRD patterns, including the SFM sample, which did not present this impurity prior to reduction. Although the structural framework was restored, the unit cell volume increased relative to the as-synthesized materials. This expansion is more pronounced in the pristine and Nb-doped samples, whereas the La-doped sample shows only a minor increase in volume.

Tab. 4.5. The lattice constants for SFM, LSFM, SFMNb in as-prepared, reduced and re-oxidized states. The values were calculated from the Rietveld refinement [98].

			SFM	**LSFM**	**SFMNb**
As-prepared	Double perovskite (*Fm-3m*)	a=b=c (Å)	7.8411(2)	7.8533(2)	7.8632(2)
		V (Å^3)	482.09	484.34	486.18
	$SrMoO_4$ amount (wt.%)		n/a	1.7	0.8
Reduced	Double perovskite (*Fm-3m*)	a=b=c (Å)	7.854(2)	7.884(1)	7.896(1)
		V (Å^3)	484.49	490.05	492.29
		Amount (wt.%)	17.7	52.2	7.6
	Ruddlesden-Popper layered perovskite (*I4/mmm*)	a=b (Å)	3.9348(6)	3.933(1)	3.9436(2)
		c (Å)	20.361(4)	20.951(9)	20.435(1)
		V (Å^3)	315.24	324.08	317.81
		Amount (wt.%)	73.2	39.2	79.1
	Iron amount (wt.%)		9.1	8.6	13.3
Re-oxidized	Double perovskite (*Fm-3m*)	a=b=c (Å)	7.8516(6)	7.8538(3)	7.8771(6)
		V (Å^3)	484.03	484.44	488.76
	Amount of $SrMoO_4$ (wt.%)		1.2	1.7	1.2

The microstructure of the reduced powders is shown in **Fig. 4.16**. Notably, the microstructure of the undoped sample appears more compact post-reduction. Although grain boundaries remain somewhat indistinct, regions featuring smaller elongated grains alongside the original rounded grains can be observed. This rectangular morphology arises from the shift to a layered perovskite structure. A limited quantity of nanoparticles was detected, though their abundance remains modest. The Nb-doped material exhibited the highest density of exsolved nanoparticles, consistent with XRD findings indicating the highest Fe content. These nanoparticles show a spherical morphology with diameters below 100 nm. The enhanced exsolution effect due to Nb-doping likely stems from the reduced valence of Fe ions in the as-prepared compound. This phenomenon is consistent with observations by Gou *et al.* [15] for analogous materials. Consequently, iron from the lattice undergoes more facile reduction at the surface, yielding observable nanoparticles. Based on the work of Lv *et al.* [16], where TEM-EDS analysis revealed no molybdenum in exsolved nanoparticles, the particles here are identified as metallic Fe, given the absence of other readily reducible transition metals at the B-site. Although niobium qualifies as a transition metal, its reduction demands significantly higher temperatures than those used in this study [15,173].

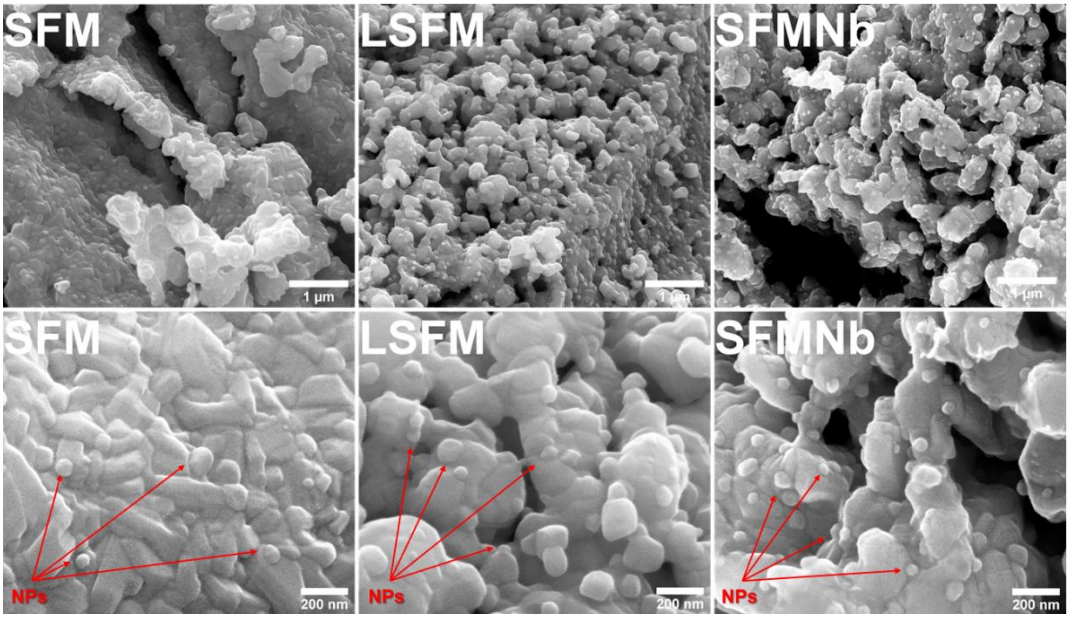


Fig. 4.16. SEM images of SFM, LSFM, and SFMNb after reduction in hydrogen at 800 °C [98].

As the reversibility of the phase transition was discovered in the ex-situ XRD studies, the high-temperature in-situ measurements were applied to complement previous findings. This allowed to probe the transformation from the layered perovskite to the double perovskite phase under an air atmosphere. The diffraction patterns collected during the heating process (50 °C increments) are depicted in **Fig. 4.17**.

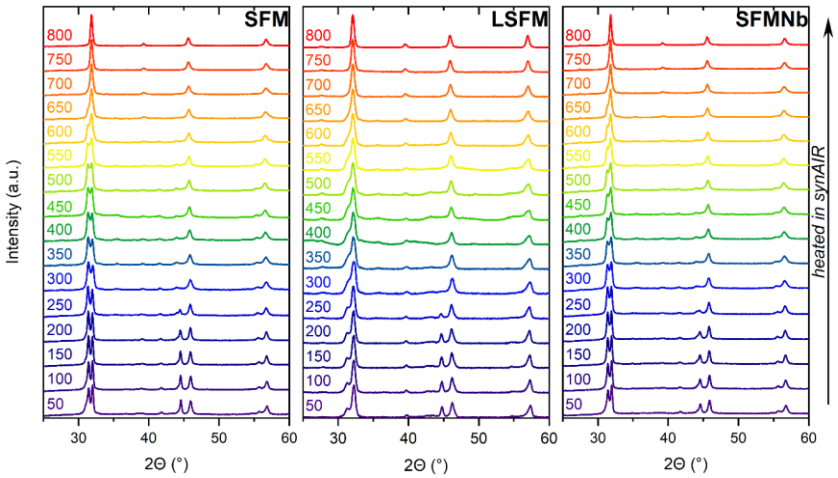


Fig. 4.17. XRD patterns of reduced SFM, LSFM, and SFMNb during in-situ re-oxidation in air [98].

Fig. 4.18 illustrates the heat maps representing the normalized intensities of the main XRD peaks associated with the Ruddlesden-Popper (RP) and double perovskite (DP) phases plotted against temperature. The (022) peak of the DP overlaps with (110) peak of the Ruddlesden-Popper phase, so the neighboring (015) RP peak is considered as a phase transition indicator. In the pristine and SFMNb samples, the intensities of these reflections remain comparable from room temperature up to approximately 600 °C, indicating the predominance of the Ruddlesden-Popper (RP) perovskite phase. Conversely, the LSFM sample exhibits a reduced amount of the RP phase. Consequently, the diffraction peak near 31° displays a diminished intensity and manifests itself as a halo spanning 31-31.5°. In all investigated compounds, the reflections systematically shift toward lower 2θ values, reflecting the progressive thermal expansion of the unit cells with increasing temperature. At around 250 °C, the shift toward higher angles is visible in all three samples, being the most intense for pristine and La-doped SFM.

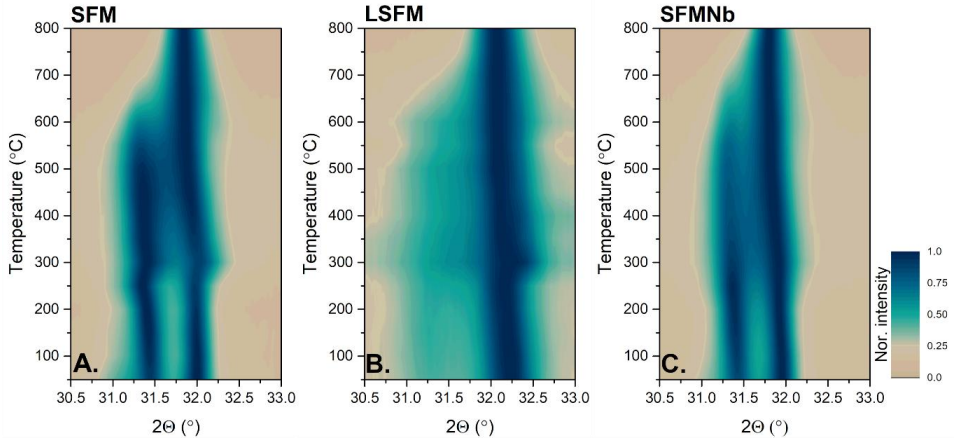


Fig. 4.18. Heatmaps of the normalized XRD peak intensity in SFM, LSFM, and SFMNb during HT-XRD. The close-up on the RP (015) and DP (022) peaks between 2Θ 30.5-33 ° [98].

The structural features evident around 250 °C in **Fig. 4.18** coincide with the disappearance of the iron-related signal at the identical temperature presented in **Fig. 4.19**. This phenomenon arises from the reincorporation of iron into the perovskite lattice, coupled with the onset of oxidation leading to the double perovskite phase. Upon further elevation of temperature, the main peaks progressively converge, as the c-parameter within the Ruddlesden-Popper phase shrinks. Ultimately, the peak signature of the Ruddlesden-Popper phase disappears within the range of 600 °C to 700 °C.

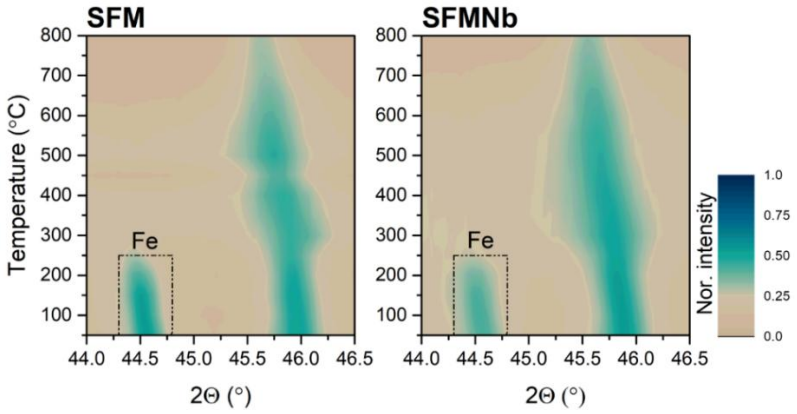


Fig. 4.19. Heatmaps of the normalized XRD peak intensity in SFM and SFMNb during HT-XRD. The close-up on the Fe peak vanishing during the oxidation [98].

Differential scanning calorimetry/thermogravimetry (DSC/TG) measurements were conducted on the pre-reduced powders to provide deeper insight into the phase transition dynamics. The results are illustrated in **Fig. 4.20**. The initial process, prominently evident in the TG curve up to 200 °C, originates from the desorption of physisorbed water. Subsequently, a more gradual mass reduction between 200 and 300 °C can be ascribed to the elimination of lattice-bound water. Beyond 300 °C, the mass exhibits a more rapid gain for both SFM and SFMNb samples, whereas for LSFM, this increase progresses more steadily. Furthermore, this upturn of the TG signal aligns with an exothermic peak in the DSC trace, which is attributed to iron oxidation. The temperature at which this occurs closely matches the temperature of the iron peak

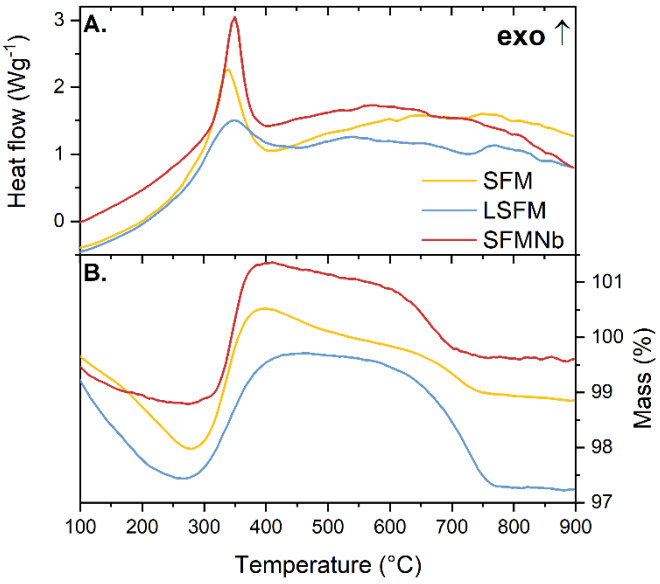


Fig. 4.20. DSC/TG curves of reduced SFM, LSFM, and SFMNb powders during re-oxidation in air [98].

disappearance observed in HT-XRD (**Fig. 4.19**). Additionally, the DSC peak exhibits the greatest intensity in the SFMNb sample, which displayed the highest quantity of exsolved Fe nanoparticles as confirmed by both XRD and SEM examinations. No other distinct peaks are visible in the DSC signal. Nevertheless, the TG curve reveals a progressive mass loss across the 350-650 °C interval for all samples except LSFM, precisely aligning with the phase transition window identified in HT-XRD. A pronounced mass decrease occurs above 700 °C (750 °C for LSFM), due to the release of excess oxygen from the Ruddlesden-Popper phase or the formation of oxygen vacancies in the materials. The cumulative mass loss by 750 °C, together with the emergence of a singular peak in HT-XRD, serves as evidence for the full completion of the phase transition to the double perovskite structure.

The O K-edge spectra acquired for pristine, La-doped, and Nb-doped SFM in three distinct states are shown in **Fig. 4.21 a-c**. The spectral peaks correspond to O 1s excitations into hybridized orbitals: Fe 3d-O 2p at approximately 530 eV, followed by Sr 4d-O 2p at ~536 eV, and Fe 4sp-O 2p at ~543 eV [174–176]. In perovskite iron compounds, Fe predominantly adopts a $3d^5$ ground state configuration. Abbate *et al.* [175] examined the ground states in $SrFeO_3$ and $LaFeO_3$, determining that Fe in $SrFeO_3$ resides in a $3d^5\underline{L}$ (Fe^{4+}) configuration (where $\underline{L}$ denotes ligand holes) whereas in $LaFeO_3$, it is $3d^5$ (Fe^{3+}). Herein, the Fe^{4+} $3d^5\underline{L}$ state is identifiable via the pre-peak at ~528 eV, which exhibits maximum intensity in re-oxidized SFM and LSFM. The as-prepared samples also feature this pre-peak, but with reduced intensity. The primary peak arising from t_{2g} orbitals in all as-prepared spectra shifts modestly to lower energies relative to Fe^{3+} oxides, indicative of Fe^{4+} presence in these conditions [175,177]. Conversely, the signal from higher-energy e_g orbitals appears merely as a minor shoulder near 534 eV. Xi *et al.* [178] attributed the intensity of e_g orbitals to structural distortions. The emergence of t_{2g} and e_g peaks results from crystal field splitting at the transition metal sites [176,178].

After reduction, substantial changes are visible in the spectra across all compounds. Initially, the t_{2g} peak displaces to higher energies and resolves into a doublet configuration. This alteration arises from the reduction of Fe^{4+} to Fe^{3+} and adheres to the pattern documented by Abbate *et al.* [175]. Concurrently, the doublet formation reflects the further splitting of t_{2g} into d_{xz}, d_{yz}, and d_{xy} orbitals, induced by either unit cell distortion or oxygen vacancy generation [178,179]. Simultaneously, crystal field splitting affects the e_g orbitals, splitting them into d_{z2} and d_{x2-y2} components, respectively. These spectral signatures align with the development of the more complex Ruddlesden-Popper layered perovskite architecture. The e_g orbital splitting is most pronounced in SFMNb. Notably, this sample yields a uniquely distinct spectrum following re-oxidation. The t_{2g} peak shifts to elevated energies, whereas the e_g peak markedly diminishes in intensity. Furthermore, the Sr 4d-O 2p-derived peak also migrates to higher energies. This is in contrast with all other samples, where the energy position of this

peak remains largely unaltered. Such a finding is especially noteworthy, as no substantive structural variations were detected via XRD, whether ex-situ or in-situ high-temperature approach. The spectral divergences in SFMNb may stem from electron transfer involving Fe-Nb or Mo-Nb orbitals.

Fig. 4.21d presents the Fe $L_{3,2}$-edges for SFM-based compounds after reduction in H_2. Acquired spectra are characteristic of Fe^{3+} in octahedral coordination [175,180–182]. As reported in [175], these spectra arise from a high-spin t_{2g}^3 e_g^2 ground state configuration of $3d^5$ electrons, with the 10Dq value determined to be 1.6 eV. This value was derived from the minima observed in the second derivative of the L_3-edge. Nonetheless, the spectra exhibit a consistent profile indicative of Fe^{3+} cations, albeit with varying intensities in the white lines. The intensity of the white line at the L-edge provides information on the occupancy of d orbitals and can imply variations in the oxidation state [183]. In the present study, a higher proportion of Fe^{2+} forms in SFM post-reduction compared to the doped variants.

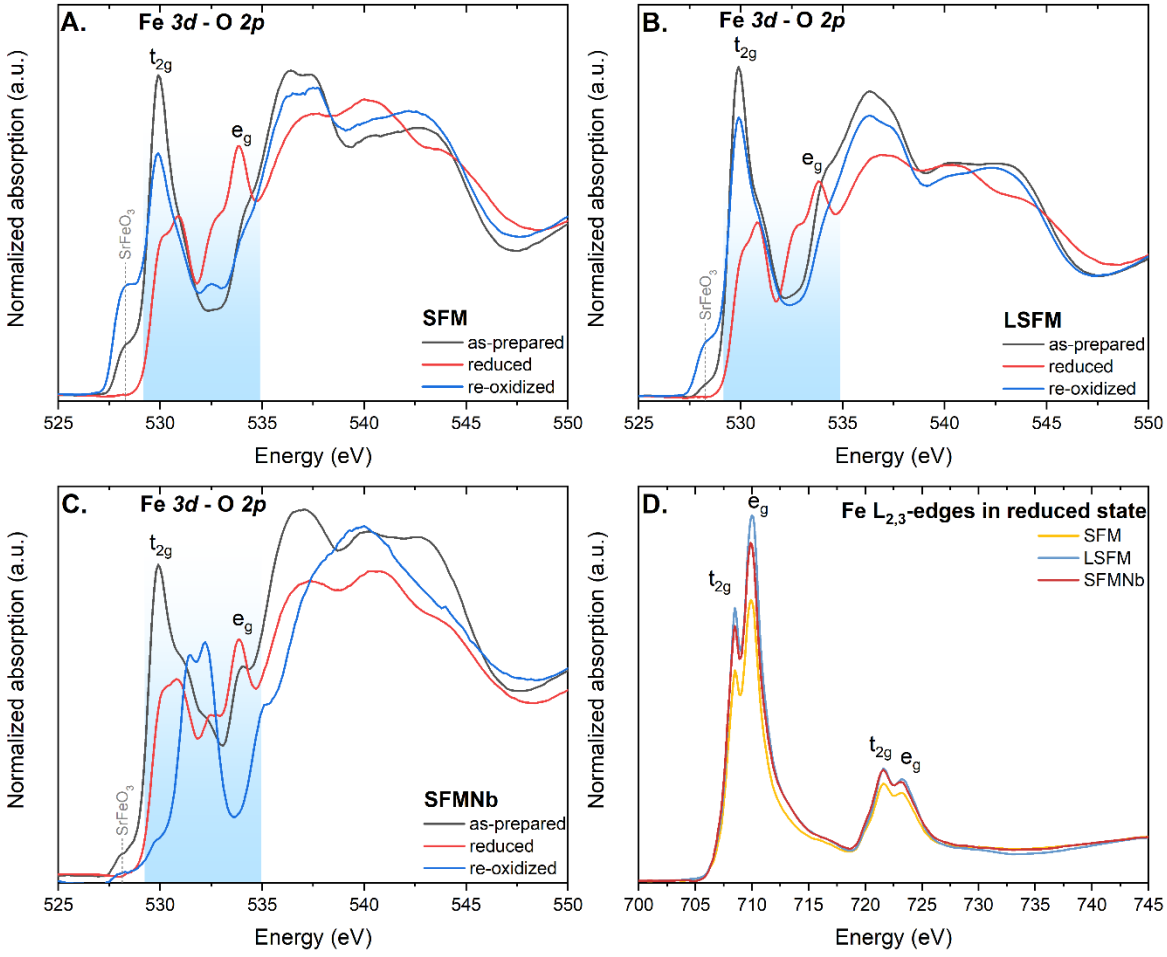


Fig. 4.21. Oxygen K-edges of SFM (A.), LSFM (B.), and SFMNb (C.) in as-prepared, reduced, and re-oxidized states, (D.) Fe $L_{3,2}$-edge of iron in reduced compounds [98].

The utilization of hard X-rays facilitated the investigation of the iron K-edge of SFM, LSFM, and SFMNb. Normalized XANES spectra are shown in **Figs. 4.22a-c**. Consistent with observations

from the $L_{3,2}$-edge analyses, K-edge spectra exhibit signatures typical of Fe^{3+} within the octahedral coordination environment of the perovskite structure [80,184]. Despite their broadly analogous overall profiles, certain notable discrepancies are discernible. Primarily, the pre-edge feature arises from the hybridization of 3d and 4p orbitals, leading to the quadrupole-allowed 1s → 3d transition [185,186]. Such 3d-4p hybridization would be absent in perfectly regular octahedral geometries; therefore, structural distortion must be inherent in SFM-based materials [186].

However, the reduction process does not alter the overall shape of the K-edge. It rather influences the intensity of the white line. The most pronounced decrease in white-line intensity occurs in the doped SFM variants, indicating a partial reduction to the lower-valence iron species, as corroborated by SEM observations. Concurrently, the pre-edge feature exhibits enhancement specifically in the undoped sample. Across all examined samples, the reduced states display the minimal white-line intensities. This finding, combined with a subtle shift in the pre-edge position, points to partial reduction involving Fe^{2+} ions. Following re-oxidation, the white-line intensity recovers nearly to its initial magnitude. For both doped SFM-based compounds, the edge position shifts upward, likely attributable to modifications in the density of states (DOS). Elevated white-line intensities correspond to diminished DOS values.

Molybdenum L_3-edges were also acquired, with normalized spectra illustrated in Figs. **4.22d-f**. Solely from the peak intensity ratio of 3:2, the octahedral coordination of molybdenum can be easily verified [187,188]. The initial peak at approximately 2523 eV arises from transitions to the t_{2g} states, whereas the subsequent peak at ~2527 eV corresponds to the excitation to the e_g state [77]. According to Vasala *et al.* [77], in the as-prepared samples, both of these states should remain unoccupied, with reduction introducing electrons specifically into the t_{2g} state. Consequently, the peak intensity in reduced samples should be diminished relative to that in the as-prepared counterparts. This behavior is observed in both the pristine SFM and the LSFM. Remarkably, the SFMNb sample deviates from this pattern, due to electron transfer between Mo and Nb cations. From the Mo-L_3 spectra, it can be deduced that molybdenum undergoes a partial reduction to the Mo^{5+} state during the reduction process, as evidenced by the partial occupancy of the t_{2g} and e_g states. An additional hallmark of the octahedral geometry is the magnitude of the d-orbital splitting, determined as the energy difference between the two minima in the second derivative of the spectra for each compound [188]. The second derivatives of the Mo L_3-edge spectra are depicted in **Figs. 4.22 g-i**. The calculated values fall within the range of 4.2-4.4 eV, which is characteristic of octahedral coordination [152,187].

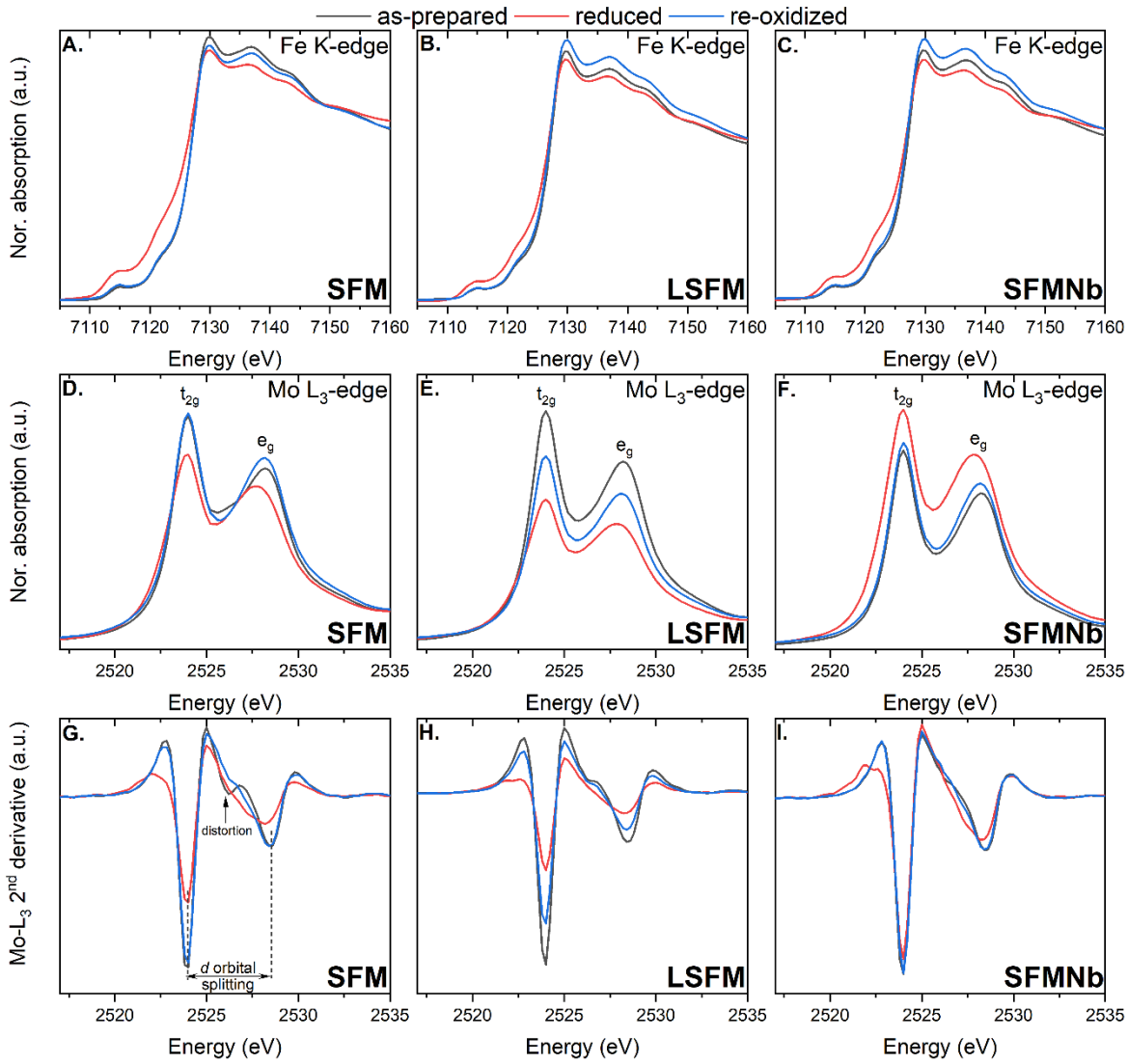


Fig. 4.22. K-edge of iron in SFM, LSFM, and SFMNb compounds (A.-C.), L_3-edge of molybdenum for same compounds (D.-F.), and 2nd derivative of Mo L3-edge (G.-I.) All spectra were collected for each sample as-prepared, reduced, and re-oxidized states [98].

The Fourier-transformed EXAFS spectra for the respective compounds are depicted in **Fig. 4.23**. Given the structural complexity of these materials, the analysis was restricted to qualitative evaluation. The prominent peak observed at approximately 1.75 Å across all samples corresponds to the Fe-O coordination bond. This Fe-O peak position aligns closely with the anticipated bond lengths derived from the crystallographic data of the synthesized compounds. In the reduced compounds, this peak exhibits a modest displacement toward higher radial distances, a feature emblematic of the Ruddlesden-Popper layered perovskite phase. The re-oxidized materials display Fe-O bond lengths comparable to those of their as-prepared counterparts, signifying the restoration of the original structural configuration. The subsequent characteristic peak arises from the Fe-Sr scattering pathway,

which generally shortens slightly after reduction due to the emergence of the RP phase. Notably, in the LSFM sample, this scattering path instead elongates, attributable to the expansion of the parent unit cell during reduction. Succeeding the Fe-Sr peak is the contribution from single-scattering paths involving Fe-Fe/Mo bonds. For the Nb-doped variant, the signal from the Fe-Nb scattering pathway overlaps with those of the Fe-Fe and Fe-Mo paths. Since Fe and Mo occupy crystallographically equivalent positions, distinguishing individual contributions to these scattering pathways proves to be unfeasible.

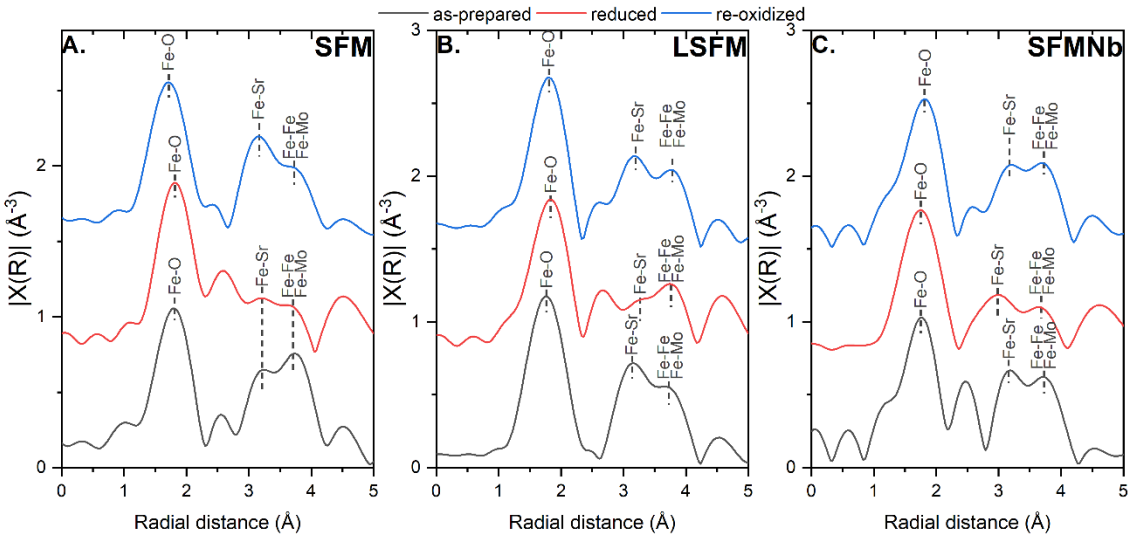


Fig. 4.23. Fourier-Transformed EXAFS of Fe K-edge in SFM, LSFM, and SFMNb in as-prepared, reduced, and re-oxidized states. The spectra were corrected for phase shift [98].

As already noted, the scattering pathways associated with Fe–Fe and Fe–Mo bonds overlap within the Fourier-transformed EXAFS spectra, making their individual differentiation unattainable. Consequently, wavelet transform analysis was employed to elucidate potential structural modifications occurring during the reduction and subsequent re-oxidation processes. The wavelet transform heat maps (phase shift uncorrected) for the LSFM compound across its three distinct states are illustrated in **Fig. 4.24**. The region exhibiting the highest intensity, appearing as red, is indicative of Fe-O bonds, while the extended bond feature in a wavevector of approximately 6 $Å^{-1}$ arises from interactions with strontium. These Fe-O and Fe-Sr bond characteristics are precisely delineated and corroborate the findings from the Fourier-transformed EXAFS analysis. At greater radial distances, two distinct halo features emerge, allowing the separation of contributions from iron and molybdenum [152]. Specifically, the halo centered around 6 $Å^{-1}$ is attributed to the Fe-Fe bond [189,190], while the halo at approximately 7.5 $Å^{-1}$ corresponds to the Fe-Mo bonds, as heavier atomic species contribute signals at elevated wavevectors [191]. Both the Fe-Fe and Fe-Mo bonds undergo alterations induced by the reduction and re-oxidation treatments. Nevertheless, the Fe-Mo bond displays more pronounced

elongation and contraction in response to these redox cycles. Notably, an extraneous signal manifests itself in the reduced LSFM sample at a wavevector of ~4.75 $Å^{-1}$. Although employing identical computational parameters, this feature is absent in the as-prepared and re-oxidized states, implying its association with exsolved nanoparticles situated on the perovskite surface.

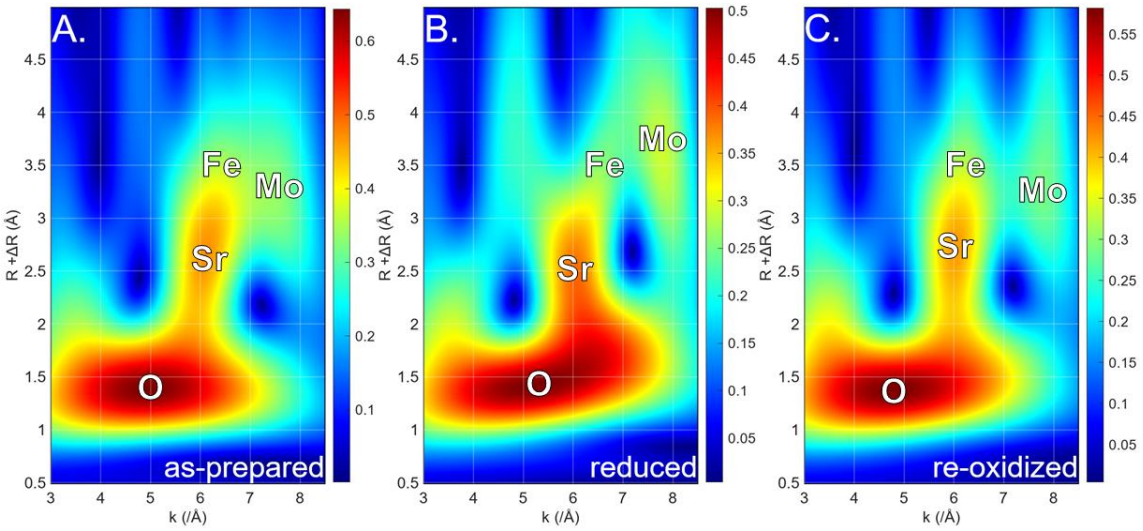


Fig. 4.24. Wavelet-Transformed Fe K-edge of LSFM compound in as-prepared, reduced, and re-oxidized states [98].

To examine the influence of La and Nb doping on the electrical properties, the direct-current four-wire method was employed. Conductivity as a function of temperature is shown in **Fig. 4.25**. In air, the three samples exhibit a conductivity maximum at 600-650 °C, reaching 14.5 S cm^{-1}, 20.2 S cm^{-1}, and 11 S cm^{-1} for SFM, LSFM, and SFMNb, respectively. Below the temperature at which this maximum is reached, all compounds display thermally activated conduction. Above 650 °C, the conductivity begins to decline. A similar trend has been reported by other groups [15,136,192–195]. This behavior is attributed to oxygen loss from the lattice, which promotes the reduction of iron and/or molybdenum and thus decreases the effective concentration of charge carriers [15]. At the same time, the formation of oxygen vacancies at elevated temperatures reduces the number of available pathways for charge transport. According to Niu *et al.* [196] and Yang *et al.* [136], conduction in SFM-based compounds can be described by double exchange between the Fe 3d-O 2p and Mo 3d-O 2p orbitals. Consequently, charge transport proceeds through a small-polaron hopping mechanism through Fe^{2+}/Mo^{6+}-O^{2-}-Fe^{3+}/Mo^{5+} pathways [136,170,194,197].

As anticipated, lanthanum doping enhances the electrical conductivity, whereas niobium incorporation yields a diminished overall conductivity. At lower temperatures, the conductivity of SFMNb slightly surpasses that of the undoped SFM material. Activation energies were determined

using the Arrhenius equation within the 300–600 °C regime, where the linear relationships between ln(σT) and 1/T were evident. The calculated activation energy (E_A) values under both atmospheric conditions are presented in **Tab. 4.6**. In general, doping reduces the activation energy for conduction. This reduction can be attributed to an elevated concentration of oxygen vacancies [197]. Even the Nb-doped variant, despite its adverse effect on conductivity, exhibits a lower E_A.

The electrical conductivity of all compounds under hydrogen exhibits a different behavior: it increases gradually throuhout the entire temperature range, consistent with established trends [15,136]. Within the conductivity plots, two distinct regimes are identifiable: a low-temperature region extending up to 500 °C and a high-temperature region beyond this threshold. These regimes correspond to changes in the slope of the conductivity curve, with the transition most evident in the Nb-doped SFM. The inflection point in the conductivity curve represents a hallmark of the small polaron hopping mechanism [194]. Wang *et al.* [197] attributed the dual slopes to the presence of two distinct charge compensation pathways, which required the evaluation of two separate activation energies. The calculated values are listed in **Tab. 4.6**. Generally, activation energies are lower in the low-temperature regime. Between 300-500 °C, doping exerts a favorable influence on the activation energy. However, in the high-temperature regime, only lanthanum doping proves advantageous with respect to activation energy. Analogous to the observations in air, LSFM demonstrates the highest conductivity over nearly the full temperature span. Solely at 800 °C, SFMNb achieves peak electrical conductivity, while at lower temperatures its performance aligns closely with that of undoped SFM. All compounds attain conductivity values at 800 °C of 25.5 S cm^{-1}, 31.4 S cm^{-1}, and 34.1 S cm^{-1} for SFM, LSFM, and SFMNb, respectively. Conductivity levels recorded in both air and hydrogen position these double perovskites as promising candidates for anode and cathode applications in solid oxide cells (SOCs), potentially enabling their deployment as electrodes in symmetrical solid oxide fuel cells (sSOFCs) [198,199]. For instance, Zheng *et al.* [198] investigated a comparable system, $Sr_2Fe_{2-x}W_xO_{6-\delta}$, exhibiting electrical conductivity near 40 S cm^{-1}, employed as electrodes in a quasi-symmetrical configuration. The same group documented the application of SFM in a symmetrical setup, achieving electrical conductivity of 50 S cm^{-1} in the H_2/Ar mixture and 13 S cm^{-1} in air [199]. Comparable conductivity magnitudes were realized for Cu-doped SFM in sSOFCs by Tian *et al.* [192]. In the study by Niu *et al.* [196], $Sr_2TiFe_{1-x}Mo_xO_{6-\delta}$ symmetrical electrodes displayed favorable electrode performance, stability, and resistance to poisoning, although the electrical conductivities in air and hydrogen did not exceed 2 S cm^{-1}. Given these benchmark values, LSFM emerges as a compelling candidate that merits further investigation as an electrode material for sSOFCs.

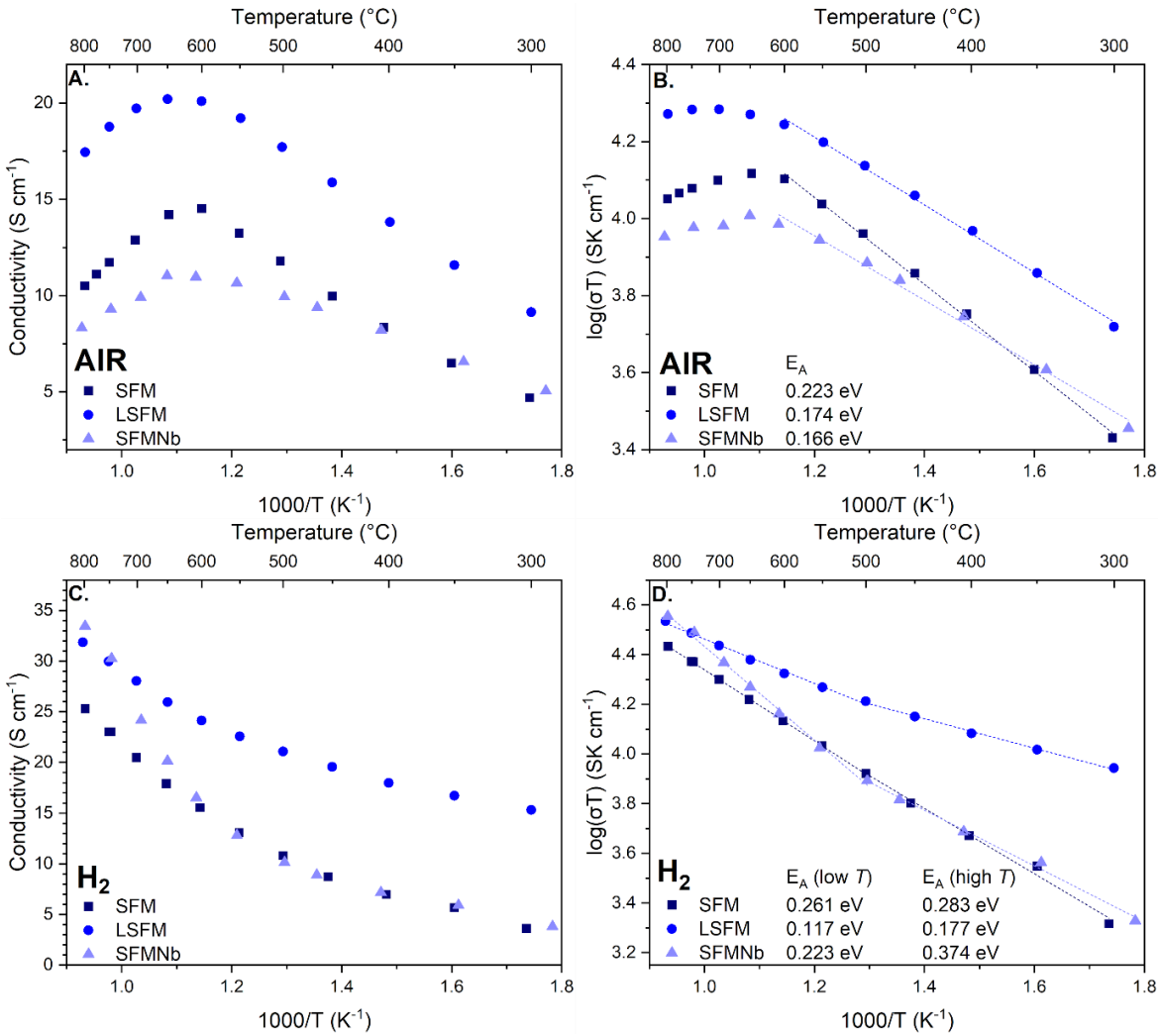


Fig. 4.25. Temperature dependence of electrical conductivity of SFM, LSFM, and SFMNb measured in air (A. & B.) and hydrogen (C. & D.) [98]

Tab. 4.6. Activation energy of electrical conduction for SFM, LSFM, and SFMNb [98].

	AIR	**H_2**	
	300-550 °C	**300-500 °C**	**500-800 °C**
SFM	0.223(4) eV	0.261(9) eV	0.283(1) eV
LSFM	0.174(4) eV	0.117(4) eV	0.177(5) eV
SFMNb	0.166(7) eV	0.223(9) eV	0.374(9) eV

Conclusions of this section:

- Both lanthanum and niobium can be successfully incorporated into the A- and B-site of the SFM double perovskite. The only impurity can be associated with $SrMoO_4$, being a typical one for the synthesis of these materials in oxidizing atmospheres.
- The reduction of pure SFM, as well as La- or Nb- doped SFM leads to the partial phase transition from double perovskite to Ruddlesden-Popper layered one. This transition is the least intense in the case of La-doped LSFM. After the re-oxidation at 800 °C in ambient air, the structure is restored back to its original double perovskite, proving the reversible character of these changes.
- In-situ oxidation studies show that firstly the iron is introduced back to the lattice at ~300 °C. This process is visible in both HT-XRD and TG/DSC. Subsequently, with the increasing temperature, the layered perovskite phase vanishes. The restoration of the double perovskite structure is completed at 700 °C.
- Not only the phase composition changes, but also the electronic states of the elements are mostly restored to their original state, as evidenced by X-ray absorption spectroscopy.
- The electrical conductivity is improved by the aliovalent doping of lanthanum in both air and hydrogen atmospheres. Thus, for further studies, LSFM was chosen as a more stable and better from the electrical point of view. In the following chapters, LSFM lattice would be used as a host, in which other transition metals are introduced to undergo the exsolution.

Considering aforementioned findings in this section the hypothesis 2 *"The double perovskite structure can be stabilized during redox cycling via aliovalent doping, such as La or Nb doping."* can be confirmed. To be more specific, it was lanthanum that offered the most significant improvement in terms of both stability and electrical conductivity. Thus, this specific element was used as a dopant in further studies presented in this thesis.

The aforementioned investigations were published in a scientific paper: **Ducka, A.,** Błaszczak, P., Zajac, M., Maximenko, A., Gazda, M., & Bochentyn, B. (2025). *Investigation of the phase transition to the Ruddlesden–Popper phase in La- or Nb-doped $Sr_2Fe_{1.5}Mo_{0.5}O_{6-\delta}$ double perovskites and the impact of lanthanum or niobium doping.* ***NANOSCALE***, *17*, 12371-12384. https://doi.org/10.1039/d5nr00596e

4.2.2. Exsolution of the Ni and Co nanoparticles from LSFM lattice for enhanced catalytic efficiency

The next group of materials analyzed was the Co- and Ni-doped LSFM synthesized by the same method as that used for the pure SFM or LSFM. The diffraction patterns of as-prepared and reduced at 800 °C compounds are presented in **Fig. 4.26** together with double perovskite and Ruddlesden-Popper layered perovskite references. It can be clearly seen that as-prepared compounds, regardless of the dopant type or doping level, crystallize in a double perovskite structure. Similarly to the compounds described in the previous section, a small quantity of $SrMoO_4$ impurity can be noticed. Based on the Rietveld refinement presented in **Tab. 4.7**, the concentration of this particular impurity is less than 6 wt.% (for 5-LSFMCo). Moreover, the Rietveld refinement also allowed to calculate the lattice constants of as-prepared compounds. Generally, the higher the doping level, the unit cell shrinks for both Ni and Co dopants. The systematic analysis is quite complex as many different valence states are available at the B-site. Based on previous findings [98], iron is present mainly in the Fe^{3+} state with 0.645 Å ionic radius. Both dopants can alter their oxidation state between 2+, 3+, and 4+. In general, the lower the valence state of the transition metal, the higher the ionic radii, with both Ni^{2+} (0.69 Å) and Co^{2+} (0.745 Å) being larger than Fe^{3+} [141]. Thus, if only the ionic radii of these cations were taken into account, the expansion of the cell would be expected. However, different variables should be taken into consideration. If the lower valency (2+) was present, then iron would partially transform to Fe^{4+} which is smaller (0.585 Å) than Fe^{3+}. Moreover, both 3+ dopant cations have smaller radii than

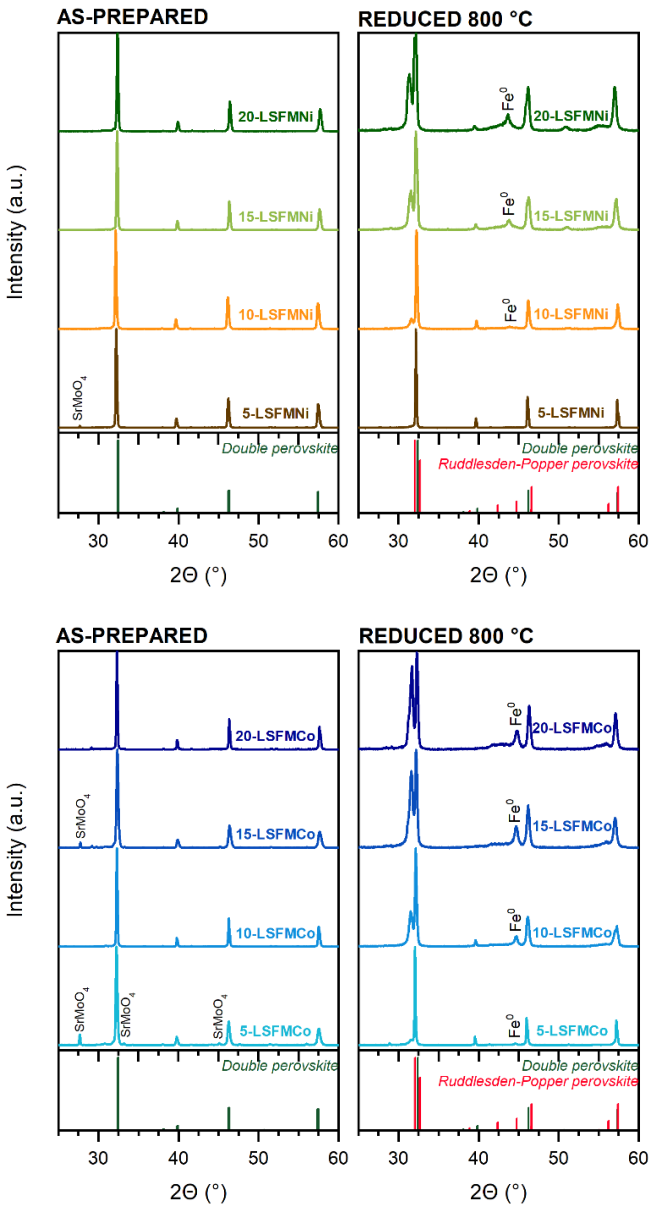


Fig. 4.26. XRD patterns of Ni- and Co-doped LSFM in as-prepared and reduced states.

Fe^{3+} (Co^{3+}: 0.61 Å and Ni^{3+}: 0.6 Å). The presence of Ni^{3+} and Co^{3+} cannot be excluded, as this is the valence state of these metals in nickelates [200] and cobaltities [184]. Combining both these effects, the systematic decrease in the unit cell size can be explained for both Ni- and Co-doping of LSFM.

After the reduction, the diffractograms start to differ significantly from as-prepared states, regardless of the doping type. The main novel feature is the clearly visible formation of an additional peak at ~31.3°, corresponding to the (015) plane of Ruddlesden-Popper layered perovskite. Unfortunately, the (022) peak of double perovskite overlaps at 32.2° with the (110) peak of the RP phase, making the differentiation more complex. Thus, the (015) plane is considered as an indicator of new phase formation. Almost all concentrations of the dopant led to the formation of a Ruddlesden-Popper phase. Only at low nickel content was the phase transition suspended. In general, the amount of layered perovskite gradually increased with the higher dopant concentration, which can be qualitatively established by the (015) height. The concentration of the Ruddlesden-Popper phase was calculated by the Rietveld refinement, and the quantitative values are presented in **Tab. 4.7**. Low addition of cobalt (5-LSFMCo) is also characterized by a low amount of newly formed phase, especially when compared to pristine LSFM. Thus, at the lowest dopant concentration, the positive impact of phase stability is observed. Unfortunately, with a larger amount of dopant, starting from 10-LSFMNi and 10-LSFMCo, the enhanced formation of the layered perovskite occurred. In addition to the presence of the RP phase, wide peak is formed at ~45°. Once again, this placement corresponds to the (0 0 10) peak visible in the reference plot. However, this peak is expected to be narrow, as well crystallized Ruddlesden-Popper structure is obtained, and all other peaks are sharp and well-defined. It is especially well visible in the 15-LSFMNi and 20-LSFMNi, where one narrow peak arises from a wider one. The wider peak is attributed to the formation of the Fe^0 phase in the *Im-3m* structure. The broadening of this particular (111) peak of iron at ~45° originates from the nanometric size of this metal, which follows the expected exsolution outcomes. Unfortunately, solely from the XRD it is impossible to determine whether the bimetallic alloy was formed, as the peak placement of the Co-Fe alloy is similar to Fe [169]. When the formation of Fe peak along the partial transition to the Ruddlesden-Popper phase occurs, the great amount of the exsolved NPs is expected, since they are already visible in XRD.

The lattice constants after the reduction were also calculated and are presented in **Tab. 4.7**. Unfortunately, unlike as in the as-prepared state, no particular trend is observed. Due to the increasing complexity of the systems, many different factors contribute to the final result. In addition to the aforementioned ionic radii changes, concentration of oxygen vacancies in both DP and RP phases is likely to increase affecting the lattice constants. Moreover, the expected exsolution will leave the iron/transition metal vacancies, leading to further structural changes.

Tab. 4.7. Lattice constants and specific phase concentrations of as-prepared and reduced LSFMs doped with cobalt or nickel.

		As-prepared		**Reduced 800 °C**			
		Double perovskite (*Fm-3m*)	**Impurity**	**Double perovskite (*Fm-3m*)**		**Ruddlesden-Popper layered perovskite (*I4/mmm*)**	
		Lattice constant a (Å)	Concentration (wt. %)	Lattice constant (Å)	Concentration (wt.%)	Lattice constants a, c (Å)	Concentration (wt. %)
Ref.	**LSFM**	7.8533	n/a	7.884	57.2	a = 3.933 c = 20.951	42.8
Co-doped	**5-LSFMCo**	7.8416	$SrMoO_4$: 6	7.866	81	a = 3.941 c = 20.386	19
	10-LSFMCo	7.8397	n/a	7.873	45.8	a = 3.933 c = 20.493	54.2
	15-LSFMCo	7.8351	$SrMoO_4$: 3.5	7.836	25.9	a = 3.926 c = 20.402	74.1
	20-LSFMCo	7.8288	n/a	7.834	21.3	a = 3.921 c = 20.477	78.7
Ni-doped	**5-LSFMNi**	7.8503	$SrMoO_4$: 1.7	7.869	100	n/a	0
	10-LSFMNi	7.8415	n/a	7.873	73.3	a = 3.922 c = 20.612	26.7
	15-LSFMNi	7.8353	n/a	7.884	49.7	a = 3.925 c = 20.677	50.3
	20-LSFMNi	7.8314	n/a	7.881	38	a = 3.925 c = 20.715	62

The microstructure of the powders after reduction was revealed by scanning electron microscopy. The structure of the Ni-doped LSFM with different doping levels is presented in **Fig. 4.27**. The behavior of Co-doped LSFM was analogous to the LSFMNi described in more detail. Firstly, the imaging revealed an evident and intense exsolution process under reductive atmospheres. The lowest number of exsolved nanoparticles is visible for the lowest doping level, namely 5-LSFMNi. In this particular sample, the exsolved nanoparticles are evenly dispersed on the grain surface, but they do not cover the area completely, as the NPs remain separated from each other. Moreover, their size distribution is even, only with some of the bigger particles in the bottom left of the picture. As the dopant concentration increases two times in 10-LSFMNi, the number of nanoparticles increases significantly. The area coverage is undoubtedly higher because the NPs are closer to each other. Although almost full coverage of the grain, the particles are still well defined with clear separation between them. Only locally can layer formation be seen, originating from the agglomeration of the exsolved metal. With increasing doping level, the exsolved nanoparticles are slightly larger for both 15- and 20-LSFMNi. However, at the same time, a higher tendency to agglomerate into layer is observed. This is clearly visible for two highest concentrations, where semi-continuous layer can be found.

Such an intense exsolution can be linked with the formation of a Ruddlesden-Popper layered perovskite. With a higher dopant concentration, not only is more RP phase formed, but also the exsolution phenomenon is more intense. Although these two appearances occur simultaneously, it is extremely difficult to determine if any of them is the trigger for the second one. If the answer is yes, then immediately new question arises: which one? Both options are possible because the exsolving nanoparticles impoverish the B-site lattice of the double perovskite, altering the A:B-sites ratio closer to the one characteristic for the Ruddlesden-Popper perovskite. In the second option, this is the phase transformation that triggers the exsolution in these compounds. In the view of solely XRD and SEM analyses, the first option seems more plausible, especially in the case of 5-LSFMNi. This particular compound did not undergo the phase transition but was still able to exsolve nanoparticles on its surface. Because of the lowest doping level and low number of the NPs exsolved, the structure remained in its original double perovskite cubic state. In this case, the deficit of B-site elements was not high enough to trigger the phase transition. As the doping level increased, the exsolution intensity was higher and more vacancies were left at the B-site leading to the formation of a more energetically favorable phase [3]. The last possibility is that the phase transition does not cause exsolution in this system, but rather enhances it. However, as mentioned before, no bold statement can be made without more advanced characterization methods. Techniques allowing in-situ observation and analysis, e.g. high-temperature XRD or more advanced environmental TEM, could give more answers about the exact nature of these phenomena and the correlation between them. Unfortunately, due to the high temperature and harsh

reducing atmospheres, reconstruction of the exact same conditions is limited or even unavailable even in advanced facilities.

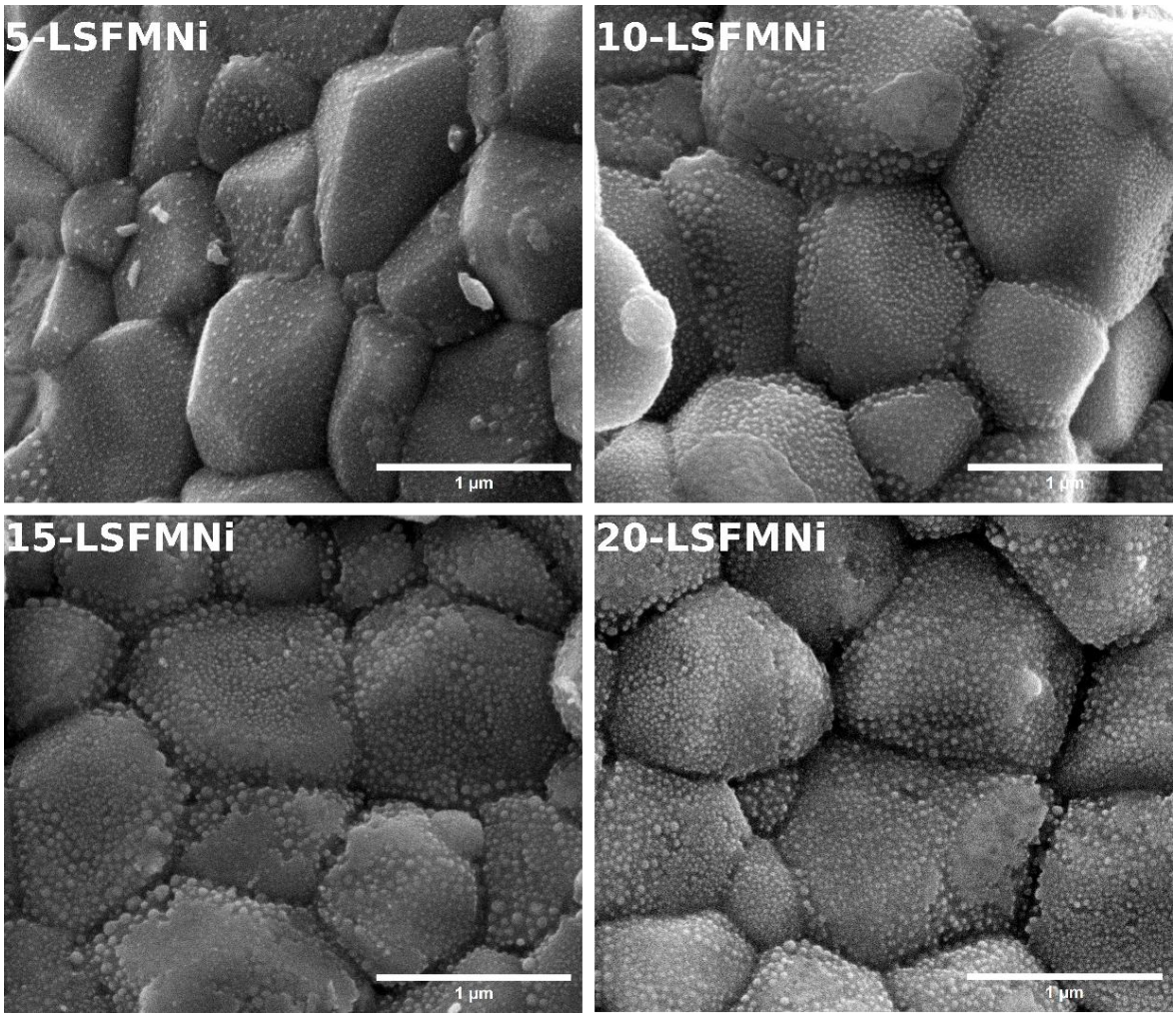


Fig. 4.27. SEM images of the reduced at 800 °C Ni-doped LSFM with varying Ni concentration.

Because SEM imaging, even coupled with EDS mapping, cannot determine the composition of the exsolved NPs, TEM imaging was utilized in collaboration with Prof. Imran Asghar from the Tampere University in Finland. The STEM images of 10-LSFMNi and 10-LSFMCo with respective elemental maps are presented in **Fig. 4.28**. The mapping of iron in both samples revealed the agglomeration of this element in round shapes along the selected grain. These areas correspond to the exsolved nanoparticles on the STEM image (the most of the grain is dark because of its thickness). Of course, the iron is also clearly visible in the grain as it is a dominant B-site element in the perovskite lattice. If we consider Ni or Co mapping, the concertation of these elements is significantly smaller, since the signal and contrast are lower. Despite the lower initial concentration of dopant in the lattice, the Ni- and Co-rich spots are clearly visible. Moreover, these spots overlap perfectly with the areas

enriched with iron. Similar observations were made in the literature on similar compounds [169,170,201–203]. This observation proves that the exsolved nanoparticles consist of bimetallic alloy. Unfortunately, because of the apparatus limitations and the domination of the signal from the lattice, the exact composition of the NPs was not established in this case.

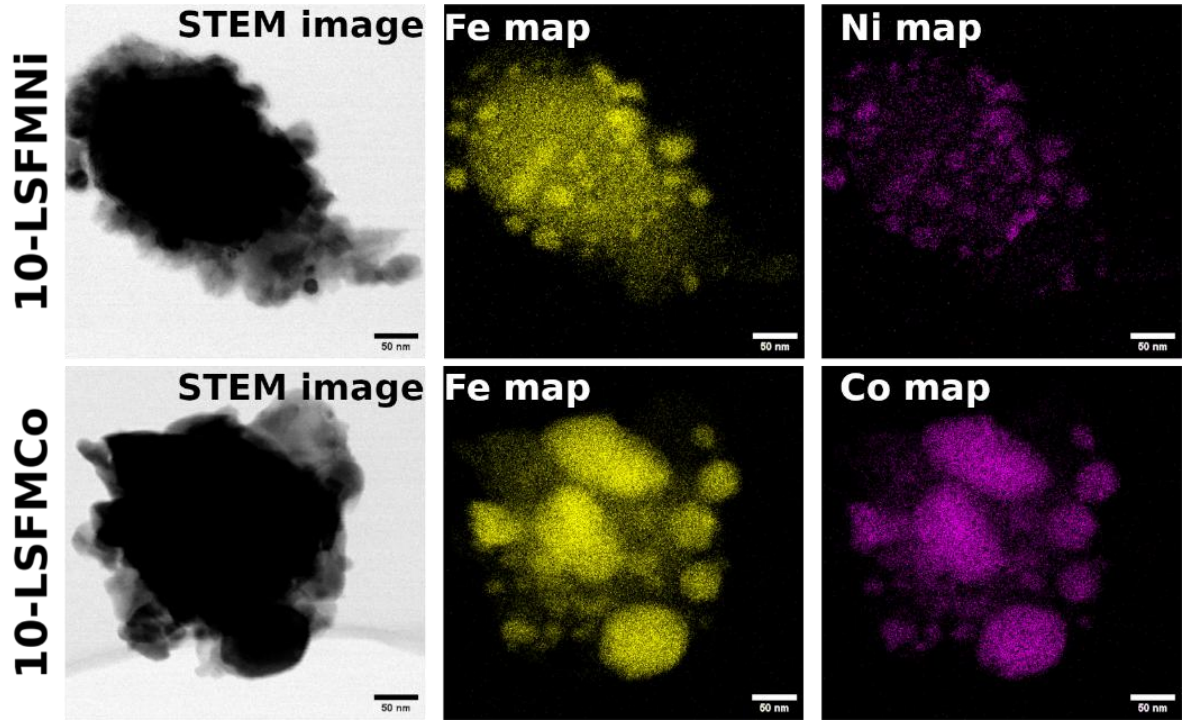
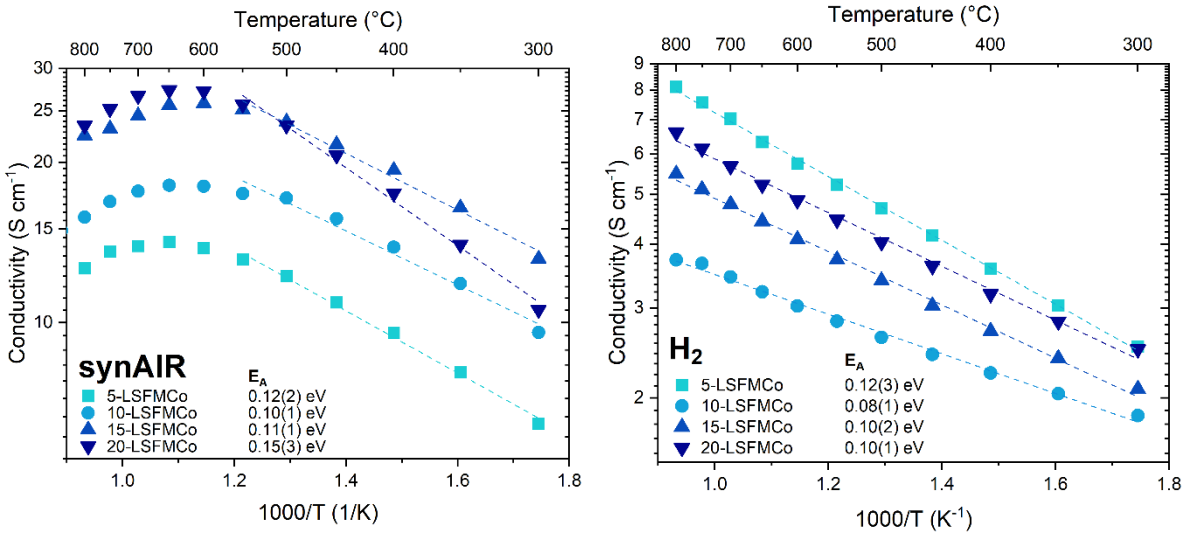


Fig. 4.28. STEM image of 10-LSFMNi and 10-LSFMCo with EDS maps of Fe and Ni or Co.

In order to determine the potential use of these materials in the Solid Oxide Cells, their electrical conductivity was measured using the DC4W method. The obtained results are presented in **Fig. 4.29** for both dopant types measured in both air and hydrogen. The characteristics for both cobalt and nickel doping are similar to those of the previous chapter regarding the increasing stability of SFM. With increasing temperature, the total conductivity increases up to 500-650 °C, at which the maximum values are obtained. With a further increase in temperature, a gradual decrease in conductivity is observed. Noteworthy, the decrease in the conductivity in the high-temperature regime is smaller for all cobalt-doped LSFM. Similarly to the electrical measurements previously described in Chapter 4.2.1, the drop in the conductivity originates from the loss of the oxygen from the perovskite lattice. As a result, it promotes the reduction of elements at the B-site, decreasing the effective concentration of charge carriers [15]. Moreover, the conduction in these compounds occurs through the Fe^{2+}/Mo^{6+}-O^{2-}-Fe^{3+}/Mo^{5+} pathways, in which the O^{2-} bridge plays a crucial role [136,170,194,197]. With the formation of the oxygen vacancies, these pathways become disrupted, leading to the drop in the conductivity at elevated temperatures. For both nickel and cobalt doping, a similar tendency can be

observed: the higher the dopant concentration, the higher the conductivity. The only two deviations from this trend can be observed: a similar conductivity of 5-LSFMNi and 10-LSFM at temperatures above 750 °C, and the highest conductivity of 15-LSFMCo at temperatures below 500 °C. In general, enhancement in the electrical conductivity can be linked with the formation of new sites available for the conduction mechanism.

After the reduction in the hydrogen atmosphere, the conduction characteristic vs. temperature differs from the behavior in air. First, the conductivity increases gradually with the temperature in the whole regime analyzed, regardless of the dopant type or its concentration. The second important difference is the lack of a clear trend between conductivity and the dopant concentration. For both Ni- and Co-doped LSFM, the samples with the lowest conductivity are 10 mol. % of dopants, namely 10-LSFMCo and 10-LSFMNi. Moreover, for these two particular compounds, the obtained conductivity is within the range of 4-5 S cm^{-1}, being rather poor but sufficient to use in SOCs. The other concentrations are characterized by a higher conductivity value, reaching the peaks of 7.9 S cm^{-1} and 15.8 S cm^{-1} at 800 °C for 5-LSFMCo and 15-LSFMNi, respectively. One of the factors that affect the electrical performance is the formation of the new phase, which strongly influences the density of the pellets and the conduction mechanism. The presence of AO planes in Ruddlesden-Popper perovskite may enhance the oxygen transport but can be unfavorable for electronic conduction. After the measurements in hydrogen, the bars were significantly more fragile and prone to breakage. Some of them even shattered right after dismounting. Another factor with influence on the conductivity is the exsolution, which leaves the B-site elements vacancies, decreasing the number of available conduction paths. Once again, unfortunately, the bold statement of the direct reason for such behavior is difficult, as it is affected by several different factors.



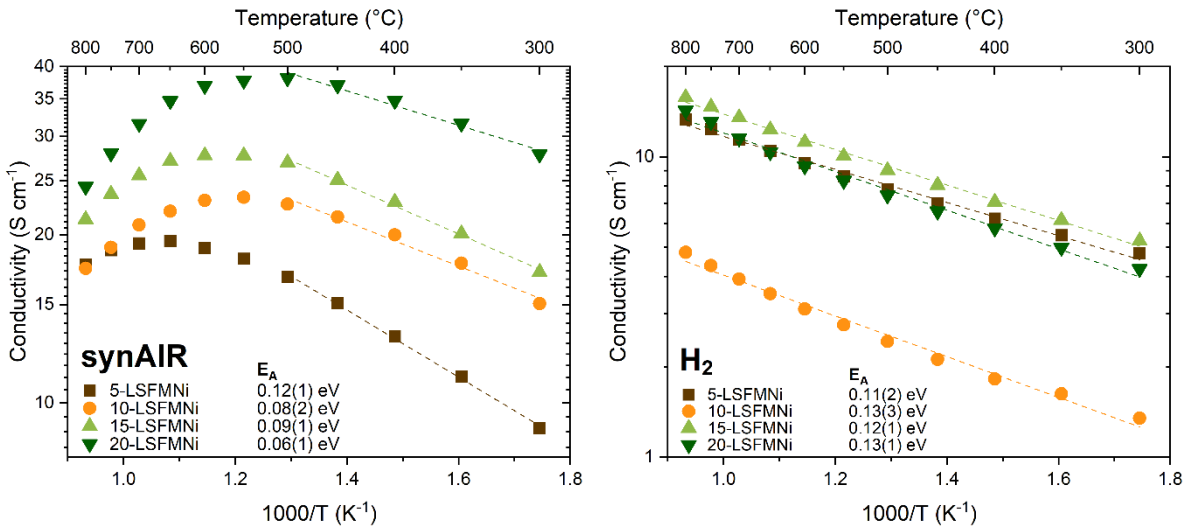


Fig. 4.29. Electrical conductivity of Ni- and Co-doped LSFM in synthetic air and hydrogen.

Although very important, electrical conductivity is not the only factor determining the good electrode material. The second one is the good catalytic performance. The Co- and Ni-doped compounds were tested for their catalytic behavior to RWGS reaction (2.23). The measured CO concentrations are presented in **Fig. 4.30**. To minimize the impact of the structure, the powders were milled and their resulting SSA was comparable ~5 m^2 g^{-1}. Additionally, the composition of the pristine perovskite already consists of elements that are important for the formation of catalytic systems for RWGS, such as Fe and Mo [204–206].

The nickel doped series shows superiority over cobalt doping. At high temperatures, it reaches more than 95% of allowed thermodynamically allowed equilibrium concentration. According to Chen *et al.* [207] such an outstanding performance of Ni-based catalysts originates from the bridging between Ni and O, allowing for stronger CO_2 adsorption to the surface. Moreover, in their studies, they have shown that high selectivity to CO formation is induced by fast carbon monoxide desorption from the active sites. In this study, the selectivity for CO reached 100 %, since no methane or other hydrocarbons were produced. According to Sengupta *et al*. [208] a better CO selectivity originates from the easier reduction of Ni or Co compared to the iron, therefore the catalytic performance of these two dopants is expected to be higher. Another benefit can be correlated with the formation of Fe-Ni nanoparticles, as the study by Wu *et al.* [209] shows enhanced sintering resistance of such alloys. In the sintering resistance, the exsolution process is also beneficial, as the NPs obtained by this method have lower tendency to migrate and agglomerate. Moreover, in catalytical tests the formation of Ruddlesden-Popper layered perovskite is beneficial, as it facilitates fast oxygen exchange [210].

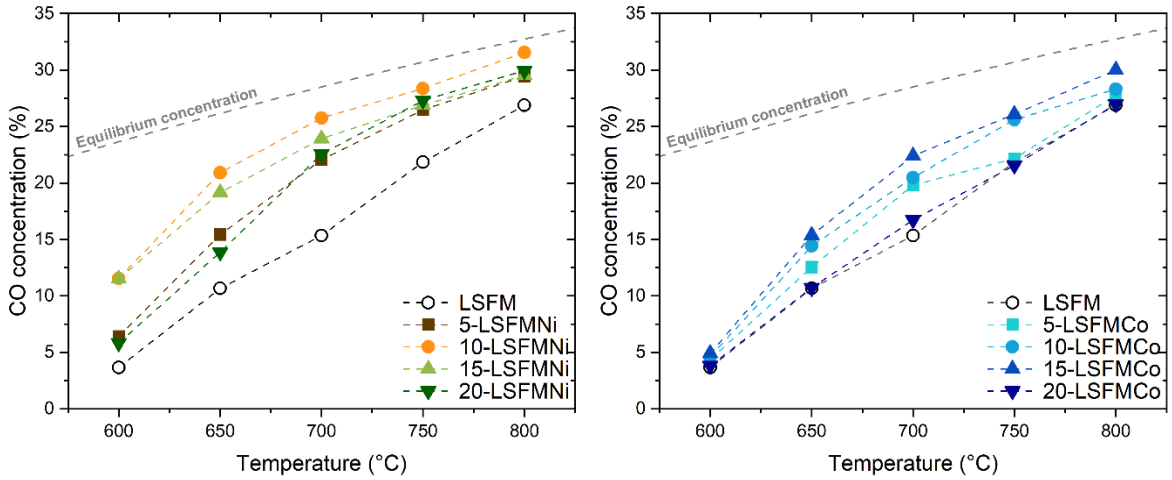


Fig. 4.30. Concentration of CO in the outlet gas stream in the catalytic tests for the RWGS reaction. The lines are guides for eyes only.

Conclusions of this section:

- Successful doping of LSFM was obtained without observation of a significant amount of secondary phases. Only traces of $SrMoO_4$ were found, which is typical of these compounds. With increasing dopant concentration for both Co and Ni, the cell shrank due to incorporation of the higher valence state of Co^{x+} and Ni^{x+} and/or partially increasing the iron state to Fe^{4+}.
- The reduction leads to the formation of a new phase: Ruddlesden-Popper layered perovskite. Only 5-LSFMNi remained stable in the double-perovskite structure. Other compounds partially transformed into RP phase. The higher concentration of the dopant yielded a higher share of layered perovskite. In addition to this newly formed phase, the wide peak of iron (or Fe-Co, Fe-Ni alloys) is visible, indicating a large amount of exsolved nanoparticles.
- In fact, SEM imaging revealed an enormous number of exsolved nanoparticles. For a higher concentration of the dopant (10-LSFMNi and more), the NPs cover almost the entire area of the grain surface. For 15- and 20-LSFMNi the coverage is so high, that a semi-continuous layer is formed. Subsequent TEM imaging and EDS mapping revealed that the exsolved nanoparticles are forming the bimetallic alloy as the spots rich in Fe and Ni/Co are overlapping.
- It cannot be boldly stated that the strain induced during the phase transition promotes the exsolution process. On the basis of the XRD and SEM analyses combined, it is more likely that the intense exsolution due to higher dopant concentration triggers the phase decomposition by the formation of the B-site deficit.

- Electrical measurements in air revealed the enhancement of the conductivity with the increase of dopant concentration for both Ni- and Co-doped LSFM. Unfortunately, no such tendency was observed in hydrogen, associated with the formation of Ruddlesden-Popper phase and significant change in the materials' porosity. Nevertheless, the obtained values are sufficient for use as an alternative SOC electrode.
- The catalytic efficiency was boosted after the nickel or cobalt was introduced into the lattice. The enhancement was superior in Ni-doped due to the bridging between Ni and O ions, leading to the stronger CO_2 adsorption to the surface. Moreover, easier reduction of Ni or Co would benefit the CO selectivity.
- Taking into the account the described results, Ni- and Co-doped LSFM arises as interesting materials with extraordinary catalytic performance owing to the intense exsolution during reduction. At the same time, serious challenges arise as the phase decomposition could lead to the delamination or cracks during reduction in SOFC. In order to still benefit from the exsolution but to minimize such structural problems, composites (e.g. with LSGM) can be prepared. In this manner, the other compound will work as a scaffold providing the mechanical stability. Another approach in application of these material is the use as a cathode in SOFC, where high electrical conductivity in air would be beneficial.

In the light of aforementioned conclusions, the hypothesis 3 *"Doping of double perovskite hosts with transition metals (Ni, Co, or Cu) will promote iron exsolution from Fe-rich B-sites. Moreover, the strain introduced through phase transition would further enhance the NPs formation."* can be partially confirmed. The doping with Ni or Co led to the extremely intense exsolution. However, the second part of this hypothesis cannot be boldly confirmed or rejected. Based on the results presented in this section, it is more likely that the exsolution promotes the phase transition, not the other way around.

4.2.3. Stabilization of Cu-doped LSFM decorated with bimetallic nanoparticles for efficient RWGS catalyst

Another dopant that was introduced to the B-site lattice of the LSFM host was copper. Because of the behavior from the previously discussed Ni and Co, the results for Cu-doped LSFM are presented separately. The results of the work are currently under consideration in high-impact journal as **Ducka** *et al. "Stabilization of Cu-doped $La_{0.3}Sr_{1.7}Fe_{1.5}Mo_{0.5}O_{6-\delta}$ decorated with bimetallic nanoparticles for the improvement of electrochemical syngas production".*

The XRD patterns shown in **Fig. 4.31** present the phase composition of the as-prepared powders, as well as samples reduced at 750 or 800 °C. After synthesis, the main phase corresponds to a double perovskite structure with *Fm-3m* symmetry (DP), which remains unchanged regardless of the B-site substitution or doping level. In addition to the main phase, a small amount of residual $SrMoO_4$ impurity is present, which is typical for SFM-based compounds and usually disappears after reduction [48,77,85,170,211,212].

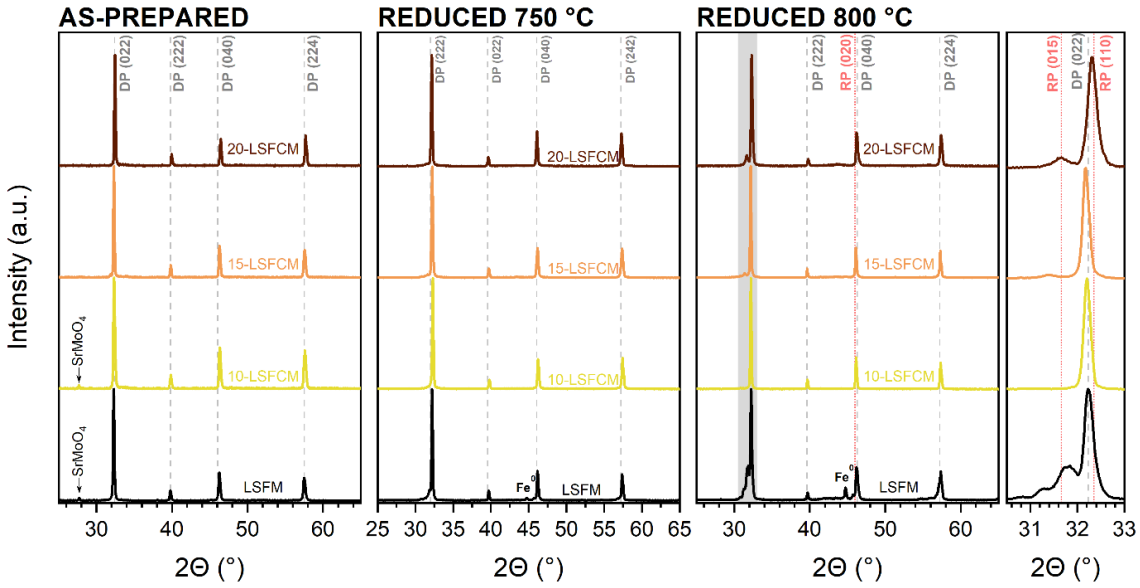


Fig. 4.31. XRD patterns of Cu-doped LSFM in as-prepared and reduced (at 750 °C and 800 °C) states.

The effect of Cu doping on the unit cell size was analyzed using the Rietveld refinement method. The calculated lattice parameters of the double perovskite are listed in **Tab. 4.8**. In general, doping leads to a reduction in unit cell size compared to pure LSFM. This behavior is attributed to the increased formation of higher oxidation states of Fe or Mo ions, caused by the incorporation of lower-valence Cu ions into the lattice. In both cases, higher oxidation states correspond to smaller ionic radii: 0.585 Å (Fe^{4+}) < 0.645 Å (Fe^{3+}) < 0.78 Å (Fe^{2+}) and 0.59 Å (Mo^{6+}) < 0.61 Å (Mo^{5+}) [141]. The largest decrease in lattice parameter is observed for 10-LSFCM relative to the reference LSFM. It is worth noting that

with a further increase in Cu content, the unit cell size remains nearly unchanged. At higher doping levels, additional shrinkage is balanced by several factors: (i) incorporation of a greater amount of larger Cu^{2+} ions, or (ii) formation of oxygen vacancies [10]. The increased formation of oxygen vacancies due to Cu doping has previously been reported by Tan *et al.* [213] and Tian *et al.* [192]. Additionally, Cu^{2+} ions in octahedral coordination, due to their electronic configuration, can induce Jahn–Teller distortion [54,214] . This effect has been described for double perovskites with a high Cu content at the B-site (e.g., $Ba_2CuWO_{6-\delta}$, $La_2CuSnO_{6-\delta}$) [54] , suggesting that similar local distortions may also occur here and influence the lattice parameters.

Tab. 4.8. The unit cell parameters for different Cu-doped LSFM. For reduced compounds, the amount of foreign phase is calculated.

	LSFM	**10-LSFCM**	**15-LSFCM**	**20-LSFCM**
As-prepared	7.852(1)	7.848(1)	7.847(2)	7.845(1)
	DP 100 %	DP 100 %	DP 100 %	DP 100 %
Reduced 700 °C	7.878(3)	7.872(1)	7.880(2)	7.884(2)
	DP 100 %	DP 100 %	DP 100 %	DP 100 %
Reduced 750 °C	7.871(2)	7.877(1)	7.878(1)	7.882(2)
	DP 89.3 % RP 10.7%	DP 100 %	DP 100 %	DP 100 %
Reduced 800 °C	7.875(4)	7.879(2)	7.881(3)	7.893(2)
	DP 47.4 % RP 52.6 %	DP 100 %	DP 87.2% RP 12.8%	DP 83.4 % RP 16.6 %

The XRD patterns of the samples reduced at 750 °C (**Fig. 4.31**) confirm that all Cu-doped materials retained the cubic double perovskite structure. No additional phases were detected and the $SrMoO_4$ impurity disappeared after reduction, as expected. On the contrary, the reference LSFM began to form a secondary phase identified as the Ruddlesden-Popper layered perovskite $Sr_3FeMoO_{7-\delta}$ (RP) that is evidenced by a shoulder at the main DP (022) peak. The RP phase crystallizes in the *I4/mmm* space group, and its formation under reducing conditions is widely reported [11,16,97,215]. Although this phase transition can promote nanoparticle formation on the surface via exsolution, it is unfavorable from a technological perspective. The abrupt change in unit cell dimensions introduces strain into the material, which may lead to cracking of the ceramic layers. A similar behavior was observed after

reduction at 750 °C. Importantly, this transition was completely suppressed in the Cu-doped samples, unlike in the reference LSFM where the RP phase continued to develop. One possible explanation for the formation of the Ruddlesden-Popper structure is the rearrangement to reduce elastic energy, leading to surface reconstruction [3], while another factor is the loss of structural oxygen. In this case, the stabilization of the structure is attributed to changes in the ionic radii of Cu, Fe, and Mo associated with their valence states. As mentioned earlier, lower oxidation states correspond to larger ionic radii [141]. The most significant change occurs for Fe, where the radius increases from 0.645 Å (Fe^{3+}) to 0.78 Å (Fe^{2+}). Additionally, Cu doping may promote the formation of some Fe^{4+} cations, which have a smaller radius (0.585 Å) than Fe^{3+}, resulting in considerable lattice expansion during reduction. Overall, changes in the oxidation state of iron during reduction lead to variations in ionic radii, generating strain within the perovskite lattice and favoring the formation of a more stable phase [3]. On the contrary, the radius changes between Cu^{2+} (0.73 Å) and Cu^{+} (0.77 Å) are relatively small and do not significantly contribute to the strain under hydrogen conditions. Although the initial incorporation of Cu introduces some strain, it is compensated for Fe/Mo oxidation and the formation of oxygen vacancies.

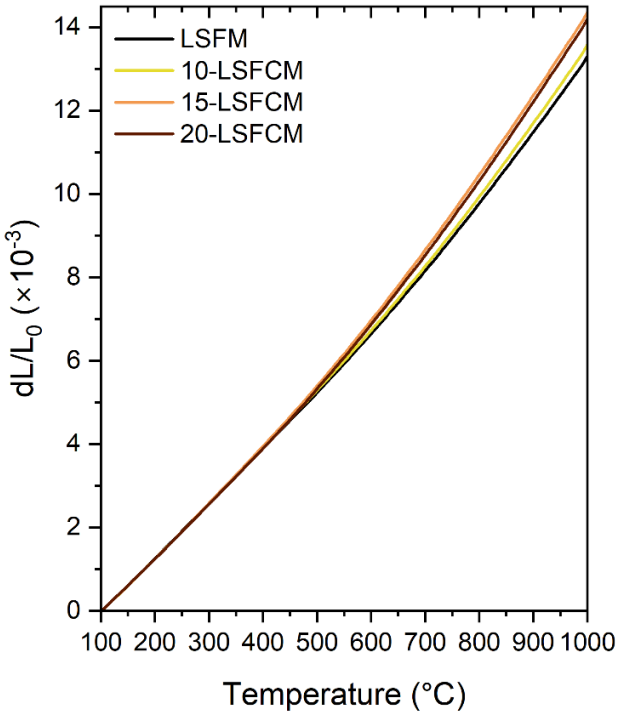


Fig. 4.32. Thermal expansion of LSFCM bars in air.

The thermal expansion coefficient was measured in rectangular bars in oxidized form. Thermal expansion curves are presented in **Fig. 4.32**. It is clearly visible that two temperature regimes can be distinguished: low temperature below 500 °C and the high one above this threshold. The change in slope is correlated with the loss of structural oxygen, leading to the creation of an oxygen vacation and the thermoreduction of Fe, Mo, or Cu cations. This requires to calculate two coefficients for each composition, which are presented in **Tab. 4.9**. The obtained values are ~$13 \cdot 10^{-6}$ K^{-1} and $17 \cdot 10^{-6}$ K^{-1} for low and high *T*, respectively. Unfortunately, such TEC values are much higher than those reported in the literature for the LSGM electrolyte, being $11.4 \cdot 10^{-6}$ K^{-1} [216]. This difference, especially at higher temperatures, presents serious challenges and threats. One challenge is associated with the layers preparation, which may be as a result characterized by weaker adhesion to the electrolyte. Moreover, the TEC mismatch is more

likely to lead to cracking and delamination during the work operation of the fuel cell. Thus, modifications must be made to lower the LSFCMs TEC, e.g. by preparation of the composites.

Tab. 4.9. Calculated thermal expansion coefficient for reference and Cu-doped double perovskites.

	Thermal expansion coefficient (TEC)	
	Low temperature region (<500 °C)	*High temperature region (>500° C)*
LSFM	(13.13±0.02) · 10^{-6} K^{-1}	(16.09±0.06) · 10^{-6} K^{-1}
10-LSFCM	(13.22±0.03) · 10^{-6} K^{-1}	(16.55±0.07) · 10^{-6} K^{-1}
15-LSFCM	(13.39±0.04) · 10^{-6} K^{-1}	(17.95±0.07) · 10^{-6} K^{-1}
20-LSFCM	(13.19±0.07) · 10^{-6} K^{-1}	(17.79±0.03) · 10^{-6} K^{-1}

The microstructure of the reduced samples was examined using SEM to verify the exsolution process. Images of different compounds reduced at different temperatures are compiled in **Fig. 4.33.** It is evident that nanoparticle exsolution begins already at 700 °C, regardless of Cu content. However, at this temperature, the effect is relatively weak in 10- and 15-LSFCM samples. In 10-LSFCM, exsolution is observed only in specific regions, where nanoparticles form at preferred crystallographic orientations of the perovskite host, similar to the Ni exsolution at (100) sites in $SrTiO_{3-\delta}$ reported by Gao *et al.* [74]. At higher Cu levels, elongated structures appear alongside small, rounded nanoparticles. When the reduction temperature increases to 750 °C, a larger number of nanoparticles is observed in all samples. In particular, 15-LSFCM shows the formation of larger agglomerates located in hollow regions between grains. The largest structures reach approximately 0.9 μm and are surrounded by nanoparticles with an average diameter of approximately 150 nm, which are significantly larger than those formed on flat grain surfaces. This suggests that nanoparticles tend to aggregate strongly in surface crevices as the temperature increases. Despite this, the nanoparticles remain generally well distributed with good dispersion. However, at higher concentrations of dopants (20-LSFCM), flakey structures appear aside from round NPs, visible mostly at grain boundaries. With a further increase in temperature, more nanoparticles form, and their average size also grows. In both 15- and 20-LSFCM samples, the development of a surface layer is observed. The formation of semi-continuous and continuous layers is driven by intense exsolution combined with partial melting of Cu-containing nanoparticles, which have relatively low melting points and exhibit fast ionic diffusion.

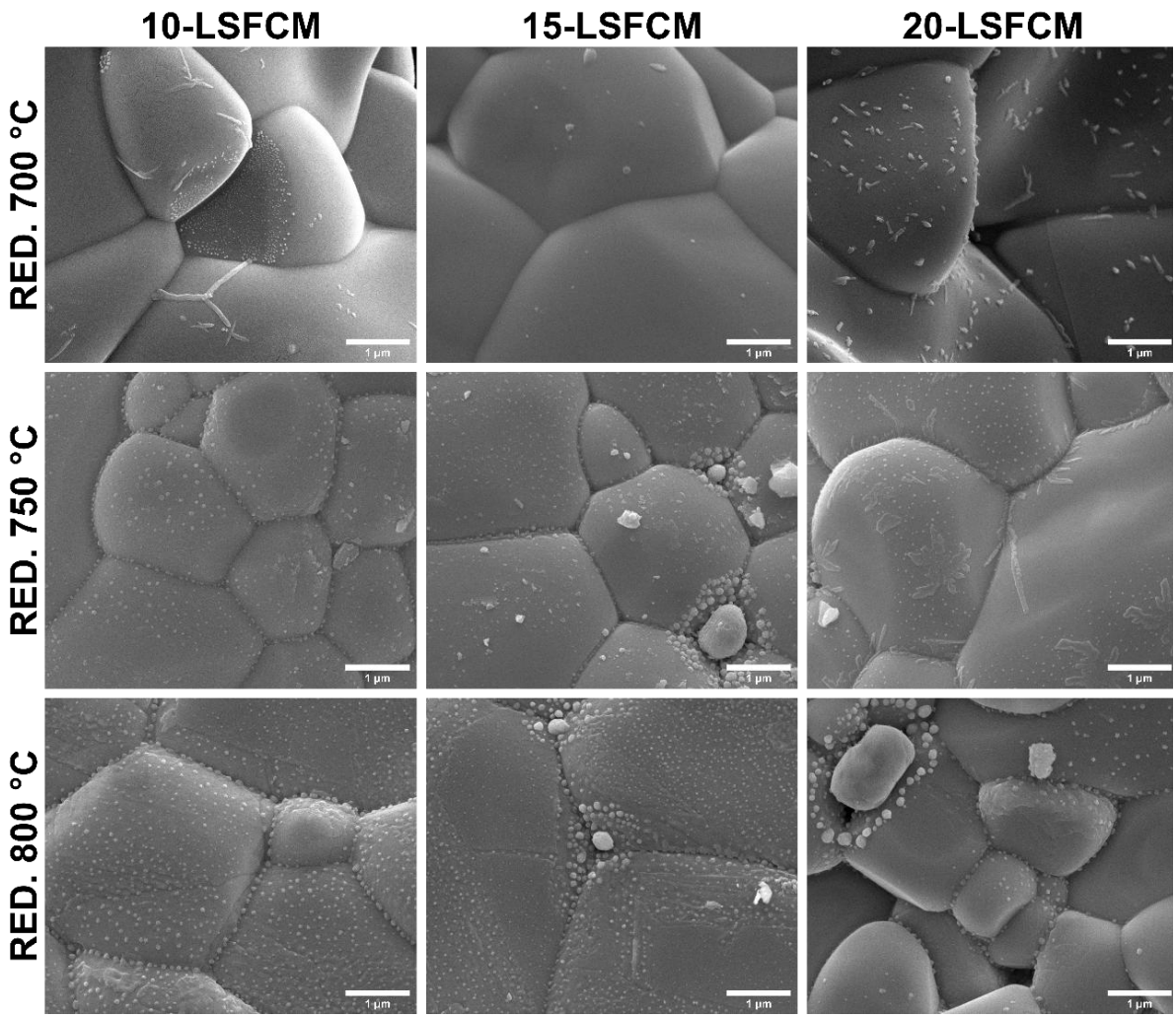


Fig. 4.33. SEM images of the Cu-doped LSFM after reduction at various temperatures.

Transmission electron microscopy combined with EDS mapping was used to examine the exsolved nanoparticles in more detail. **Fig. 4.34** shows the elemental maps for 15-LSFCM reduced at 750 °C. The lanthanum dopant at the A-site is uniformly distributed within the Sr sublattice, with no visible agglomeration, similar to the distribution observed for molybdenum. However, the structure of the exsolved nanoparticles is not uniform, as revealed by HRTEM images. Nanoparticles with cores surrounded by thin shells are observed throughout the reduced samples. Elemental mapping of Fe and Cu shows that Fe-rich regions coincide with the nanoparticle cores, while an increased Cu concentration corresponds to the shell regions. Copper mapping revealed more of sickle-like shapes surrounding the Fe core, indicating formation of a discontinuous outer layer or cracking of the shells. The aforementioned observations suggest the formation of a complex Fe-Cu core-shell-like structure during reduction through a bimodal exsolution process.

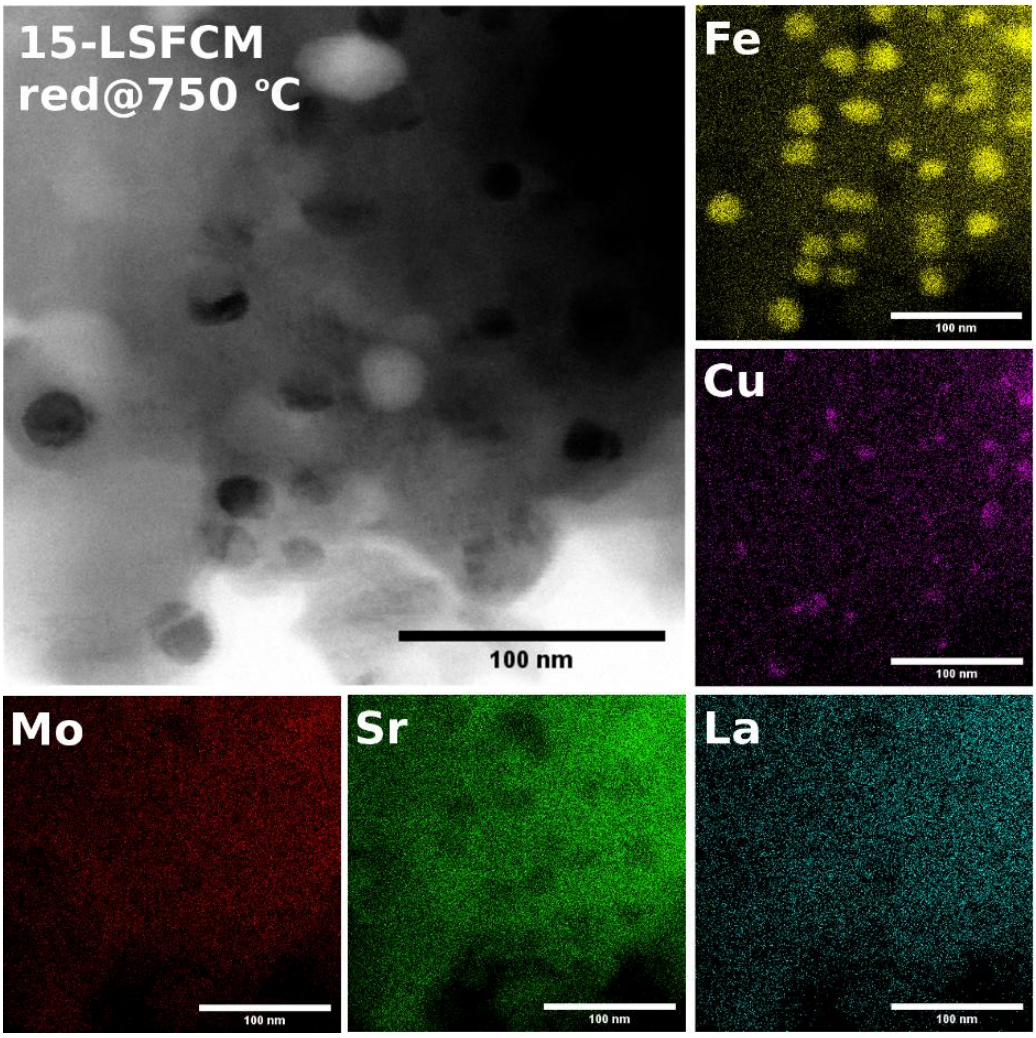


Fig. 4.34. STEM image of 15-LSFCM reduced at 750 °C with STEM-EDS elemental maps.

The nature of these Fe-Cu quasi-core-shell structures suggests a complex formation mechanism. The proposed formation mechanism, illustrated in **Fig. 4.35**, can be divided into several steps. First, the more easily reducible Cu cations exsolve onto the perovskite surface. As the temperature increases, these nanoparticles grow until conditions allow iron exsolution. Because previously exsolved Cu sites act as favorable nucleation points, iron exsolves at the same locations. Smaller iron nanoparticles initially form beneath the surface and then grow with increasing temperature, leading to the development of Fe-Cu core-shell structures. At excessively high reduction temperatures, copper from the shell may partially evaporate, leaving only a thin outer layer. Moreover, the remaining layer can then crack revealing the iron core. In some cases, iron nanoparticles are only partially covered with copper, either due to complete copper evaporation or because iron exsolves at more locations, given its higher concentration at the B-site compared to Cu. Importantly, the nanoparticles remain well anchored to the surface, which is a key advantage of the exsolution process. Further and more detailed imaging

is planned to reveal the exact composition of the NPs. Moreover, another benefit from formation of such structures is their non-continuous outer copper layer. As the cracking exposes the Fe core, both active metals are simultaneously exposed to reactant gases, which can boost the catalytic efficiency.

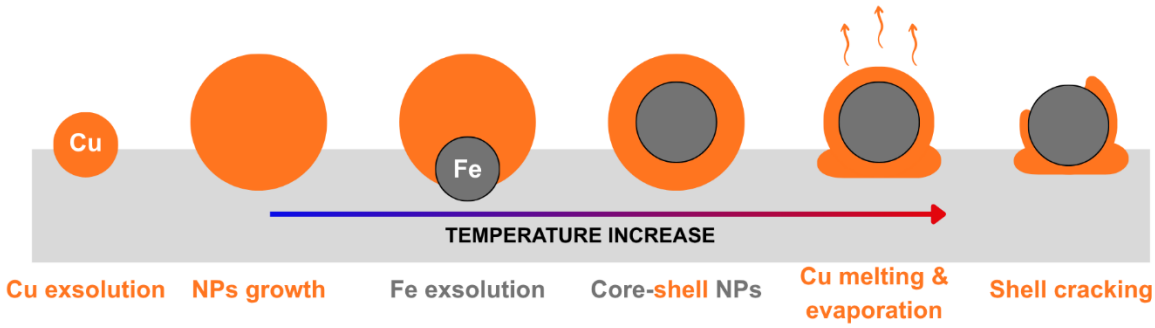


Fig. 4.35. Proposed mechanism of the formation of core-shell nanoparticles in LSFCM compounds.

The reducibility of the powders was evaluated using the TPR technique. The reduction profiles of the pristine LSFM and Cu-doped samples are shown in **Fig. 4.36** on the left. In all cases, two distinct regions were identified in the profiles, labeled α and β. Depending on the composition of the double perovskite, the first group of peaks is assigned to the complex surface reduction of copper and/or iron. Compared to pure LSFM, the α peaks of Cu-doped samples gradually shift to lower temperatures with increasing dopant content. At the same time, the overall peak intensity increases, indicating enhanced reducibility of LSFCM materials because of the higher amount of easily reducible copper cations. Metallic copper clusters promote the reduction of Fe species through a spillover mechanism [217]. The copper reduction peak is not clearly separated and overlaps with the Fe^{3+} to Fe^{2+} reduction, which begins at about 350 °C. The lower onset temperature of the main peak also correlates with the increasing copper content. A shoulder observed in the α region around 500 °C, absent in pure LSFM, corresponds to a second stage of iron reduction and is typically associated with the formation of mixed FeO-Fe species [218]. This process ultimately leads to the formation of embedded core–shell nanoparticles, as illustrated in **Fig. 4.35**. At higher temperatures, the reduction continues with the release of lattice oxygen and a further reduction of iron species. The bulk reduction continues until the β region appears, where the remaining FeO is reduced to metallic Fe. This effect is particularly pronounced in highly doped samples, indicating that Cu incorporation increases the overall degree of reduction and promotes the formation of a larger fraction of exsolved nanoparticles. In practice, SEM observations show that Cu doping affects mainly the size rather than the number of nanoparticles. Nevertheless, the shift of FeO-Fe cluster reduction to lower temperatures confirms the positive effect of Cu on iron reduction kinetics. This enhancement can be explained by two mechanisms: (i) hydrogen spillover via Cu^0 particles, and/or (ii) higher hydrogen diffusivity in copper and Fe-Cu alloys [219].

Temperature-programmed oxidation (TPO) was performed on previously reduced samples to evaluate their ability to reversibly bind oxygen at the surface and within the lattice. The oxidation profiles, shown in **Fig. 4.36** (right), were also divided into α and β regions. The reference LSFM sample exhibits a strong oxidation peak at relatively low temperature compared to the other samples. This peak is not solely due to the oxidation of Fe nanoparticles on the surface, as our previous work [98] showed that LSFM does not strongly tend to exsolve small nanoparticles. Instead, this effect is related to the transition between the surface Ruddlesden-Popper phase and the double perovskite structure, which requires oxygen uptake by the lattice. Re-oxidation of Fe nanoparticles appears as a shoulder on the main peak and as a small signal in the β region. On the contrary, all LSFCM samples display similar TPO profiles in the α region, corresponding to surface oxidation of nanoparticles, regardless of Cu content. Meanwhile, the intensity of the peaks in the β region increases with the amount of iron exsolved from the structure. Oxidation is largely complete at around 550 °C, confirming the reversible nature of the exsolution process in these ceramic materials.

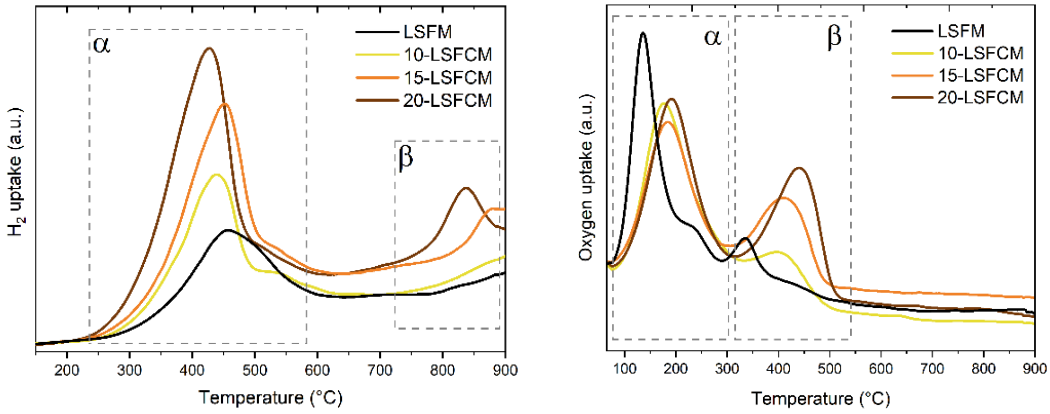


Fig. 4.36. H_2-TPR (left) and O_2-TPO (right) profiles of Cu-doped LSFM.

The Fe K-edge was measured for each composition in both the as-prepared (oxidized) and reduced states, as shown in **Fig. 4.37A** and Fig. **4.37B**, respectively. The edge shape is characteristic of Fe^{3+} in octahedral coordination, as expected for a double perovskite structure [80,98]. However, slight distortions of the octahedral environment are indicated by the presence of pre-edge features, which arise from 3d-4p orbital hybridization. Without this hybridization, only weak quadrupole 1s-3d transitions would occur, but their intensity would be very low. Structural distortions lead to mixing between the Fe 3d and O 2p orbitals, which enhances the 1s to 3d transition and makes the pre-edge feature more pronounced [183–185,220]. Although no major changes are observed in the XANES region of the as-prepared samples upon doping, differences appear in the intensity of the pre-edge feature (see inset in **Fig. 4.37A**). In general, increasing Cu content leads to higher pre-edge intensity, indicating a greater distortion of the FeO_6 octahedra [184]. Such distortions can improve both

electronic and ionic conductivity in SFM-based materials by facilitating charge carrier mobility [10,221–224]. However, excessive distortion may negatively affect electrical conductivity [10]. At the same time, catalytic activity is expected to benefit from structural distortion, as reported for methane oxidation [223] and hydrogen oxidation [10].

On the contrary, the Fe K-edge spectra of the reduced samples show notable differences, even though the overall edge shape remains similar. Key changes are observed in the white line intensity and pre-edge features. The white line, associated with the dipole-allowed 1s to 4p transition, depends on the number of unoccupied p-states. A decrease in its intensity indicates a higher contribution of metallic character due to more delocalized electrons [183]. On the basis of this, a higher Cu content corresponds to a greater amount of metallic iron in the material. This agrees with the TPR results, where the highest hydrogen uptake was observed for 20-LSFCM. At the same time, the increasing intensity of the pre-edge features suggests lower symmetry and stronger distortions, likely caused by oxygen loss from the lattice during the formation of Fe-Cu nanoparticles on the surface.

Cu K-edge spectra for samples reduced at 750 °C are shown in **Fig. 4.37C**, together with reference spectra for metallic Cu and CuO. For all Cu-doped samples, the spectra closely resemble that of metallic copper, including both the pre-edge feature and overall edge shape. Combined with SEM and TEM observations, this confirms that the nanoparticles formed on the perovskite surface consist of metallic copper. Therefore, the addition of Cu not only enhances the reducibility of iron but also promotes the formation of metallic copper.

In addition to XANES, a Fourier transform analysis of EXAFS was carried out. The results for the as-prepared samples and those reduced at 750 °C are shown in **Figs. 4.38A** and **4.38B**, respectively. Similarly to the XANES region, the FT-EXAFS profiles of the as-prepared samples are comparable across different Cu contents. Three main peaks can be identified, corresponding to Fe-O, Fe-Sr, and Fe-TM (transition metal) scattering paths, which agree with the expected bond distances in the double perovskite structure. The intensity of FT-EXAFS peaks depends on the coordination number around Fe and the degree of structural disorder. In general, greater disorder leads to lower peak intensity. Based on this, Cu incorporation increases distortion and disorder around Fe centers, which is consistent with the XANES pre-edge analysis. This effect may result from the presence of aliovalent Cu ions near Fe or, more likely, from changes in oxygen non-stoichiometry. A slight shift in the Fe-O scattering path is also observed with Cu doping, in agreement with Rietveld refinement results showing a decrease in unit cell size. As the lattice contracts, the bond lengths become shorter. Additionally, changes in the Fe-O distance reflect distortion of the FeO_6 octahedra.

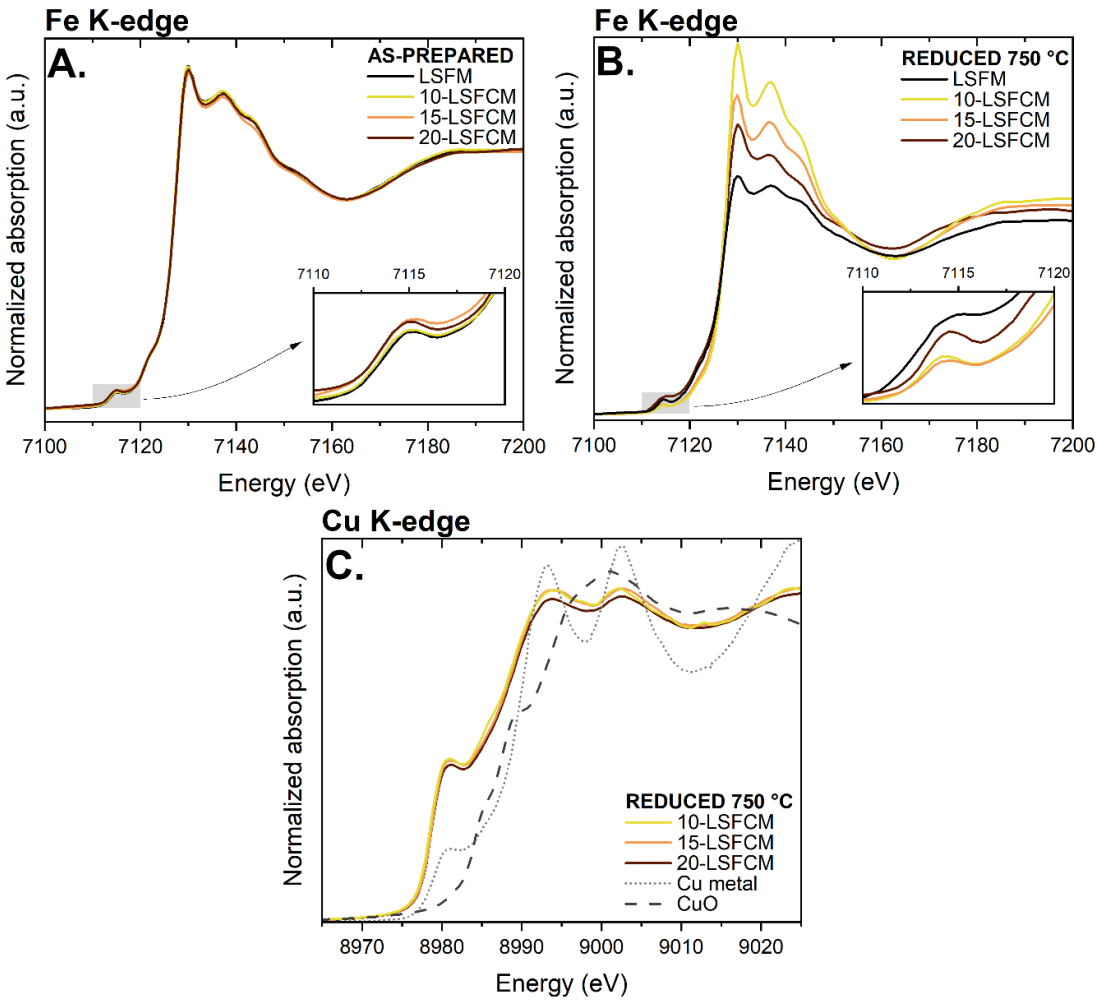


Fig. 4.37. Normalized XANES of the K-edges: Fe K-edge in as-prepared (A.), reduced compounds (B.), Cu K-edge in reduced perovskites (C.)

After reduction at 750 °C, the FT-EXAFS spectra show clearer differences between samples. The Fe–O scattering path becomes longer, particularly for pure LSFM and 20-LSFCM, while the change is less pronounced for 10-LSFCM and 15-LSFCM. This behavior matches the XRD results, where a higher Cu content led to expansion of the unit cell after reduction. These changes are associated with the formation of oxygen vacancies and possible variations in Fe and Mo oxidation states, which affect bond lengths. It is also possible that a small amount of the Ruddlesden-Popper phase formed already at 750 °C in samples with high Cu content, although it remained below the detection limit of XRD and was therefore not visible in diffraction patterns of 20-LSFCM. Further evidence of the onset of this phase transition is provided by changes in the Fe-Sr scattering path. The values for 10-LSFCM and 15-LSFCM are similar, while 20-LSFCM shows a noticeable shift toward shorter distances, resembling the behavior of reference LSFM, which clearly transforms into the RP phase according to XRD. Thus, FT-EXAFS analysis indicates that even small amounts of the Ruddlesden-Popper phase

may form during reduction, affecting the electronic structure despite being undetectable by less sensitive techniques. As a result, even minor fractions of this secondary phase can influence material properties, such as electrical conductivity.

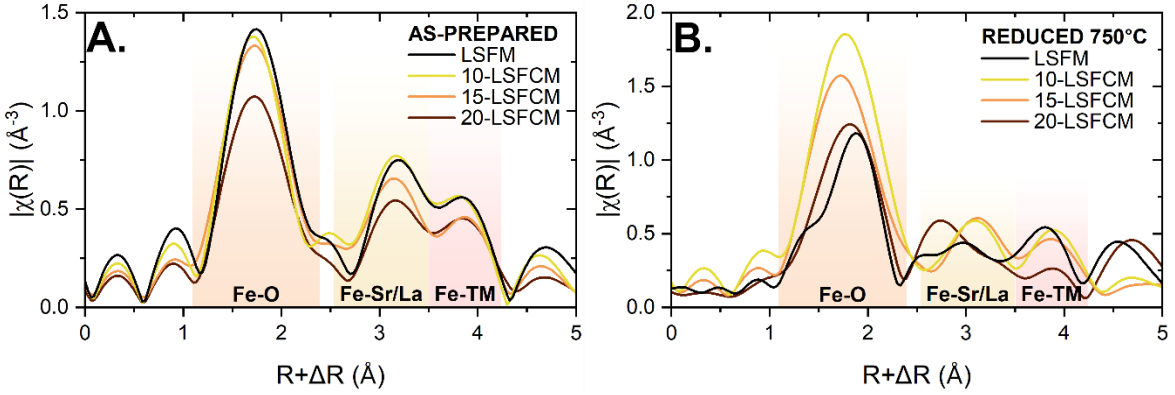


Fig. 4.38. Fourier-Transformed EXAFS (corrected for phase shift) of the Fe K-edges: as-prepared (A.) and reduced (B.) state. TM: Fe, Cu, Mo

The electrical conductivity of the samples was measured in both synthetic air and hydrogen. Measurements in pure H_2 were performed after pre-reduction at 750 °C. The temperature dependence of the conductivity is shown in **Fig. 4.39**. Under $pO_2 \approx 0.21$, all samples exhibit similar behavior. Conductivity gradually increases with temperature up to a maximum value for each composition. This trend is commonly reported [136,192,195,196] and is related to the thermally activated formation of oxygen vacancies in doped SFM. As a result, the valence state of transition metal cations partially decreases, accompanied by an increase in the oxygen vacancy concentration [225]. At higher temperatures, the loss of lattice oxygen affects the conduction mechanism, which proceeds via double exchange between the Fe 3d and O 2p orbitals, as well as Mo 3d and O 2p orbitals [136,196]. Consequently, further formation of oxygen vacancies leads to a decrease in conductivity at elevated temperatures [12].

The temperature at which maximum conductivity occurs differs between samples. For undoped LSFM and 10-LSFCM, it is around 650 °C, while for higher Cu content it shifts to about 550 °C. The maximum conductivities are 20.2 S cm^{-1}, 14.4 S cm^{-1}, 21.7 S cm^{-1}, and 23.4 S cm^{-1} for LSFM, 10-LSFCM, 15-LSFCM, and 20-LSFCM, respectively. In general, increasing Cu content (except for 10-LSFCM) leads to higher conductivity, with the highest value observed for 20-LSFCM. Above 750 °C, all samples except 10-LSFCM show a similar behavior. The improvement in conductivity is attributed to additional hopping sites created by Cu 3d and O 2p orbitals that participate in double exchange [192,213]. At the same time, greater lattice distortion in 15- and 20-LSFCM enhances conductivity by shortening Fe-O bonds [222]. However, several competing factors influence conductivity: (i) reduction of Fe-O-Fe conduction pathways due to oxygen vacancy formation [12], (ii)

increased lattice distortion, which can enhance transport [10,136,221–224], (iii) introduction of new hopping sites by Cu doping [192,213], and (iv) changes in the electronic density of states caused by the dopant [10,54,136,213,224].

In hydrogen, conductivity increases continuously with temperature, reaching maximum values at 750 °C and showing semiconducting behavior. The maximum conductivities are 29.5 S cm^{-1}, 26.1 S cm^{-1}, 26.2 S cm^{-1}, and 18.6 S cm^{-1} for LSFM, 10-LSFCM, 15-LSFCM, and 20-LSFCM, respectively. At lower temperatures, slight Cu doping improves conductivity, while above 500 °C the values become comparable to undoped LSFM. However, 20-LSFCM shows the lowest conductivity in hydrogen. This decrease can be explained by several factors: (i) lower mechanical integrity (change in the density and worse contact between the grains), and (ii) partial evaporation of copper due to its low boiling point at the nanoscale. SEM observations after DC4W measurements revealed the formation of new structures in addition to exsolved nanoparticles, associated with partial melting of Cu nanoparticles. As a result, the reduced amount of copper lowers the number of available hopping sites, decreasing conductivity. At the same time, the amount of molten Cu is insufficient to form continuous conductive pathways across the surface. Despite this decrease, the conductivity remains adequate for use as an electrode in solid oxide cells.

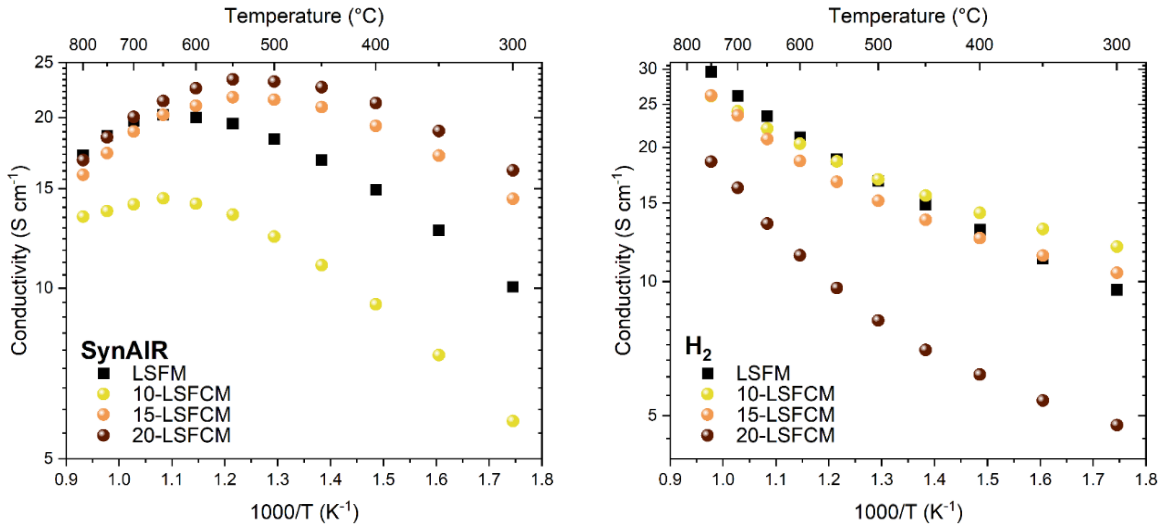


Fig. 4.39. Electrical conductivity of LSFCM in synthetic air and hydrogen.

After electrical measurements, the samples were removed and examined by SEM. In addition to the exsolved nanoparticles, dendritic structures were observed in all Cu-doped samples. This phenomenon, shown in **Fig. 4.40**, has not been previously reported for SFM-based materials. The most developed structures were found in the 20-LSFCM sample, where they covered a large portion of the surface. The extent of dendrite formation increased with the Cu content, meaning that a higher Cu

loading led to larger and more highly branched structures. The formation mechanism is related to the relatively low Hüttig temperature (at which the surficial diffusion is possible) and low melting point of Cu nanoparticles, which promote their partial liquefaction on the LSFM surface. Under an applied electric field, this partially molten copper migrates and forms two-dimensional nanostructures. No specific orientation of the dendrites was identified, as they tend to nucleate and grow mainly along grain boundaries.

Importantly, these dendritic structures did not form during the standard reduction in hydrogen or after electrical tests under $pO_2 \approx 0.21$. Small flakey structures were visible after the reduction of higher-doped LSFCM; however, their size was considerably smaller. This indicates that both a reducing atmosphere and an electric field are necessary for their formation. The dendrites are very thin, on a nanometer scale, which is why they were not detected in EDS mapping and did not appear to alter the overall elemental composition. Because the surface and the gas-solid interface play a key role in catalytic and electrocatalytic processes, the presence of these structures contributes to improved material performance.

The formation of two-dimensional dendritic nanostructures at elevated temperatures under a hydrogen atmosphere and an applied electric field is a novel observation that has not been reported so far. Therefore, further advanced studies are required to fully understand the mechanisms responsible for their development. In particular, the use of PEEM (photoelectron emission microscopy) combined with ion milling is planned to investigate the detailed chemical structure of the dendrites.

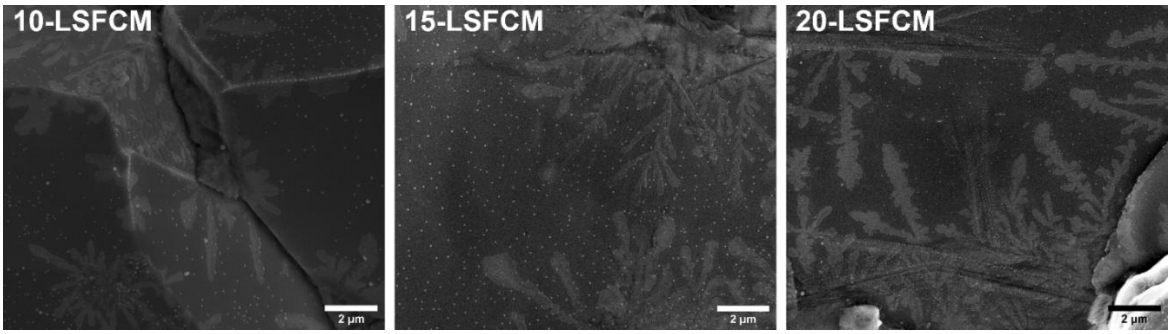


Fig. 4.40. SEM images of dendritic structures formed after electrical tests.

Before catalytic testing, the powders were ball milled to obtain similar specific surface areas, which are presented in **Tab. 4.10**. Achieving comparable surface areas minimized the influence of the microstructure on the catalytic performance in the RWGS reaction. It is also important to note that the total reactant flow rate was set to a relatively high value of 80 ml min^{-1} yielding GHSV and WHSV parameters of 11,087 h^{-1} and 64,000 $mLg^{-1}h^{-1}$, respectively. Using a higher flow rate allowed a clearer differentiation of catalytic performance and highlighted the improved activity of LSFCM materials. In addition, slightly lower CO_2 conversion reduced mass and heat transfer limitations, enabling

evaluation under kinetically controlled conditions. This is relevant for the intended application in SOEC systems operating under unpressurized, high-flow co-electrolysis conditions.

Tab. 4.10. Specific surface area of Cu-doped compounds after milling. Apparatus uncertainty is 5%.

	SSA ($m^2 g^{-1}$)
LSFM	5.69
10-LSFCM	4.36
15-LSFCM	4.89
20-LSFCM	4.94

The measured CO concentration at the reactor outlet is shown in **Fig. 4.41A**. The pristine LSFM exhibited the lowest CO production in the intermediate temperature range. The use of Cu-doped samples resulted in a gradual increase in CO concentration. Although similar CO levels were reached at 800 °C for all samples, LSFCM catalysts generally produced 12-56% higher CO concentrations in the 600-750 °C range compared to the undoped material.

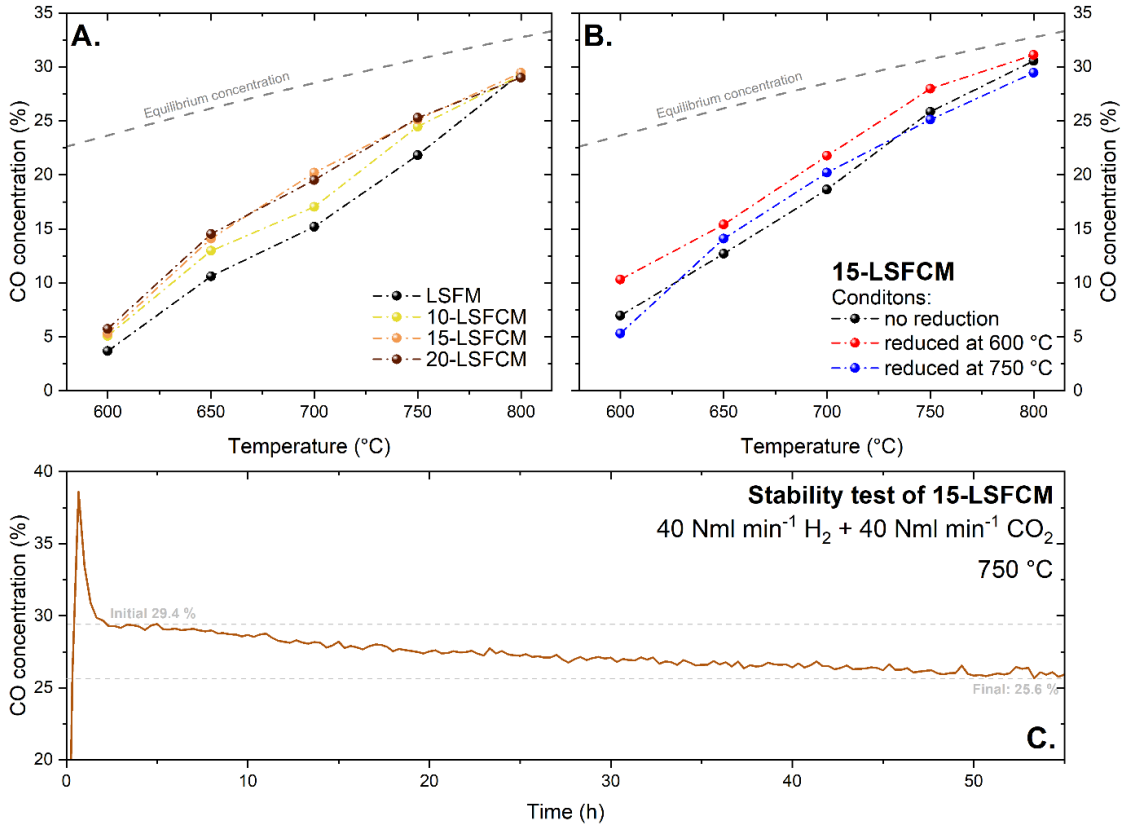


Fig. 4.41. Concentration of CO in the outlet stream for RWGS reaction measured in fixed bed reactor: A. for different compounds, B. for 15-LSFCM in different activation approaches, and C. in time-stability test of 15-LSFCM.

No methane or higher hydrocarbons were detected in the outlet stream over the tested temperature range, indicating 100% selectivity toward CO formation in all experiments. For all catalysts, the CO concentration increased with rising temperature, reflecting a higher CO_2 conversion. However, unlike undoped LSFM, the LSFCM samples deviated from a linear trend and showed a more parabolic behavior, suggesting a change in the temperature-dependent activation energy and a possible change in the reaction mechanism [226]. The 15-LSFCM and 20-LSFCM samples showed some of the highest performance among Cu-based catalysts. In this system, not only Cu acts as an active site, but the entire material contributes to the high activity. The increase in performance with a higher Cu content is associated with (i) enhanced exsolution of catalytically active bimetallic nanoparticles and (ii) a higher concentration of oxygen vacancies in LSFCM perovskites [10,225,227,228]. Oxygen vacancies promote the adsorption of CO_2 and H_2, facilitating CO_2 reduction to CO, and also aid CO desorption due to weaker surface interactions [227,228]. The La-Fe-Mo-based lattice further supports activity, as these elements are known to be effective in RWGS reactions. According to in-situ DRIFTS studies by Shiyan *et al.* [229], CO_2 can adsorb on metal sites, surface oxygen, or oxygen vacancies to form carbonate species, which react with hydrogen to produce formate intermediates. Additional studies on WO_3 hydrogenation showed that Cu nanoparticles mainly act as sites for hydrogen spillover, supplying H^* species that migrate across the surface. Another mechanism proposed by Thompson *et al.* [230] involves a redox cycle, where metal particles are oxidized by CO_2, releasing CO, and then reduced back by H_2, forming H_2O. In the present system, LSFCM catalysts likely follow a combined mechanism: Cu nanoparticles facilitate hydrogen spillover and enhance reducibility, while oxygen vacancies support carbonate and formate formation.

The role of Cu nanoparticles was further examined for 15-LSFCM by varying the reduction temperature between 600 and 750 °C. The catalytic results, including a non-activated sample, are shown in **Fig. 4.41B**. The activation temperature strongly affected performance. Lower reduction temperatures led to a higher Cu to Fe ratio at the surface and limited the growth, melting, and evaporation of Cu particles. This confirms that Cu plays a key role by adsorbing hydrogen and transferring reactive hydrogen species to surficial oxygen atoms. The resulting oxygen vacancies can then be filled by CO_2, producing CO. This redox mechanism is consistent with the findings by Ren *et al.* [231] for Cu-Fe systems. Additionally, exposed Fe nanoparticles or iron oxides on the surface may also contribute through direct redox pathways, as described by Loiland *et al.* [232].

Although catalytic activity depends on metallic Cu, the formation of Fe-Cu nanoparticles improves stability. Iron enhances CO_2 conversion and, more importantly, limits copper diffusion and sintering [233]. It also helps stabilize Cu against oxidation and weakens the C-O bond in CO_2 by

electron donation [234]. Therefore, the ability to tune the Cu to Fe ratio in exsolved nanoparticles is an advantage of LSFCM materials. By controlling the activation conditions, catalysts with optimal activity and stability can be designed. A long-term stability test (**Fig. 4.41C**) performed for 15-LSFCM showed that, after an initial fluctuation associated with sudden gas exchange in the reactor, the CO concentration stabilized at about 29.4% and gradually decreased to 25.6% after approximately 50 hours. The degradation rate slowed over time, but further optimization of composition, microstructure, and activation is still needed for practical SOEC applications.

It is also important that LSFM-based materials can be regenerated through re-oxidation followed by reduction, restoring active sites after deactivation [98]. The LSFCM catalysts combine the benefits of an active support and exsolved nanoparticles, resulting in high performance. At the same time, they maintain good electrical conductivity and compatibility with other SOEC components, making them promising candidates for fuel electrode applications.

Conclusions of this section:

- Redox stability is enhanced after the incorporation of copper into the LSFM lattice. Only at high Cu-concentration and high reduction temperature the Ruddlesden-Popper phase is formed. The higher stability was corelated with the smaller change in ionic radii between different Cu oxidation states. Moreover, the copper doping favors the formation of a higher share of oxygen vacancies and leads to the distortion of FeO_6 octahedrons.
- Even with a stable structure, the exsolution is observed at temperatures ranging between 700-800 °C. With the increase of the temperature, this phenomenon is more pronounced, as more nanoparticles are present on the surface. At 800 °C agglomeration of NPs is also noticed. The TEM imaging of 15-LSFCM revealed that Fe is clearly agglomerates in areas corresponding to exsolved nanoparticles. Although less visible, the copper can be found in areas directly surrounding the iron, forming more “sickle-like” shapes. On the basis of these findings, the formation of quasi core-shell NPs was stated and the proposed mechanism was presented. This mechanism consists of several steps, namely: copper exsolution, iron exsolution at similar sites, melting and evaporation of copper, and lastly the breaking of the outer shell exposing the iron core.
- The addition of the copper to the LSFM host promotes the reduction of the iron, which was evidenced both by in-situ TPR measurements and ex situ XAS analysis of K-edge of iron. In TPR not only the higher H_2 consumption was revealed but also shift to the lower reduction temperatures with increasing Cu concentration. Decrease in the white line intensity of Fe K-edge proved this observation, revealing higher share of metallic iron. At the same time, the K-edge of copper shown complete reduction to Cu^0.

- The electrical tests revealed good conductivity in both air and hydrogen atmospheres. After these tests the samples were subjected to imaging in order to confirm the exsolution. Interestingly, in addition to the exsolved nanoparticles, large dendritic structures were revealed. Their formation was not observed after "conventional" reduction, only after combining three factors at once: hydrogen atmosphere, high-temperature, and electric field. As these structures remained invisible in EDS analysis, it was stated that they are 2D features. Such observation was never before reported in the literature concerning SFM-based materials and further more advanced analyses are to be undertaken.
- The catalytic efficiency for the RWGS reaction was examined, which showed the superior behavior of LSFCM perovskites by the enhanced reducibility of the compounds and a high share of the oxygen vacancies. By varying the activation temperature, it was possible to distinguish the influence of the perovskite host, the exsolved Cu^0, and the exsolved Cu-Fe nanoparticles. By catalytic examination, the pivotal role of Cu nanoparticles was stated, responsible for the H_2 adsorption and the transfer of the H^* radicals. Noteworthy, the 15- and 20-LSFCM showed the topmost performance among other Cu-based catalysts, which arises from the synergistic effects between exsolved nanoparticles and active host support.
- Taking into the account that Cu-doping leads to the enhanced redox stability, the risk of delamination during the typical SOFC operation can be minimized. Unfortunately, at the same time, the risk of thermal mismatch is high. To overcome this, either a composite may be prepared or the additional of functional layers can be done. In light of very promising aforementioned results, further application of LSFCMs as fuel electrode in SOC is planned, especially in co-electrolysis in SOEC.

As these results complement the previous chapter, the hypothesis 3 *"Doping of double perovskite hosts with transition metals (Ni, Co, or Cu) will promote iron exsolution from Fe-rich B-sites. Moreover, the strain introduced in phase transition would further enhance the NPs formation"* can be once again partially confirmed. In fact, it was observed that the addition of copper is enhancing the reduction of the iron, evidenced in the XAS studies. Also, the higher the doping level, the more nanoparticles exsolved. However, the second part of this hypothesis is rather not applicable in this material as Cu was surprisingly found to boost the redox stability of the compounds.

Moreover, considering aforementioned conclusions, especially the TEM-EDS mapping, the hypothesis 4 *"Owing to disparities in melting and reduction temperatures between copper and iron, exsolved nanoparticles will not form a solid Fe-Cu solution, rather cation separation will be observed"*

can be confirmed. It is evident that the iron and copper are not present in the exactly same spots. Thus, the formation of core-shell or quasi core-shell is likely.

The research presented in this chapter is currently under consideration in the high-impact scientific journal as **Ducka** *et al. "Stabilization of Cu-doped* $La_{0.3}Sr_{1.7}Fe_{1.5}Mo_{0.5}O_{6-\delta}$ *decorated with bimetallic nanoparticles for the improvement of electrochemical syngas production"*, under review.

4.2.4. Dual-doping with Cu-Co or Cu-Ni of the B-site of LSFM for improved stability and intense exsolution

Taking into the account the discoveries presented in two previous chapters, namely extraordinary exsolution but poor stability in Ni/Co-doped LSFM and enhanced redox stability in Cu-doped LSFM, a new idea arose. If both of these dopants (Ni+Cu or Co+Cu) would be introduced simultaneously into B-site, a synergetic effect can be developed with both good redox stability and intense exsolution. To verify this hypothesis, a new series of materials was synthesized. To minimize the number of variables, the dopant concentration was fixed at 0.2 and only the ratio between Ni/Co and Cu was changing. For specific formulas and abbreviations, please be referred to **Tab. 3.1** in Chapter 3.1.2.

The XRD patterns of as-prepared and reduced compounds are presented in **Fig. 4.42**. Right after the reduction, the structure consists predominantly of peaks characteristic for double perovskite in *Fm-3m* structure with marked Miller indices for specific crystallographic planes. In all of the analyzed compounds, small traces of additional phases can be found, visualized by small peaks of Mo- and Fe-rich phases. After the reduction at 750 °C, the structure remains in the cubic one of double perovskite. No additional Fe- or Mo-rich phases were found, suggesting they either completely vanish after the reduction or transform into cubic phase overlapping with DP peaks. At the same time, no peaks characteristic for iron or iron-transition metal alloy is observed. However, when the temperature is increased to the 800 °C, the phase transition to Ruddlesden-Popper layered perovskite occurs. Similarly like in Chapter 4.2.2, where only nickel and cobalt doping was presented, the dual-doped LSFM with nickel and copper is found to be slightly more stable than its cobalt counterpart, especially for high copper concentration. Moreover, also similarly to previously presented research, the higher share of nickel or cobalt in the lattice leads to the enhanced formation of the layered perovskite phase.

Unfortunately, it was impossible to fully stabilize the structure after the highest reduction temperature. In case of the nickel presence, the positive impact of copper addition is visible as lower amount of Ruddlesden-Popper is formed, owing to the higher stability of Ni-doped LSFM over cobalt ones like described in Chapter 4.2.2. Unfortunately, the copper doping was not able to suppress the phase transition in the cobalt-copper co-doped LSFMs. However, it must be kept in mind that the overall dopant concentration remained quite high (0.2) which is also an important factor regarding stability. It cannot be undoubtedly denied nor confirmed that at lower total dopant concentration, the structure would remain stable. However, due to the preliminary nature of these results, more work needs to be done and the change of the total dopant concentration is one of the tasks for further work.

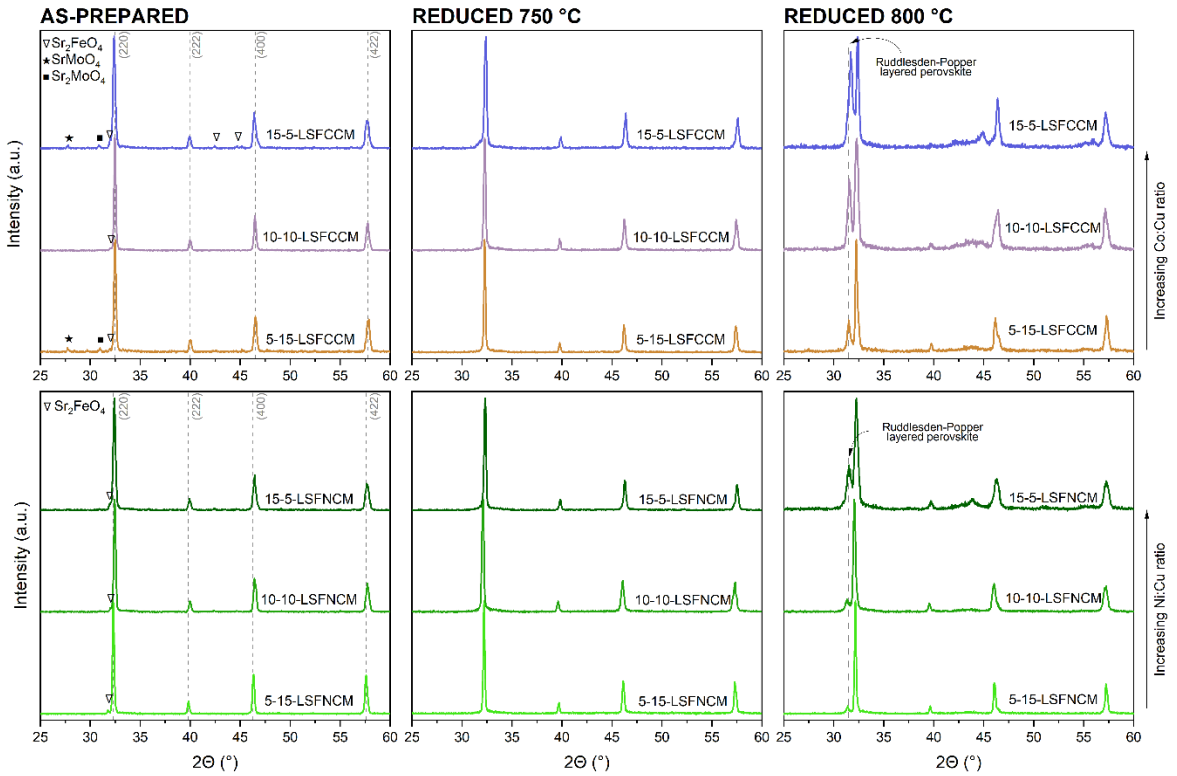


Fig. 4.42. XRD patterns of dual-doped LSFM with different Co:Cu and Ni:Cu ratio: as-prepared, reduced at 750 °C, and reduced at 800 °C.

The second characterization method used was scanning electron microscopy, which allowed to reveal the exsolution phenomenon. The SEM images of reduced (800 °C) powders are presented in **Fig. 4.43**. The exsolved nanoparticles are clearly visible in all of the analyzed compositions. With the increasing Ni/Co:Cu ratio the intensity of the exsolution process is higher and for 15-5-LSFCCM, which is the composition with the highest Co:Cu ratio, the exsolution is the most intense, as NPs are covering the whole area of the grain surface. Some larger nanoparticles can also be found among even distribution of smaller ones.

Interestingly, in the high-copper concentrated samples, both with nickel and cobalt, the addition of branch-like lighter dendritic structures is visible, even without the presence of the external electric field like in purely Cu-doped LSFM. Due to the relatively high reduction temperature, especially for copper nanoparticles, it is likely that these structures originate from partially melted copper. It is even more possible, since their presence is mostly observed in the samples where the concentration of copper is the highest. Another interesting observation is the formation of the layer on the grains exclusively in 10-10-LSFNCM sample. In previously described results concerning Ni-doping, the layer was formed only in the compounds of high dopant concentration and with extraordinary exsolution. In this case, the number of exsolved nanoparticles is definitely not that impressive, yet clearly a layer is formed. Thus,

the origin of layer in this specific compound remains unknown, unfortunately. The further, surface-sensitive techniques are to be utilized.

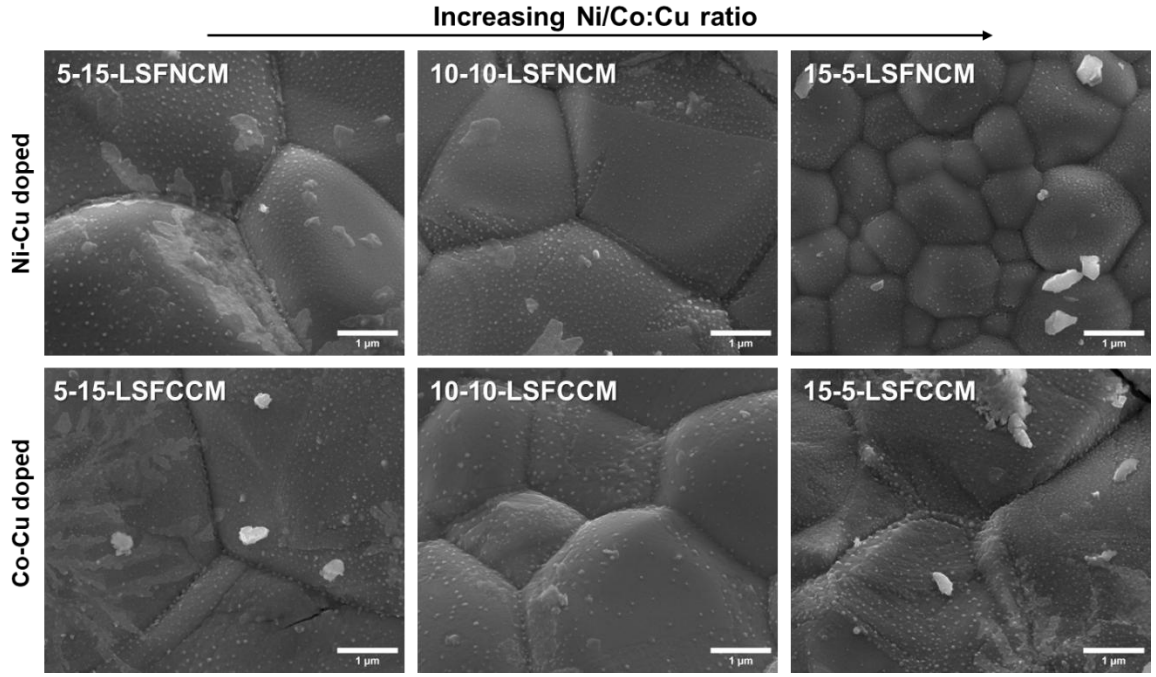


Fig. 4.43. SEM images of reduced (800 °C) dual-doped LSFM with different Co:Cu and Ni:Cu ratio.

Lastly, the transmission electron microscopy was applied to see if the elements are exsolving similarly like they behaved in the single-doped perovskites. The STEM image with specific elemental maps of 10-10-LSFNCM are presented in **Fig. 4.44** along with HRTEM image of the exsolved nanoparticle. The visible NP is clearly anchored to the surface, which is one of the main features of exsolution phenomenon. Slightly less than half of the nanoparticle is embedded into the perovskite host. This as a result enhances the stability of the exsolved species, providing higher agglomeration resistance. Moreover, in the HRTEM image, the crystalline inner part of the nanoparticle can be identified by the parallel lattice fringes. At the same time, the outer layer of the NP is partially built of more amorphous phase. This difference suggests the formation of two different phases during the exsolution.

In the STEM image, a huge number of nanoparticles was found, surprisingly, some of them were definitely poorly attached to the surface, evidencing the diversity of the NPs. EDS mapping revealed that the areas in which nanoparticles are present corresponds well with the Fe- and Ni-rich spots in elemental maps. Due to the highest concentration of the iron, its share in the exsolved nanoparticles is dominant and as a result this element gives the highest signal in maps. The second most intense is the nickel, which rich spots can be correlated with the exsolved NPs. This observation proves once again that nickel and iron are co-exsolving forming the bimetallic particles, similarly like in case of

single-doped LSFM. When the copper is concerned, its concentration is definitely the lowest, as the signal is slightly smaller than the nickel one. It is in a contrary to the initial Ni:Cu ratio equal to unity. However, the impoverishment of the copper can be easily understood and explained by already aforementioned melting of this element at high reduction temperatures. Although the concentration is lower, the Cu-rich spots can be clearly found in the vicinity of the Fe- and Ni-rich spots. Their closure can be observed more directly in the overlay maps: red Fe map with green Ni maps lead to the formation of yellowish spots, while the blue copper map is visible in the neighborhood of the nanoparticle. Moreover, the copper swathing the nanoparticle rather than being completely separated. This insight is adequate to the behavior of copper explained in Chapter 4.2.3, which was found also to occur in bimetallic doping of LSFM where ternary nanoparticles are exsolved. The mechanism of formation can be proposed and it would be analogous to the one presented in **Fig. 4.35.**

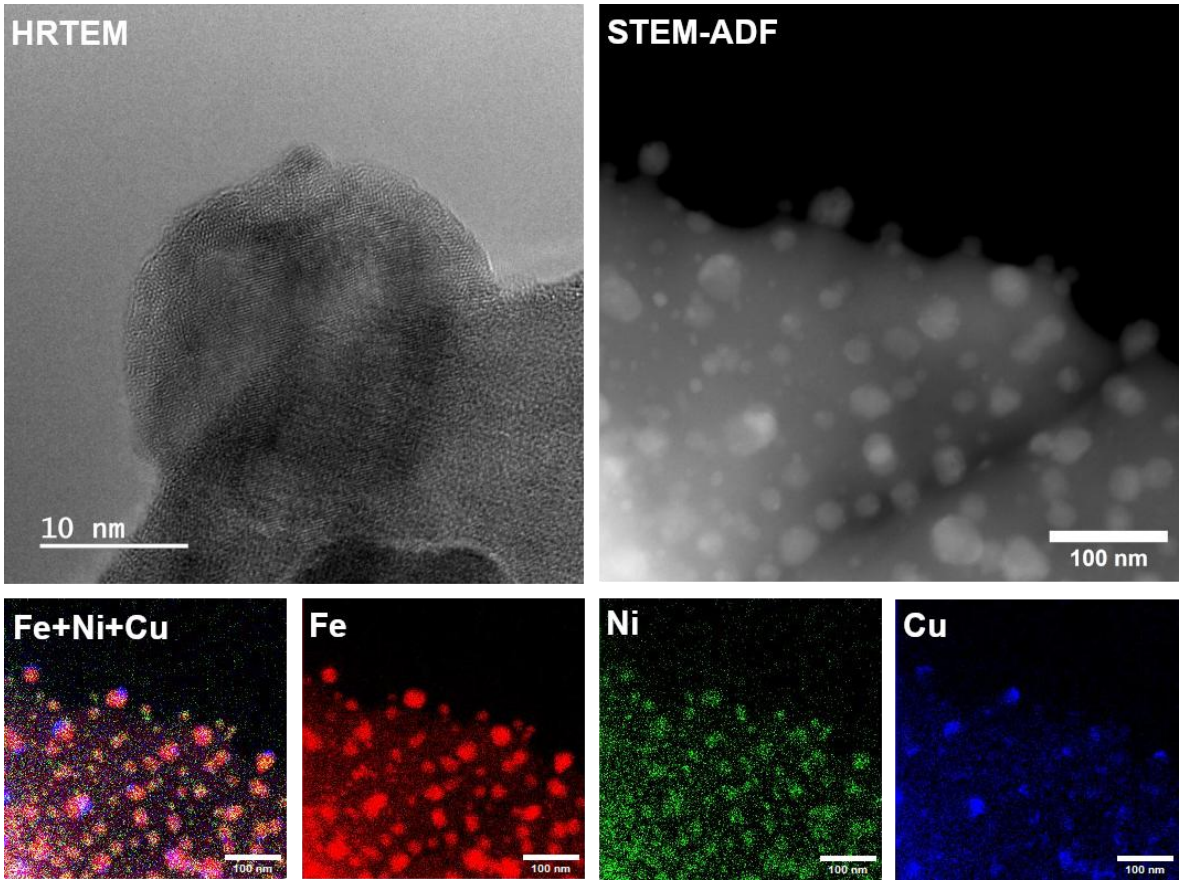


Fig. 4.44. HRTEM image of the exsolved nanoparticle from 10-10-LSFNCM, STEM-ADF image with corresponding elemental maps.

Conclusions of this section:

- The doping of two different transition metals (Ni+Cu or Co+Cu) with total 0.2 concentration at B-site, leads dominantly to the formation of double perovskite structure with traces of additional Fe- and Mo-rich phases. After the reduction at 750 °C the structure remains in the cubic one and the additional phases disappear in the XRD patterns. Unfortunately, the reduction at 800 °C promotes the phase transition to the Ruddlesden-Popper layered perovskite. The higher share of the copper leads to the more stable structure but the formation of RP phase is inevitable. Similarly like the studies on Ni- or Co-doped perovskite, the nickel tends to be more stable with stability enhanced by the addition of the copper.
- The exsolution in these systems is less intense than for LSFMNi or LSFMCo, but remains significant, especially for high Ni/Co:Cu ratios. The STEM-EDS mapping done on 10-10-LSFNCM revealed the formation of ternary nanoparticles consisting of bimetallic Fe-Ni part, partially surrounded by copper-rich area. This observation links the two previously reported studies from Chapters 4.2.2 and 4.2.3.

The copper doping helped to maintain higher stability in with Ni-Cu-doped LSFM, however it was impossible to overcome phase transition completely. It can be stated that addition of copper helps to stabilize the structure, yet it cannot be fully suppressed at temperature as high as 800 °C. Moreover, due to the preliminary nature of these studies, more analyses are planned to be undertaken soon.

5. Summary and final conclusions

This thesis covers the area of single perovskite $SrTiO_{3-\delta}$ (STO) and double perovskite $Sr_2Fe_{1.5}Mo_{0.5}O_{6-\delta}$ (SFM) doped with transition metals to perform the exsolution phenomenon. The both A- and B-sites doping can be performed to tune redox stability, exsolution behavior, and catalytic performance, while avoiding extensive formation of additional phases. On the basis of the results presented it can be stated that the primary aim of this thesis is accomplished.

First, the STO-based single perovskites were synthesized and analyzed. The A-site was co-doped with La and Ce according to our previous study [24]. The B-site doping focused on addition of Ni together with secondary transition metal (Fe, Co, or Cu). In consequence, the single-phase STO-based perovskites with only minor impurities were obtained presenting thermal expansion coefficients compatible with YSZ and NiO-YSZ and ensuring mechanical compatibility with typical solid oxide cell components. Under reducing conditions, these STO-based materials preserved the perovskite structure while exsolving metallic nanoparticles. The usage of the TEM revealed that the exsolved nanoparticles are formed by bimetallic Ni-Co and Ni-Fe alloys grown epitaxially on the STO-host. Nickel reducibility was clearly enhanced by the presence of a secondary transition metal, as shown by X-ray absorption measurements. However, the highest content of the exsolved nanoparticles was observed in the Ni-only doped compound (LSCT-Ni), due to the highest concentration of nickel in the initial structure. In LSCT-based perovskites, electronic transport evolved from low-value conductivity with purely thermally activated behavior in air (10^{-5}-10^{-3} S cm^{-1}) to significantly higher and partially metallic-like conduction (up to about 10 S cm^{-1}) after reduction. The metallic behavior was observed for LSCT-Ni, LSCT-NiFe and LSCT-NiCu, where metallic nanoparticles exsolved on the surface. Finally, Hypothesis 1 was only partially confirmed: secondary transition-metal doping indeed facilitated nickel reduction but did not increase the exsolved nanoparticle population compared with LSCT-Ni.

The second group of materials analyzed in this thesis were the SFM-based double perovskites, where lanthanum and niobium were successfully incorporated into A- and B-sites, respectively. Only small traces of typical $SrMoO_4$ impurity were found. After the reduction, these materials underwent the partial yet reversible transformation to the Ruddlesden-Popper layered perovskite. It was found that the addition of the lanthanum lowers the concentration of the newly formed RP phase, increasing the redox stability of the system. The in-situ oxidation studies were undertaken to understand the reversibility of the phase transition. It was found that exsolved iron is firstly re-incorporated into the lattice at about 300 °C evidenced in both TGA and HT-XRD studies. With the temperature increase, the layered perovskite also transforms back to the original cubic structure of the double-perovskite. The reoxidation

process is finished at temperatures >700 °C for all three dopants. In addition to the enhanced redox stability, La-doping led to the boost in electrical conductivity in both air and hydrogen. This phenomenon occurred due to the aliovalent doping of A-site of the perovskite. Taking both redox stability and better electrical performance, lanthanum was selected also in further work with other SFM-based compositions. These findings confirmed Hypothesis 2, with La substitution in particular stabilizing the double-perovskite framework during redox cycling while enhancing electrical transport.

As the LSFM was found to be stable, but the exsolution was not significantly intensive, another dopant must have been selected for the nanoparticles formation. Firstly, the nickel or cobalt were introduced into the B-site of LSFM with variety of concentrations analyzed. Regardless the dopant concentration, the ratio of Fe:Mo was kept constant at 3. After the reduction, increasing Ni or Co content resulted in progressive formation of Ruddlesden-Popper phases together with extensive exsolution of Fe-containing nanoparticles, and only the sample with the lowest Ni content (5-LSFMNi) remained in the double-perovskite form. SEM imaging revealed extremely dense nanoparticle coverage at higher dopant levels, approaching semi-continuous layers, while STEM-EDS mapping confirmed formation of bimetallic Fe-Ni or Fe-Co alloys. The combined structural and microstructural evidence suggested that intense exsolution driven by high dopant content created B-site deficiencies that promote phase decomposition. In other words, exsolution and the B-site vacancy formation likely triggered the transition from double perovskite to Ruddlesden-Popper layered perovskite. Electrical measurements shown enhanced conductivity in air with increasing dopant content, while hydrogen-atmosphere behavior was complicated by RP formation and porosity changes, although the conductivities remained sufficient for SOC electrode. Catalytic tests demonstrated that Ni and Co doping substantially boosted CO_2 reduction activity, with Ni-doped samples being the best among studied ones reaching more than 90 % of the theoretical CO concentration. Consequently, Hypothesis 3 was also only partially confirmed. Ni/Co doping indeed promoted intense Fe-rich nanoparticle exsolution, but the proposed exsolution enhancement by strain from the phase transition was not supported. Instead, the studies indicated that exsolution itself was a driver of phase decomposition.

Another metal which was studied as a dopant in LSFM-based double perovskites was copper. Addition of copper even further improved redox stability with RP phase forming only at the highest Cu concentration and higher reduction temperature. Despite, the structural stability, LSFCMs was still able to exsolve the nanoparticles at temperatures ranging between 700 and 800 °C. However, in case of copper exsolution the higher reduction temperature was not beneficial for the process, as nanometric Cu could be more easily melted and evaporated from the perovskite structure. STEM-EDS studies revealed quasi core-shell particles with Fe-rich cores surrounded by Cu-containing regions. The

supposed mechanism of NPs formation was presented consisting of Cu exsolution, followed by Fe exsolution, then melting and partial evaporation of copper. The final step is the cracking of the copper shell exposing the iron core. Combined TPR and XAS analyses shown that that Cu doping significantly promotes Fe reduction. Electrical measurements confirmed high conductivity in both air and hydrogen. After tests in hydrogen, SEM imaging revealed the formation of previously unreported two-dimensional dendritic surface features. Catalytically, LSFCMs exhibited excellent RWGS performance, with Cu nanoparticles playing a critical role in hydrogen activation and H* transfer. These microstructural and spectroscopic observations confirmed Hypothesis 4: Fe and Cu did not form a homogeneous solid solution in the exsolved state but segregated into core-shell or quasi core-shell architectures, consistent with their different surface mobilities and melting temperatures.

Lastly, taking into account the discoveries in Ni/Co- and Cu-doped LSFMs, the preliminary results in dual-doping (Ni+Cu or Co+Cu) was presented. The total concentration of the dopant was fixed at 0.2. The synthesis yielded predominantly double perovskite structure, but Fe- and Mo-rich phases were found in the XRD patterns. Reduction at 750 °C maintained the cubic perovskite and removed the secondary phases, but at 800 °C the Ruddlesden-Popper phase appeared in all compositions. The increasing Cu-concentration clearly improved the stability compared with Cu-free Ni/Co systems yet could not fully suppress this transformation. Exsolution in these co-doped materials was also less extreme but remained substantial, especially at high Ni/Co:Cu ratios. STEM-EDS on 10-10-LSFNCM revealed ternary nanoparticles with a Fe-Ni areas partially surrounded by a Cu-rich region, which directly linked the bimetallic Fe-Ni exsolution behavior and quasi core-shell Fe-Cu features observed in the binary-doped systems.

Taken together, these results demonstrated that carefully designed A- and B-site doping in $SrTiO_{3-\delta}$ and $Sr_2Fe_{1.5}Mo_{0.5}O_{6-\delta}$-based perovskites enabled tuning of their properties with most respect to the redox stability, exsolution phenomenon, electrical and catalytic characterization. The work clarified that exsolution capability, dopant chemistry and phase stability are tightly interlinked: very high exsolution intensity in double perovskites can drive phase decomposition, whereas Cu doping can decouple intense redox activity from catastrophic structural breakdown and generate Fe-Cu NPs that are both structurally robust and catalytically active.

Although, the work on this thesis is completed, the studies on STO- and SFM-based systems are still ongoing. The main future pathways focus on the dual-doping of LSFM to dive into the properties of these materials and to examine them in operating fuel cells, which remained technically challenging due to the strong TEC mismatch.

List of the candidate's publications and achievements

Publications in the field of PhD thesis:

1. **Ducka, A.,** Błaszczak, P., Zając, M., Mizera, A., d'Acapito, F., & Bochentyn, B. (2024). „*Limited dissolution of transition metals in the nanocrystalline cerium (IV) oxide"*. CERAMICS INTERNATIONAL, 50, 50921-50933. https://doi.org/10.1016/j.ceramint.2024.10.004; 100 pkt. MNiSW
2. **Ducka, A.,** Błaszczak, P., Zając, M., Maximenko, A., Gazda, M., & Bochentyn, B. (2025). *„Investigation of the phase transition to the Ruddlesden–Popper phase in La- or Nb-doped $Sr_2Fe_{1.5}Mo_{0.5}O_{6-\delta}$ double perovskites and the impact of lanthanum or niobium doping."* NANOSCALE, 17, 12371-12384. https://doi.org/10.1039/d5nr00596e; 140 pkt. MNiSW
3. Błaszczak, P., Zając, M., **Ducka, A.,** Matlak, K., Wolanin, B., Wang, S.-F., Mandziak, A., Bochentyn, B., & Jasiński, P. (2022). *„High-temperature Co-electrolysis of CO_2/H_2O and direct methanation over Co-impregnated SOEC. Bimetallic synergy between Co and Ni."* INTERNATIONAL JOURNAL OF HYDROGEN ENERGY, 47, 35017-35037. https://doi.org/10.1016/j.ijhydene.2022.08.057, 140 pkt. MNiSW
4. Błaszczak, P., **Ducka, A**., Wolanin, B., Matlak, K., Machowski, G., Prześniak-Welenc, M., Wang, S.-F., Bochentyn, B., & Jasiński, P. (2023). *"Fabrication of wormhole-like YSZ and Ni-YSZ by the novel soft-hard template CTAB/NaCl-assisted route. Suppressing Ni coalescence in SOFC."* JOURNAL OF THE EUROPEAN CERAMIC SOCIETY, 43, 438-451. https://doi.org/10.1016/j.jeurceramsoc.2022.09.054, 140 pkt. MNiSW
5. Błaszczak, P., Mäkinen, P., Mroziński, A., **Ducka, A.,** Jasiński, G., Himanen, O., & Jasiński, P. (2025). *„Uncovering the electrochemical processes and understanding the causes of the degradation via EIS-DRT in large-scale solid oxide fuel cell."* APPLIED ENERGY, 125983. https://doi.org/10.1016/j.apenergy.2025.125983; 200 pkt. MNiSW

Publications apart from PhD thesis:

6. **Ducka, A.,** Trawiński, B., Bochentyn, B., Dubiel, A., & Kusz, B. (2021). *„Structure and thermoelectric properties of nickel-doped copper selenide synthesised in a hydrogen atmosphere." MATERIALS RESEARCH BULLETIN*, *133*, 111042. https://doi.org/10.1016/j.materresbull.2020.111042, 100 pkt. MNiSW

Citation metrics (by June 2026):

	Google Scholar	**Web of science**	**Scopus**	**ResearchGate**
Citations	101	79	83	85
Hirsch index	4	4	4	5

Achievements during PhD studies:

1. Principal investigator of the Polish Science Centre (NCN) Project PRELUDIUM (UMO-2022/45/N/ST5/02933)
2. Scholarship holder in Polish Science Centre (NCN) Project SONATA BIS (UMO-2021/42/E/ST5/00450)
3. Scholarship holder in Polish Science Centre (NCN) Project OPUS (UMO-2021/43/B/ST8/01831)
4. Beneficent of IDUB Francium, Molybdenum, Nitrogenium, and Oxygenium programmes.
5. Principal investigator or experimentalist in synchrotron proposals:
    a. PIRX at National Synchrotron Radiation Centre, Poland (PI and experimentalist)
    b. STXM at National Synchrotron Radiation Centre, Poland (experimentalist)
    c. ASTRA at National Synchrotron Radiation Centre, Poland (PI and experimentalist)
    d. LISA at European Synchrotron Radiation Facility, France (PI and experimentalist)
    e. ESCA at Elletra Sincrotrone, Italy (experimentalist)
6. Participant in two summer schools:
    a. Joint European Summer School (JESS2022) on Fuel Cell, Electrolyser and Battery Technologies (11-17.09.2022)
    b. Budapest School on Modern X-ray Science 2023 (3-6.10.2023)

Conferences

1. 23rd International Conference on Solid State Ionics (SSI-23); Materials Research Society (MRS); Boston, MA, USA (17-22.07.2022), **poster presentation:** „Synthesis and characterization of nanocrystalline ceria $Ce_{1-x}M_xO_{2-\delta}$ (M = Mn, Fe, Co, Ni, Cu, x= 0.1, 0.15, 0.2)”
2. International Symposium of Systems with Fast Ionic Transport (ISSFIT15), Croatian Association of Crystallographers, Dubrovnik, Croatia (18-22.04.2023), **oral presentation** „Exsolution of the bimetallic nanoparticles from La,Ce,Ni-doped strontium titanate: an impact of secondary transition metal”
3. XVIIIth Conference of the European Ceramic Society, European Ceramics Society (ECerS), Lyon, France, (2-6.07.2023):
    a. **oral presentation** „Phase transition to Ruddlesden-Popper layered perovskite under reductive atmosphere in $Sr_2Fe_{1.5}Mo_{0.5}O_{6-\delta}$ induced by La-doping”
    b. **poster presentation** „Forming Ni-Fe and Co-Fe alloys on the surface of $(La,Sr,Ce)(Me,Ti)O_3$ via topotactic ion-exchange exsolution”
4. Budapest School on Modern X-ray Science 2023 (3-6.10.2023), **poster presentation**: „Transition between double perovskite and Ruddlesden-Popper phase in $Sr_2Fe_{1.5}Mo_{0.5}O_6$-based compounds during reduction and oxidation”
5. International Symposium SYLINDA, Kraków, Poland (7-8.03.2024), **poster presentation**: „X-ray absorption spectroscopy for the investigation of reversible phase transition in $Sr_2Fe_{1.5}Mo_{0.5}O_6$-based compounds”

6. 46th IMAPS Poland Conference, Gdańsk, Poland (22-25.09.2024), **poster presentation:** „Enhanced nanoparticle exsolution in Ni-doped strontium ferrite molybdates: impact of the phase transition”
7. Pacific Rim Meeting on Electrochemical and Solid State Science (PRiME2024), Honolulu, HI, USA, (6-11.10.2024), **oral presentation** „Influence of the Transition Metal Doping on the Properties of $Sr_2Fe_{1.5}Mo_{0.5}O_6$ Double Perovskite for Solid Oxide Fuel Cells”
8. The 19th Conference on Functional and Nanostructured Materials FNMA 2024, (21 and 23.11.2024), Online, **oral presentation**: „Optimizing $La_{0.3}Sr_{1.7}Fe_{1.5}Mo_{0.5}O_6$ Double Perovskite in Solid Oxide Fuel Cells: The Role of Transition Metal Doping”
9. LEAPS Meets Advanced Materials for Energy Conference 2025, Sopot, Poland (18-23,05.2025) **poster presentation**: „Influence of the doping on the properties and phase transition in double perovskite $Sr_2Fe_{1.5}Mo_{0.5}O_6$: synchrotron studies”
10. SOFC-XIX, Stockholm, (12-18.07.2025), **poster presentation** “Nanoparticulate Catalytic Systems for CO_2 Reduction in Solid Oxide Electrolyzer Based on Ni-/Co-Doped Double Perovskites”
11. EFCH2 2025, European Fuel Cells and Hydrogen, Piero Lunghi Conference, Capri, Italy (17-19.09.2025) **oral presentation** „Dual-Doping of Transition Metals into the Double Perovskite $La_{0.3}Sr_{1.7}Fe_{1.5}Mo_{0.5}O_{6-\delta}$ for Potential Electrode Material in SOECs: Increased Stability in Hydrogen”

List of figures

Fig. 1.1. *Scheme of H_2-technology for energy conversion [1].* *14*

Fig. 1.2. *The annual number of publications concerning SOFC or SOEC technologies searched by title in the "Web of Science" [3]* *15*

Fig. 1.3. *Statistics on publications on bimetallic exsolution: compositions (a) and applications (b) [5].* *17*

Fig. 2.1. *The SOFC working principle [3].* *20*

Fig. 2.2. *I-V curve of the SOFC with specific losses [18].* *23*

Fig. 2.3. *I-V curve with power density of the SOFC [1].* *23*

Fig. 2.4. *Nyquist plot of the exemplary EIS measurement with equivalent circuit fitted [19]…* *24*

Fig. 2.5. *DRT spectra of the cell at different operation temperatures [19].* *24*

Fig. 2.6. *The SOEC working principle [3].* *25*

Fig. 2.7. *Energy demand of the H2O and CO2 electrolysis reactions depicting the total energy needed (squares) with an indication of the electricity demand (points) and the heat demand (triangles) [27]* *26*

Fig. 2.8. *The types of materials considered for anode/fuel electrode (a) and cathode/air electrode (b) [3].* *28*

Fig. 2.9. *Electrical conductivity of Ni-YSZ cermets with different Ni content [1]* *29*

Fig. 2.10. *The ionic conductivity in air for most common electrolyte materials [44]* *32*

Fig. 2.11. *The ideal cubic crystal structure of single perovskite ABX_3. Created in VESTA software.* *33*

Fig. 2.12. *The difference between doped single perovskites and ordered double perovskites [68]* *35*

Fig. 2.13. *Representation of different B-site ordering types in double perovskites: (a) rock-salt, (b) layered, and (c) columnar [54].* *36*

Fig. 2.14. *Scheme of disorder in double perovskites: (a) completely ordered, (b) antisite (AS) disorder, and (c) antiphase boundary (APB) [54].* *37*

Fig. 2.15. *Presentation of Mo and Fe d band and O p band center for different Fe:Mo ratio [80].* *40*

Fig. 2.16. *The ideal cubic crystal structure of $Sr_2Fe_{1.5}Mo_{0.5}O_{6-\delta}$. Created in VESTA software.* *40*

Fig. 2.17. *The ideal cubic crystal structure of $Sr_3Fe_{1.5}Mo_{0.5}O_{7-\delta}$. Created in VESTA software.* *42*

Fig. 2.18. *a. The scheme of exsolution process in oxides; b. processes in the exsolution phenomenon: steps include surface, then bulk reduction, ion diffusion, and particle nucleation and growth [101].* *43*

Fig. 2.19. *Change in the Gibbs free energy of reduction reaction of different oxides at various temperatures [7].* *45*

Fig. 2.20. *Co-segregation energies for different dopants in* $PrBaMn_{1.7}T_{0.3}O_{6-\delta}$ *calculated by DFT [105,106].* *45*

Fig. 2.21. *Visual representations of a. wetting angle and b. dihedral angle [108]* *46*

Fig. 2.22. *Change of ΔG during nucleation and growth of nanoparticles [108]* *46*

Fig. 2.23. *Scheme for beneficial exsolution from A-site deficient perovskites [73].* *48*

Fig. 2.24. *A scheme for different exsolution mechanisms and pathways [112].* *49*

Fig. 2.25. *Possible nanoparticle structures for bimetallic exsolution [5].* *50*

Fig. 2.26. *The mechanism of topotactic ion exchange exsolution [105].* *51*

Fig. 2.27. *XRD patterns for transition metal-doped ceria [134].* *53*

Fig. 2.28. $L_{3,2}$*-edges of transition metals in doped ceria [134].* *54*

Fig. 3.1. *Sample prepared for DC4W measurements.* *61*

Fig. 4.1. *XRD diffraction patterns of LSCT-NiM in as-prepared and reduced at 900 °C states.* *68*

Fig. 4.2. *Thermal expansion of the LSCT-NiM bars in the oxidized form.* *68*

Fig. 4.3. *The SEM images of reduced pellets of LSCT-NiM.* *70*

Fig. 4.4. *STEM-ADF image of reduced LSCT-NiCo, STEM-EDS elemental maps of Ni (green) and Co (red) with respect to Ti (blue).* *70*

Fig. 4.5. *(a) TEM image of an exsolved nanoparticle attached to the host matrix; (b) SAED pattern from an area selected inside the host material; (c) SAED pattern from a selected area including the exsolved nanoparticle along with the host material.* *72*

Fig. 4.6. *STEM-ADF image of LSFC-NiFe (up), overlapped (up) and individual (down) large-area STEM-EDS elemental maps of Ce (red), Ti (green) and Sr (blue) revealing the partial segregation of* CeO_2*.* *73*

Fig. 4.7. *STEM-ADF image of exsolved nanoparticle from LSCT-NiFe with respective STEM-EDS elemental maps of Fe (green), Ni (red), and Ti (blue).* *74*

Fig. 4.8. *The Ni K-edges of LSCT-NiM compounds: as-prepared (AP) and reduced (RED). The insets enlarge the changes in edge (inset 1°) and pre-peak (inset 2°).* *76*

Fig. 4.9. *The first (left) and second (right) derivatives of Ni K-edge of LSCT-NiM compounds.* *77*

Fig. 4.10. *Fourier-Transformed EXAFS of Ni K-edges of LSCT-NiM.* *78*

Fig. 4.11. *K-edges of Fe, Co, and Cu in doped LSCT-NiM in as-prepared and reduced states (A.-C.) with corresponding FT-EXAFS spectra (D.-F.).* *79*

Fig. 4.12. *The* $L_{3,2}$*-edges of Ti in doped titanates.* *80*

Fig. 4.13. *$M_{5,4}$-edges of cerium in LSCT-NiM. The peaks from specific Ce oxidation states are marked. 81*

Fig. 4.14. *Electrical conductivity of LSCT-based perovskites measured in air (A.) and in hydrogen after external reduction (B.). The empty shapes represent the calculated conductivity with Bruggeman correction. 83*

Fig. 4.15. *XRD patterns for SFM, LSFM, and SFMNb in as-prepared, reduced and re-oxidized states [98]. 86*

Fig. 4.16*. SEM images of SFM, LSFM, and SFMNb after reduction in hydrogen at 800 °C [98]. 89*

Fig. 4.17. *XRD patterns of reduced SFM, LSFM, and SFMNb during in-situ re-oxidation in air [98]. 90*

Fig. 4.18. *Heatmaps of the normalized XRD peak intensity in SFM, LSFM, and SFMNb during HT-XRD. The close-up on the RP (015) and DP (022) peaks between 2Θ 30.5-33 ° [98]. 90*

Fig. 4.19. *Heatmaps of the normalized XRD peak intensity in SFM and SFMNb during HT-XRD. The close-up on the Fe peak vanishing during the oxidation [98]..... 91*

Fig. 4.20. *DSC/TG curves of reduced SFM, LSFM, and SFMNb powders during re-oxidation in air [98]..... 91*

Fig. 4.21. *Oxygen K-edges of SFM (A.), LSFM (B.), and SFMNb (C.) in as-prepared, reduced, and re-oxidized states, (D.) Fe $L_{3,2}$-edge of iron in reduced compounds [98]. 93*

Fig. 4.22. *K-edge of iron in SFM, LSFM, and SFMNb compounds (A.-C.), L_3-edge of molybdenum for same compounds (D.-F.), and 2nd derivative of Mo L3-edge (G.-I.) All spectra were collected for each sample as-prepared, reduced, and re-oxidized states [98]. 95*

Fig. 4.23*. Fourier-Transformed EXAFS of Fe K-edge in SFM, LSFM, and SFMNb in as-prepared, reduced, and re-oxidized states. The spectra were corrected for phase shift [98]. 96*

Fig. 4.24. *Wavelet-Transformed Fe K-edge of LSFM compound in as-prepared, reduced, and re-oxidized states [98]. 97*

Fig. 4.25. *Temperature dependence of electrical conductivity of SFM, LSFM, and SFMNb measured in air (A. & B.) and hydrogen (C. & D.) [98] 99*

Fig. 4.26. *XRD patterns of Ni- and Co-doped LSFM in as-prepared and reduced states..... 101*

Fig. 4.27. *SEM images of the reduced at 800 °C Ni-doped LSFM with varying Ni concentration. 105*

Fig. 4.28. *STEM image of 10-LSFMNi and 10-LSFMCo with EDS maps of Fe and Ni or Co. 106*

Fig. 4.29. *Electrical conductivity of Ni- and Co-doped LSFM in synthetic air and hydrogen.108*

Fig. 4.30. *Concentration of CO in the outlet gas stream in the catalytic tests for the RWGS reaction. The lines are guides for eyes only. 109*

Fig. 4.31. *XRD patterns of Cu-doped LSFM in as-prepared and reduced (at 750 °C and 800 °C) states.* *111*

Fig. 4.32. *Thermal expansion of LSFCM bars in air.* *113*

Fig. 4.33. *SEM images of the Cu-doped LSFM after reduction at various temperatures.*..... *115*

Fig. 4.34. *STEM image of 15-LSFCM reduced at 750 °C with STEM-EDS elemental maps.*. *116*

Fig. 4.35. *Proposed mechanism of the formation of core-shell nanoparticles in LSFCM compounds.*..... *117*

Fig. 4.36. *H_2-TPR (left) and O_2-TPO (right) profiles of Cu-doped LSFM.* *118*

Fig. 4.37. *Normalized XANES of the K-edges: Fe K-edge in as-prepared (A.), reduced compounds (B.), Cu K-edge in reduced perovskites (C.)*..... *120*

Fig. 4.38. *Fourier-Transformed EXAFS (corrected for phase shift) of the Fe K-edges: as-prepared (A.) and reduced (B.) state. TM: Fe, Cu, Mo* *121*

Fig. 4.39. *Electrical conductivity of LSFCM in synthetic air and hydrogen.* *122*

Fig. 4.40. *SEM images of dendritic structures formed after electrical tests.*..... *123*

Fig. 4.41. *Concentration of CO in the outlet stream for RWGS reaction measured in fixed bed reactor: A. for different compounds, B. for 15-LSFCM in different activation approaches, and C. in time-stability test of 15-LSFCM.* *124*

Fig. 4.42. *XRD patterns of dual-doped LSFM with different Co:Cu and Ni:Cu ratio: as-prepared, reduced at 750 °C, and reduced at 800 °C.*..... *130*

Fig. 4.43. *SEM images of reduced (800 °C) dual-doped LSFM with different Co:Cu and Ni:Cu ratio.* *131*

Fig. 4.44. *HRTEM image of the exsolved nanoparticle from 10-10-LSFNCM, STEM-ADF image with corresponding elemental maps.* *132*

List of tables

Tab. 2.1. *Summary of order in $A_2BB'O_6$ double perovskites [54]..... 38*

Tab. 2.2. *The exemplary double perovskites, their ordering, structure, and potential application in SOCs [68]. 39*

Tab. 3.1. *The summary of synthesized double-perovskite compounds based on $Sr_2Fe_{1.5}Mo_{0.5}O_{6-\delta}$. 56*

Tab. 4.1. *Lattice unit constants and concentration of impurities in STO-based compounds. The goodness of fit was below 2. ..... 67*

Tab. 4.2. *Atomic concentration obtained from EDS method on TEM lamella of LSCT-NiCo with respect to host and nanoparticle exsolved. 71*

Tab. 4.3*. Atomic concentration obtained from EDS method on TEM lamella of LSCT-NiFe with respect to host and two different nanoparticles exsolved..... 74*

Tab. 4.4*. The density and porosity of as-prepared and reduced LSCT-based pellets measured and calculated using Archimedes principle. The values are given with 5% uncertainty. 82*

Tab. 4.5. *The lattice constants for SFM, LSFM, SFMNb in as-prepared, reduced and re-oxidized states. The values were calculated from the Rietveld refinement [98]. 88*

Tab. 4.6. *Activation energy of electrical conduction for SFM, LSFM, and SFMNb [98]..... 99*

Tab. 4.7*. Lattice constants and specific phase concentrations of as-prepared and reduced LSFMs doped with cobalt or nickel. 103*

Tab. 4.8. *The unit cell parameters for different Cu-doped LSFM. For reduced compounds, the amount of foreign phase is calculated. 112*

Tab. 4.9. *Calculated thermal expansion coefficient for reference and Cu-doped double perovskites.....114*

Tab. 4.10. *Specific surface area of Cu-doped compounds after milling. Apparatus uncertainty is 5%. 124*

Literature

[1] O'Hayre R, Cha S-W, Colella W, Prinz F. Fuel cell fundamentals. 2023. https://doi.org/10.1016/B978-0-323-99485-9.00006-X.

[2] Choudhury A, Chandra H, Arora A. Application of solid oxide fuel cell technology for power generation - A review. Renewable and Sustainable Energy Reviews 2013;20:430–42. https://doi.org/10.1016/j.rser.2012.11.031.

[3] Feng P, Yang K, Liu X, Zhang J, Li Z-P. A review of advanced SOFCs and SOECs: Materials, innovative synthesis, functional mechanisms, and system integration. EScience 2026;6:100460. https://doi.org/10.1016/j.esci.2025.100460.

[4] Tayari F, Teixeira SS, Graca MPF, Nassar KI. A Comprehensive Review of Recent Advances in Perovskite Materials: Electrical, Dielectric, and Magnetic Properties. Inorganics 2025, Vol 13, Page 67 2025;13:67. https://doi.org/10.3390/inorganics13030067.

[5] Tang C, Kousi K, Neagu D, Metcalfe IS. Trends and Prospects of Bimetallic Exsolution. Chemistry - A European Journal 2021;27:6666–75. https://doi.org/10.1002/chem.202004950.

[6] Tsiotsias AI, Charisiou ND, Yentekakis I V., Goula MA. Bimetallic Ni-based catalysts for CO2 methanation: A review. Nanomaterials 2021;11:1–34. https://doi.org/10.3390/nano11010028.

[7] Kim YH, Jeong H, Won BR, Jeon H, Park C ho, Park D, et al. Nanoparticle Exsolution on Perovskite Oxides: Insights into Mechanism, Characteristics and Novel Strategies. Nano-Micro Letters 2023 16:1 2023;16:33-. https://doi.org/10.1007/s40820-023-01258-4.

[8] Mariani P, Sun X, Mascotto S, Raimondo L, Sassella A, Monticelli D, et al. Critical assessment of the exsolution process in Cu-doped SrTiO3 by a combined spectroscopic approach. Inorg Chem Front 2024;12:311–27. https://doi.org/10.1039/d4qi02391a.

[9] Mariani P, Orsilli J, Stoffel H, Mascotto S, Monticelli D, Berretti E, et al. Bimetallic Fe–Ni exsolution from A site deficient SrTiO3: insight into the reciprocal role of metal active centers. Inorg Chem Front 2026. https://doi.org/10.1039/d5qi02469b.

[10] Tang YX, Zhang Q, Wang YM, Zhou XL, Zhang M, Yuan RH, et al. Regulating catalytic activity with geometry distortion of Sr2FeMoO6 anode. J Alloys Compd 2025;1024:180113. https://doi.org/10.1016/j.jallcom.2025.180113.

[11] Li Y, Singh M, Zhuang Z, Jing Y, Li F, Maliutina K. Efficient reversible CO / CO2 conversion in solid oxide cells with a phase-transformed fuel electrode. Sci China Mater 2021;64:1114–26. https://doi.org/https://doi.org/10.1007/s40843-020-1531-7.

[12] Osinkin DA, Antonova EP, Shubin KS, Bogdanovich NM. Influence of nickel exsolution on the electrochemical performance and rate-determining stages of hydrogen oxidation on Sr1.95Fe1.4Ni0.1Mo0.5O6-δ promising electrode for solid state electrochemical devices. Electrochim Acta 2021;369:137673. https://doi.org/10.1016/j.electacta.2020.137673.

[13] Yang Y, Wang Y, Yang Z, Chen Y, Peng S. A highly active and durable electrode with in situ exsolved Co nanoparticles for solid oxide electrolysis cells. J Power Sources 2020;478:229082. https://doi.org/10.1016/J.JPOWSOUR.2020.229082.

[14] Feng J, Yang G, Dai N, Wang Z, Sun W, Rooney D, et al. Investigation into the effect of Fe-site substitution on the performance of Sr2Fe1.5Mo0.5O6 anodes for SOFCs 2014. https://doi.org/10.1039/c4ta03216k.

[15] Gou M, Ren R, Sun W, Xu C, Meng X, Wang Z, et al. Nb-doped Sr2Fe1.5Mo0.5O6-δ electrode with enhanced stability and electrochemical performance for symmetrical solid oxide fuel cells. Ceram Int 2019;45:15696–704. https://doi.org/10.1016/j.ceramint.2019.03.130.

[16] Lv H, Lin L, Zhang X, Song Y, Matsumoto H, Zeng C, et al. In Situ Investigation of Reversible Exsolution/Dissolution of CoFe Alloy Nanoparticles in a Co-Doped Sr2Fe1.5Mo0.5O6−δ Cathode for CO2 Electrolysis. Advanced Materials 2020;32. https://doi.org/10.1002/ADMA.201906193.

[17] Lv H, Lin L, Zhang X, Gao D, Song Y, Zhou Y, et al. In situ exsolved FeNi3 nanoparticles on nickel doped Sr2Fe1.5Mo0.5O6-δ perovskite for efficient electrochemical CO2 reduction reaction. J Mater Chem A Mater 2019;7:11967–75. https://doi.org/10.1039/c9ta03065d.

[18] Gebregergis A, Pillay P, Bhattacharyya D, Rengaswemy R. Solid Oxide Fuel Cell Modeling. IEEE Transactions on Industrial Electronics 2009;56:139–48. https://doi.org/10.1109/TIE.2008.2009516.

[19] Błaszczak P, Mäkinen P, Mroziński A, **Ducka A**, Jasiński G, Himanen O, et al. Uncovering the electrochemical processes and understanding the causes of the degradation via EIS-DRT in large-scale solid oxide fuel cell. Appl Energy 2025;393:125983. https://doi.org/10.1016/j.apenergy.2025.125983.

[20] Zhao X, Joseph B, Kuhn J, Ozcan S. Biogas Reforming to Syngas: A Review. IScience 2020;23:101082. https://doi.org/10.1016/J.ISCI.2020.101082.

[21] Skutina L, Filonova E, Medvedev D, Maignan A. Undoped Sr2MMoO6 Double Perovskite Molybdates (M = Ni, Mg, Fe) as Promising Anode Materials for Solid Oxide Fuel Cells. Materials 2021;14. https://doi.org/10.3390/MA14071715.

[22] Saadabadi SA, Illathukandy B, Aravind PV. Direct internal methane reforming in biogas fuelled solid oxide fuel cell; the influence of operating parameters. Energy Sci Eng 2021;9:1232–48. https://doi.org/10.1002/ESE3.887.

[23] Bochentyn B, Chlipała M, Gazda M, Wang SF, Jasiński P. Copper and cobalt co-doped ceria as an anode catalyst for DIR-SOFCs fueled by biogas. Solid State Ion 2019;330:47–53. https://doi.org/10.1016/j.ssi.2018.12.007.

[24] Błaszczak P, Łapiński M, Wang SF, Jasiński P, Bochentyn B. Exsolution of Ni nanoparticles on the surface of cerium and nickel co-doped lanthanum strontium titanate as a new anodic layer for DIR-SOFC. Anti-coking potential and H2S poisoning resistance of the prepared material. Int J Hydrogen Energy 2020;45:29186–200. https://doi.org/10.1016/j.ijhydene.2020.07.162.

[25] Bochentyn B, Błaszczak P, Gazda M, Fuerte A, Wang SF, Jasiński P. Investigation of praseodymium and samarium co-doped ceria as an anode catalyst for DIR-SOFC fueled by biogas. Int J Hydrogen Energy 2020;45:29131–42. https://doi.org/10.1016/j.ijhydene.2020.07.146.

[26] Hołówko B, Błaszczak P, Chlipała M, Gazda M, Wang SF, Jasiński P, et al. Structural and catalytic properties of ceria layers doped with transition metals for SOFCs fueled by biogas. Int J Hydrogen Energy 2020;45:12982–96. https://doi.org/10.1016/j.ijhydene.2020.02.144.

[27] Riedel M, Heddrich MPP, Friedrich KAA. Experimental Analysis of the Co-Electrolysis Operation under Pressurized Conditions with a 10 Layer SOC Stack. J Electrochem Soc 2020;167:024504. https://doi.org/10.1149/1945-7111/ab6820.

[28] Ioannidou E, Neophytides S, Niakolas DK. Experimental Clarification of the RWGS Reaction Effect in H2O/CO2 SOEC Co-Electrolysis Conditions. Catalysts 2019, Vol 9, Page 151 2019;9:151. https://doi.org/10.3390/CATAL9020151.

[29] Stoots CM, O'Brien JE, Herring JS, Hartvigsen JJ. Syngas production via high-temperature coelectrolysis of steam and carbon dioxide. J Fuel Cell Sci Technol 2009;6:0110141–01101412. https://doi.org/10.1115/1.2971061.

[30] Zhang X, Song Y, Wang G, Bao X. Co-electrolysis of CO2 and H2O in high-temperature solid oxide electrolysis cells: Recent advance in cathodes. Journal of Energy Chemistry 2017;26:839–53. https://doi.org/10.1016/j.jechem.2017.07.003.

[31] Błaszczak P, Zając M, **Ducka A**, Matlak K, Wolanin B, Wang S-F, et al. High-temperature Co-electrolysis of CO2/H2O and direct methanation over Co-impregnated SOEC. Bimetallic synergy between Co and Ni. Int J Hydrogen Energy 2022. https://doi.org/10.1016/J.IJHYDENE.2022.08.057.

[32] Chen X, Guan C, Xiao G, Du X, Wang JQ. Syngas production by high temperature steam/CO2 coelectrolysis using solid oxide electrolysis cells. Faraday Discuss 2015;182:341–51. https://doi.org/10.1039/c5fd00017c.

[33] Wang Y, Liu T, Lei L, Chen F. High temperature solid oxide H2O/CO2 co-electrolysis for syngas production. Fuel Processing Technology 2017;161:248–58. https://doi.org/10.1016/j.fuproc.2016.08.009.

[34] Yue X, Irvine JTS. (La,Sr)(Cr,Mn)O3/GDC cathode for high temperature steam electrolysis and steam-carbon dioxide co-electrolysis. Solid State Ion 2012;225:131–5. https://doi.org/10.1016/J.SSI.2012.06.015.

[35] Stambouli AB, Traversa E. Solid oxide fuel cells (SOFCs): A review of an environmentally clean and efficient source of energy. Renewable and Sustainable Energy Reviews 2002;6:433–55. https://doi.org/10.1016/S1364-0321(02)00014-X.

[36] Atkinson A, Barnett S, Gorte RJ, Irvine JTSS, McEvoy AJ, Mogensen M, et al. Advanced anodes for high-temperature fuel cells. vol. 3. European Association for Cardio-Thoracic Surgery; 2004. https://doi.org/10.1038/NMAT1040.

[37] Hussain S, Yangping L. Review of solid oxide fuel cell materials: cathode, anode, and electrolyte. Energy Transitions 2020;4:113–26. https://doi.org/10.1007/s41825-020-00029-8.

[38] Goodenough JB, Huang YH. Alternative anode materials for solid oxide fuel cells. J Power Sources 2007;173:1–10. https://doi.org/10.1016/j.jpowsour.2007.08.011.

[39] Shu L, Sunarso J, Hashim SS, Mao J, Zhou W, Liang F. Advanced perovskite anodes for solid oxide fuel cells: A review. Int J Hydrogen Energy 2019;44:31275–304. https://doi.org/10.1016/j.ijhydene.2019.09.220.

[40] Nechache A, Hody S. Alternative and innovative solid oxide electrolysis cell materials: A short review. Renewable and Sustainable Energy Reviews 2021;149. https://doi.org/10.1016/j.rser.2021.111322.

[41] Błaszczak P, **Ducka A**, Wolanin B, Matlak K, Machowski G, Prześniak-Welenc M, et al. Fabrication of wormhole-like YSZ and Ni-YSZ by the novel soft-hard template CTAB/NaCl-assisted route. Suppressing Ni coalescence in SOFC. J Eur Ceram Soc 2023;43:438–51. https://doi.org/10.1016/j.jeurceramsoc.2022.09.054.

[42] Liu Z, Zhao Z, Shang L, Ou D, Cui D, Tu B, et al. LSM-YSZ nano-composite cathode with YSZ interlayer for solid oxide fuel cells. Journal of Energy Chemistry 2017;26:510–4. https://doi.org/10.1016/j.jechem.2016.11.019.

[43] Petric A, Huang P, Tietz F. Evaluation of La–Sr–Co–Fe–O perovskites for solid oxide fuel cells and gas separation membranes. Solid State Ion 2000;135:719–25. https://doi.org/10.1016/S0167-2738(00)00394-5.

[44] Kharton V V., Marques FMB, Atkinson A. Transport properties of solid oxide electrolyte ceramics: a brief review. Solid State Ion 2004;174:135–49. https://doi.org/10.1016/j.ssi.2004.06.015.

[45] Cawley JD. Binary Oxide Ceramics: Al2O3, ZrO2, Structure and Properties of. Encyclopedia of Materials: Science and Technology 2001:524–33. https://doi.org/10.1016/b0-08-043152-6/00100-5.

[46] Rahmawati F, Permadani I, Syarif DG, Soepriyanto S. Electrical properties of various composition of yttrium Doped-Zirconia prepared from local zircon sand. International Journal of Technology 2017;8:939–46. https://doi.org/10.14716/ijtech.v8i5.876.

[47] Sepúlveda E, Mangalaraja R V., Udayabhaskar R, Cobo R, Berzal ME, Jiménez J, et al. Preparation of LSGM electrolyte via fast combustion method and analysis of electrical properties for ReSOC. Journal of Electroceramics 2022 49:2 2022;49:85–93. https://doi.org/10.1007/s10832-022-00294-7.

[48] Alvarado-Flores JJ, Mondragón-Sánchez R, Ávalos-Rodríguez ML, Alcaraz-Vera JV, Rutiaga-Quiñones JG, Guevara-Martínez SJ. Synthesis, characterization and kinetic study of the Sr2FeMoO6-δ double perovskite: New findings on the calcination of one of its precursors. Int J Hydrogen Energy 2021;46:26185–96. https://doi.org/10.1016/J.IJHYDENE.2021.01.191.

[49] Du Z, Zhao H, Yi S, Xia Q, Gong Y, Zhang Y, et al. High-Performance Anode Material Sr2FeMo0.65Ni0.35O6−δ with In Situ Exsolved Nanoparticle Catalyst. ACS Nano 2016;18:31. https://doi.org/10.1021/acsnano.6b03979.

[50] Kim GS, Lee BY, Accardo G, Ham HC, Moon J, Yoon SP. Improved catalytic activity under internal reforming solid oxide fuel cell over new rhodium-doped perovskite catalyst. J Power Sources 2019;423:305–15. https://doi.org/10.1016/j.jpowsour.2019.03.082.

[51] Ding H, Tao Z, Liu S, Yang Y. A redox-stable direct-methane solid oxide fuel cell (SOFC) with Sr2FeNb0.2Mo0.8O6−δ double perovskite as anode material. J Power Sources 2016;327:573–9. https://doi.org/10.1016/J.JPOWSOUR.2016.07.101.

[52] Bian L, Duan C, Wang L, Chen Z, Hou Y, Peng J, et al. An all-oxide electrolysis cells for syngas production with tunable H 2 / CO yield via co-electrolysis of H 2 O and CO 2. J Power Sources 2021;482:228887. https://doi.org/10.1016/j.jpowsour.2020.228887.

[53] Bartel CJ, Sutton C, Goldsmith BR, Ouyang R, Musgrave CB, Ghiringhelli LM, et al. New tolerance factor to predict the stability of perovskite oxides and halides. Sci Adv 2019;5. https://doi.org/10.1126/sciadv.aav0693.

[54] Vasala S, Karppinen M. A2B′B″O6 perovskites: A review. Progress in Solid State Chemistry 2015;43:1–36. https://doi.org/10.1016/j.progsolidstchem.2014.08.001.

[55] Sato T, Takagi S, Deledda S, Hauback BC, Orimo S-I. Extending the applicability of the Goldschmidt tolerance factor to arbitrary ionic compounds OPEN 2016. https://doi.org/10.1038/srep23592.

[56] Li Z, Yang M, Park JS, Wei SH, Berry JJ, Zhu K. Stabilizing Perovskite Structures by Tuning Tolerance Factor: Formation of Formamidinium and Cesium Lead Iodide Solid-State Alloys. Chemistry of Materials 2015;28:284–92. https://doi.org/10.1021/acs.chemmater.5b04107.

[57] McColm TD, Irvine JTS. B site doped strontium titanate as a potential SOFC substrate. Ionics (Kiel) 2001;7:116–21. https://doi.org/10.1007/BF02375477/METRICS.

[58] Park KB, Choi J, Na TW, Kang JW, Park K, Park HK. Oxygen Reduction Behavior of HDH TiH2 Powder during Dehydrogenation Reaction. Metals 2019, Vol 9, Page 1154 2019;9:1154. https://doi.org/10.3390/met9111154.

[59] Tao S, Irvine JTS. Discovery and Characterization of Novel Oxide Anodes for Solid Oxide Fuel Cells. Chem Rec 2004;4:83–95. https://doi.org/10.1002/tcr.20003.

[60] Alves Lima Almeida D, Polo Fonseca C, Gomes Ferreira - N, Furukawa R, Mijanur Rahman M, Kaneta Y, et al. Strontium Titanate-based Composite Anodes for Solid Oxide Fuel Cells. ECS Trans 2008;13:181. https://doi.org/10.1149/1.3050390.

[61] Mahato N, Banerjee A, Gupta A, Omar S, Balani K. Progress in material selection for solid oxide fuel cell technology: A review. Prog Mater Sci 2015;72:141–337. https://doi.org/10.1016/j.pmatsci.2015.01.001.

[62] Kyriakou V, Neagu D, Papaioannou EI, Metcalfe IS, Sanden MCM Van De, Tsampas MN. Co-electrolysis of H2O and CO2 on exsolved Ni nanoparticles for efficient syngas generation at controllable H2/CO ratios. Appl Catal B 2019:117950. https://doi.org/10.1016/j.apcatb.2019.117950.

[63] O'Leary W, Giordano L, Park J, Nonnenmann SS, Shao-Horn Y, Rupp JLM. Influence of Sr-Site Deficiency, Ca/Ba/La Doping on the Exsolution of Ni from SrTiO 3 . J Am Chem Soc 2023;145:13768–79. https://doi.org/10.1021/jacs.2c12011.

[64] Mizera A, Kowalczyk A, Chmielarz L, Drożdż E. Catalysts based on strontium titanate doped with Ni/Co/Cu for dry reforming of methane. Materials 2021;14. https://doi.org/10.3390/ma14237227.

[65] Chien AC, Liao BY, Chen WY, Chien AC. Studies of exsolution and catalytic activity of metal nanocatalysts from parent perovskite. Catal Sci Technol 2021;11:4570–80. https://doi.org/10.1039/d1cy00530h.

[66] Cavazzani J, Squizzato E, Brusamarello E, Glisenti A. Exsolution in Ni-doped lanthanum strontium titanate: a perovskite-based material for anode application in ammonia-fed Solid Oxide Fuel Cell. Int J Hydrogen Energy 2022. https://doi.org/10.1016/J.IJHYDENE.2022.02.133.

[67] Ren H, Zhi G, Chen C, Fang H, Lin Z, Lin L, et al. In situ exsolution of Ni–Co alloys from A-site-deficient perovskite for efficient ammonia decomposition. Int J Hydrogen Energy 2024;96:385–95. https://doi.org/10.1016/j.ijhydene.2024.11.315.

[68] Xu X, Zhong Y, Shao Z. Double Perovskites in Catalysis, Electrocatalysis, and Photo(electro)catalysis. Trends Chem 2019;1:410–24. https://doi.org/10.1016/j.trechm.2019.05.006.

[69] Thommy L, Joubert O, Hamon J, Caldes MT. Impregnation versus exsolution: Using metal catalysts to improve electrocatalytic properties of LSCM-based anodes operating at 600 °C. Int J Hydrogen Energy 2016;41:14207–16. https://doi.org/10.1016/j.ijhydene.2016.06.088.

[70] Li J, Wei B, Yue X, Zhe L. A Highly Efficient and Robust Perovskite Anode with Iron–Palladium Co-exsolutions for Intermediate-Temperature Solid-Oxide Fuel Cells. ChemSusChem 2018;11:2593–603. https://doi.org/10.1002/cssc.201800641.

[71] Neagu D, Irvine JTS. Enhancing electronic conductivity in strontium titanates through correlated A and B-site doping. Chemistry of Materials 2011;23:1607–17. https://doi.org/10.1021/CM103489R/ASSET/IMAGES/CM103489R.SOCIAL.JPEG_V03.

[72] Neagu D, Oh TS, Miller DN, Ménard H, Bukhari SM, Gamble SR, et al. Nano-socketed nickel particles with enhanced coking resistance grown in situ by redox exsolution. Nat Commun 2015;6. https://doi.org/10.1038/ncomms9120.

[73] Neagu D, Tsekouras G, Miller DN, Ménard H, Irvine JTS. In situ growth of nanoparticles through control of non-stoichiometry. Nat Chem 2013;5:916–23. https://doi.org/10.1038/nchem.1773.

[74] Gao Y, Lu Z, You TL, Wang J, Xie L, He J, et al. Energetics of Nanoparticle Exsolution from Perovskite Oxides. Journal of Physical Chemistry Letters 2018;9:3772–8. https://doi.org/10.1021/acs.jpclett.8b01380.

[75] King G, Woodward PM. Cation ordering in perovskites. J Mater Chem 2010;20:5785–96. https://doi.org/10.1039/b926757c.

[76] Cussen EJ, Battle PD. The influence of structural disorder on the magnetic properties of Sr2Fe1 − xGaxTaO6(0 ≤x≤ 1). J Mater Chem 2003;13:1210–4. https://doi.org/10.1039/b211286h.

[77] Vasala S, Lehtimäki M, Haw SC, Chen JM, Liu RS, Yamauchi H, et al. Isovalent and aliovalent substitution effects on redox chemistry of Sr2MgMoO6 - δ SOFC-anode material. Solid State Ion 2010;181:754–9. https://doi.org/10.1016/J.SSI.2010.03.037.

[78] Wang FY, Zhong G Bin, Luo S, Xia L, Fang LH, Song X, et al. Porous Sr2MgMo1 − xVxO6 − d ceramics as anode materials for SOFCs using biogas fuel. Catal Commun 2015;67:108–11. https://doi.org/10.1016/j.catcom.2015.04.019.

[79] Cernea M, Vasiliu F, Plapcianu C, Bartha C, Mercioniu I, Pasuk I, et al. Preparation by sol–gel and solid state reaction methods and properties investigation of double perovskite Sr2FeMoO6. J Eur Ceram Soc 2013;33:2483–90. https://doi.org/10.1016/J.JEURCERAMSOC.2013.03.026.

[80] Xi XA, Liu JW, Luo WZ, Fan Y, Zhang JJ, Luo J-LJ-LL, et al. Unraveling the Enhanced Kinetics of Sr2Fe1+xMo1-xO6-δ Electrocatalysts for High-Performance Solid Oxide Cells. Adv Energy Mater 2021;11:1–10. https://doi.org/10.1002/aenm.202102845.

[81] Su C, Wang W, Liu M, Tadé MO, Shao Z. Progress and Prospects in Symmetrical Solid Oxide Fuel Cells with Two Identical Electrodes. Adv Energy Mater 2015;5. https://doi.org/10.1002/AENM.201500188.

[82] Skutina LS, Vylkov AI, Bainov IN, Chistyakov KA, Kuznetsov DK, Pavlenko OB, et al. Catalytic properties of Sr2Ni0.75Mg0.25MoO6–δ based composites for application in hydrocarbon-fuelled solid oxide fuel cells. Int J Hydrogen Energy 2021;46:16899–906. https://doi.org/10.1016/j.ijhydene.2021.03.159.

[83] Skutina LS, Vylkov AI, Medvedev DA, Filonova EA. Features of structural, thermal and electrical properties of Mo-based composite materials as fuel electrodes for high-temperature applications. J Alloys Compd 2017;705:854–61. https://doi.org/10.1016/j.jallcom.2017.02.193.

[84] Liu Q, Dong X, Xiao G, Zhao F, Chen F. A novel electrode material for symmetrical SOFCs. Advanced Materials 2010;22:5478–82. https://doi.org/10.1002/adma.201001044.

[85] Dos Santos-Gómez L, León-Reina L, Porras-Vázquez JM, Losilla ER, Marrero-López D. Chemical stability and compatibility of double perovskite anode materials for SOFCs. Solid State Ion 2013;239:1–7. https://doi.org/10.1016/J.SSI.2013.03.005.

[86] Xi X, Fan Y, Zhang J, Luo J, Fu X. In situ construction of hetero-structured perovskite composites with exsolved Fe and Cu metallic nanoparticles as efficient CO2 reduction electrocatalysts for high performance solid oxide electrolysis cells. J Mater Chem A Mater 2022;10:2509–18. https://doi.org/10.1039/d1ta07678g.

[87] Wang Y, Liu T, Liu · Tong. A highly active and stable Sr2Fe1.5Mo0.5O6-δ-Ce0.8Sm0.2O1.95 ceramic fuel electrode for efficient hydrogen production via a steam electrolyzer without safe gas. Int J Coal Sci Technol 2022;8:4–11. https://doi.org/10.1007/s40789-022-00470-8.

[88] Wright JH, Virkar A V., Liu Q, Chen F. Electrical characterization and water sensitivity of Sr2Fe1.5Mo0.5O6−δ as a possible solid oxide fuel cell electrode. J Power Sources 2013;237:13–8. https://doi.org/10.1016/j.jpowsour.2013.02.079.

[89] Yang Y, Wang YY, Yang Z, Lei Z, Jin C, Liu Y, et al. Co-substituted Sr 2 Fe 1.5 Mo 0.5 O 6-δ as anode materials for solid oxide fuel cells: Achieving high performance via nanoparticle exsolution. J Power Sources 2019;438:226989. https://doi.org/10.1016/j.jpowsour.2019.226989.

[90] Xu C, Sun W, Ren R, Yang X, Ma M, Qiao J, et al. A highly active and carbon-tolerant anode decorated with in situ grown cobalt nano-catalyst for intermediate-temperature solid oxide fuel cells. Appl Catal B n.d.;282:119553.

[91] Wang Y, Liu T, Li M, Xia C, Zhou B, Chen F. Exsolved Fe–Ni nano-particles from Sr2Fe1.3Ni0.2Mo0.5O6 perovskite oxide as a cathode for solid oxide steam electrolysis cells. J Mater Chem A Mater 2016;4:14163–9. https://doi.org/10.1039/c6ta06078a.

[92] Ruddlesden SN, Popper P. The compound Sr 3 Ti 2 O 7 and its structure . Acta Crystallogr 1958;11:54–5. https://doi.org/10.1107/s0365110x58000128.

[93] Zhou C-L, Ma W-B, Zhang Z-L, - al, Davis M, Yu Z, et al. Review on Ruddlesden–Popper perovskites as cathode for solid oxide fuel cells. Journal of Physics: Materials 2021;4:022002. https://doi.org/10.1088/2515-7639/abe392.

[94] Veith GM, Greenblatt M, Croft M, Ramanujachary K V., Hattrick-Simpers J, Lofland SE, et al. Synthesis and characterization of Sr 3FeMoO 6.88:: An oxygen-deficient 2D analogue of the double perovskite Sr 2FeMoO 6. Chemistry of Materials 2005;17:2562–7. https://doi.org/10.1021/cm048839r.

[95] Chroneos A, Parfitt D, Kilner JA, Grimes RW. Anisotropic oxygen diffusion in tetragonal La2NiO4+δ: molecular dynamics calculations. J Mater Chem 2009;20:266–70. https://doi.org/10.1039/b917118e.

[96] Shan P, Ye H, Qian B, Zheng Y, Xiao G. Boosting the catalytic activity of high-order Ruddlesden–Popper perovskite SrEu2Fe2O7-δ air electrode by A-site La doping for CO2 electrolysis in solid oxide electrolysis cells. Fuel 2024;367:131507. https://doi.org/10.1016/j.fuel.2024.131507.

[97] Park S, Kim Y, Han H, Chung YS, Yoon W, Choi J, et al. In situ exsolved Co nanoparticles on Ruddlesden-Popper material as highly active catalyst for CO2 electrolysis to CO. Appl Catal B 2019;248:147–56. https://doi.org/10.1016/j.apcatb.2019.02.013.

[98] **Ducka A**, Błaszczak P, Zając M, Maximenko A, Gazda M, Bochentyn B. Investigation of the phase transition to the Ruddlesden-Popper phase in La- or Nb-doped Sr2Fe1.5Mo0.5O6-δ double perovskites. Impact of lanthanum or niobium doping. Nanoscale 2025:12371–84.

[99] Wang Z, Yin YM, Yu Y, Song Y, Ma ZF, Yin J. Roles of Fe-Ni nanoparticles and SrLaFeO4 substrate in the performance and reliability of a composite anode prepared through in-situ

exsolution for intermediate temperature solid oxide fuel cells (I). Int J Hydrogen Energy 2018;43:10440–7. https://doi.org/10.1016/J.IJHYDENE.2018.04.090.

[100] Kim JH, Kim JK, Liu J, Curcio A, Jang JS, Kim ID, et al. Nanoparticle Ex-solution for Supported Catalysts: Materials Design, Mechanism and Future Perspectives. ACS Nano 2021;15:81–110. https://doi.org/10.1021/acsnano.0c07105.

[101] Kousi K, Tang C, Metcalfe IS, Neagu D, Kousi K, Metcalfe S, et al. Emergence and Future of Exsolved Materials. Small 2021. https://doi.org/10.1002/smll.202006479.

[102] Papaioannou EI, Neagu D, Ramli WKW, Irvine JTS, Metcalfe IS. Sulfur-Tolerant, Exsolved Fe–Ni Alloy Nanoparticles for CO Oxidation. Top Catal 2019;62:1149–56. https://doi.org/10.1007/S11244-018-1053-8/FIGURES/6.

[103] Kothari M, Jeon Y, Miller DN, Pascui AE, Kilmartin J, Wails D, et al. Platinum incorporation into titanate perovskites to deliver emergent active and stable platinum nanoparticles. Nat Chem 2021;13:677–82. https://doi.org/10.1038/s41557-021-00696-0.

[104] Schmalzried H, Backhaus-Ricoult M. Internal Solid State Reactions. Progress in Solid State Chemistry 1993;22:1–57.

[105] Joo S, Kwon O, Kim K, Kim S, Kim H, Shin J, et al. Cation-swapped homogeneous nanoparticles in perovskite oxides for high power density. Nat Commun 2019;10:1–9. https://doi.org/10.1038/s41467-019-08624-0.

[106] Kwon O, Sengodan S, Kim K, Kim GG, Jeong HY, Shin J, et al. Exsolution trends and co-segregation aspects of self-grown catalyst nanoparticles in perovskites. Nat Commun 2017;8:1–7. https://doi.org/10.1038/ncomms15967.

[107] Neagu D, Irvine JTS, Wang J, Yildiz B, Opitz AK, Fleig J, et al. Roadmap on exsolution for energy applications. Journal of Physics: Energy 2023;5:031501. https://doi.org/10.1088/2515-7655/acd146.

[108] Gao Y, Chen D, Saccoccio M, Lu Z, Ciucci F. From material design to mechanism study: Nanoscale Ni exsolution on a highly active A-site deficient anode material for solid oxide fuel cells. Nano Energy 2016;27:499–508. https://doi.org/10.1016/j.nanoen.2016.07.013.

[109] Neagu D, Kyriakou V, Roiban I-L, Aouine M, Tang C, Caravaca A, et al. In Situ Observation of Nanoparticle Exsolution from Perovskite Oxides: From Atomic Scale Mechanistic Insight to Nanostructure Tailoring. ACS Nano 2019:12996–3005. https://doi.org/10.1021/acsnano.9b05652.

[110] Jo YR, Koo B, Seo MJ, Kim JK, Lee S, Kim K, et al. Growth Kinetics of Individual Co Particles Ex-solved on SrTi0.75Co0.25O3-δ Polycrystalline Perovskite Thin Films. J Am Chem Soc 2019;141:6690–7. https://doi.org/10.1021/jacs.9b01882.

[111] Kim YH, Jeong H, Won BR, Myung J ha. Exsolution Modeling and Control to Improve the Catalytic Activity of Nanostructured Electrodes. Advanced Materials 2023;35:2208984. https://doi.org/10.1002/adma.202208984.

[112] Kwon O, Joo S, Choi S, Sengodan S, Kim G. Review on exsolution and its driving forces in perovskites. JPhys Energy 2020;2. https://doi.org/10.1088/2515-7655/ab8c1f.

[113] Myung JH, Neagu D, Miller DN, Irvine JTS. Switching on electrocatalytic activity in solid oxide cells. Nature 2016 537:7621 2016;537:528–31. https://doi.org/10.1038/nature19090.

[114] Kwak NW, Jeong SJ, Seo HG, Lee S, Kim YJ, Kim JK, et al. In situ synthesis of supported metal nanocatalysts through heterogeneous doping. Nat Commun 2018;9:1–8. https://doi.org/10.1038/s41467-018-07050-y.

[115] Li J, Yu Y, Yin YM, Zhou N, Ma ZF. A novel high performance composite anode with in situ growth of Fe-Ni alloy nanoparticles for intermediate solid oxide fuel cells. Electrochim Acta 2017;235:317–22. https://doi.org/10.1016/j.electacta.2017.03.103.

[116] Lu J, Zhu C, Pan C, Lin W, Lemmon JP, Chen F, et al. Highly efficient electrochemical reforming of CH4/CO2 in a solid oxide electrolyser. Sci Adv 2018;4. https://doi.org/10.1126/sciadv.aar5100.

[117] Choi YM, Compson C, Lin MC, Liu M. Ab initio analysis of sulfur tolerance of Ni, Cu, and Ni-Cu alloys for solid oxide fuel cells. J Alloys Compd 2007;427:25–9. https://doi.org/10.1016/j.jallcom.2006.03.009.

[118] Cheng Z, Wang JH, Choi Y, Yang L, Lin MC, Liu M. From Ni-YSZ to sulfur-tolerant anode materials for SOFCs: Electrochemical behavior, in situ characterization, modeling, and future perspectives. Energy Environ Sci 2011;4:4380–409. https://doi.org/10.1039/c1ee01758f.

[119] Buharon M, Singh S, Komarala EP, Rosen BA. Expanding possibilities for solid-phase crystallization by exsolving tunable Pd-NiO core-shell nanostructures. CrystEngComm 2018;20:6372–6. https://doi.org/10.1039/c8ce01294f.

[120] Horlick SA, Huang YL, Robinson IA, Wachsman ED. Controlling exsolution with a charge-balanced doping approach. Nano Energy 2021;87:106193. https://doi.org/10.1016/j.nanoen.2021.106193.

[121] Joo S, Seong A, Kwon O, Kim K, Lee JH, Gorte RJ, et al. Highly active dry methane reforming catalysts with boosted in situ grown Ni-Fe nanoparticles on perovskite via atomic layer deposition. Sci Adv 2020;6:1–9. https://doi.org/10.1126/sciadv.abb1573.

[122] Islam QA, Paydar S, Akbar N, Zhu B, Wu Y. Nanoparticle exsolution in perovskite oxide and its sustainable electrochemical energy systems. J Power Sources 2021;492:229626. https://doi.org/10.1016/j.jpowsour.2021.229626.

[123] Lin C, Jang JB, Zhang L, Stach EA, Gorte RJ. Improved Coking Resistance of “intelligent” Ni Catalysts Prepared by Atomic Layer Deposition. ACS Catal 2018;8:7679–87. https://doi.org/10.1021/acscatal.8b01598.

[124] Onn TM, Monai M, Dai S, Fonda E, Montini T, Pan X, et al. Smart Pd Catalyst with Improved Thermal Stability Supported on High-Surface-Area LaFeO3 Prepared by Atomic Layer Deposition. J Am Chem Soc 2018;140:4841–8. https://doi.org/10.1021/jacs.7b12900.

[125] Weber ML, Sohn YJ, Dittmann R, Waser R, Menzler NH, Guillon O, et al. Reversibility limitations of metal exsolution reactions in niobium and nickel co-doped strontium titanate. J Mater Chem A Mater 2023;11:17718–27. https://doi.org/10.1039/d3ta02927a.

[126] Joo S, Lim C, Kwon O, Zhang L, Zhou J, Wang J-Q, et al. The first observation of Ni nanoparticle exsolution from YSZ and its application for dry reforming of methane. Materials Reports: Energy 2021;1:100021. https://doi.org/10.1016/J.MATRE.2021.100021.

[127] Jiang Y, Ye L, Zhang S, Xia C. Doped ceria with exsolved Fe0 nanoparticles as a Sr-free cathode for CO2 electrolysis in SOECs at reduced temperatures. J Mater Chem A Mater 2022;10:9380–3. https://doi.org/10.1039/d2ta00684g.

[128] Soni S, Vats · V S, Sudhish Kumar ·, Dalela · B, Mishra M, Meena · R S, et al. Structural, optical and magnetic properties of Fe-doped CeO 2 samples probed using X-ray photoelectron spectroscopy. Journal of Materials Science: Materials in Electronics 2018;29:10141–53. https://doi.org/10.1007/s10854-018-9060-x.

[129] Ansari AA. Optical and structural properties of sol-gel derived nanostructured CeO2 film. Journal of Semiconductors 2010;31:0530011–5. https://doi.org/10.1088/1674-4926/31/5/053001.

[130] Babitha KK, Sreedevi A, Priyanka KP, Sabu B, Varghese T. Structural characterization and optical studies of CeO2 nanoparticles synthesized by chemical precipitation. Indian Journal of Pure and Applied Physics 2015;53:596–603.

[131] Dhannia T, Jayalekshmi S, Santhosh Kumar MC, Prasada Rao T, Chandra Bose A. Effect of iron doping and annealing on structural and optical properties of cerium oxide nanocrystals. Journal of Physics and Chemistry of Solids 2010;71:1020–5. https://doi.org/10.1016/j.jpcs.2010.04.011.

[132] **Ducka A,** Błaszczak P, Zając M, Mizera A, d'Acapito F, Bochentyn B. Limited dissolution of transition metals in the nanocrystalline cerium (IV) oxide. Ceram Int 2024;50:50921–33. https://doi.org/10.1016/j.ceramint.2024.10.004.

[133] Avila-Paredes HJ, Kim S. The effect of segregated transition metal ions on the grain boundary resistivity of gadolinium doped ceria: Alteration of the space charge potential. Solid State Ion 2006;177:3075–80. https://doi.org/10.1016/j.ssi.2006.08.017.

[134] Yang X, Chen J, Panthi D, Niu B, Lei L, Yuan Z, et al. Electron doping of Sr2FeMoO6-δ as high performance anode materials for solid oxide fuel cells. J Mater Chem A Mater 2019;7:733–43. https://doi.org/10.1039/c8ta10061f.

[135] Li X, Zhao H, Xu N, Zhou X, Zhang C, Chen N. Electrical conduction behavior of La, Co co-doped SrTiO3 perovskite as anode material for solid oxide fuel cells. Int J Hydrogen Energy 2009;34:6407–14. https://doi.org/10.1016/j.ijhydene.2009.05.079.

[136] Ruiz-Morales JC, Canales-Vázquez J, Savaniu C, Marrero-López D, Núñez P, Zhou W, et al. A new anode for solid oxide fuel cells with enhanced OCV under methane operation. Physical Chemistry Chemical Physics 2007;9:1821–30. https://doi.org/10.1039/B617266K.

[137] Hatta AH, Jalil AA, Hassan NS, Hamid MYS, Rahman AFA, Teh LP, et al. A review on recent bimetallic catalyst development for synthetic natural gas production via CO methanation. Int J Hydrogen Energy 2021. https://doi.org/10.1016/j.ijhydene.2021.10.213.

[138] De S, Zhang J, Luque R, Yan N. Ni-based bimetallic heterogeneous catalysts for energy and environmental applications. Energy Environ Sci 2016;9:3314–47. https://doi.org/10.1039/C6EE02002J.

[139] R.D. S. Revised Effective Ionic Radii and Systematic Studies of Interatomie Distances in Halides and Chaleogenides. Acta Crystallogr 1976;32:751–67. https://doi.org/10.1023/A:1018927109487.

[140] Kim J, Ferree M, Gunduz S, Millet JMM, Aouine M, Co AC, et al. Exsolution of nanoparticles on A-site-deficient lanthanum ferrite perovskites: its effect on co-electrolysis of CO2 and H2O. J Mater Chem A Mater 2022;10:2483–95. https://doi.org/10.1039/D1TA07389C.

[141] Jain A, Ong SP, Hautier G, Chen W, Richards WD, Dacek S, et al. Commentary: The materials project: A materials genome approach to accelerating materials innovation. APL Mater 2013;1. https://doi.org/10.1063/1.4812323.

[142] Ding XP, Kim WK, Tan KK. Ceramic materials for thermal barrier coatings. J Eur Ceram Soc 2004;24:1–10. https://doi.org/10.1017/S0004972700011849.

[143] Osinkin DA, Bronin DI, Beresnev SM, Bogdanovich NM, Zhuravlev VD, Vdovin GK, et al. Thermal expansion, gas permeability, and conductivity of Ni-YSZ anodes produced by different

techniques. Journal of Solid State Electrochemistry 2014;18:149–56. https://doi.org/10.1007/s10008-013-2239-4.

[144] Usami T, Salman SA, Kuroda K, Gouda MK, Mahdy A, Okido M. Synthesis of Cobalt-Nickel Nanoparticles via a Liquid-Phase Reduction Process. J Nanotechnol 2021;2021. https://doi.org/10.1155/2021/9401024.

[145] Hou B, Lin M, Wei Y, Lu X, Mi S, Bao C. First-Principles Study on Exsolution of Ni and Ni–M (M = Fe, Co, Cr, Cu) Alloy Nanoparticles in the SrTiO3 Model as the Perovskite Cathode of Solid Oxide Electrolysis Cells. The Journal of Physical Chemistry C 2024;128:2867–75. https://doi.org/10.1021/acs.jpcc.3c07287.

[146] Cacciamani G, De Keyzer J, Ferro R, Klotz UE, Lacaze J, Wollants P. Critical evaluation of the Fe-Ni, Fe-Ti and Fe-Ni-Ti alloy systems. Intermetallics (Barking) 2006;14:1312–25. https://doi.org/10.1016/j.intermet.2005.11.028.

[147] Cortez OA, Moura FJ, de Albuquerque Brocchi E, de Siqueira RNC, de Souza RFM. Fe-Ni Alloy Synthesis Based on Nitrates Thermal Decomposition Followed by H2 Reduction. Metallurgical and Materials Transactions B: Process Metallurgy and Materials Processing Science 2014;45:2033–9. https://doi.org/10.1007/s11663-014-0221-x.

[148] Mariani P, Orsilli J, Stoffel H, Mascotto S, Monticelli D, Berretti E, et al. Bimetallic Fe–Ni exsolution from A site deficient SrTiO3: insight into the reciprocal role of metal active centers. Inorg Chem Front 2026;13:3154–69. https://doi.org/10.1039/d5qi02469b.

[149] Budnik J, Gazda M, Maximenko A, Mielewczyk-Gryń A, Pośpiech J, Wachowski S, et al. Sr(Fe,Co)O3−δ Mixed Conductors: How Cobalt Drives Oxygen Vacancy Formation. Chemistry of Materials 2025;37:8822–34. https://doi.org/10.1021/acs.chemmater.5c01904.

[150] Iglesias-Juez A, Chiarello GL, Patience GS, Guerrero-Pérez MO. Experimental methods in chemical engineering: X-ray absorption spectroscopy—XAS, XANES, EXAFS. Canadian Journal of Chemical Engineering 2022;100:3–22. https://doi.org/10.1002/cjce.24291.

[151] Rudolph B, Tsiotsias AI, Ehrhardt B, Dolcet P, Gross S, Haas S, et al. Nanoparticle Exsolution from Nanoporous Perovskites for Highly Active and Stable Catalysts. Advanced Science 2023;10:1–12. https://doi.org/10.1002/advs.202205890.

[152] Mesquita A, Magnavita Oliveira ET, Bonette de Carvalho H. Local and electronic structure of Sr1-xGdxTiO3 probed by X-ray absorption spectroscopy. J Alloys Compd 2021;861. https://doi.org/10.1016/j.jallcom.2020.157975.

[153] Zhao Q, Cheng XL. Study on the Ti K, L2,3, and M Edges of SrTiO3 and PbTiO3. Journal of Physical Chemistry A 2020;124:322–7. https://doi.org/10.1021/acs.jpca.9b09053.

[154] Begum-Hudde V, Lojewski T, Rothenbach N, Eggert B, Eschenlohr A, Ollefs K, et al. Nature of excitons in the Ti L and O K edges of x-ray absorption spectra in bulk SrTiO3 from a combined first principles and many-body theory approach. Phys Rev Res 2023;5. https://doi.org/10.1103/PhysRevResearch.5.013199.

[155] Wu M, Xin HL, Wang JO, Li XJ, Yuan XB, Zeng H, et al. Investigation of the multiplet features of SrTiO3 in X-ray absorption spectra based on configuration interaction calculations. J Synchrotron Radiat 2018;25:777–84. https://doi.org/10.1107/S160057751800423X.

[156] Melcher CL, Friedrich S, Cramer SP, Spurrier MA, Szupryczynski P, Nutt R. Cerium oxidation state in LSO:Ce scintillators. IEEE Trans Nucl Sci 2005;52:1809–12. https://doi.org/10.1109/TNS.2005.856594.

[157] Kujawska K, Dominów M, Zdankiewicz J, Witkowska A, Liao Y Le, Wang SF, et al. Surface Modification of Ni-YSZ Anodes with a Cobalt NPs-Exsolving Perovskite Layer to Improve the Stability of Biogas-Fed SOFC. Catalysts 2026, Vol 16, Page 251 2026;16:251. https://doi.org/10.3390/CATAL16030251.

[158] Li R, Zhang C, Liu J, Zhou J, Xu L. Study on the electrical conductivity of In-doped SrTiO3 with B-site deficiency prepared by sol–gel method. Mater Res Express 2019;6:105914. https://doi.org/10.1088/2053-1591/AB3FE5.

[159] Łącz A, Drożdż E. Porous Y and Cr–doped SrTiO3 materials—electrical and redox properties. Journal of Solid State Electrochemistry 2019 23:10 2019;23:2989–97. https://doi.org/10.1007/S10008-019-04386-3.

[160] Fu QX, Mi SB, Wessel E, Tietz F. Influence of sintering conditions on microstructure and electrical conductivity of yttrium-substituted SrTiO3. J Eur Ceram Soc 2008;28:811–20. https://doi.org/10.1016/J.JEURCERAMSOC.2007.07.022.

[161] Lacz A, Lach R, Drozdz E. Effect of nickel addition on the physicochemical properties of SrTiO3-based materials. Ceram Int 2022;48:24906–14. https://doi.org/10.1016/J.CERAMINT.2022.05.144.

[162] Tang Y, Baumann S, Nijmeijer A, Guillon O, Meulenberg WA. Functional properties of highly stable SrTi0.95-xZr0.05NixO3-δ for use as oxygen transport membranes. J Eur Ceram Soc 2025;45:117715. https://doi.org/10.1016/J.JEURCERAMSOC.2025.117715.

[163] Li L, Qin X, Liu Y, Xin H, Zhang J, Li D, et al. Fabrication and thermoelectric properties of n-type (Sr0.9Gd0.1)TiO3 oxides. Functional Materials Letters 2014;7. https://doi.org/10.1142/S1793604714500143.

[164] Marina OA, Canfield NL, Stevenson JW. Thermal, electrical, and electrocatalytical properties of lanthanum-doped strontium titanate. Solid State Ion 2002;149:21–8. https://doi.org/10.1016/S0167-2738(02)00140-6.

[165] Huang X, Zhao H, Shen W, Qiu W, Wu W. Effect of fabrication parameters on the electrical conductivity of YxSr1−xTiO3 for anode materials. Journal of Physics and Chemistry of Solids 2006;67:2609–13. https://doi.org/10.1016/J.JPCS.2006.08.004.

[166] Yu N, Liu T, Chen X, Miao M, Ni M, Wang Y. Co-generation of liquid chemicals and electricity over Co-Fe alloy/perovskite anode catalyst in a propane fueled solid oxide fuel cell. Sep Purif Technol 2022;291. https://doi.org/10.1016/j.seppur.2022.120890.

[167] Xi X, Cao ZS, Shen XQ, Lu Y, Li J, Luo JL, et al. In situ embedding of CoFe nanocatalysts into Sr3FeMoO7 matrix as high-performance anode materials for solid oxide fuel cells. J Power Sources 2020;459. https://doi.org/10.1016/j.jpowsour.2020.228071.

[168] Awasthi A, Bhatt YJ, Krishnamurthy N, Ueda Y, Garg SP. The reduction of niobium and tantalum pentoxides by silicon in vacuum. vol. 315. 2001.

[169] Suntivich J, Hong WT, Lee YL, Rondinelli JM, Yang W, Goodenough JB, et al. Estimating hybridization of transition metal and oxygen states in perovskites from o k -edge X-ray absorption spectroscopy. Journal of Physical Chemistry C 2014;118:1856–63. https://doi.org/10.1021/jp410644j.

[170] Abbate M, De Groot FMF, Fuggle JC, Fujimori A, Strebel O, Lopez MF, et al. Controlled-valence properties of La1-xSrxFeO3 and La1-xSrxMnO3 studied by soft-x-ray absorption spectroscopy. Phys Rev B 1992;46:4511–9. https://doi.org/10.1103/PhysRevB.46.4511.

[171] Wu Z, Benfatto M, Pedio M, Cimino R, Mobilio S, Barman S, et al. Theoretical analysis of x-ray-absorption near-edge fine structure at the O and metal edges of LaFe and LaCo. Phys Rev B Condens Matter Mater Phys 1997;56:2228–33. https://doi.org/10.1103/PhysRevB.56.2228.

[172] Frati F, Hunault MOJY, De Groot FMF. Oxygen K-edge X-ray Absorption Spectra. Chem Rev 2020;120:4056–110. https://doi.org/10.1021/acs.chemrev.9b00439.

[173] Xi XA, Liu JW, Luo WZ, Fan Y, Zhang JJ, Luo J-LJ-LL, et al. Unraveling the Enhanced Kinetics of Sr2Fe1+xMo1-xO6-δ Electrocatalysts for High-Performance Solid Oxide Cells. Adv Energy Mater 2021;11:1–10. https://doi.org/10.1002/aenm.202102845.

[174] Liao Y, Xi X, Chen H, Liu J, Fu XZ, Luo JL. The emerging Sr2FeMoO6-based electrocatalysts for solid oxide electrochemical cell: synthesis, modulation and applications. Chemical Synthesis 2024;4. https://doi.org/10.20517/cs.2023.47.

[175] Sun H, Xu X, Hu Z, Tjeng LH, Zhao J, Zhang Q, et al. Boosting the oxygen evolution reaction activity of a perovskite through introducing multi-element synergy and building an ordered structure. J Mater Chem A Mater 2019;7:9924–32. https://doi.org/10.1039/c9ta01404g.

[176] Kuiper P, Searle BG, Rudolf P, Tjeng LH, Chen CT. X-ray magnetic dichroism of antiferromagnet Fe2O3: The orientation of magnetic moments observed by Fe 2p x-ray absorption spectroscopy. Phys Rev Lett 1993;70:1549–52. https://doi.org/10.1103/PhysRevLett.70.1549.

[177] Kuo CY, Hu Z, Yang JC, Liao SC, Huang YL, Vasudevan RK, et al. Single-domain multiferroic BiFeO3 films. Nat Commun 2016;7:1–7. https://doi.org/10.1038/ncomms12712.

[178] Baker ML, Mara MW, Yan JJ, Hodgson KO, Hedman B, Solomon EI. K- and L-edge X-ray absorption spectroscopy (XAS) and resonant inelastic X-ray scattering (RIXS) determination of differential orbital covalency (DOC) of transition metal sites. Coord Chem Rev 2017;345:182–208. https://doi.org/10.1016/j.ccr.2017.02.004.

[179] Budnik J, Gazda M, Maximenko A, Mielewczyk-Gryń A, Pośpiech J, Wachowski S, et al. Sr(Fe,Co)O3−δ Mixed Conductors: How Cobalt Drives Oxygen Vacancy Formation. Chemistry of Materials 2025;37:8822–34. https://doi.org/10.1021/ACS.CHEMMATER.5C01904.

[180] Westre TE, Kennepohl P, DeWitt JG, Hedman B, Hodgson KO, Solomon EI. A multiplet analysis of Fe K-edge 1s → 3d pre-Edge features of iron complexes. J Am Chem Soc 1997;119:6297–314. https://doi.org/10.1021/ja964352a.

[181] Yamamoto T. Assignment of pre-edge peaks in K-edge x-ray absorption spectra of 3d transition metal compounds: electric dipole or quadrupole? X-Ray Spectrometry 2008;37:572–84. https://doi.org/10.1002/xrs.1103.

[182] Freitas AP, André RF, Poucin C, Le TKC, Imbao J, Lassalle-Kaiser B, et al. Guidelines for the Molybdenum Oxidation State and Geometry from X-ray Absorption Spectroscopy at the Mo L2,3-Edges. Journal of Physical Chemistry C 2021;125:17761–73. https://doi.org/10.1021/acs.jpcc.1c01875.

[183] Aritani H, Tanaka T, Funabiki T, Yoshida S, Eda K, Sotani N, et al. Study of the local structure of molybdenum-magnesium binary oxides by means of Mo L3-edge XANES and UV-vis spectroscopy. Journal of Physical Chemistry 1996;100:19495–501. https://doi.org/10.1021/jp9615464.

[184] Li D, Li H, Wen Q, Gao C, Song F, Zhou J. Investigation on Photo-Assisted Fenton-like Mechanism of Single-Atom Mn–N–Fe–N–Ni Charge Transfer Bridge Across Six-Membered Cavity of Graphitic Carbon Nitride. Adv Funct Mater 2024;34:1–14. https://doi.org/10.1002/adfm.202313631.

[185] Zhu L, Li Z, Yang M, Zhou Y, Chen J, Xie F, et al. An Effective Approach to Enhance Hydrogen Evolution Reaction and Hydrogen Oxidation Reaction by Ni Doping to MoO3. Small 2023;19:1–8. https://doi.org/10.1002/smll.202303481.

[186] Muñoz M, Farges F, Argoul P. Continuous Cauchy wavelet transform of XAFS spectra. Physica Scripta T 2005;T115:221–2. https://doi.org/10.1238/Physica.Topical.115a00221.

[187] Tian C, Cheng J, Yang J. A highly active cathode material of Cu-doped Sr2Fe1.5Mo0.5O6 for symmetrical solid oxide fuel cells. Journal of Materials Science: Materials in Electronics 2021;32:1258–64. https://doi.org/10.1007/s10854-020-04898-z.

[188] Chen L, Xu J, Wang X, Xie K. Sr2Fe1.5+xMo0.5O6 cathode with exsolved Fe nanoparticles for enhanced CO2 electrolysis. Int J Hydrogen Energy 2020;45:2–8. https://doi.org/10.1016/j.ijhydene.2020.02.140.

[189] Rath MK, Lee KT. Superior electrochemical performance of non-precious Co-Ni-Mo alloy catalyst-impregnated Sr2FeMoO6-δ as an electrode material for symmetric solid oxide fuel cells. Electrochim Acta 2016;212:678–85. https://doi.org/10.1016/j.electacta.2016.07.037.

[190] Wu Y, Li H, Zhang P, Tong S, Han X, Chen H, et al. Multiphase engineering regulation of double perovskite and RP structure heterojunction interfaces for solid oxide fuel cells. Sustainable Materials and Technologies 2024;40:e00905. https://doi.org/10.1016/j.susmat.2024.e00905.

[191] Niu B, Jin F, Zhang L, Shen P, He T. Performance of double perovskite symmetrical electrode materials Sr2TiFe1–xMoxO6–δ (x = 0.1, 0.2) for solid oxide fuel cells. Electrochim Acta 2018;263:217–27. https://doi.org/10.1016/J.ELECTACTA.2018.01.062.

[192] Wang Y, Lei X, Zhang Y, Chen F, Liu T. In-situ growth of metallic nanoparticles on perovskite parent as a hydrogen electrode for solid oxide cells. J Power Sources 2018;405:114–23. https://doi.org/10.1016/J.JPOWSOUR.2018.10.023.

[193] Zheng K, Lach J, Czaja P, Gogacz M, Czach P, Brzoza-Kos A, et al. Designing high-performance quasi-symmetrical solid oxide cells with a facile chemical modification strategy for Sr2Fe2−xWxO6−δ ferrites electrodes with in situ exsolution of nanoparticles. J Power Sources 2023;587. https://doi.org/10.1016/j.jpowsour.2023.233707.

[194] Zheng K, Swierczek K, Polfus JM, Sunding MF, Pishahang M, Norby T. Carbon Deposition and Sulfur Poisoning in SrFe0.75Mo0.25O3-δ and SrFe0.5Mn0.25Mo0.25O3-δ Electrode Materials for Symmetrical SOFCs. J Electrochem Soc 2015;162:1078–87. https://doi.org/10.1149/2.0981509jes.

[195] Barrat S, Fernández-Gutiérrez Z, Calvo-Mola C, Tostivint PA, Bruyère S, Pilloud D, et al. Modeling of the perovskite nickelate SmNiO3 nucleation from amorphous thin films: A Volmer's thermodynamical approach. Acta Mater 2025;282:120509. https://doi.org/10.1016/J.ACTAMAT.2024.120509.

[196] Carrillo AJ, Serra JM. Exploring the Stability of Fe–Ni Alloy Nanoparticles Exsolved from Double-Layered Perovskites for Dry Reforming of Methane. Catalysts 2021;11:741. https://doi.org/10.3390/catal11060741.

[197] Luo Y, Chang X, Wang J, Zhang D, Fu L, Gu XK, et al. Precise Regulation of In Situ Exsolution Components of Nanoparticles for Constructing Active Interfaces toward Carbon Dioxide Reduction. ACS Nano 2025;19:1463–77. https://doi.org/10.1021/acsnano.4c14279.

[198] Yang Y, Li W, Yang S, Shen X, Han Z, Yu H, et al. Ni-Substituted Sr2FeMoO6−δ as an Electrode Material for Symmetrical and Reversible Solid-Oxide Cells. ACS Appl Mater Interfaces 2024;16:21790–8. https://doi.org/10.1021/acsami.4c00509.

[199] Watanabe R, Karasawa F, Yokoyama C, Oshima K, Kishida M, Hori M, et al. Highly stable Fe/CeO2 catalyst for the reverse water gas shift reaction in the presence of H2S. RSC Adv 2023;13:11525–9. https://doi.org/10.1039/D3RA01323E.

[200] Gao Y;, Xiong K;, Zhu B, Gao Y, Xiong K, Zhu B. Design of Cu/MoOx for CO2 Reduction via Reverse Water Gas Shift Reaction. Catalysts 2023, Vol 13, Page 684 2023;13:684. https://doi.org/10.3390/CATAL13040684.

[201] Dai H, Deng X, Zhang A, Zhu Y, Xiao X, Wang Y, et al. Mo-based bimetallic oxide catalysts for the reverse water gas shift reaction. Int J Hydrogen Energy 2024;68:1–7. https://doi.org/10.1016/J.IJHYDENE.2024.04.238.

[202] Chen CH, Chen HK, Huang WH, Chen CL, Choojun K, Sooknoi T, et al. Reversal of methanation-oriented to RWGS-oriented Ni/SiO2 catalysts by the exsolution of Ni2+ confined in silicalite-1. Green Chemistry 2023;25:7582–97. https://doi.org/10.1039/D3GC02399K.

[203] Sengupta S, Jha A, Shende P, Maskara R, Das AK. Catalytic performance of Co and Ni doped Fe-based catalysts for the hydrogenation of CO 2 to CO via reverse water-gas shift reaction. J Environ Chem Eng 2019;7:102911. https://doi.org/10.1016/j.jece.2019.102911.

[204] Wu J, Zhang W, Chen H, Yu W, Sun B, Zhu M, et al. Enhanced sintering resistance of NiFe-based RWGS catalysts through Cu doping. Greenhouse Gases: Science and Technology 2024;14:1113–21. https://doi.org/10.1002/GHG.2314.

[205] Orsini F, Ferrero D, Cannone SF, Santarelli M, Felli A, Boaro M, et al. Exsolution-enhanced reverse water-gas shift chemical looping activity of Sr2FeMo0.6Ni0.4O6-δ double perovskite. Chemical Engineering Journal 2023;475. https://doi.org/10.1016/j.cej.2023.146083.

[206] Farzin YA, Babaei A, Ataie A. Low-temperature synthesis of Sr2FeMoO6 double perovskite; structure, morphology, and magnetic properties. Ceram Int 2020;46:16867–78. https://doi.org/10.1016/J.CERAMINT.2020.03.264.

[207] Carrillo AJ, Serra JM. Exploring the stability of Fe–Ni alloy nanoparticles exsolved from double-layered perovskites for dry reforming of methane. Catalysts 2021;11. https://doi.org/10.3390/catal11060741.

[208] Tan W, Hu P, Feng T, Zhao S, Wang S, Song H, et al. Effects of Cu Substituting Mo in Sr2Fe1.5Mo0.5O6−δ Symmetrical Electrodes for CO2 Electrolysis in Solid Oxide Electrolysis Cells. Nanomaterials 2025;15. https://doi.org/10.3390/nano15080585.

[209] Lufaso MW, Woodward PM. Jahn-Teller distortions, cation ordering and octahedral tilting in perovskites. Acta Crystallogr B 2004;60:10–20. https://doi.org/10.1107/S0108768103026661.

[210] Du Z, Zhao H, Yi S, Xia Q, Gong Y, Zhang Y, et al. High-Performance Anode Material Sr2FeMo0.65Ni0.35O6 - δ with in Situ Exsolved Nanoparticle Catalyst. ACS Nano 2016;10:8660–9. https://doi.org/10.1021/ACSNANO.6B03979/ASSET/IMAGES/LARGE/NN-2016-03979R_0011.JPEG.

[211] Naiqing Z, Kening S, Derui Z, Dechang J. Study on Properties of LSGM Electrolyte Made by Tape Casting Method and Applications in SOFC. Journal of Rare Earths 2006;24:90–2. https://doi.org/10.1016/S1002-0721(07)60331-7.

[212] Yang B, Yu X, Halder A, Zhang X, Zhou X, Mannie GJA, et al. Dynamic Interplay between Copper Tetramers and Iron Oxide Boosting CO2 Conversion to Methanol and Hydrocarbons under Mild Conditions. ACS Sustain Chem Eng 2019;7:14435–42. https://doi.org/10.1021/ACSSUSCHEMENG.9B01561.

[213] Błaszczak P, Mizera A, Bochentyn B, Wang S-F, Jasiński P. Preparation of methanation catalysts for high temperature SOEC by β-cyclodextrin-assisted impregnation of nano-CeO2 with transition metal oxides. Int J Hydrogen Energy 2021. https://doi.org/10.1016/J.IJHYDENE.2021.10.144.

[214] Depuydt PJ, Parlee NAD. The diffusion of hydrogen in liquid iron alloys. Metallurgical Transactions 1972 3:2 1972;3:529–36. https://doi.org/10.1007/BF02642058.

[215] Haas O, Vogt UF, Soltmann C, Braun A, Yoon W, Yang XQ, et al. The Fe K-edge X-ray absorption characteristics of La 1 À x Sr x FeO 3 À d prepared by solid state reaction. Mater Res Bull 2009;44:1397–404. https://doi.org/10.1016/j.materresbull.2008.11.026.

[216] Rondinelli JM, Spaldin NA. Structure and Properties of Functional Oxide Thin Films : Insights From Electronic-Structure Calculations. Advanced Materials 2011;23:3363–81. https://doi.org/10.1002/adma.201101152.

[217] Martinson A, Guinn M, Mortensen P, Hona RK. Correlation Between Conductivity and Oxygen Evolution Reaction Activity in Perovskite Oxides CaMnO3-δ, Ca0.5Sr0.5MnO3-δ and SrMnO3-δ. Sustainable Chemistry 2025;6. https://doi.org/10.3390/suschem6010003.

[218] Zhang X, Pei C, Chang X, Chen S, Liu R, Zhao ZJ, et al. FeO6 Octahedral Distortion Activates Lattice Oxygen in Perovskite Ferrite for Methane Partial Oxidation Coupled with CO2 Splitting. J Am Chem Soc 2020;142:11540–9. https://doi.org/10.1021/jacs.0c04643.

[219] Rath MK, Lee KT. Characterization of novel Ba2LnMoO6 (Ln = Pr and Nd) double perovskite as the anode material for hydrocarbon-fueled solid oxide fuel cells. J Alloys Compd 2018;737:152–9. https://doi.org/10.1016/j.jallcom.2017.12.090.

[220] Lim T, Jo K, Lee H. Oxygen Vacancy and Valence Band Structure of Ba0.5Sr0.5Fe1−xCuxO3−δ (x = 0–0.15) with Enhanced ORR Activity for IT-SOFCs. Materials 2023.

[221] Liu HX, Li SQ, Wang WW, Yu WZ, Zhang WJ, Ma C, et al. Partially sintered copper–ceria as excellent catalyst for the high-temperature reverse water gas shift reaction. Nature Communications 2022 13:1 2022;13:867-. https://doi.org/10.1038/s41467-022-28476-5.

[222] Dole H, Caravaggio G, Ahledel N, Aoun R, Radfarnia H, Zanganeh KE. Role of Oxygen Vacancies in Fe/Ru-Based Catalysts for the Reverse Water Gas Shift Reaction: Performance and Characterization. ACS Omega 2026;11:10304–19. https://doi.org/10.1021/acsomega.5c11416.

[223] Zhang L, Zhou Q, He Q, He T. Double-perovskites A2FeMoO6-δ (A = Ca, Sr, Ba) as anodes for solid oxide fuel cells. J Power Sources 2010;195:6356–66. https://doi.org/10.1016/j.jpowsour.2010.04.021.

[224] Li S, Liu X, Ma J, Xu F, Lyu Y, Perathoner S, et al. Develop High-Performance Cu-Based RWGS Catalysts by Controlling Oxide–Oxide Interface. ACS Catal 2025;15:3475–86. https://doi.org/10.1021/ACSCATAL.4C07729.

[225] Thompson RS, Langlois GG, Li W, Brann MR, Sibener SJ. Reverse water-gas shift chemistry inside a supersonic molecular beam nozzle. Appl Surf Sci 2020;515:145985. https://doi.org/10.1016/J.APSUSC.2020.145985.

[226] Ren J, Abbasi Z, Xu N, Lou H, Xu G, Xu Q, et al. Materializing equilibrium conversion of reverse water-gas shift reaction over CuFe/CeZrOx catalyst at low temperature. Sep Purif Technol 2025;368:132966. https://doi.org/10.1016/J.SEPPUR.2025.132966.

[227] Loiland JA, Wulfers MJ, Marinkovic NS, Lobo RF. Fe/γ-Al2O3 and Fe–K/γ-Al2O3 as reverse water-gas shift catalysts. Catal Sci Technol 2016;6:5267–79. https://doi.org/10.1039/C5CY02111A.

[228] Pahija E, Panaritis C, Gusarov S, Shadbahr J, Bensebaa F, Patience G, et al. Experimental and Computational Synergistic Design of Cu and Fe Catalysts for the Reverse Water–Gas Shift: A Review. ACS Catal 2022;12:6887–905. https://doi.org/10.1021/ACSCATAL.2C01099.

[229] Ko J, Kim BK, Han JW. Density Functional Theory Study for Catalytic Activation and Dissociation of CO2 on Bimetallic Alloy Surfaces. Journal of Physical Chemistry C 2016;120:3438–47. https://doi.org/10.1021/ACS.JPCC.6B00221.